

# **Development of Novel Electrode Concepts for Proton Exchange Membrane Water Electrolyzers**

**vorgelegt von  
Melanie Bühler**

**an der  
Albert-Ludwigs-Universität Freiburg**





Dissertation zur Erlangung des Doktorgrades der  
Technischen Fakultät der  
Albert-Ludwigs-Universität Freiburg im Breisgau

Freiburg im Breisgau 2019



Dekan: Herr Prof. Dr. Rolf Backofen

Erstgutachter: Herr Prof. Dr. Stefan Glunz

Zweitgutachter: Herr Prof. Dr. Simon Thiele

Datum der Abgabe: 26.11.2019

Datum der Prüfung: 07.02.2020

Melanie Bühler

IMTEK – Institut für Mikrosystemtechnik

Professur für Anwendungsentwicklung

Technische Fakultät

Albert-Ludwigs-Universität Freiburg im Breisgau



Der härteste und wichtigste Kampf des 21. Jahrhunderts wird ohne Waffen geführt. Die Werkzeuge dieses Kampfes heißen: Energieeffizienz, Energie sparen und erneuerbare Energien.“

(Franz Alt, 2007)





## Abstract

In this thesis, the development of porous transport electrodes (PTEs) for proton exchange membrane water electrolyzers (PEMWEs) is presented. Compared to state of the art, the catalysts for the oxygen and hydrogen evolution are not deposited on the proton exchange membrane (PEM) but directly on porous titanium and carbon substrates. This approach bears the potential to improve the electrical connection of the catalyst particles as well as to facilitate manufacturing of membrane electrode assemblies (MEAs). As PTEs for the oxygen evolution at the anode side are not yet commercially available, the electrode development in this work focuses mainly on the fabrication and optimization of anodic PTEs based on commercial titanium substrates. The main goal on the cathode side is the reduction of the noble-metal loading. The most important results of this work are:

- A comprehensive electrochemical and structural characterization of different MEAs based on state-of-the-art towards PTE-based MEAs revealed a more profound understanding on performance limiting parameters for PEMWE. The results of this study can be the base for further optimizing MEAs.<sup>1</sup>
- In the frame of a material study for anodic PTEs, influences of titanium substrates and composition of the catalyst layer were evaluated. The in this work for 200 h continuous operated anodic PTE with an IrO<sub>2</sub>-loading of 1.4 mg cm<sup>-2</sup> und 9 wt% Nafion reached a current density of 4 A cm<sup>-2</sup> at 2.2 V and could therefore be developed with a performance similar to state-of-the-art CCM-based approaches.<sup>2</sup>
- PTEs with reduced noble-metal content were successfully developed both for the anode and cathode side, respectively. Anodic PTEs showed a by 160 mV reduced cell voltage of 1.95 V at 5 A cm<sup>-2</sup>, when 1.2 mg<sub>Ir</sub> cm<sup>-2</sup> of an IrO<sub>2</sub>-catalyst supported on titanium dioxide was deposited on porous titanium substrates.<sup>3</sup> Noble-metal free cathodic PTEs based on [Mo<sub>3</sub>S<sub>13</sub>]<sup>2-</sup>-nanoclusters reached a current density of 4 A cm<sup>-2</sup> at 2.36 V at a loading of 3 mg cm<sup>-2</sup>, even after 100 h continuous operation at 1 A cm<sup>-2</sup>.<sup>4</sup> Both catalysts were for the first time characterized in full-cell PEMWE tests and the performance of the noble-metal free PTE-based MEA was to the best of the authors knowledge highest so far reported when using a non-noble catalyst for the hydrogen evolution side.
- By use of the in this work developed anodic PTEs, the direct membrane deposition (DMD) as a cost-efficient manufacturing technique for PEMWE MEAs could be studied.<sup>5</sup> To allow for a symmetric DMD approach as presented for PEM fuel cells, approaches for the structural optimization of anodic PTEs are presented in this work.<sup>6</sup>

The PTE-based MEAs developed in this work, show the potential to reduce the noble-metal content and manufacturing costs for PEMWEs. The comprehensive material studies performed in this work can serve as base for the further optimization of PTEs, with the focus on the not yet commercially available anodic PTEs.

## Deutsche Zusammenfassung

In dieser Arbeit wird die Entwicklung von porösen Transportelektroden (PTEs) für Polymer-Elektrolyt-Membran Wasserelektrolyseure (PEMWE) vorgestellt. Im Vergleich zum Stand der Technik werden hierbei die Katalysatoren für die Sauerstoff- und Wasserstoffentwicklung nicht auf die Polymer-Elektrolyt-Membran (PEM), sondern direkt auf poröse Titan- und Kohlenstoffsubstrate aufgebracht. Dieser Ansatz verbessert die elektrische Anbindung der Katalysatorpartikel und birgt das Potential einer vereinfachten Herstellung für Membran-Elektroden-Einheiten (MEEs). Da PTEs für die Sauerstoffentwicklung an der Anode bisher nicht kommerziell erhältlich sind, konzentriert sich die Elektrodenentwicklung in dieser Arbeit hauptsächlich auf die Herstellung und Optimierung anodenseitiger PTEs basierend auf kommerziell erhältlichen Titansubstraten. Kathodenseitig steht die Reduzierung des Edelmetallgehalts im Vordergrund. Die wichtigsten Ergebnisse dieser Arbeit sind:

- Eine umfassende elektrochemische und strukturelle Charakterisierung verschiedener MEEs ausgehend vom Stand der Technik hin zu einer PTE-basierten MEE führte zu einem tieferen Verständnis von leistungslimitierenden Faktoren für die PEMWE. Die Ergebnisse dieser Studie können nun als Diskussionsbasis für die Optimierung von MEEs dienen.<sup>1</sup>
- In einer Materialstudie für anodenseitige PTEs konnte der Einfluss von Titansubstraten und die Zusammensetzung der Katalysatorschicht untersucht werden. Die in dieser Arbeit über 200 h kontinuierlich betriebenen PTE mit einer  $\text{IrO}_2$ -Beladung von  $1.4 \text{ mg cm}^{-2}$  und 9 wt% Nafion erzielte eine Stromdichte von  $4 \text{ A cm}^{-2}$  bei 2.2 V und konnte somit mit einer Leistung vergleichbar zum Stand der Technik entwickelt werden.<sup>2</sup>
- PTEs mit reduziertem Edelmetallgehalt wurden sowohl für Kathode als auch für die Anode erfolgreich entwickelt. Anodenseitig konnte eine um 160 mV reduzierte Zellspannung von 1.95 V bei  $5 \text{ A cm}^{-2}$  erreicht werden, indem  $1.2 \text{ mg}_{\text{Ir}} \text{ cm}^{-2}$  eines auf Titanoxid geträgerten  $\text{IrO}_2$ -Katalysators auf poröse Titansubstrate aufgebracht wurde.<sup>3</sup> Edelmetallfreie kathodenseitige PTEs basierend auf  $[\text{Mo}_3\text{S}_{13}]^{2-}$ -Nanoclustern erzielten bei einer Beladung von  $3 \text{ mg cm}^{-2}$  eine Stromdichte von  $4 \text{ A cm}^{-2}$  bei 2.36 V, nach 100 h kontinuierlichem Betrieb bei  $1 \text{ A cm}^{-2}$ .<sup>4</sup> Beide Katalysatoren wurden erstmalig in Vollzell-PEMWE Tests charakterisiert. Nach besten Wissen der Autorin konnte die bisher höchste Leistung mit einer edelmetallfreien Elektrode für die Wasserstoffentwicklung erzielt werden.
- Mit Hilfe der in dieser Arbeit entwickelten anodenseitigen PTEs konnte die Direkt-Membran-Deposition (DMD) als kosteneffiziente Herstellungsmethode für PEMWE MEEs untersucht werden.<sup>5</sup> Um einen symmetrischen DMD-Aufbau wie für PEM Brennstoffzellen zu ermöglichen, wurden in dieser Arbeit Möglichkeiten für die strukturelle Optimierung der anodenseitigen PTEs vorgestellt.<sup>6</sup>

Die in dieser Arbeit entwickelten PTE-basierten MEEs zeigen das Potential zur Reduzierung des Edelmetallgehaltes und der Herstellungskosten für PEMWEs. Umfassende Materialstudien können als Grundlage für die weitere Optimierung von PTE-basierten MEEs dienen, wobei der Fokus auf der bisher nicht kommerziell erhältlichen anodenseitigen PTE liegt.

# Table of Content

<b>Abstract.....</b>	<b>ix</b>
<b>Deutsche Zusammenfassung.....</b>	<b>x</b>
<b>Table of Content .....</b>	<b>xi</b>
<b>Notation .....</b>	<b>xiv</b>
<b>1 Introduction.....</b>	<b>- 1 -</b>
1.1 Transition from fossil fuels to renewable energy sources in a future hydrogen economy.-	1 -
1.2 Proton exchange membrane water electrolysis (PEMWE) as key technology for the sustainable production of green hydrogen.....	4 -
<b>2 PEMWE: functional components, working principle and electrode development .....</b>	<b>- 7 -</b>
2.1 Functional components of a PEMWE cell .....	- 7 -
2.2 Influence of functional components on the polarization behavior of PEMWEs .....	- 11 -
2.3 PEMWE electrode development .....	- 17 -
2.4 Structure of this thesis .....	- 19 -
<b>3 Materials and Methods.....</b>	<b>- 21 -</b>
3.1 Commercial MEA materials .....	- 21 -
3.2 Fabrication of electrodes via spray coating.....	- 22 -
3.3 Sintering of Ti-MPLs.....	- 26 -
3.4 Electrochemical characterization .....	- 27 -
3.4.1 Test cell and test bench to test the different MEA-configurations.....	- 27 -
3.4.2 Recording and analysis of MEA polarization data .....	- 29 -
3.4.3 Three-electrode-setup.....	- 30 -
3.5 Structural characterization.....	- 31 -
3.5.1 Morphology and surface structure.....	- 31 -
3.5.2 Chemical composition .....	- 32 -
3.5.3 Catalyst ink stability and thickness of deposited Nafion layers .....	- 33 -
<b>4 From Catalyst Coated Membranes to Porous Transport Electrode Based Configurations in PEM Water Electrolyzers *</b> .....	<b>- 35 -</b>
4.1 Abstract .....	- 35 -
4.2 Introduction .....	- 36 -
4.3 Experimental.....	- 37 -
4.4 Results and Discussion.....	- 40 -
4.4.1 Design of Experiments and Research Hypothesis .....	- 40 -
4.4.2 Influence of Cathode PTE (cPTE) on the Polarization Behavior.....	- 42 -

4.4.3 Influence of Anode PTE (aPTE) and Symmetric PTE (c/a PTE) on the Polarization Behavior .....	- 44 -
4.4.4 Influence of Nafion Impregnated Anode PTE (ai PTE) on the Polarization Behavior .....	- 46 -
4.5 Conclusions.....	- 48 -
4.6 Critical discussion .....	- 49 -
<b>5 Optimization of anodic porous transport electrodes for proton exchange membrane water electrolyzers *</b> .....	<b>- 51 -</b>
5.1 Abstract.....	- 51 -
5.2 Introduction.....	- 52 -
5.3 Experimental .....	- 54 -
5.4 Results and Discussion .....	- 56 -
5.4.1 Influence of the titanium porous transport layer on cell polarization .....	- 56 -
5.4.2 Influence of the Nafion content in the catalyst layer .....	- 58 -
5.4.3 Influence of the IrOx loading .....	- 60 -
5.5 Conclusions.....	- 65 -
5.6 Critical Discussion.....	- 66 -
<b>6 IrO<sub>2</sub> coated TiO<sub>2</sub> core-shell microparticles advance performance of low loading proton exchange membrane water electrolyzers *</b> .....	<b>- 67 -</b>
6.1 Introduction.....	- 68 -
6.2 Synthesis and characterization of the IrO <sub>2</sub> @TiO <sub>2</sub> catalyst .....	- 69 -
6.3 MEA preparation and characterization.....	- 70 -
6.3.1 Catalyst inks: preparation and stability test .....	- 70 -
6.3.2 Fabrication of porous transport electrodes .....	- 71 -
6.3.3 Structural characterization of porous transport electrodes .....	- 71 -
6.3.4 MEA testing .....	- 71 -
6.4 Results: MEA preparation and characterization .....	- 72 -
6.4.1 Catalyst inks: preparation and stability test .....	- 72 -
6.4.2 Structural characterization of porous transport electrodes .....	- 73 -
6.4.3 MEA testing .....	- 74 -
6.5 Summary and Conclusion.....	- 78 -
6.6 Supporting information.....	- 79 -
6.7 Outlook: gradient sized catalyst layers based on IrO <sub>2</sub> @TiO <sub>2</sub> to reduce the noble metal loading .....	- 81 -
<b>7 Development of titanium based MPLs for anodic Ti-PTLs .....</b>	<b>- 85 -</b>
7.2 First studies on developing a binder based Ti-MPL .....	- 86 -
7.3 First studies on developing sintered Ti-powder MPLs .....	- 88 -
7.4 Outlook: via MPLs towards advanced DMD-configurations for PEMWE.....	- 91 -

<b>8 Noble metal free Mo<sub>3</sub>S<sub>13</sub>-NCNT catalyst based cathodic PTEs*</b>	<b>- 93 -</b>
8.1 Introduction	- 94 -
8.2 Synthesis and characterization of Mo <sub>3</sub> S <sub>13</sub> -NCNT catalyst	- 95 -
8.3 MEA preparation and characterization	- 96 -
8.4 Full-cell characterization	- 96 -
8.4.1 Variation of the Mo <sub>3</sub> S <sub>13</sub> -NCNT-loading	- 96 -
8.4.2 Performance of Mo <sub>3</sub> S <sub>13</sub> -NCNT under high cell current density	- 98 -
8.5 Critical discussion	- 100 -
<b>9 Summary</b>	<b>- 103 -</b>
<b>10 Outlook</b>	<b>- 105 -</b>
<b>List of publications</b>	<b>- 107 -</b>
Publications in peer reviewed journals	- 107 -
Conference contributions	- 107 -
<b>Acknowledgements</b>	<b>- 109 -</b>
<b>References</b>	<b>- 111 -</b>
<b>Erklärung</b>	<b>- 121 -</b>

# Notation

## List of symbols

Symbol	Meaning	Unit
$a$	Tafel slope	V
$b$	Tafel coefficient	V
$d$	diameter	m
$F$	Faraday constant	C mol <sup>-1</sup>
$\Delta G_R$	Gibbs free energy of reaction	J mol <sup>-1</sup>
$h$	height (ultrasonic spray nozzle)	m
$\Delta H_R$	reaction enthalpy	J mol <sup>-1</sup>
$I$	electrical current	A
$i$	current density	A m <sup>-2</sup>
$i_0$	exchange current density	A m <sup>-2</sup>
$P$	ultrasonic power	W
$p$	pitch (spray pattern)	m
$R$	universal gas constant	J K <sup>-1</sup> mol <sup>-1</sup>
$r$	flow rate	m <sup>3</sup> min <sup>-1</sup>
$R_{cell}$	ohmic cell resistance	$\Omega$
$S$	electrochemically active site	-
$s$	shaping air	Pa
$\Delta S_R$	reaction entropy	J K <sup>-1</sup> mol <sup>-1</sup>
$T$	temperature	K
$v$	velocity (path speed)	m s <sup>-1</sup>
$V_{cell}$	cell voltage	V
$V_{rev}$	reversible cell voltage	V
$V_{th}$	thermoneutral cell voltage	V
$wt\%$	weight %	%
$z$	number of electrons	-
$\alpha$	activity	-
$\beta$	charge transfer coefficient	-
$\varepsilon_V$	voltage efficiency	%
$\eta$	overpotential	V
$\sigma_{mem}$	specific proton conductivity of the membrane	S m <sup>-1</sup>

## List of abbreviations

<b>Abbreviation</b>	<b>Meaning</b>
<i>aPTE</i>	anodic porous transport electrode
<i>ai PTE</i>	impregnated anodic porous transport electrode
<i>aPTL</i>	anodic porous transport layer
<i>CCM</i>	catalyst coated membrane
<i>CL</i>	catalyst layer
<i>cPTE</i>	cathodic porous transport electrode
<i>cPTL</i>	cathodic porous transport layer
<i>ECSA</i>	electrochemical surface area
<i>EDX</i>	energy dispersive X-ray spectroscopy
<i>FIB – SEM</i>	focused ion beam scanning electron microscopy
<i>GO</i>	graphene oxide
<i>GWP</i>	global warming potential
<i>HER</i>	hydrogen evolution reaction
<i>HFR</i>	high frequency resistance
<i>IPA</i>	2-Propanol
<i>MEA</i>	membrane electrode assembly
<i>MPL</i>	micro porous layer
<i>NCNT</i>	nitrogen doped carbon nanotube
<i>NP</i>	nanoparticles
<i>OCV</i>	open circuit voltage
<i>OER</i>	oxygen evolution reaction
<i>PEG</i>	polyethylene glycol
<i>PEM</i>	proton exchange membrane
<i>PEMFC</i>	proton exchange membrane fuel cell
<i>PEMWE</i>	proton exchange membrane water electrolysis
<i>PFSA</i>	perfluorosulfonic acid
<i>PTE</i>	porous transport electrode
<i>PTFE</i>	polytetrafluoroethylene
<i>PTL</i>	porous transport layer
<i>rGO</i>	reduced graphene oxide
<i>SEM</i>	scanning electron microscopy
<i>TEM</i>	transmission electron microscopy
<i>TGA</i>	thermogravimetric analysis
<i>TSI</i>	turbiscan stability index
<i>UNFCCC</i>	United Nations Framework Convention on Climate Change
<i>XPS</i>	X-ray photoelectron spectroscopy





# 1 Introduction

## 1.1 Transition from fossil fuels to renewable energy sources in a future hydrogen economy

Already in the 1990s, many researchers warned of the direct destructive impact of industrialization on global climate.<sup>7</sup> The consequences of human-made air-, water- and land-pollution as well as the environmental exploitation on all living organisms were however not taken seriously and were ignored for too long.<sup>8, 9</sup> The most prominent environmental change, global warming, is being recognized for years by various institutes monitoring the sea and land temperatures<sup>10, 11</sup> and was identified to be caused by an **anthropogenic greenhouse effect**.<sup>12, 13</sup> The greenhouse effect in general describes the entrapment of heat in form of infrared light emitted by the earth and re-emission in all directions via greenhouse gases in the atmosphere. The natural greenhouse effect is essential to establish a global mean surface near temperature of around 15 °C suitable for living organisms, whereas temperatures without the greenhouse effect would be as low as -18 °C.<sup>14</sup> However, the releasing of large amounts of industrial pollutants increases the amount of greenhouse gases in the atmosphere. By this, an unnaturally high entrapment of infrared radiation is caused, leading to global warming with drastic consequences for nature and living organisms on earth.<sup>15, 16</sup> The impact of greenhouse gases in the atmosphere on global warming depends on three parameters: the lifetime of the exposed greenhouse gas molecules in the atmosphere, the concentration and the capacity to entrap infrared light.<sup>17</sup> Fig. 1 A shows the atmospheric greenhouse gas emissions in the year 2017 of the 43 Annex I parties of the United Nations Framework Convention on Climate Change (UNFCCC) divided into contributions from carbon dioxide (CO<sub>2</sub>), methane (CH<sub>4</sub>), nitrous oxide (N<sub>2</sub>O) and fluorinated gases.<sup>18</sup> CO<sub>2</sub>-emissions contributed to the largest amount of 80.9 % of greenhouse gas emissions.

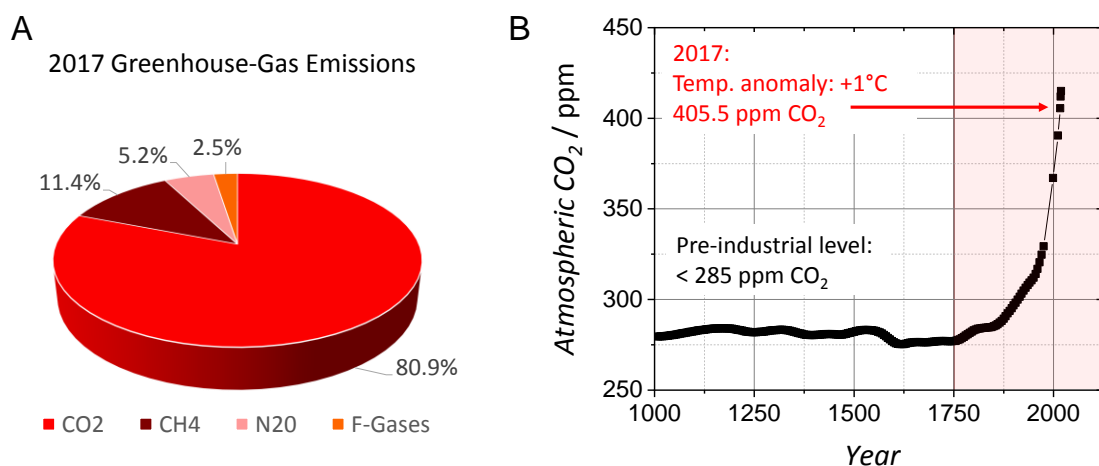


**Fig. 1** A Greenhouse gas emissions of Annex I parties (UNFCCC) in 2017.<sup>18</sup> B CO<sub>2</sub> concentrations in the atmosphere from pre-industrial level until today. Data until the year 1975 was drawn from the analysis of air in ice cores<sup>19</sup>, values from 1999 and 2011 are of IPCC reports AR3<sup>20</sup> and AR5<sup>21</sup>, value 2017 is from the WMO Greenhouse Gas Bulletin No.14: November 2018<sup>22</sup>, values 2018 and 2019 are from CO<sub>2</sub> earth daily<sup>23</sup>. In the year 2017 a temperature anomaly of +1 °C compared to the pre-industrial level was reported in a special report of the IPCC in 2018.<sup>24</sup>

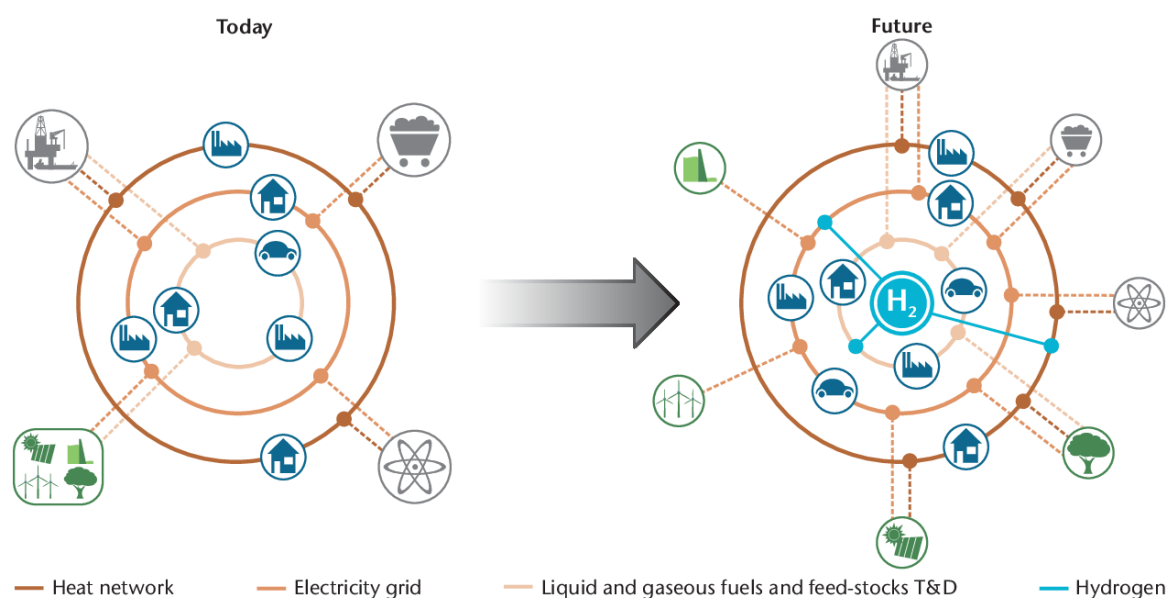
To assess the potential risk of different greenhouse gases on global warming, the global warming potential (GWP) was introduced in the Kyoto protocol<sup>25</sup> as common measure. It quantifies the amount of heat energy that is absorbed by the greenhouse gas combined with its lifetime in the atmosphere over a period of 100 years. The GWP of CO<sub>2</sub> is used as reference and therefore equals one.<sup>26</sup> High-GWP sources with GWPs several thousand times higher than CO<sub>2</sub> are fluorinated gases

used e.g. as refrigerants. Due to their destructive effect on ozone depletion, most fluorinated gases were banned from production starting in 1987 with the Montreal protocol<sup>27</sup>, but they still account for 2.5 % of the total greenhouse gas emissions in 2017. Methane and NH<sub>2</sub> are side products of the agricultural sector and have GWP values almost 20 times and 300 times higher than CO<sub>2</sub>, respectively. Agricultural capacities are expected to grow with the risk of e.g. a non-regulated use of toxic fertilizers and rapid deforestation.<sup>28–30</sup> When (rain) forests are burned to give way to fields and plants, CO<sub>2</sub> is set free in the atmosphere and less CO<sub>2</sub> is bound.<sup>31</sup> Other large sources for CO<sub>2</sub> emissions are the burning of fossil fuels as coal, gas and oil for the energy and industrial sector and the production of lime, cement and ammonia.<sup>32</sup> Whereas the number of **CO<sub>2</sub> sources** increased rapidly during the last decades, CO<sub>2</sub> sinks as forests, land and oceans were more and more destroyed or are oversaturated.<sup>33</sup> Before the industrial revolution, atmospheric CO<sub>2</sub> was at a quite stable level of lower than 300 ppm.<sup>34–36</sup> The implementation of a fossil fuel based economy in the 1750s led to a rapid increase of atmospheric CO<sub>2</sub>, which has nowadays exceeded 415 ppm (Fig. 1 B).<sup>19–23</sup> Compared to preindustrial levels, this resulted in a temperature anomaly of +1 °C in the year 2017.<sup>24</sup> The indicated direct correlation between man-made increasing atmospheric CO<sub>2</sub> concentrations and global warming should therefore not be further ignored or trivialized by policy makers and society.<sup>37, 38</sup>

The increase of CO<sub>2</sub> emissions does not only influence the global temperature but also accounts for the acidification of oceans with severe consequences for sensitive ecosystems and organisms like coral reefs<sup>39</sup>. Their worldwide monitored mortality of 30 % since the 1980s was reported by several institutions.<sup>40</sup> Veron et al. have determined a required reduction of the CO<sub>2</sub> content to below 350 ppm to protect the corals<sup>41</sup>, but this value is now clearly exceeded (Fig. 1 B). Corals can adapt to changes in the CO<sub>2</sub> environment<sup>42</sup>, but Frieler et al. stated, that to save more than 10 % of the global coral reefs, the global increase in temperature must stay below 1.5 °C.<sup>43</sup> The mortality of sensitive habitats as coral reefs is not the only consequence of global warming. Hansen et al. warned, that a global temperature rise of 2 °C above preindustrial level would most likely cause the melting of huge ice shelves, a slowing down of air and water circulation, the rise of the sea level and also extreme weather scenarios.<sup>44</sup> When ecosystems suffer from climate change, the basis of existence for human beings living in those areas, will be in danger. In the worst case scenario, climate change could even cause a mass movement of millions of people.<sup>45, 46</sup>

To stop global warming, a drastic reduction of greenhouse gas emissions, especially of CO<sub>2</sub>, is essential by all countries worldwide. Therefore, almost 200 members of the UNFCCC signed the '**Paris agreement**' in 2016 with legally binding contracts and measures to keep global warming well **below 2 °C**.<sup>47</sup> The most promising way to reduce CO<sub>2</sub> emissions is the (complete) transition from fossil energy carriers towards **sustainable energy sources** like wind, solar, hydro and biomass. Within the EU, 20 % of renewables were planned to be installed by the year 2020 as stated in the EU2020 roadmap in 2011.<sup>48</sup> In 2017, the share of renewables to reach the final EU energy target was as high as 17.4 %<sup>49</sup> However, to reach the goal of reducing greenhouse-gas emissions in the EU by over 80% until the year 2050 compared to levels of 1990 (EU2050 roadmap), approximately 55 % of the total energy consumption must be guaranteed by renewables.<sup>50</sup> Renewable energy sources like wind or solar are highly dependent on their fluctuating environment and are not necessarily installed close to the final consumer. Consequently, a fluctuating production of electricity is the case and its storage and distribution is an essential technological challenge to balance the power grid.<sup>51–53</sup> **Storage concepts** for high power applications are e.g. pumped hydroelectric storage and compressed air energy storage with efficiencies of 65–85 % and 60–80 % respectively.<sup>51</sup> Batteries based on lithium ion or nickel metal hydride with efficiencies up to 80 % are in principle suitable to store electrical energy on smaller

scales, but the partly limited cycle life, toxic components and severe self-discharge are drawbacks when being coupled with fluctuating renewables for the longterm storage of green electricity.<sup>54</sup> In hydrogen storage concepts, electrical energy is converted in a water electrolyzer into chemical energy via splitting water with the help of electricity into hydrogen and oxygen. The gases can then be on demand reconverted into electricity in a fuel cell. Water electrolyzers were originally developed e.g. to supply oxygen within submarines, but nowadays gained great attention due to the production of pure, sustainable hydrogen.<sup>55, 56</sup> Hydrogen is on the one hand an intermediate medium in the energy storage concept for renewables, but on the other hand a promising sustainable second energy carrier for the transition from a fossil fuel based economy **towards a hydrogen economy**.<sup>57–60</sup> Applications are the growing market of fuel cell vehicles as alternative to combustion engines in the transportation sector<sup>61</sup> or the use in the chemical industry.<sup>62</sup> Power-to-gas concepts for the long distance distribution of methanized hydrogen produced by electrolysis via the existing natural gas grid are currently under investigation.<sup>63, 64</sup> Fig. 2 shows the scenario of a future hydrogen economy supplying the heat network, electricity grid as well as the transportation and industrial sector.<sup>65</sup> In such a future scenario, the impact of fossil fuels and nuclear energy is reduced and green energy sources like biomass, solar and wind are more prominent or even dominant.



**KEY POINT:** *Hydrogen can link different energy sectors and energy T&D networks and thus increase the operational flexibility of future low-carbon energy systems.*

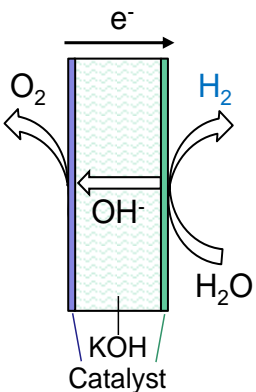
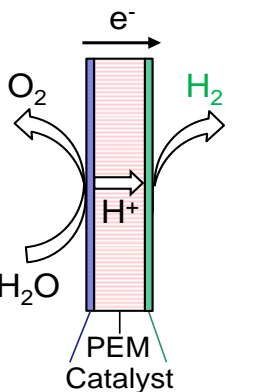
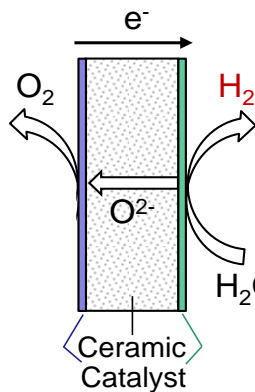
**Fig. 2** Schematic of a future hydrogen economy supplying the heat network, electricity grid as well as the transportation and industrial sector.<sup>65</sup> Fossil fuels and nuclear power will play a minor role in this hydrogen based future scenario.

In the year 2015, the worldwide largest power-to-gas demonstrator plant ‘Energiepark Mainz’ was put into operation in Germany.<sup>66, 67</sup> In the park, hydrogen is produced with an efficiency of 60 % via a 6 MW (peak power) water electrolyzer coupled to a wind park and distributed e.g. via the natural gas grid. The project is a collaboration of the city of Mainz (wind park, natural gas grid), the Linde group (gas purification and distribution) and Siemens (electrolyzer). The worldwide largest 10 MW (peak power) electrolyzer plant ‘Refhyne’ will start its operation in 2020 at Shell’s Rhineland Refinery in Wesseling, Germany with the expertise of e.g. Shell (operator) and ITM power (electrolyzer). A successful ‘Refhyne’ project will have a great impact on greenhouse gas emissions, since a refinery is expected to save up to 20 % of its CO<sub>2</sub> emissions when implementing sustainable production routes for hydrogen.<sup>68</sup>

## 1.2 Proton exchange membrane water electrolysis (PEMWE) as key technology for the sustainable production of green hydrogen

The success of an electrolyzer system is depending on its cost, efficiency and lifetime. Three major water electrolyzer techniques are currently under investigation and are being improved continuously: alkaline, proton exchange membrane (PEM) and solid oxide water electrolysis, with the latter one being in research state and not yet commercialized. Table 1 summarizes the main characteristics, advantages as well as the disadvantages of the different systems.<sup>67, 69–73</sup>

**Table 1:** Comparison of the three main water electrolysis systems: alkaline, PEM, solid oxide.

	Alkaline	Proton Exchange Membrane (PEM)	Solid oxide
Schematic			
Anode	$2\text{OH}^- \rightarrow \frac{1}{2} \text{O}_2 + 2\text{e}^- + \text{H}_2\text{O}$	$\text{H}_2\text{O} \rightarrow 2\text{H}^+ + 2\text{e}^- + \frac{1}{2} \text{O}_2$	$\text{O}^{2-} \rightarrow \frac{1}{2} \text{O}_2 + 2\text{e}^-$
Cathode	$2 \text{H}_2\text{O} + 2\text{e}^- \rightarrow \text{H}_2 + 2\text{OH}^-$	$2\text{H}^+ + 2\text{e}^- \rightarrow \text{H}_2$	$\text{H}_2\text{O} + 2\text{e}^- \rightarrow \text{H}_2 + \text{O}^{2-}$
Electrolyte	Liquid: alkaline solution	Solid: polymer membrane	Solid: ion conduct. ceramic
Noble catalyst	Partly Pt, Ir, Rh, Ni, Co, Fe	Yes IrOx, RuOx, Pt/C	No Perovskites, Ceria
Temperature	80 °C – 90 °C	20 °C – 100 °C	700 °C – 1000 °C
(com.) Voltage efficiency	62-82 %	67-82 %	81-86 %
Drawbacks	<ul style="list-style-type: none"> <li>Distance between electrodes: ohmic losses</li> <li>Alkaline electrolyte: high maintaining costs, special chemical stability requirements for components</li> </ul>	<ul style="list-style-type: none"> <li>Titanium needed at the anode (corrosive environment)</li> <li>Noble metal catalysts needed</li> </ul>	<ul style="list-style-type: none"> <li>Durability: temperature gradients induce mechanical stress</li> <li>Not yet on commercial level, no longterm experience</li> </ul>
Advantages	<ul style="list-style-type: none"> <li>Non noble metal catalysts</li> <li>Longterm experience, established technology</li> <li>Large capacities</li> </ul>	<ul style="list-style-type: none"> <li>Low ohmic resistance (compact system)</li> <li>Pressurized operation</li> <li>Dynamic operation mode (short distance between functional components)</li> </ul> <p>→ most suitable for coupling with fluctuating renewable energy sources</p>	<ul style="list-style-type: none"> <li>Installation in hot exhaust steam pipelines on industrial sites</li> <li>Non noble metal catalysts</li> </ul>

Alkaline water electrolyzers have been extensively studied and are commercially available as a reliable option for the production of green hydrogen. The use of a liquid electrolyte is however a drawback regarding high maintenance efforts and the limited dynamic operation of the system.<sup>74</sup> Especially the latter is of high importance, for coupling the electrolyzer with fluctuating energy sources such as wind or solar panels. Solid oxide water electrolyzers are still on research level, but very interesting devices due to the possibility of a direct integration in hot exhaust steam pipes of industrial plants. Temperature gradients of several hundred degrees can however induce mechanical stress and lead to material failures.<sup>75</sup> PEMWE is considered as most promising candidate to bridge the gap between the production of green electricity and the production of emission free hydrogen while maintaining a high power density, due to the flexible operation, compact system design as well as operation at high pressures and moderate temperatures.<sup>76</sup>

One promising way to optimize PEMWE applications for future large-scale operation is the development of smart fabrication routes to improve the central component of the PEMWE cell, the **membrane electrode assembly (MEA)**. Commercial MEA-configurations for PEMWEs are based on the **catalyst coated membrane (CCM)** with the catalyst layers (CLs) being deposited directly on the membrane (see schematic in Table 1).<sup>76</sup> PEMWEs are therefore limited to only one MEA-design with the need of producing a mechanically stable, freestanding membrane to be coated with the CLs from both sides. The need of a freestanding membrane can limit membrane development when polymers are difficult to process into a several cm<sup>2</sup> large sheet. Another drawback is the need of several costly fabrication steps and devices to transfer the catalyst layers onto the free standing membrane e.g. via the established DECAL transfer process as described in more detail in chapter 2.<sup>77, 78</sup> In the final MEA, the CCM is mechanically sandwiched between porous transport layers (PTLs) made of titanium at the anode side and carbon at the cathode side. The electrical interface between the PTLs and CLs is therefore only established at direct contact points of the titanium or carbon substrates with the CL. Only at this points direct electron pathways are established to electrically connect the catalyst particles within the CL. In case of a low in-plane conductivity of the CL, which is the case for low catalyst loadings, some parts of the CL might not be electrically connected and are therefore inactive.<sup>79</sup> As all current needs to be distributed by the few direct electrical contact areas, the formation of hot-spots that could damage the membrane is another risk.<sup>80</sup>

Optimized, **alternative MEA-configurations** to CCM-configurations that could solve the production, performance and durability related limitations as described above are not yet commercially available. For PEM fuel cells (PEMFCs) however, a broad range of materials and MEA-configuration exist as e.g. sandwiching a free standing membrane between gas diffusion electrodes (GDEs) made of porous carbon substrates coated with a platinum on carbon (Pt/C) based catalyst layer or direct membrane deposition (DMD) configurations with the membrane being directly deposited on the GDEs.<sup>81</sup> The key to transfer these alternative MEA-configurations to PEMWE is the availability and optimization of freestanding **porous transport electrodes (PTEs)** for PEMWE as equivalent to GDEs in PEMFC. For the cathode side in PEMWEs, the same GDEs as used in PEMFC are usually applied, as platinum is active for both the oxygen reduction reaction (ORR) in PEMFC and the hydrogen evolution reaction (HER) in PEMWE. There was so far however no PTE commercially available for the oxygen evolution reaction (OER) at the anode side in PEMWE, most probably due to the difficulty of depositing the iridium-based catalysts on coarse commercial titanium PTLs with pores up to 20 times larger than the thickness of the catalyst layers (see chapter 2). The availability and development of high performing PTEs for PEMWE is therefore the most pressing challenge to provide alternative MEA-configurations for commercial PEMWEs. Advantages such as an increased mass activity of the catalysts due to an optimized electrical interface towards the PTLs, reduced fabrication costs and novel insights in the polarization behavior are expected. Thus, efficiency related optimization parameters for the development of PEMWE MEAs can be provided.



## 2 PEMWE: functional components, working principle and electrode development

### 2.1 Functional components of a PEMWE cell

Due to their fast response time and high specific energy density, PEMWEs are currently under investigation to be coupled with fluctuating renewable energy sources.<sup>82–84</sup> Since a thin solid polymer electrolyte in the form of a proton exchange membrane (PEM) is in direct contact with the catalyst layers, ohmic resistances are low and a fast start up and shut down operation is possible. To operate a PEMWE cell, some more functional parts are necessary which are pressed against the membrane and catalysts to ensure a sufficient water supply, removal of gases, thermal management, electrical connection and mechanical stability. Fig. 3 shows the PEM coated with CLs for the OER and HER forming the CCM. The CCM is clamped between PTLs made of titanium at the anode side and carbon at the cathode side, respectively. Both the CCM and the PTLs are explained in more detail in this chapter. Titanium flow fields at the outer-most side of the PEMWE cell mechanically stabilize all parts and are used to set an appropriate assembly pressure. The channel structure of the flow fields can be meander shaped or a parallel finger structure, with the latter one being considered as more advantageous for an evenly distributed water supply and gas removal.<sup>85</sup> To prevent oxidation and thus an increase in electrical resistance, usually a thin gold coating is applied on the flow fields.<sup>86, 87</sup>

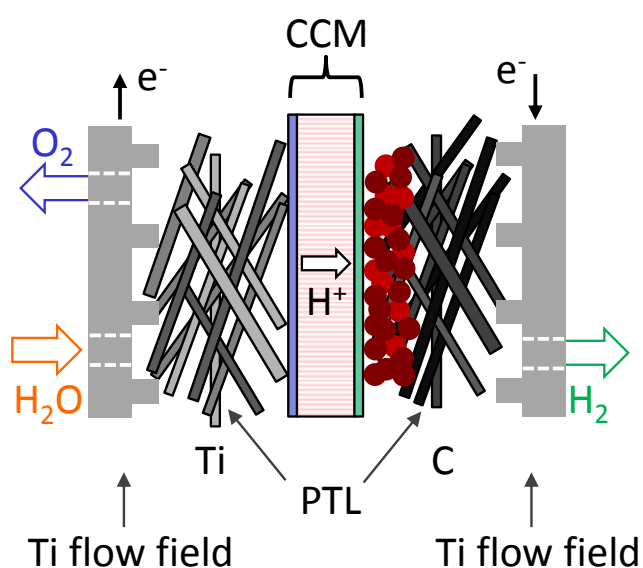


**Fig. 3** Functional components of a PEMWE cell with the catalyst coated membrane (CCM) in the middle for the hydrogen and oxygen evolution reaction. Porous transport layers are pressed onto the CCM and subsequently the flow fields.

All different materials and their interfaces influence the electrochemical performance and therefore the efficiency of the PEMWE cell. Besides performance, also durability and cost are dependent on the single components. The interplay of materials from the nanometre scale (catalysts) up to several millimetres (flow fields) is the most interesting challenge from an engineering point of view. A high surface roughness on the nanometre scale is for example essential in order to obtain a catalyst layer with a high electrochemically active surface area.<sup>57</sup> An increased surface roughness on the millimetre scale is however disadvantageous in terms of an

even distribution of the assembly pressure or direct electrical and protonic interfaces as well as for the deposition of protective coatings.<sup>84</sup>

### Membrane electrode assembly (MEA)

The PEMWE MEA typically consists of a CCM that is typically made of a proton conductive polymer membrane as solid electrolyte coated with catalyst layers for the OER and HER (Fig. 4). At the anode side, water is split into oxygen, protons and electrons. Gaseous oxygen is removed from the PEMWE cell, whereas electrons travel through the external electrical circuit towards the cathode side. Protons take another path, which is through the PEM, to be electrochemically reduced at the cathode side to gaseous hydrogen. In both catalyst layers so called three-phase-boundaries need to be present as electrochemically active sites to drive the splitting of water.<sup>88</sup> The three phases are i) electrical pathways within the catalyst layer and towards the external current source ii) proton conductive pathways established via the ionomer in the catalyst layers iii) a porous network to supply reactants and remove products from the active sites. The inlets in Figure 5 show the oxygen and hydrogen evolution reaction exemplary at one catalyst particle per electrode. At the anode side unsupported iridium-based catalysts are usually applied with primary particle sizes in the nanometre range and agglomerates in the micrometre range.<sup>62, 89</sup> At the cathode side, finely dispersed platinum particles in the nanometre range supported on conductive carbon are available with the advantage of an increased active surface area compared to the anode side.

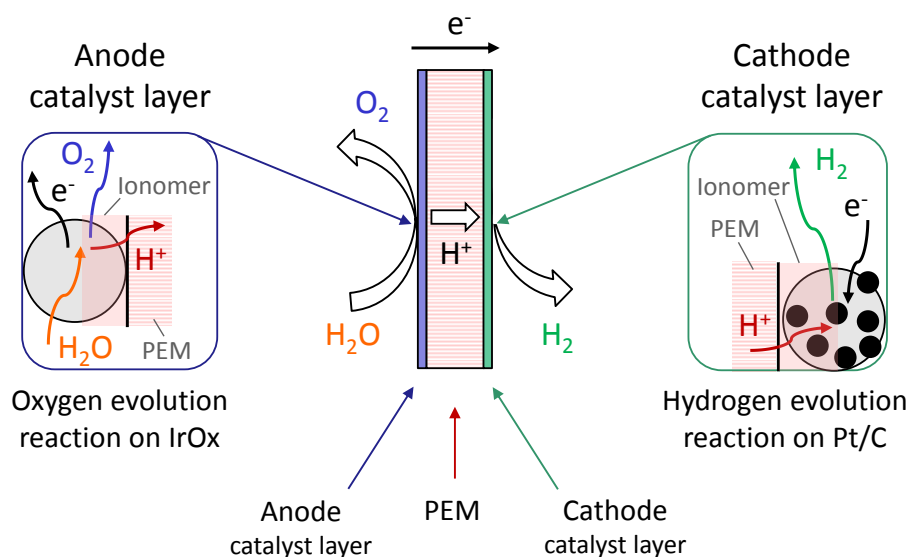


**Fig. 4** Catalyst coated membrane (CCM) of a PEMWE cell. The PEM coated from both sides with catalyst layers for the oxygen evolution reaction (anode) and hydrogen evolution reaction (cathode).

CCMs provide a good protonic interface between the catalyst layers and the PEM and are manufactured either via direct deposition of the catalyst layers onto the membrane or via the DECAL transfer process (Fig. 5).<sup>77, 90</sup> The latter is widely used in industry as the wrinkling of the membrane when being coated with the liquid catalyst ink can be prevented. For the transfer process, the catalyst layers are deposited on Teflon blanks as transfer substrates. The membrane is placed in between the coated Teflon blanks and a hot press step transfers the catalyst layers onto the PEM. The pressure and heat applied during the hot press step is important to form a mechanically stable interface between the polymer membrane and the porous catalyst layer. Due to the presence of ionomer as binder and proton conductive phase in the catalyst layer, a continuous proton pathway from the reaction sites towards the membrane is established.



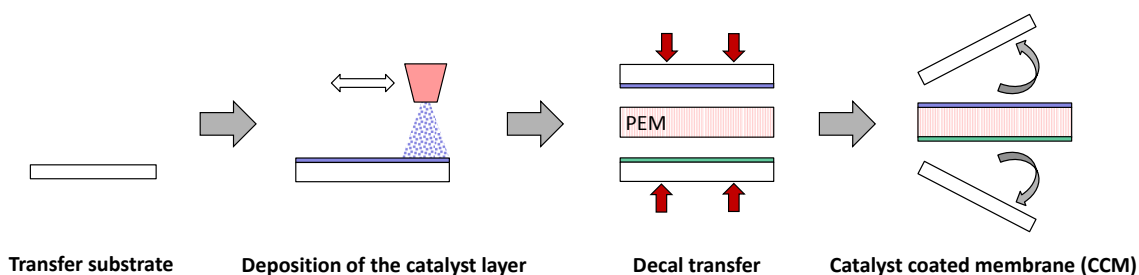


**Fig. 5** Conventional DECAL transfer process to fabricate catalyst coated membranes (CCMs): Catalyst layers are deposited on transfer substrates and then hot pressed onto a membrane.

The membrane material usually used for PEMWE applications is Nafion (trademark of Chemours). Nafion is a perfluorosulfonic acid (PFSA) polymer which consists of a hydrophobic PTFE backbone and hydrophilic sulfonated side chains (Fig. 6).<sup>91, 92</sup> The PTFE backbone establishes a good mechanical and chemical stability under PEMWE operation conditions, whereas the side chain allows for water uptake that is essential for proton conductivity. The exact mechanism of proton conductivity in PFSA membranes is widely discussed. Latest findings claim the importance of an increased porosity and higher number of microchannels within the membrane to improve proton conductivity via non-bulk water along an increased interfacial area established by the hydrophilic side chains of Nafion.<sup>93</sup> The two basic proton conduction mechanisms in Nafion are the Grotthuss mechanism via the sulfonated side chains and the vehicle mechanism via water molecules (Fig. 6).<sup>94</sup> Nafion membranes are available in different thicknesses and with fiber reinforcement to increase the mechanical stability of thin membranes at high-pressure operation. The thinner the membrane, the shorter the distance for protons to travel and therefore the lower the protonic resistance of the PEMWE cell.

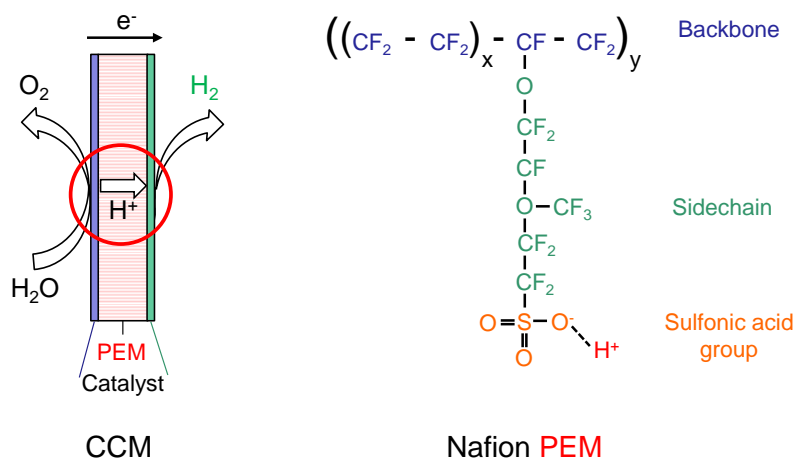


**Fig. 6** Structure and mechanisms of proton conductivity in Nafion as proton exchange membrane (PEM) in the catalyst coated membrane (CCM) configuration.

Catalyst layers are fabricated via deposition of a catalyst ink directly onto the membrane or the transfer sheets. Catalyst inks are usually prepared via mixing the catalyst powder, solvents and a certain amount of ionomer, via ultrasonication.<sup>95</sup> The optimum amount of ionomer is essential for the porosity of the catalyst layer, the amount of three-phase-boundaries, the mechanical stability of the porous catalyst layer and a sufficient transport of protons from or towards the membrane. The catalyst ink can e.g. be spray coated, printed or doctor bladed on a solid substrate. Drying of the layer usually under elevated temperatures close to the evaporation points of the solvents, form a porous catalyst layer.<sup>57</sup> Typical catalyst materials used in PEMWE are platinum group based

noble metals such as iridium, ruthenium or platinum with loadings of  $0.5 - 3 \text{ mg cm}^{-2}$ .<sup>96</sup> The electrochemical active surface area is usually increased via using supported catalysts as e.g. platinum on carbon (Pt/C) for the cathode side or iridium mixed with titanium particles on the anode side.<sup>87</sup> In 2.3 the catalyst layer and electrode development is explained in more detail as the development of PTEs as alternative to CCMs is studied in this work.

### Porous transport layers

To evenly distribute gases and water over the catalyst layers, PTLs are pressed against the CCM from both sides (Fig. 7). The porous material needs to be electrically and thermally conductive as well as chemically stable under PEMWE operation conditions. The conditions are especially harsh at the anode side where high potentials ( $> 2 \text{ V}$ ) are applied in combination with the acidic environment of the proton conductive PEM. Therefore, titanium materials are used at the anode side, whereas cheaper and softer carbon materials can be used at the cathode side.<sup>97</sup> Carbon PTLs are well studied from PEMFC research and application and are available in various forms.<sup>98</sup> Carbon cloth or paper materials coated with a carbon based microporous layer (MPL) to smoothen the surface towards the CCM are used to increase the electrical interface between catalyst particles and carbon PTL. Fully freestanding electrodes with the catalyst layer deposited onto the carbon PTL + MPL to form a cathodic PTE are available as well.

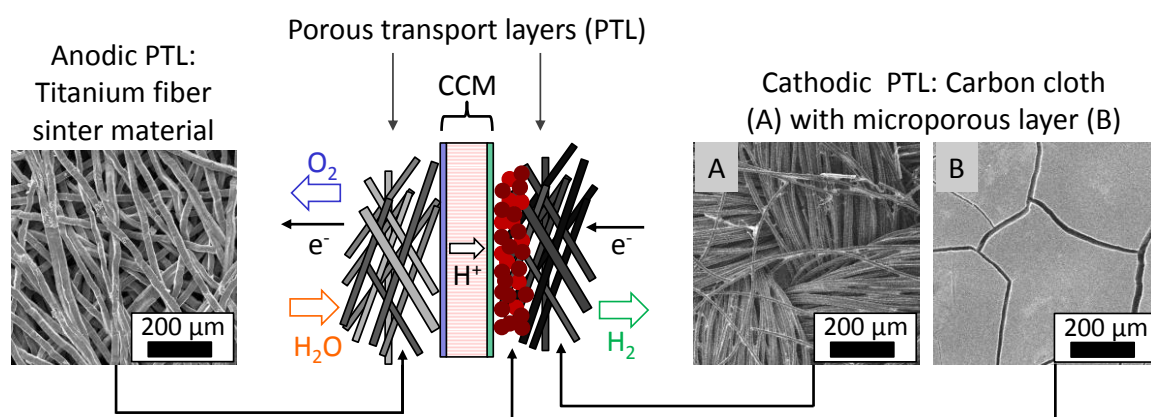
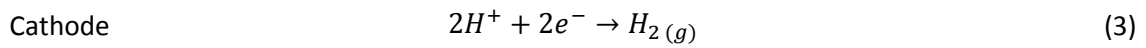
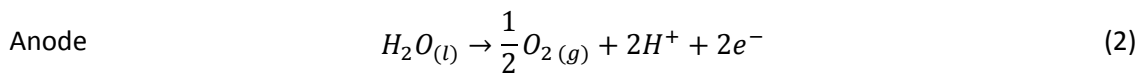
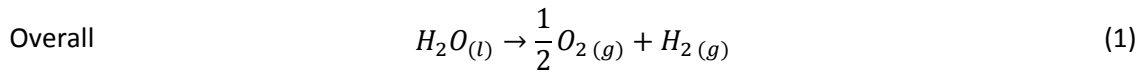


**Fig. 7** Catalyst coated membrane (CCM) sandwiched between the titanium porous transport layer (PTL) at the anode side and carbon PTL at the cathode side. Carbon PTLs are available with a microporous layer (MPL) to smoothen the surface towards the PEM.

The variety of different PTLs as used for the cathode side is not yet available for the anode side of PEMWEs. Standard materials are porous titanium fiber- or powder-sinter materials as used in the filter industry.<sup>99</sup> Those materials are far more expensive than carbon based materials and are not yet fully optimized for PEMWE. The hard titanium materials and sophisticated fabrication route e.g. via sintering are drawbacks for a flexible development on research level. Titanium PTLs are applied with thicknesses varying from  $300 \mu\text{m}$  to  $1 \text{ mm}$ , whereas carbon cloth PTLs in the range of  $400 \mu\text{m}$  are already considered as thick for PEMWE applications as carbon paper materials with thicknesses of around  $200 \mu\text{m}$  are more common. An increased thickness of the PTL leads to increased electrical resistances, which are even more pronounced due to the large pores of the commercial titanium materials leading to a poor electrical interface towards the catalyst layer.<sup>100</sup> The optimization of PTLs for PEMWE in terms of efficiency and cost is an urgent topic and should be combined with the development of a titanium based MPL for titanium PTLs to reduce interfacial resistances between PTL and catalyst layer.<sup>100–103</sup>

## 2.2 Influence of functional components on the polarization behavior of PEMWEs

All functional parts of a PEMWE cell are necessary to ensure a safe and durable electrolysis operation. However, every additional component increases electrical, protonic and thermal resistances, which increase the theoretically needed energy to drive the water splitting reaction. Therefore, a deep understanding of the influences of every part used in the PEMWE cell on the polarization behavior is necessary to optimize state of the art systems. The overall chemical reaction of splitting liquid water into gaseous hydrogen and oxygen is shown in Equation 1, as well as the half-cell reactions at the anode and the cathode (oxygen and hydrogen evolution) in Equations 2 and 3.<sup>104</sup>



The thermodynamic quantity describing the spontaneous or forced nature of a chemical reaction is the change in Gibbs free energy  $\Delta G_R$  calculated as the change in reaction enthalpy  $\Delta H_R$  minus the entropy  $T \cdot \Delta S_R$  (Gibbs-Helmholtz Eq. 4). The change in reaction enthalpy  $\Delta H_R$  (total energy demand) is the energy needed to establish the chemical bonds of the products hydrogen and oxygen minus the energy needed to build the chemical bond of the reactant water. The entropy term  $T \cdot \Delta S_R$  (thermal energy demand) represents the thermal input to the system with  $\Delta S_R$  being a measure for the change in disorder of the thermodynamic system.

$$\Delta G_R = \Delta H_R - T \cdot \Delta S_R \quad (4)$$

The splitting of water is an endothermic process, as the change in Gibbs free energy is positive (Fig. 8) and the activation barrier with the size of the activation energy  $E_A$  needs to be overcome. The activation barrier can be decreased by use of catalysts, which enhance the chemical reaction but do not participate in it. Besides the use of a catalyst, a certain amount of electrical and thermal energy input are needed for water electrolysis.

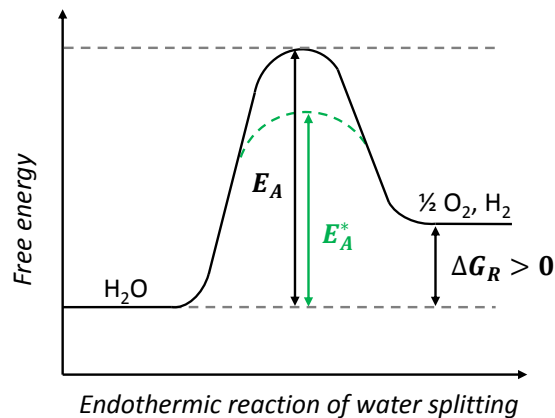


**Fig. 8** Energy diagram of the endothermic chemical reaction of water splitting. An activation barrier  $E_A$  needs to be overcome to reach the final energy level of  $+\Delta G$  of the products oxygen and hydrogen.

The Gibbs free energy at standard conditions (1 atm, 298 K) is calculated via the change in entropy and enthalpy of the products and reactants as  $\Delta G_R^0 = 236.483 \text{ kJ mol}^{-1}$ .<sup>104</sup> The reversible cell voltage  $V_{rev}^0$  is a measure for the minimum amount of electrical work needed to split water (Eq. 5). The change in Gibbs free energy at standard conditions is hereby divided by the number of transferred electrons  $z = 2$  (see Eq.2 and Eq.3) and the Faraday constant  $F = 96485 \text{ C mol}^{-1}$ .

$$V_{rev}^0 = \frac{\Delta G_R^0}{z \cdot F} = 1.229 \text{ V} \quad (5)$$

When standard conditions are left, temperature and concentration of the reactants and products influence the electrode potential.<sup>105</sup> The change in Gibbs free energy (Eq. 6) is therefore the Gibbs free energy at standard conditions plus a term taking into account the temperature  $T$  and reaction rate coefficient  $k$ .  $R = 8.314 \text{ J K}^{-1} \text{ mol}^{-1}$  is the universal gas constant.

$$\Delta G_R = \Delta G_R^0 + RT \cdot \ln(k) \quad (6)$$

The Nernst-Equation (Eq. 7) combines Equation 5 and 6 to describe the thermodynamic cell voltage  $V_{rev}$  with the reaction rate coefficient expressed as the activities  $\alpha$  (concentrations) of reactants and products according to their stoichiometric factors (see Eq. 1-3).

$$V_{rev} = V_{rev}^0 - \frac{RT}{zF} \cdot \ln\left(\frac{\alpha[H_2O]}{\alpha[H_2] \cdot \alpha[O_2]^{1/2}}\right) \quad (7)$$

When considering real PEMWE operation, the thermal energy input is rather small, since PEMWE is a low temperature application operated below 373.15 K (=100 °C, boiling point of water). Therefore, the largest amount of energy needed to split water is supplied via electrical energy, increasing the theoretically lowest possible voltage for splitting water to the thermoneutral voltage at standard conditions  $V_{th}^0$  (Eq. 8).

$$V_{th}^0 = \frac{\Delta H_R^0}{z \cdot F} = 1.481 \text{ V} \quad (8)$$

The second change in real PEMWE operation is the applied electrical current through the cell and therefore reversible thermodynamic equilibrium conditions are left. The open circuit voltage (OCV)  $V_{th}^0$  is increased due to the transfer of charges and therefore irreversible voltage losses in the PEMWE cell. The chemical reaction of the OER and HER at the catalysts causes activation losses at the anode and cathode in form of activation overpotential ( $\eta_{act,an} + \eta_{act,cat}$ ). Protonic and electrical resistances in bulk materials and at interfaces are measured as ohmic losses  $\eta_{ohm}$  and an insufficient transport of gases and water induces mass transport losses  $\eta_{mass}$ . The real overall PEMWE cell voltage is calculated as in as sum of all overpotentials and the OCV (Eq. 9).

$$V_{cell} = V_{th}^0 + \eta_{act} + \eta_{ohm} + \eta_{mass} \quad (9)$$

Figure 10 shows the current-voltage characteristic (polarization curve) of a PEMWE cell with the thermoneutral OCV as lowest possible energy input to drive the chemical reaction of water splitting. When a current is applied, the different voltage losses from Equation 7 increase the overall cell voltage with contributions in different regions of the polarization curve. At low current

densities, activation losses (Fig. 9 A) mainly increase the cell voltage, whereas at moderate current densities, ohmic losses (Fig. 9 B) are dominant and at high current densities, with large amounts of gases produced, mass transport losses become an issue (Fig. 9 C).

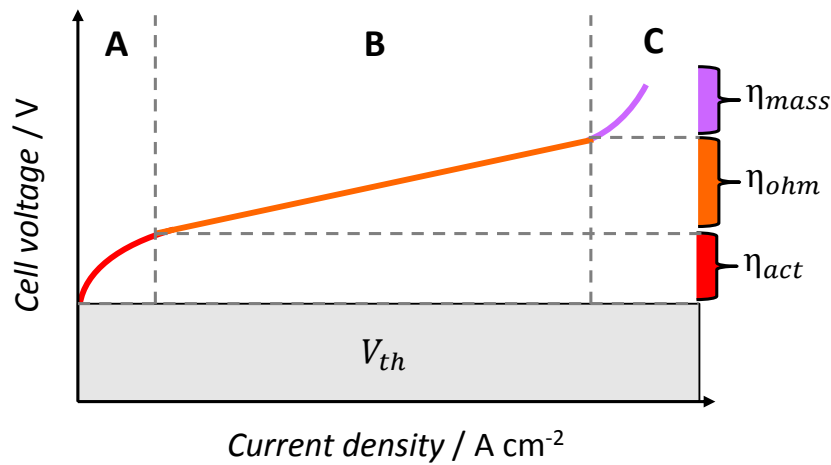


**Fig. 9** Polarization curve (current-voltage characteristic) of a PEMWE cell. The thermoneutral cell voltage is the minimum required electrical energy input to drive the reaction of water splitting. Irreversible losses in the kinetic (A), ohmic (B) and mass transport region (C) occur however during operation of the cell and increase the overall cell voltage.

The thermodynamic cell voltage is used to calculate the voltage efficiency of the PEMWE system as the ratio between the cell voltage  $V_{cell}$  and the reversible voltage  $V_{rev}$  (Eq.10). The voltage efficiency of PEMWE systems is currently in the range of 67-82 %.<sup>73</sup>

$$\varepsilon_V = \frac{V_{cell}}{V_{rev}} \quad (10)$$

To know the different voltage loss mechanisms and the contributing functional parts of the PEMWE cell is an essential step towards the optimization of the overall performance and efficiency. The activation losses due to the OER at the anode and HER at the cathode side as well as ohmic and mass transport losses are explained in more detail in the following section.

#### A: Kinetic region

Activation losses are dependent on the thermal dynamics of chemical reactions at the electrodes, which is basically the transfer of electrons to and from the catalyst surfaces, respectively.<sup>106</sup> Catalysts are used to reduce the activation barrier for both half-cell reactions. An appropriate catalyst can be chosen according to the Sabatier principle, which states the perfect balance between ad- and desorption energy of reactants and products onto and from the catalyst surface.<sup>107</sup> The interaction between catalyst, products, reactants and intermediate products should therefore neither be too strong nor too weak. For the OER, metal oxides are suitable catalyst materials since they are covered with an oxide layer anyways during operation of the PEMWE cell due to the applied high voltages in aqueous solution. The oxygen evolution reaction at the anodic catalyst involves a four-step electron transfer and the formation of adsorbed intermediate products. As several possible pathways for the OER are proposed<sup>104</sup>, Equations 11-13 and Fig. 10 exemplarily describe the electrochemical oxide pathway according to Bockris et al. on an electrochemically active site S.<sup>108</sup> The double arrows indicate redox-reactions with a forward and backward reaction happening at the same time. At thermodynamic equilibrium, both reactions are balanced and the net current density (transferred charges) is zero.

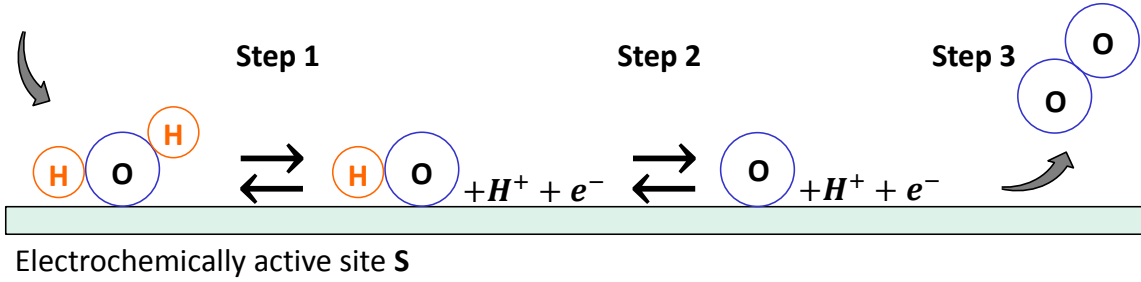
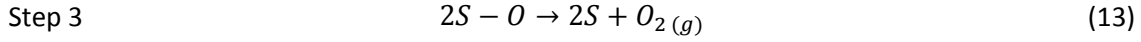
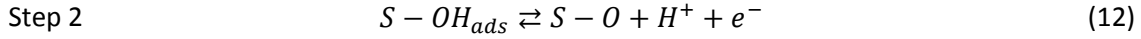
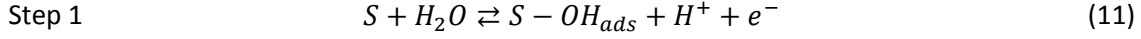


**Fig. 10** 3-step oxygen evolution reaction due to water splitting at the surface of an electrochemically active site S.

The current densities of the forward and backward reaction at thermodynamic equilibrium are equal and called the exchange current density  $i_0$ . The exchange current density depends on the temperature and the catalyst material used with its specific activity for the desired chemical reaction and the electrochemical surface area (ECSA), which depends on number of active sites per unit mass of catalyst. The exchange current density for the OER at the anode e.g. on the most active catalyst ruthenium oxide (RuOx) is with  $i_{0,an} = 1.2 \cdot 10^{-8} \text{ A cm}^{-2}$  several orders of magnitudes smaller than for the HER at the cathode e.g. on Pt/C with an exchange current density of  $i_{0,cat} = 2 \cdot 10^{-1} \text{ A cm}^{-2}$ .<sup>109, 110</sup> The OER is therefore the rate-determining step for the overall splitting of water.

When leaving thermodynamic equilibrium conditions, due to an applied activation overpotential  $\eta_{act}$ , a net current density will be established at the electrode surface. The Butler-Volmer equation (Eq. 14) describes the exponential increase of the current density with increasing overpotential as combination of anodic and cathodic processes. The charge transfer coefficient  $\beta$  is dependent on the electron transfer at the electrode and is a measure for how the activation barrier is reduced by a catalyst. At high overpotentials, the Butler-Volmer equation can be simplified (Eq. 15) and solved for the activation overpotential in the Tafel Equation (Eq. 16).

$$i = i_0 \cdot \left\{ \exp \frac{\beta_{forward} z F \eta_{act}}{RT} - \exp \frac{-\beta_{backward} z F \eta_{act}}{RT} \right\} \quad (14)$$

$$i = i_0 \cdot \exp \frac{\beta_{forward} z F \eta_{act}}{RT} \quad (15)$$

The Tafel Equation describes the linear relation between current density and overpotential on the logarithmic scale. From the extrapolated Tafel-slope  $a$  the exchange current density can be derived, as shown in Fig. 11.

$$\eta_{act} = \frac{RT}{\beta_{forward}zF} \cdot \log\left(\frac{i}{i_0}\right) = a \cdot \log(i) - b \quad (16)$$

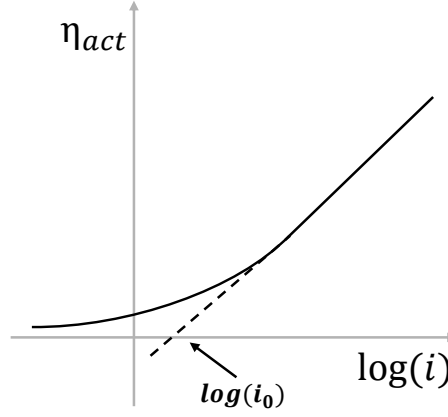


**Fig. 11** The activation overpotential as function of the current density. The (Tafel) slope of the curve extrapolated gives the exchange current density  $i_0$ .

The forward reactions at the anode and cathode in PEMWE are the oxygen and hydrogen evolution reactions. The anodic and cathodic activation potentials can therefore be written as in Equations 17 and 18. The overall activation losses increasing the cell voltage (Eq. 9) are the sum of the activation losses at both electrodes  $\eta_{act,an} + \eta_{act,cat} = \eta_{act}$ .

$$\eta_{act,an} = \frac{RT}{\beta_{an}zF} \cdot \ln\left(\frac{i}{i_{0,an}}\right) \quad (17)$$

$$\eta_{act,cat} = \frac{RT}{\beta_{cat}zF} \cdot \ln\left(\frac{i}{i_{0,cat}}\right) \quad (18)$$

To reduce the activation overpotential, the catalyst loading per geometric electrode area can be increased and the catalyst itself should have an ECSA. The accessibility of the catalyst particles for reactants as well as the electrical and protonic pathways within the catalyst layer and towards the interfaces of membrane and PTL are as well important to establish three-interphase reaction sites. The availability and activity of enough catalyst material will determine the kinetic region and is therefore the first basic concern when developing high performing PEMWE cells, as activation overpotentials define the slope of the polarization curve at low current densities.

## B: Ohmic region

Ohmic losses are proportional to the applied current and follow Ohm's law in the linear region of the polarization curve at moderate current densities (Eq. 19). The ohmic cell resistance  $R_{cell}$  is the sum of all material related protonic and electrical resistances in series. Ohmic resistances originate from the anode and cathode electrodes ( $R_{an} + R_{cat}$ ), flow fields and PTLs ( $R_{plates}$ ) and the largest is attributed to the ionic resistance of the membrane ( $R_{mem}$ ). The membrane resistance is calculated with the thickness of the membrane  $l_{mem}$ , the applied current density  $i$  and the

specific proton conductivity of the membrane  $\sigma_{mem}$ , which is dependent on the degree of hydration and the temperature (Eq. 20).

$$\eta_{ohm} = I \cdot R_{cell} = I \cdot (R_{an} + R_{cat} + R_{plates} + R_{mem}) \quad (19)$$

$$\eta_{ohm,mem} = I \cdot R_{mem} = \frac{l_{mem} \cdot i}{\sigma_{mem}} \quad (20)$$

Besides low protonic and electrical resistances of the bulk materials, interfacial resistances have to be minimized as well. In CCM-configurations, the protonic interface between catalyst layer and PEM is considered as optimal, whereas the electrical interface towards the PTL is only established at direct contact between the PTL and the catalyst particles. As shown in section 2.1.2 when describing the carbon and titanium based PTLs, a smooth interface between the coarse PTL and the catalyst layer can be realized via an MPL. For the cathode side, various carbon based PTL+MPL systems exist, but for the rate determining anode side, titanium based PTL+MPLs are not yet available. The electrical interface between PTL and CL is therefore not optimal at the anode side as pathways for electrons are only established at direct contact points of the PTL with the CL. As consequence, parts of the catalyst layer could be insufficient electrically connected, which would lead to a reduced amount of active sites and thus reduced specific mass activity of the anodic catalyst in the CCM-configuration.<sup>111</sup> The development of MPLs to smoothen the surface of the Ti-PTLs and the direct deposition of the CLs to form porous transport electrodes (PTEs) is therefore highly motivated to reduce electrical interfacial resistances between PTL and CL (see section 2.3).

### C: Mass transport region

At high current densities, there are no limitations due to reaction kinetics and thus the overall reaction rate is mainly dependent on the sufficient supply of reactants to the active sites. The supply with reactants is hindered, when the transport of water towards the active sites is blocked. This is the case when gas bubbles are not removed from the catalyst layers and the nearby channels into the porous PTL. The mass transport overpotential is therefore increasing with an increasing diffusion limitation for gases. The Nernst Equation in combination with Fick's law of diffusion<sup>104, 106</sup> describes the mass transport overpotential dependent on the oxygen and hydrogen concentration at the electrode-membrane interface  $c_i$  compared to the concentration at a reference point outside of the electrode  $c_{rp}$  (Eq. 21).

$$\eta_{mass} = \frac{RT}{zF} \cdot \ln \left( \frac{c_i}{c_{rp}} \right) \quad (21)$$

An insufficient removal of gas bubbles from the catalyst layers not only decreases the efficiency, but also increases the risk of high gas crossover through the PEM.<sup>112</sup> High gas crossovers bear also the risk of the formation of a highly explosive gas mixture, as already 4 mol % H<sub>2</sub> in air (room temperature and atmospheric pressure) is considered as safety risk for the operation of a PEMWE system.<sup>113</sup> From an engineering point of view, the porous network within the catalyst layers and the PTLs needs to be optimized for the counter flow of gases and water to not limit the transport of one or the other species.<sup>101, 114</sup>



## 2.3 PEMWE electrode development

The most complex functional component influencing all three major loss regions is the catalyst layer due to the simultaneous presence of catalyst particles, ionomer and pore space to establish enough three-phase boundaries as active sites. An insufficient electrical interface of the catalyst particles towards the PTL increases ohmic losses and so does a bad protonic interface of the ionomer phase in the catalyst layer towards the PEM. The activity of the catalyst for the OER as well as the ECSA strongly influence the kinetic region. A good accessibility of catalyst particles for water and gas distribution is essential at high current densities for a sufficient mass transport. An optimized catalyst layer composition as well as optimized interfaces between the CL, PEM and PTL is therefore crucial when developing high performing PEMWE MEAs.

Structural catalyst layer optimization is achieved by increasing the surface area of the catalyst material using nanoparticles and by introducing (electrically conductive) supports (Fig. 13 A).<sup>115</sup> A mesoporous support can additionally enhance mass transport within the catalyst layer. A major problem when depositing the (supported) catalyst layer on the PEM to form a CCM, is the non-optimized interface towards the PTL. Especially when approaching low loadings with a reduced electrical in-plane conductivity within the CL, parts of the CL might be inactive.<sup>111, 96</sup> An alternative MEA design gaining more and more attention in research and industry is therefore the PTE configuration. In this configuration, the catalyst layers are directly deposited onto the PTLs to establish a direct electrical interface towards all catalyst particles. The goal is to reduce the inactive catalyst layer regions and at the same time to provide a mechanically stable support for thin catalyst layers.<sup>96</sup> Advanced supported catalyst layers in combination with the PTE-configuration are therefore a promising development approach. In the following subsections, some examples of increased catalyst surface areas via supporting materials on the catalyst layer scale and the development of PTE-configurations are discussed and motivated. Both approaches influenced the work in this thesis as shown in section 2.4.

### Catalyst supports for PEMWE

*Carbon* - A reliable catalyst support used in PEMFCs as well as on the cathode side in PEMWEs are carbon nanoparticles on which platinum is decorated (Pt/C). The advantage of carbon as support is the formation of a nanoporous carbon matrix with a sufficiently high electrical conductivity. Pt nanoparticles can be decorated on carbon powders by several chemical synthesis routes and the Pt/C powders form a stable catalyst ink when mixed with solvents and ionomer for e.g. spray coating.<sup>116–118</sup> The degradation mechanisms of Pt/C during PEMWE operation is currently under investigation with one assumption of the corrosion of the carbon support, or the removal of platinum from the support.<sup>119–121</sup> Carbon supports can only be used at the cathode side in PEMWE, as a high degradation rate due to the high potentials and acidic environment at the anode would lead to the degradation of the supporting matrix.<sup>97</sup> Nevertheless, Kong et al. presented an OER catalyst consisting of IrO<sub>2</sub> nanoparticles supported on graphene, with a good stability and activity at least in a three-electrode-setup.<sup>122</sup> Graphene can be doped with e.g. sulfur to attach functional non-noble metal [Mo<sub>3</sub>S<sub>13</sub>]<sup>2-</sup> clusters as presented by Pham et al. for the HER in acidic environment.<sup>123</sup> The porous support ensured the accessibility of the catalytic active sites even at high loadings and at the same time increased the electrical conductivity of the CL. Furthermore, the S-dopant in the graphene structure established additional active centers as the Mo-atoms of the [Mo<sub>3</sub>S<sub>13</sub>]<sup>2-</sup> cluster attached to the S-atoms of the graphene support.

*Noble metals* - Supporting materials or structures on the anode side need to withstand the harsh environment and fast degradation rates. The straightforward idea is therefore to use an inert

noble metal as support. Porous thin films for the anode side made of nanoporous Au-IrO<sub>2</sub> composites showed a highly increased specific mass activity due to the conductive, porous Au support.<sup>124</sup> The idea of using a noble (conductive) and at the same time electrochemically active support was followed by Audichon et al. with a compound of IrO<sub>2</sub> on RuO<sub>2</sub>.<sup>125</sup> Whereas RuO<sub>2</sub> is even more active for the oxygen evolution reaction than IrO<sub>2</sub>, it suffers from relatively fast degradation rates. The combination of RuO<sub>2</sub> with IrO<sub>2</sub> is therefore a way to gain highly efficient OER electrodes with a reduced degradation rate compared to pure RuO<sub>2</sub>-based CLs.<sup>126</sup> 3D catalyst layers with the more stable IrO<sub>2</sub> building the supporting layer itself are therefore a promising alternative to noble (active) metal supports. Faustini et al. presented hollow spherical Ir-based structures consisted of a porous Ir-matrix decorated with Ir-nano-needles to increase the specific surface area.<sup>127</sup> The microporosity of the spheres additionally led to the enhanced distribution of gases and water.

*Titanium oxide* - A compromise between durability and cost is the use of titanium as supporting material. As titanium withstands the high voltage and acidic environment at the anode side, it is used as durable PTL substrate and catalyst support. Rozain et al. mixed TiO<sub>2</sub> particles with IrO<sub>2</sub> to prepare CCM-configurations.<sup>128</sup> A reduced ohmic resistance most probably due to the increased interfacial area towards the PTL, was the case. Bernt et al. used a commercial IrO<sub>2</sub>/TiO<sub>2</sub> powder from Umicore to determine the optimum Nafion content of the anode catalyst layer in a CCM-configuration.<sup>87</sup> The increased interfacial contact area between CL and PTL was again mentioned as main reason for the improved performance compared to unsupported IrO<sub>2</sub> catalysts, as well as the increased mass specific activity due to the increased specific active surface area. Bernt et al. pointed out the importance of an optimized electrical interface between PTL and CL, especially at low loadings, with a reduced in-plane conductivity.<sup>87</sup> An intermediate contact of catalyst and support was reached by Mazúr et al.<sup>129</sup> and Oakton et al.<sup>130</sup> with the synthesis of IrO<sub>2</sub>/TiO<sub>2</sub> nanoparticles. Wang et al. introduced Ti<sub>4</sub>O<sub>7</sub> for the synthesis of (Ir/Ti<sub>4</sub>O<sub>7</sub>) particles.<sup>131</sup> Besides titanium on powder base, Yoo et al. also studied 3D TiO<sub>2</sub> nanotubes as supporting frames to be doped with IrOx and RuOx.<sup>132</sup> In CCM-configurations however, there will always be a limit of direct contact points of the PTL with the catalyst layer and therefore the risk of inactive parts of the catalyst as well as of the formation of hot-spots.<sup>80, 111</sup>

### **PTEs in combination with supported catalysts**

Kang et al. showed the effect of an increased specific mass transport activity of cathodic PTEs vs. CCM-configurations by making the hydrogen bubble formation visible in the holes of a laser structured PTL-foil.<sup>133</sup> In case of the catalyst coated foil as well as in case of the coated membrane, the same bubble formation pattern along the edges of the holes was monitored indicating that only those parts of the catalyst layer being in direct contact with the PTL are active during PEMWE operation. At the anode side, no commercial PTEs are available due to the sophisticated fabrication of suitable porous titanium substrates with smooth surfaces. First attempts to manufacture a titanium based MPL are still research based and were not yet used for PTE-development.<sup>102</sup> Promising works on anodic PTEs however exist, as Polonsky et al. sprayed TaC supported IrO<sub>2</sub> catalyst layers directly on a Ti-felt.<sup>134</sup> By this, the ionomer had not only the function of a binder, but also of the proton conductive phase in the catalyst layer. Choe et al. electrodeposited the iridium catalyst directly on a Ti-felt, which increased as well the mass specific activity and additionally was identified as a barrier for titanium oxidation (degradation).<sup>135</sup> A comprehensive study on how to optimize PTEs for PEMWE was to the best of the authors knowledge not provided so far.

## 2.4 Structure of this thesis

This work presents the development of novel PTE-based electrodes for PEMWE when using first standard materials, fabrication and characterization techniques as widely used in PEMWE MEA development (chapter 3). A test-cell and test-bench was co-designed in this thesis with PhD-student Friedemann Hegge and is presented as well in the materials and methods chapter 3. Chapters 4-8 show the results of developing PTEs in this work and are partly published or submitted as full research paper as indicated below. The contributions of the author of this thesis are clearly marked in this section as well as in every results chapter in this thesis.

- In chapter 4, the influence on the polarization behavior when gradually changing the MEA-configuration from a standard CCM-configuration towards a full PTE-configuration is evaluated. For this, data from electrochemical and structural characterization of the MEAs is combined with the idea of a structural model of the different electrode-membrane interface. This chapter (except the section 'critical discussion') is left as published in the original peer-reviewed research paper with the author of this thesis being the first author of the publication.<sup>1</sup>
- In chapter 5, parameters to optimize PTEs for the anode side in PEMWEs were evaluated via screening different Ti-substrates, catalyst and ionomer loadings. With the most reproducible electrode configuration, a stability test of 200 h at a constant current hold was performed. This chapter (besides the critical discussion) is left as published in the original peer-reviewed research paper with the author of this thesis being the first author of the publication.
- In chapter 6, results of implementing a supported  $\text{IrO}_2@\text{TiO}_2$  catalyst for the OER at PTEs for the anode side are presented. As this particular work was submitted as full research paper with a joint 1<sup>st</sup> authorship of the author of this thesis (MEA fabrication and characterization) with Dr. Chuyen Pham (synthesis and characterization of the catalyst materials), the contributions of the author of this thesis to chapter 6 were:
  - Sections 6.1 (introduction) and 6.5 (summary and conclusion) are left as submitted for publishing with minor contributions from the author of this thesis.
  - Section 6.2 (synthesis and characterization of  $\text{IrO}_2@\text{TiO}_2$  catalyst) was written by the author of this thesis based on the original scientific data contributed by Dr. Chuyen Pham in the submitted manuscript.
  - Sections 6.3 and 6.4 (MEA preparation and characterization) were left as submitted in the original research paper with major contributions of the author of this thesis.
  - Section 6.6 (supporting information) contains parts of the supporting information as originally submitted and indicates the contribution of the author of this thesis directly in section 6.7.
  - Section 6.7 (outlook) is not part of the submitted research paper and shows results of gradient catalyst layer structures using the  $\text{IrO}_2@\text{TiO}_2$  catalyst as evaluated by the author of this thesis.
- In chapter 7, approaches to fabricate a titanium based MPL on commercial Ti-PTLs via simple deposition techniques as spray coating, painting or doctor blading in combination

with sintering are evaluated. The results of this chapter shall serve as preliminary studies for further development steps.

- In chapter 8, results of applying a novel non-noble metal catalyst for the HER at the cathode side in PEMWEs are presented. As this particular work was submitted as full research paper with a joint 1<sup>st</sup> authorship of the author of this thesis with Peter Holzapfel, the contributions of the author of this thesis are clearly stated in the following:
  - Sections 8.1 (introduction), 8.2 (synthesis and characterization of  $\text{Mo}_3\text{S}_{13}$ -NCNT catalyst), 8.3 (MEA preparation and characterization) and 8.5 (critical discussion) were written by the author of this thesis based on the data regarding catalyst characterization provided by co-authors and own measurement data regarding MEA-characterization.
  - Section 8.4 (full-cell characterization) was left as submitted with major contributions of the author of this thesis.

The structural changes in every development step are schematically shown in Fig. 12 to give a better overview. The numbers refer to the above summarized results chapter of this thesis. Chapters 4-8 are completed each with a critical view and outlook to discuss disadvantages and advantages of the presented development approaches. After summarizing the main results of this work, a comprehensive outlook states the next development steps for further optimizing PTEs for PEMWE applications.

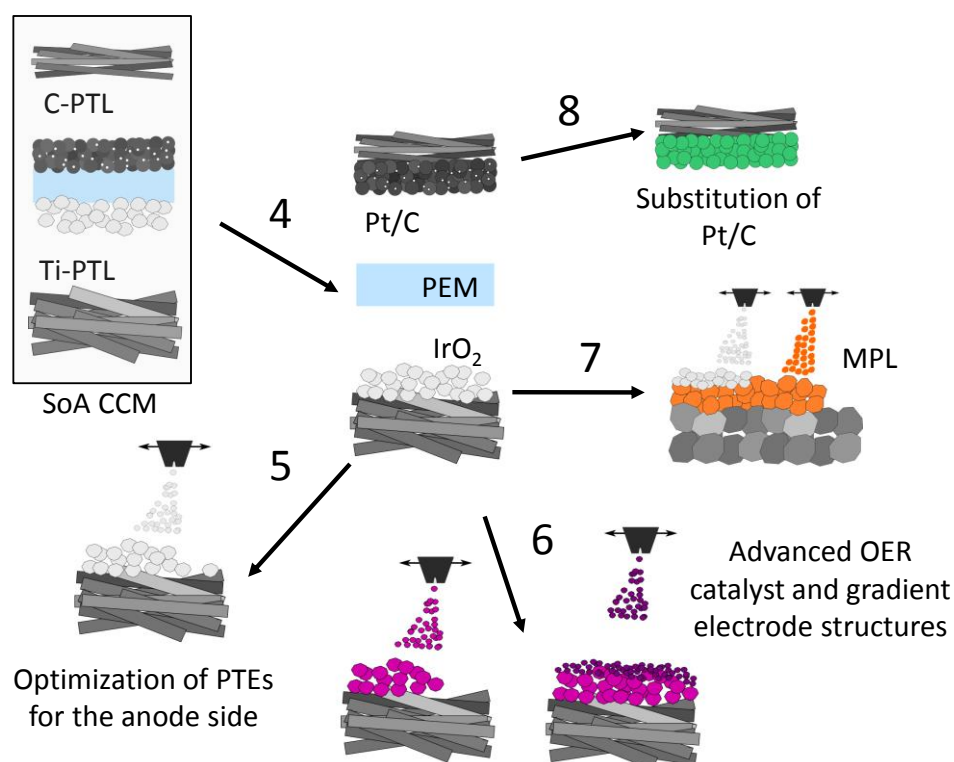


**Fig. 12** Overview on the development steps for PTEs in PEMWE application in this work. The numbers refer to the respective chapters of this thesis.

### 3 Materials and Methods

Standard MEA components purchased from commercial suppliers were used as reference systems for the structure and performance of the PTEs developed in this work (section 3.1). Spray coating was the main fabrication technique to deposit CLs and ionomer layers on various substrates (section 3.2). The process of sintering to fabricate binder-free Ti-MPLs is described in section 3.3. In the subsequent sections 3.4 and 3.5. tools for the structural and electrochemical characterization of the electrodes developed in this work as well as of the commercial and in-house synthesized catalyst materials are presented.

#### 3.1 Commercial MEA materials

Besides anodic PTEs, all other components of the MEA could be purchased for testing and for further deposition of CLs. Nafion membranes of the types N117 (175  $\mu\text{m}$ ), N115 (150  $\mu\text{m}$ ) and N212 (50  $\mu\text{m}$ ) were purchased by FuelCellStore and IonPower. Nafion membranes coated with the  $\text{IrO}_2$ -based anode (1.5  $\text{mg cm}^{-2}$ ) and Pt/C-based cathode (0.5  $\text{mg cm}^{-2}$  60 % Pt/C) to form complete CCMs were purchased from FuelCellsEtc, as well as half-sided CCMs (Fig. 13).

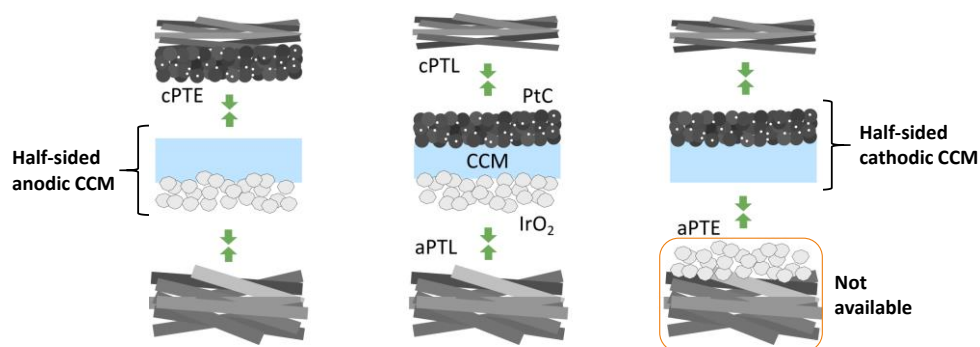


**Fig. 13** Overview on commercial MEA-components purchased for the development of PTEs in this work and the characterization of different MEA-configurations. PTEs for the anode side are not yet commercially available.

PTLs for the anode side were 1 mm thick porous titanium substrates purchased from Mott (powder sinter, 40 % porosity, 50  $\mu\text{m}$  particle size) and Bekaert (fiber sinter, 76 % porosity, 20  $\mu\text{m}$  fiber diameter) as in Fig. 14 A,B. The sheets were laser cut into 4 and 5  $\text{cm}^2$  squares to be used as substrates for the PTEs or to be pressed against the anode side of a CCM. The PTLs were cleaned in an ultrasonic bath for 10 min in an alkaline cleaning solvent (Borer Chemie, 5 vol % Deconex OP153 in DI-water) to remove organic contaminations. The PTLs were rinsed and sonicated for 10 min first in 2-Propanol and subsequently in DI-water. For the cathode side, 410  $\mu\text{m}$  thick carbon-cloth PTLs with MPL (type GDL-CT) and cathodic PTEs based on the GDL-CT with 0.5  $\text{mg cm}^{-2}$  60 % Pt/C (type SL-GDE) were purchased from FuelCellsEtc (Fig. 14 C.1 and C.2).

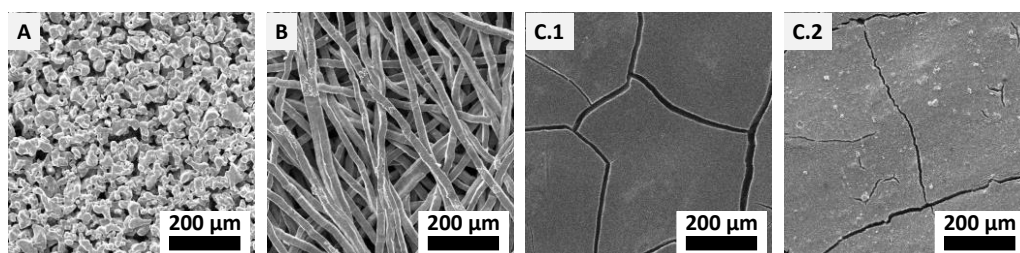


**Fig. 14** Porous powder- and fiber-sintered titanium PTLs for the anode side (A,B) Porous carbon cloth with MPL (C.1) and Pt/C-based CL on top forming the cPTE (C.2).

### 3.2 Fabrication of electrodes via spray coating

To fabricate thin catalyst layers, titanium based intermediate layers as well as Nafion coatings, the spray deposition device Exacta Coat from Sono-Tek was used (Fig. 15). A liquid ink (e.g. containing the metal particles or Nafion dispersion mixed with alcoholic solvents) is inserted in the syringe pump (A) and pumped through a tubing system towards the ultrasonic nozzle in the spray chamber of the spray coater (B). At the tip of the nozzle (48 kHz, type AccuMist), the ink is atomized to a fine mist (C). By defining a spray path along which the nozzle moves in the x- and y-direction, a homogeneous layer can be deposited on various substrates (D). The substrates are placed on a hot plate. The hot plate is heated to temperatures slightly below or above the boiling point of the solvents to ensure the immediate evaporation of solvents once the ink touches the surface of the substrate. In this way, the porosity and infiltration depths of the sprayed ink can be controlled.

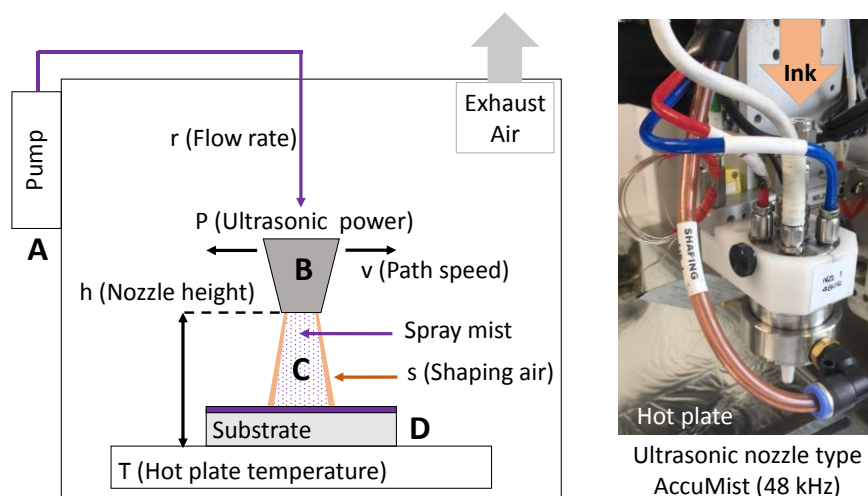


**Fig. 15** Schematic setup of the spray coater with the syringe pump (A), the ultrasonic nozzle (B), the atomized ink (C) and the substrate placed on the hot plate (D). The picture on the right side shows the ultrasonic nozzle type AccuMist as used in this work.

**Flow rate  $r$ :** Defines the amount of liquid ink per time unit that is pumped via the syringe pump through the tubing of the spray coater towards the ultrasonic nozzle to be deposited on the substrate. If the flow rate is too low, particle sedimentation in the tubing and blockage of the nozzle can occur; if the flow rate is too high, an insufficient drying of the deposited layers can lead to wrinkling of the membranes or the complete wetting of porous substrates.

**Path speed  $v$ :** Defines the time for spray coating of one complete layer. The lower the path speed, the higher the amount of deposited ink per time and area and the higher the risk of insufficient and inhomogeneous drying. The path speed in combination with the flow rate is therefore used to control the deposited layer thickness.

**Hot plate temperature  $T$ :** Defines the temperature of the substrates to be coated and thus the evaporation rate of solvents. The temperature is usually set higher than the boiling temperature of the solvents used in the inks, in order to ensure a sufficient and fast drying of the sprayed layer as soon as it touches the surface of the substrate. The infiltration behavior and porosity of the deposited layer are dependent on the drying behavior. Upper limits for the temperature are however the thermal stability of the used substrates. When toxic solvents are used, the exhaust air of the spray coater needs to be controlled at any time to prevent the flow of vapor out of the chamber towards the operator of the spray coater.

**Ultrasonication power P:** Defines the droplet size of the spray mist. To prevent heating and blockage of the nozzle, the sonication power needs to be adjusted together with a sufficient flow rate. A low sonication power does not atomize the inks sufficiently. This leads to the formation of inhomogeneous layers due to the uncontrollable drying behavior of large droplets on the surface of the substrates.

**Shaping air s:** Is needed to form a defined spray mist that is directed towards the substrate. Without the shaping air, the small droplets within the mist are distributed in the whole chamber of the spray coater and removed by the exhaust air stream. The pressure of the shaping air should not be too high to dislocate the sprayed layers on the substrate.

**Nozzle height h:** Defines the diameter of the sprayed mist cone together with the applied shaping air at the surface of the substrate. A high nozzle height leads to a diffusive coverage of the surface, whereas the nozzle in close distance to the surface focuses the sprayed mist in a smaller diameter. The nozzle height should be sufficiently high to prevent spraying of the ink directly deep into the pores of porous substrates.

**Spray pattern and pitch p:** Define the homogeneity and the surface roughness of the final deposited layers. The width per sprayed line equals the diameter of the formed spray mist of the ultrasonic nozzle. To cover the surface line-by-line, the distance between the lines (pitch) should therefore equal the width of one sprayed line (Fig. 16 A).

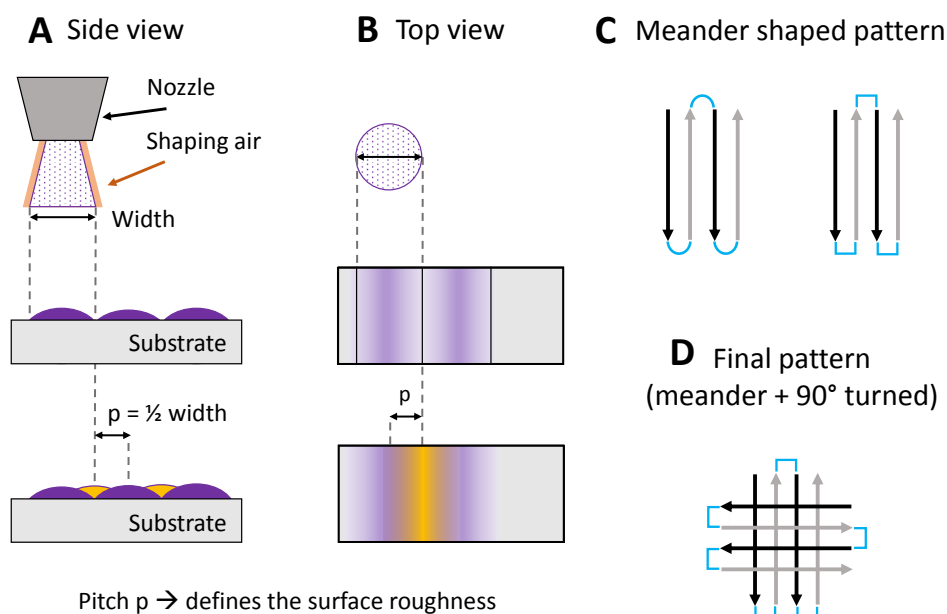


**Fig. 16** The design of the spray pattern decides over the homogeneity of the deposited layer. The pitch between the sprayed lines should be at least half of the width of the spray mist created by the nozzle and the shaping air (A,B). Layers in this work were deposited via a meander shaped 90° turned pattern with rectangular turning points (C,D).

Considering the thickness distribution of the sprayed line, the distance between the lines should be half of the width, to bring the peaks of the deposited lines closer together (Fig. 16 B). A meander shaped pattern is usually used since it bears the advantage that the nozzle does not have to be turned on and off after every line (Fig. 16 C). The turning points of the meander shaped pattern can be adjusted from circular to rectangular. By this, vibrations and in the extreme case oscillations of the spray coater due to the abrupt turning movement of the device can be reduced. To further increase the homogeneity of the deposited layers, every second layer can be sprayed 90° turned to the layer before (Fig. 16 D).

The spray pattern (meander +90° turned), nozzle height ( $h = 37$  mm), and shaping air ( $s = 0.6$  kPa) were kept constant, but the other spray parameters need to be adjusted for ever new ink composition and substrate to reach the desired homogeneity of the deposited layers (Table 2).

**Table 2** Inks and spray coating parameters of the main metal and ionomer inks used in this work.

Anode				
Ink components and mixing			Spray coating	
Metal powder	IrO <sub>2</sub> Premion (AlfaAesar) IrO <sub>2</sub> /TiO <sub>2</sub> 75 wt% Elyst (Umicore)	IrO <sub>2</sub> @TiO <sub>2</sub> (in-house synthesized)	Flow rate	4.5 ml min <sup>-1</sup>
Ionomer	1-10 wt% Nafion D520 (FuelCellStore)	1 wt% Nafion D520 (FuelCellStore)	Path speed	170 mm s <sup>-1</sup>
Additives	-	-	Pitch	0.75 mm
Solvents	2-Propanol + H <sub>2</sub> O (1:1)	Methanol + H <sub>2</sub> O (3:1)	Power	5 W
Mixing	30 min ultrasonication, 16 h stirring, 30 min sonication		Temp.	120 °C
Cathode				
Ink components and mixing			Spray coating	
Metal powder	Pt/C HiSpec 9100 (60 % Pt) (Alfa Aesar)	Mo <sub>3</sub> S <sub>13</sub> -NCNT hybrid (in-house synthesized)	Flow rate	Pt/C: 0.33 ml min <sup>-1</sup> MoS: 0.45 ml min <sup>-1</sup>
Ionomer	20 wt% Nafion D520 (FuelCellStore)	20 wt% Nafion D520 (FuelCellStore)	Path speed	Pt/C: 140 mm s <sup>-1</sup> MoS: 110 mm s <sup>-1</sup>
Additives	-	10 wt% C-black (Vulcan XC-72R, FuelcellsEtc)	Pitch	0.75 mm
Solvents	2-Propanol + H <sub>2</sub> O (3:1)	2-Propanol + H <sub>2</sub> O (1:1)	Power	Pt/C: 4.5 W MoS: 5 W
Mixing	40 min ultrasonication	30 min ultrasonication 48 h stirring 30 min ultrasonication	Temp.	Pt/C: 90 °C MoS: 110 °C
Nafion coating				
Ink components and mixing			Spray coating	
Metal powder	-		Flow rate	0.2 ml min <sup>-1</sup>
Ionomer	2.5 wt% Nafion D2020 (FuelCellStore)		Path speed	90 mm s <sup>-1</sup>
Additives	-		Pitch	0.5 mm
Solvents	2-Propanol		Power	2.5 W
Mixing	5 min vortex mixer		Temp.	60 °C, 120 °C

In this work, several metal inks as well as ionomer inks were sprayed on dense Nafion membranes as well as on porous titanium and carbon PTLs. The ink composition and stability defines the final layer composition and therefore ink mixing and ink treatment during spray coating are essential. Sedimentation either in the syringe or in the long tubing of the spray coater has to be prevented. To avoid inhomogeneous sprayed layers with another noble metal and Nafion content as desired, the following improved workflow for spray coating was applied to stabilize the metal inks:



**Ink mixing:** To avoid an exothermic reaction of the catalyst with the alcoholic solvents, first the catalyst powders, followed by water were added. The solvents and subsequently Nafion as ionomer or binder were inserted while ensuring a homogeneous mixture after every new component was added. The complete ink was kept in motion via a magnetic stirrer and placed in an ice bath to be further mixed with an ultrasonic tip for 30 min (Hielscher, model UIS250L, 0.55 W, 90 % amplitude). After sonication, the ink was placed on a magnetic stirrer overnight. Right before spray coating, the sonication step was repeated.

**Spray coating workflow:** The inks were vortexed and inserted in the syringe of the spray coater with the magnetic stirrer turned on 90 % maximum power. Only a fraction (ca. 15 ml) of the ink was loaded into the syringe at once to avoid sedimentation of particles. The other part of the ink was placed on a magnetic stirrer to repeat the vortex mixing prior to the next loading step. The flow rate of the pump was set to a high value to prevent sedimentation in the tubing. The as-delivered setup of the spray coater was modified to minimize the length of the tubing between syringes and spray nozzle. Therefore, any valves and connectors between syringe and nozzle were removed and the outlet of the syringe directly connected with the inlet of the nozzle. The sonication power at the nozzle was set to a maximum value of 5.5 W to form the spray mist at high flow rates.

Especially unsupported IrO<sub>2</sub> inks and titanium inks for the intermediate layer were prone to sedimentation, since the binder content needed to be as low as possible (electrical conductivity within the final layer, no shielding of active particles). Pt/C inks for the cathode side were more stable as the particles are in the nanometer range and more Nafion is usually used. The choice and ratio of solvents in the ink influence the particle stability and drying rate due to different evaporation temperatures. When a new ink was used, a series of vials with different ratios and types of solvents was prepared and placed on the shelf for 24 h. The degree of sedimentation was decisive for the choice of the final ink composition. The standard anodic inks consisted of 1 wt% solids and the cathodic inks of 2 wt% solids. Solids consisted of metal powders, the ionomer and other solid additives (Eq. 23). The ionomer was added to the ink in form of a Nafion dispersion with e.g. 5 or 20 wt% ionomer in an alcoholic solution (FuelCellStore, Nafion D520 and D2020). The solvents in the dispersion as well as additional solvents (Methanol, 2-Propanol, DI-water), accounted for 99 wt% (anodes) and 98 wt% (cathodes) solvent part of the final ink, respectively (Eq. 24).

$$\text{wt\% solids} \quad m_{\text{solids}} = m_{\text{metal powder}} + m_{\text{ionomer}} + m_{\text{additives}} \quad (23)$$

$$\text{wt\% solvents} \quad m_{\text{solvents}} = m_{\text{additional solvents}} + m_{\text{solvents dispersion}} \quad (24)$$

To determine the noble metal loading of the sprayed catalyst layers, a rectangular 1 cm<sup>2</sup> metal piece was placed on a magnetic stripe and spray coated as well. The metal piece was weighted before coating and in regular steps when a certain number of layers was deposited. The final weight to be spray coated was calculated as the sum of the desired catalyst loading and the ionomer content in the ink. EDX and TGA measurements were conducted to analyze the real sprayed Nafion content (section 3.4).

### 3.3 Sintering of Ti-MPLs

Sintering of Ti-particles was applied to fabricate a mechanically stable MPL on top of commercial porous titanium substrates. Ti-inks containing Ti-powder, solvents and binders were deposited on the Ti-PTLs, dried and placed in a tubular furnace. The sintering of the particles to form a continuous, porous compound was reached via setting the maximum process temperature to 1000 °C. By this, the oxide film on the titanium particles was removed<sup>99</sup> and an intermediate contact between the Ti-particles was reached to form the MPL. To prevent the infiltration of the porous Ti-PTL that was directly coated with the Ti-ink, a densification step of the dried Ti-ink was not performed. Binders were necessary to deposit a homogeneous Ti-layer, were burned out during sintering. Risks are hereby the formation of oxide layers and carbon residues of not fully burned binders. Both effects can lead to a low electrical conductivity, low degree of interconnected particles and impurities reducing the mechanical strength. In literature, a few straightforward approaches for the fabrication of a sintered Ti-layer were presented and were the basis for the trials in this work.<sup>136–138</sup> The furnace used in this work (MTI, model OTF-1200X) was equipped with a continuous gas flow and ceramic holders to place the substrates (Fig.17). Different heating and cooling rates were tested with holding times at several intermediate temperature steps with the maximum temperature of 1000 °C. A sophisticated process parameter control of heating and cooling rates as well as the number and value of intermediate temperature hold steps is required to prevent mechanical stress in the layers. When burning a polymeric binder, the formation of carbon residues can be prevented by supplying an oxygen stream through the glass tubing. Gaseous CO<sub>2</sub> is then ideally removed from the samples with the exhaust air.

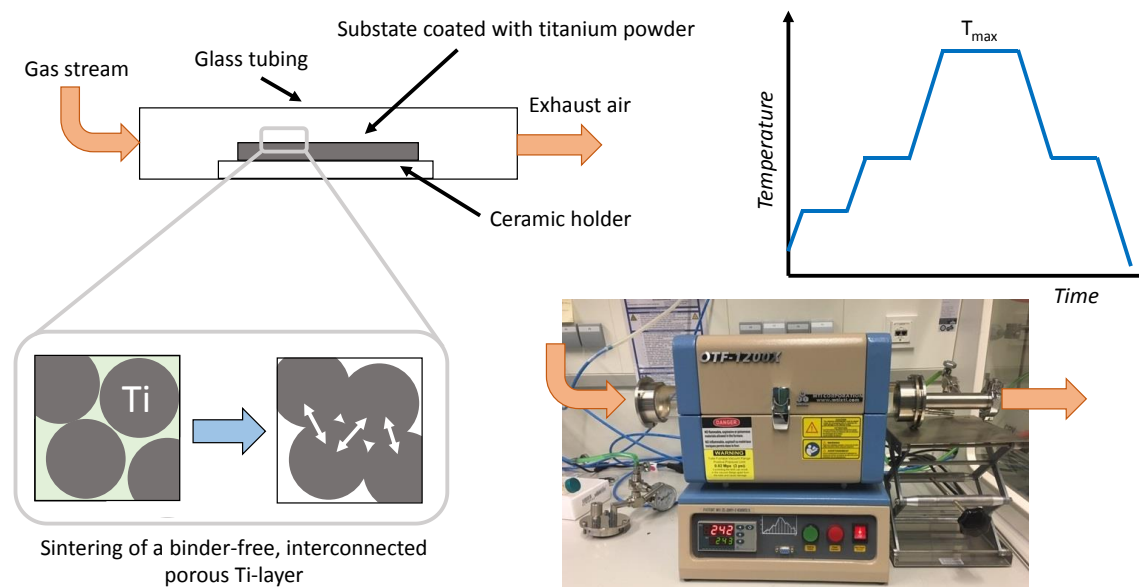


**Fig. 17** High temperature furnace with the glass tubing holding the substrates placed on ceramic holders. A sophisticated process control is required to fabricate a mechanically stable, binder free Ti-PTL. The furnace is connected to the exhaust air.

As an oxygen containing atmosphere causes the risk of oxidation of the titanium particles, forming gas ( $H_2+N_2$ ) was used in combination with the sintering of a binder free titanium layer. By this, the oxygen at the surface of the titanium layers was reduced to gaseous  $H_2O$  and removed from the substrates by the exhaust air. To prevent particles from the sinter furnace entering directly into the exhaust air system of the laboratory, a water-filled wash-bottle was connected to the outlet of the furnace.

### 3.4 Electrochemical characterization

A self-designed test cell as well as a self-build test bench co-designed of the author of this thesis with the PhD-student Friedemann Hegge was used. The different test-setups e.g. for recording polarization curves are described as well as the operation conditions for MEA-testing. For the characterization of the commercial catalyst materials used in this work as well as of the advanced catalysts synthesized in-house by Dr. Chuyen Pham, a three-electrode setup was used to characterize the kinetics and catalytic activity of the different catalysts.

#### 3.4.1 Test cell and test bench to test the different MEA-configurations

The in-house designed test cell enabled a simple layer-by-layer assembly from the cathode side, via the membrane up to the anode side. The water in- and outlets were screwed into the most outer parts of the cell which are 20 mm thick Al-plates (Fig. 17 A). The Al-plates held the heating elements to set the cell temperature to 80 °C and guided eight M5 screws to fix the inner cell parts. The screws were tightened in three steps of 3.0, 5.0 and 8.5 Nm. The potentiostat to apply voltage or current to the MEA was connected to 2 mm thick Cu-plates, which were electrically insulated from the Al-plates via a self-adhesive polymer foil (Fig. 17 B). The Cu-plates were electrically connected with 12 mm thick Ti flow fields with a milled 5 cm<sup>2</sup> parallel channel structure for the distribution of gases and water (Fig. 17 C). The flow fields used in chapter 7 were coated with a ca. 300 nm thick gold layer to improve the long-term durability (prevent oxidation of the titanium surface) and to reduce electrical resistances between flow field and PTLs. A temperature sensor was inserted in the cathodic flow field to monitor the cell temperature. The MEA (Fig. 17 D) consisting of the membrane, catalyst layers and PTLs was sandwiched between the two titanium flow fields. PTFE frames were used to center the PTLs and PTEs, respectively. The PTFE frames as well acted as hard stops to set the compression of the porous materials (Fig. 17 E). The Ti-PTLs were assumed incompressible during cell assembly and therefore 1 mm thick frames (same thickness as the PTLs) were used at the anode side. The carbon PTLs and PTEs respectively were however made of a woven carbon cloth material, which can be compressed to a high degree. In several preliminary tests with different thicknesses of the PTFE frames at the cathode side, a relatively high compression rate of 60 % was leading to the lowest interfacial resistances. This compression corresponds to a PTFE-frame thickness of 150 µm at the cathode.

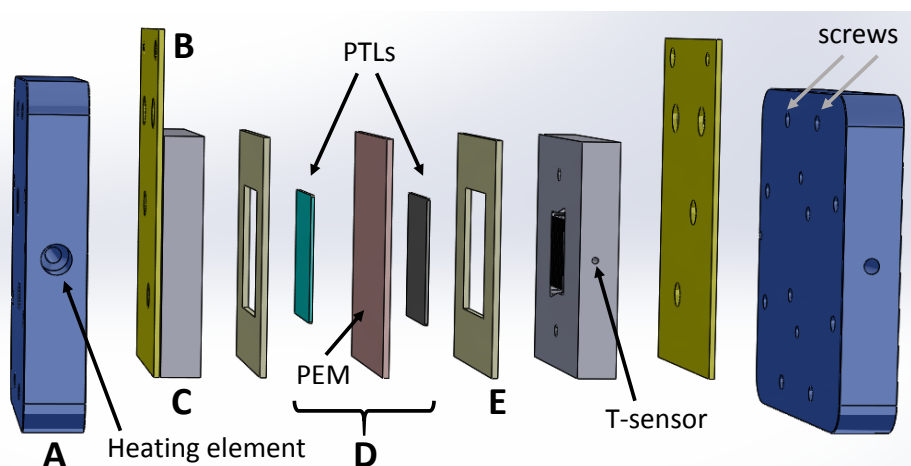


**Fig. 17** Solid Works drawing of the in-house designed test cell with the Al-plates (A) holding the screws and the heating elements, the Cu-plates (B) for the electrical connection, the Ti flow fields (C) as well as the PEM, CLs and PTLs forming the MEA (D) with the PTLs or PTEs respectively placed in PTFE frames (E).

An even distribution of the assembly pressure over the active area is essential to establish a homogeneous interfacial area between all parts of the MEA as by this, an even current and temperature distribution is established. With the help of a pressure sensitive paper (Fujifilm, Prescale) the assembly pressure can be evaluated. To this end, the pressure paper is assembled instead of the PEM in a standard MEA-test cell setup. After 10 s the cell can be disassembled and the pressure distribution on the paper is analyzed with a mapping software (Fujifilm, FPD-8010E). The assembly pressure applied on the active area of the MEAs assembled in the in-house fabricated test-cell was calculated to be approximately 24 MPa. The assembly pressure is a sensible parameter as it defines the interfacial contact between all different layers, which should be as high as possible. However, too much pressure can decrease the pore sizes within the porous layers that could then increase mass transport losses. The assembly pressure should as well not be too high to prevent damage of soft functional parts as e.g. the membrane or the cPTL. Damaging the membrane would lead to an electrical short and gas crossover (holes in the membrane) and reduced electrode functionality (CL can show cracks or detachment from the PTL and PEM). Fig. 18 A shows the side of the pressure paper that was pressed against the anodic Ti-PTL. The parallel finger structure of the flow field is visible as well as the even pressure distribution over the active area of 5 cm<sup>2</sup>. Fig. 18 B shows the other side of the pressure with the cathodic PTL still attached.

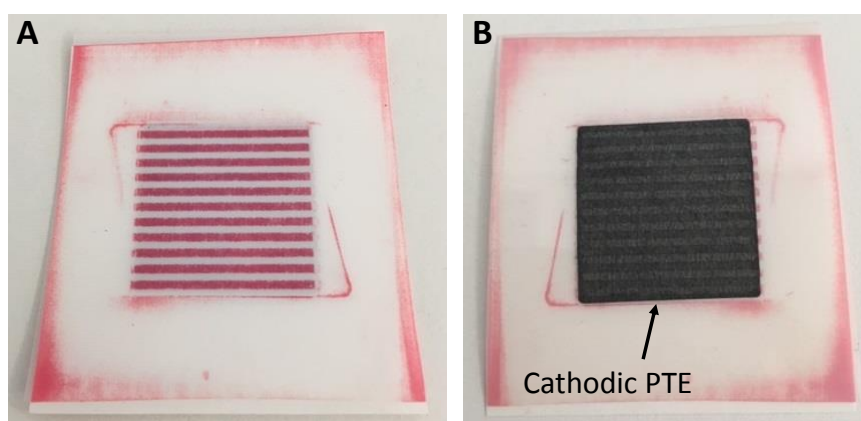


**Fig. 18** Pressure paper after disassembly of the test cell (the pressure paper was assembled instead of the PEM). A Front side of the pressure paper pressed against the anodic PTL. The finger structure of the flow field is clearly visible as well as the positions of the water in- and outlet. B Back side of the pressure paper with the cathodic PTE pressed into the pressure paper.

The test cell (Fig. 19 A) was connected to a peristaltic pump (Ismatec, model IP 65) (Fig. 19 B) enabling the separate supply with DI-water of the anode and cathode side at a flow rate of 40 ml min<sup>-1</sup>. At the anodic water in- and outlet, inline temperature sensors were assembled to monitor possible temperature gradients over the test cell (Fig. 19 C). Between the pump and the test cell, a thermostat (Lauda, model Ecoline 003, set to 88 °C) was placed to pre-heat the water flowing into the test cell to around 80 °C (Fig. 19 D). The water bath of the thermostat needed to be refilled every 12 h to ensure a continuous heating rate. The water-gas mixture leaving the anode and cathode side of the test cell was pumped into separate gas-liquid separators (Fig. 19 E). Oxygen was directly released of the anodic compartment, whereas hydrogen was directed to the exhaust system. The anodic gas-water separator could be opened to refill fresh Di-water into both compartments via opening the connecting valve in-between the compartments (Fig. 19 F). The refilling of fresh water was necessary during longterm-testing, as no ion exchanger to purify the DI-water was available. A Scribner 857 potentiostat (Fig. 19 G) was connected to the test cell. The test setups used in this work are explained in more detail in the next section.

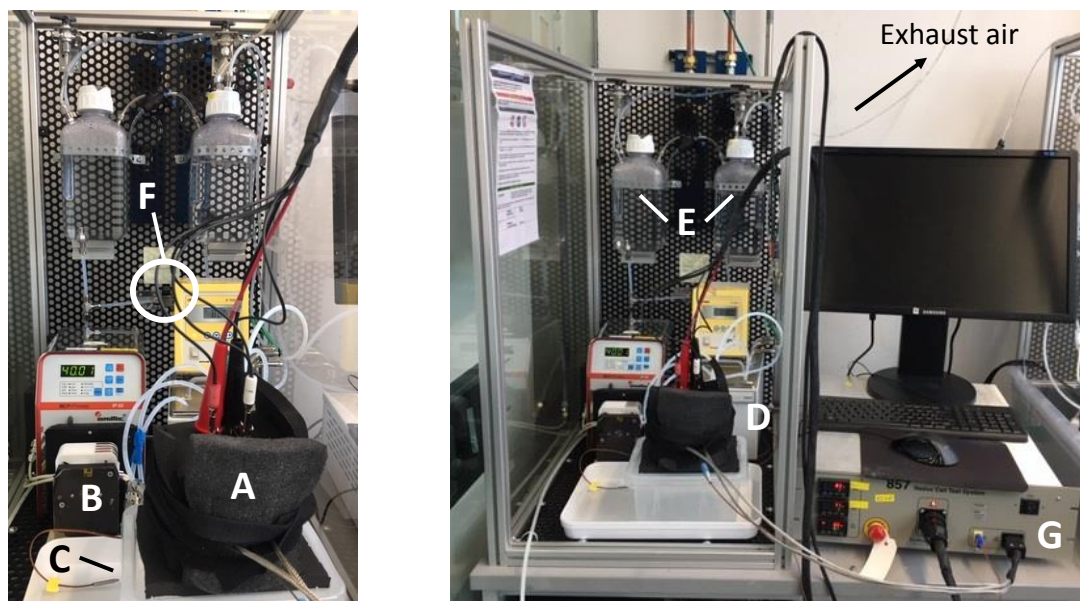


**Fig. 19** The test cell (A) assembled in the test bench and connected to the peristaltic pump (B), in-line temperature sensors (C), the thermostat (D) and the gas-liquid separators (E) for the anode and cathode side respectively. A valve between the anodic and cathodic compartment (F) enables the refilling of the cathodic compartment with fresh DI-water as the lid of the H<sub>2</sub>-compartment is directly connected with the exhaust air system of the laboratory. The test cell is connected to a potentiostat model 857 from Scribner (G).

### 3.4.2 Recording and analysis of MEA polarization data

The cell voltage and in parallel the high frequency resistance (HFR) were recorded after a stable cell temperature of 80 °C was observed. Prior to recording the polarization data, a break-in procedure was applied to activate the catalyst layers of the MEA and to condition the relatively thick Nafion membranes. The **break-in** procedure (activation of the catalyst) for the anodic PTEs was a 15 times repeated voltage driven cycling from 1.4 V - 2.2 V in 200 mV steps (each step held for 30 s). The break-in procedure for the thicker non-noble catalyst layers at the cathode side consisted of constant current holds of 2.5 A for 300 s and 15 times repeated voltage driven cycling from 1.4 - 2.2 V and 2.2 - 2.3 V, respectively in 200 mV steps (each held for 30 s). The break-in protocol was terminated by applying the constant current step of 2.5 A again for 300 s. The **polarization curve** was recorded in several segments with the highest resolution in the kinetic region where every current step was held for 120 s. For the anodic PTEs, the segments were from 0 A - 0.04 A in 10 mA steps, from 0.05 A - 1 A in 50 mA steps, from 1.25 A - 3 A in 250 mA steps, from 3.5 A - 5 A in 500 mA and from 6 A on in 500 mA or 1000 mA steps. For the cathodic PTEs, the segments were from 0 A - 0.025 A in 25 mA steps, from 0.05 A - 0.5 A in 50 mA steps, from 0.6 A - 1 A in 100 mA steps, from 1.5 A - 5.5 A in 500 mA and from 6 A on in 500 mA or 1000 mA steps. A constant current step with 2.5 A for 300 s completed the test protocol. The HFR was measured in parallel at a frequency of 1 kHz. To compare the **stability** of the MEAs to literature<sup>139, 140</sup>, a constant current hold was applied for 200 h while recording the cell voltage and HFR. During the stability test, polarization curves were recorded to calculate degradation rates and to study the change in kinetic, ohmic and mass transport region.

According to Suermann et al.<sup>141</sup> the contributions of the kinetic, ohmic and mass transport overpotential to the overall cell voltage were extracted from the polarization data. Fig. 20 exemplary shows the cell voltage (voltage losses in region A,B and C) as well as the HFR (ohmic losses in region B) as recorded during testing the MEA. The HFR gives an information about the ohmic resistances in the membrane, cell parts and within the interfaces of the different functional



layers as the PTL, CLs and PEM. To evaluate the contributions of the mass transport and kinetic overpotential, the HFR-free cell voltage is evaluated, based on the measured HFR and cell voltage. This curve represents influences on region A and C of the polarization curve, as the HFR of region B is removed. A steep slope of the HFR-free cell voltage would indicate strong mass transport losses due to an insufficient transport of water and gases e.g. due to a too low porosity of the catalyst layer. The kinetic overpotential has the strongest impact at low current densities and therefore a zoom in the low current density region of the HFR-free cell voltage plotted on a semi-logarithmic scale, is used to analyze kinetic losses.

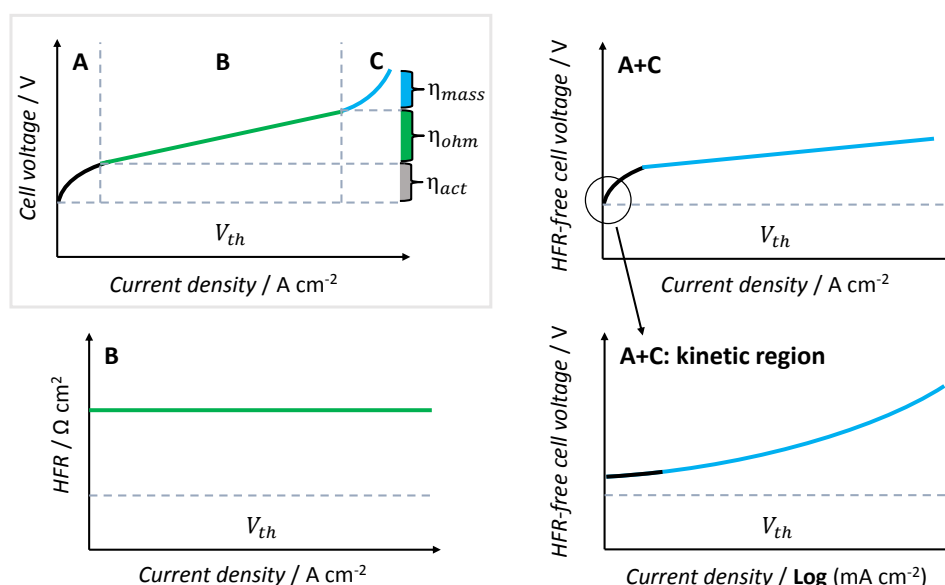


**Fig. 20** Analysis method of the polarization data in this work: The recorded cell voltage is divided into contributions from the kinetic (A), ohmic (B) and mass transport region (C).

### 3.4.3 Three-electrode-setup

For catalyst development, measuring the activity of the catalyst material for the desired reaction prior to conducting full-cell tests is an essential characterization.<sup>142</sup> A three-electrode setup is hereby used to study the intrinsic activity of a catalyst without influences from other functional parts like in the PEMWE cell. In a three-electrode setup, a glassy carbon disc mounted on a rotating disc electrode tip can be used as working electrode (WE). The catalyst powder mixed with ionomer is deposited on the RDE. By rotating the electrode, evolving gas bubbles are removed and thus mass transport problems limited. The WE is inserted in an acidic 0.5-1 M H<sub>2</sub>SO<sub>4</sub> electrolyte solution for the HER and 0.1 M HClO<sub>4</sub> electrolyte solution for the OER to mimic the acidic conditions close to the Nafion membrane under PEMWE operation conditions. A counter electrode (CE) is needed to balance the electron transfer at the WE and is usually realized with a Pt-wire immersed as well in the electrolyte. A reference electrode (RE) is needed to determine the overpotential at the WE compared to a known value. A reversible hydrogen electrode (RHE) is commonly used as RE. Via a linear sweep voltammetry (LSV) measurement, the potential of the WE is linearly increased and the corresponding current density is recorded. Once the onset potential (in V vs. RE) is reached, the reaction starts and thus the current density increases exponentially. The onset potential is therefore a thermodynamic value and correlated with the Gibbs free energy of the chemical reaction taking place. The current density at a given potential or per mass of catalyst material is used to describe the catalyst activity. The difference between the thermodynamically determined potential needed to drive the reaction and the experimentally needed potential to reach a certain current density is the overpotential at this current density. Plotting the current density vs. the

potential on a semi-logarithmic scale, gives the third important information about the catalyst material, which is the Tafel slope (in  $\text{V dec}^{-1}$ ) in the linear region. The slope is an indicator for the type of reaction mechanism at the catalyst surface and therefore a measure for the kinetics.<sup>143</sup> Catalyst characterization using the three-cell-setup was performed by Dr. C. Pham.

### 3.5 Structural characterization

The microscopic and spectroscopic techniques<sup>144–146</sup> presented in this section were used to characterize the morphology and surface structure of catalyst materials and sprayed electrodes as well as the chemical composition of the different materials and layers. The ink stability was as well studied, as this is a crucial fabrication parameter for spray coating. The results from the structural analysis were used to better explain and understand the electrochemical performance of the catalysts and electrodes in this work as well as to show the successful synthesis of novel catalysts prepared by Dr. C. Pham.

#### 3.5.1 Morphology and surface structure

**Transmission electron microscopy (TEM)** was used to image catalyst particles that were deposited in a thin film on a TEM grid. Due to the interaction of the applied electron beam (120 kV) with the atoms in the sample, an image at a typical resolution of ca. 0.3 nm of the catalyst particles can be provided. Light areas in the image show parts of the sample where the electrons were transmitted and darker areas show parts of the sample where only a few electrons did transmit through thicker parts of the sample. The gained information about the particle size and degree of agglomeration are important material characteristics as they influence the activity of the catalyst as well as the stability within a catalyst ink due to interaction with the solvents. Fig. 21 exemplary shows TEM images of the commercial  $\text{IrO}_2$  catalyst (Alfa Aesar, type Premion) used in this work (TEM device from FEI, model Talos L120C). Especially in case of the in-house synthesized  $\text{IrO}_2@\text{TiO}_2$  catalyst, TEM was an important tool to analyze the core-shell structure of the  $\text{IrO}_2$  catalyst attached to the  $\text{TiO}_2$  cores. TEM images were provided by Dr. C. Pham.

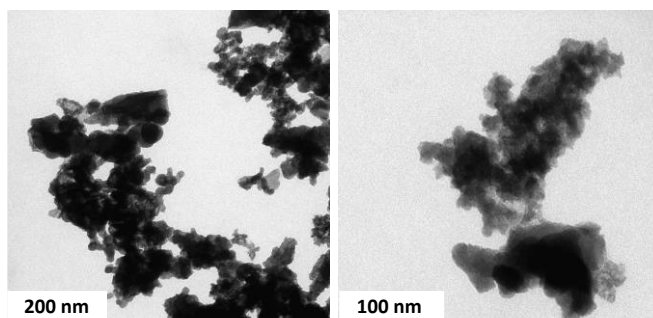


**Fig. 21** Exemplary TEM images of  $\text{IrO}_2$  catalyst powder used to fabricate the anodic electrodes in this work. The primary particle size as well as the size of agglomerates are important material characteristics.

**Scanning electron microscopy (SEM)** was applied to image the surface of the PTLs and electrodes. By this, the distribution and size of metal particles, the average coverage of the substrates and the surface roughness was visualized. Samples were attached to self-adhesive carbon pads and placed on metal holders with a diameter of 1 cm. The samples were cleaned in a  $\text{N}_2$  flow and fixed at the metal holders in the vacuum chamber of the SEM (Tescan, model Vega-3). Two types of electrons resulting from the interaction of the primary electron beam with the sample are used for imaging: backscattered (reflected) electrons of the primary electron beam and secondary electrons that were ejected from surface near atoms. Bright areas in the SEM image prepared by backscattered electrons show parts of the material consisting of atoms of high atomic numbers (in this work e.g.

iridium, platinum or titanium). SEM-images using secondary electrons show the topography of the sample at a standard resolution of 1-20 nm.

By **focused ion beam scanning electron microscopy (FIB-SEM)**, cross-section of the electrodes could be imaged. During FIB-SEM, first a protective platinum layer is deposited on the samples surface. A several  $\mu\text{m}^2$  large area is then defined to be removed by an ion beam. The time of exposing the surface to the ion beam defines the depths of the cut volume and processing time. The exposed cross section can then be polished by an ion beam to remove redeposited material. Tilting the sample holder in direction of an electron source then allows for SEM imaging of the cross-section. The porosity, particle size and quality of interfacial contact areas of the CL were hereby of main interest in this work. With the information gained from repeated FIB-SEM imaging, 3D-models of a certain volume of the sample can be created e.g. to study transport mechanisms in porous layers.<sup>147</sup> FIB-SEM analysis was performed with devices from Zeiss (Crossbeam 540 with GEMINI II and Neon 40 EsB). FIB-SEM data was provided by PhD-students C. Klose, F. Hegge, D. McLaughlin and M. Bierling

### 3.5.2 Chemical composition

By **energy dispersive X-ray spectroscopy (EDX)**, the chemical composition of a material can be determined and the surface near spatial distribution of different atoms. In this work, a device from Oxford Instruments, model X-Max 150 with Aztec software was used for EDX-analysis. The sample preparation was the same as for the SEM or FIB-SEM analysis, as the same vacuum chamber was used for EDX. After imaging the area of interest via SEM, a mapping of the atoms in the surface near layer in this area was performed. For this, the surface was scanned by the electron beam, while detecting the intensity and number of X-rays. X-rays are released from the material in two steps: the primary electron beam creates holes in the inner shell of an atom due to ejecting secondary electrons. The hole is then filled with an electron from a higher energy level (electron shell in greater distance from the core) while releasing X-rays with a characteristic intensity. Via detecting the intensity of the released X-ray, the elemental composition of a material can be evaluated and via mapping a larger area, the distribution of the different atoms can be determined. EDX-data was provided by PhD-student D. McLaughlin.

**X-ray photoelectron spectroscopy (XPS)** was applied to study the molecular structure of the synthesized catalysts. The surface of the sample is hereby irradiated by X-rays, which cause the emission of electrons from inner electron shells of the atom. The binding energy of the emitted electrons and the number of electrons with the same binding energy are detected. The position of intensity peaks in the XPS spectra at a certain binding energy is therefore used to identify atoms and the size of the peak correlates to the number of counted electrons with a certain binding energy revealing the atomic composition of the substrate. XPS spectra were recorded using a Quantera II and analyzed using a CasaXPS software. XPS-data was provided by D. Escalera-López.

The **thermogravimetric analysis (TGA)** of the sprayed catalyst layers was used to determine the composition of the whole volume of the catalyst layer in terms of the real Nafion and noble metal content. For this, catalyst layers with the same calculated final  $\text{IrO}_2$  loading but different Nafion contents were sprayed and scratched off the PTFE sheets in the spray coater. Ca. 15 mg of every powder were burned under air atmosphere to remove carbon residues from the final samples. The weight of the powder was recorded while increasing the temperature as exemplary shown in Fig. 22. The loss of weight at a certain temperature can be related to the breaking of molecular bonds and therefore to the burning of a specific material, in this case the ionomer Nafion<sup>148</sup>. The first slope until a temperature of ca. 300 °C is reached can be related to the evaporation of solvents



(residues of 2-Propanol and water). From then on until 1000 °C the loss of weight can be related to the amount of burned Nafion. The final weight is then the remaining metal content of the original sprayed catalyst layer. TGA-data was provided by A. Warmbold.

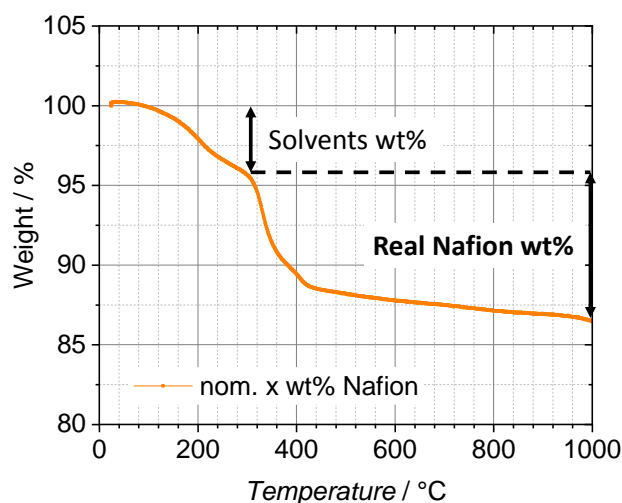


**Fig. 22** Exemplary TGA analysis of an  $\text{IrO}_2$ -metal and Nafion containing catalyst layer. The loss of weight can be correlated to the burning of Nafion until the final weight of the remaining metal part is reached.

### 3.5.3 Catalyst ink stability and thickness of deposited Nafion layers

A **turbiscan stability index (TSI)** measurement was performed to study the stability of the catalyst inks used for spray coating. For this, catalyst inks were prepared with the appropriate amount of solvents and ionomer and filled in glass vials. The degree of sedimentation was evaluated over a duration of 24 h by measuring the transmission and backscattering signals of the luminescent diode over the full length of the sample. Transmission and backscattering data was recorded from the bottom of the vial to the meniscus of the ink. The combination of both transmission and backscattering at different levels of the ink vial was then used as measure for the transparency and therefore the solid parts. TSI-measurements were performed by PhD-student D. Seeberger.

**Confocal Raman imaging** (WITec, model alpha 300) was used to accurately measure the thickness of deposited Nafion layers in this work. Samples for Raman imaging were prepared by spray coating several layers of Nafion on a flat glass substrate. A confocal depth scan was performed and the spectral information was analysed to extract the layer thickness. Raman spectra are generated by irradiating a sample with a laser beam. A part of the incident light is inelastically scattered from the sample, and from this scattered light the so-called Stokes shift (red-shifted with respect to the excitation laser wavelength) is analysed in the spectrometer of the Raman microscope. Raman spectroscopy is a type of vibrational spectroscopy, which detects molecular bonds within a sample based on the vibrations of these bonds. Thus, from virtually any material (besides pure metals) a highly specific Raman spectrum is obtained, and Raman imaging can therefore not only be used to identify unknown bulk samples, but also to perform imaging based on chemical contrast since the confocal microscope adds spatial resolution to the system. In this case, the Raman spectrum of Nafion was analysed along the z-axis to determine layer thicknesses. The intensity of the symmetric stretching mode  $\nu_s(\text{C-F})$  of Nafion at  $732 \text{ cm}^{-1}$  was summarized and thresholded within a depth scan using Otsu's method. Further, the resulting depth profile was compensated for spherical aberration to avoid an underestimation of the actual layer thickness since a metallurgical objective was used in the microscope. Raman measurements were performed by PhD-student T. Böhm.



## 4 From Catalyst Coated Membranes to Porous Transport Electrode Based Configurations in PEM Water Electrolyzers \*

### 4.1 Abstract

So far the superior cell polarization behavior of membrane electrode assemblies (MEAs) using catalyst coated membranes (CCMs) as compared to those using porous transport electrodes (PTEs) was a paradigm in proton exchange membrane water electrolyzers (PEMWEs). However, this paradigm was so far neither systematically investigated nor understood. In this study, we investigate the changes in PEMWE polarization behavior upon gradually changing the MEA from a full CCM towards a full PTE-type configuration. We explain all observed findings based on the idea for a structural model of discontinuous catalyst layers. Our results show, that for current densities above  $750 \text{ mA cm}^{-2}$ , PTE-based MEAs can result in a better polarization behavior than CCMs. Therefore, the prevailing paradigm was disproved. CCMs showed better kinetics, while PTE-type configurations performed more reproducible than CCMs despite rougher surfaces. Due to the trend of a stabilizing HFR-free cell voltage, an improved mass transport behavior of the PTE-type configurations at high current densities is assumed. Within the error-tolerance, no clear differences between PTE and CCM-based configurations in ohmic resistance could be determined. We conclude that PTE-based configurations for PEMWE, as alternatives to standard CCM-configurations, could be highly important for future manufacturing techniques depending on the application's needs.

---

\*The sections in this chapter (besides the critical discussion in section 5.6) have been published identically as an original research paper at the *Journal of the Electrochemical Society* (impact factor of 3.12 in 2018<sup>149</sup>)

*Bühler, M., Holzapfel, P., McLaughlin, D. and Thiele, S., From Catalyst Coated Membranes to Porous Transport Electrode Based Configurations in PEM Water Electrolyzers, J. Electrochem. Soc., 166(14), F1070-F1078 (2019).*

The individual contributions were as follows:

- M. Bühler: idea, literature research, fabrication and electrochemical characterization of anodic PTEs, writing of the manuscript
- P. Holzapfel: Contributions to MEA fabrication and characterization
- D. McLaughlin: FIB-SEM and EDX images of anodic PTEs
- S. Thiele: supervision of the scientific work

The author thanks T. Böhm and D. Abed el-Hafez for Raman imaging and preparation of thin Nafion coatings on the aPTEs.

## 4.2 Introduction

Proton exchange membrane water electrolyzers (PEMWEs) are considered a central technology for a future hydrogen-based economy.<sup>56</sup> The most important element for PEMWE operation is the membrane electrode assembly (MEA). The MEA consists of anode and cathode catalyst layers and a solid polymer electrolyte membrane in between. There is no doubt that the right choice of materials for PEMWE MEAs is essential to improve lifetime, performance and cost. So far this fact resulted in a carbon supported platinum catalyst for the cathode, pristine or titanium supported iridium catalyst for the anode and Nafion both as proton exchange membrane (PEM) material and as additive for the catalyst layers.<sup>76</sup> The standard MEA-configuration is a catalyst coated membrane (CCM), with both catalyst layers deposited onto the membrane.<sup>72</sup> To enable a multiphase transport to and from the catalyst layers, porous transport layers (PTLs) are pressed against the CCM from both sides. For the anode side, porous titanium substrates are used to meet the durability necessities of PEMWE operation conditions. Titanium PTLs come in many different forms, with fiber or powder sintered structures being the base case.<sup>150</sup> On the cathode side, typically carbon-based PTLs are used. These PTLs are already widely studied for PEM fuel cell applications (e.g.<sup>151</sup>). CCMs are manufactured either by directly depositing catalyst layers on the membrane or via the DECAL process.<sup>78</sup> The latter consists in using Teflon blanks as a transfer substrate, on which the catalyst layers are manufactured on in a first step, and then hot-pressed on the PEM in a second step. The DECAL process is usually applied, because direct spraying on the membrane can result in membrane deformation due to the wetting behavior of solvents in the deposited ink. Alternative manufacturing routes for PEMWE MEAs, other than the above-described CCM approach, are seldom investigated.

One other MEA-configuration that appears sporadically is the PEM sandwiched between porous transport electrodes (PTEs), which are the PTLs coated directly with the catalyst layers. Grigoriev et al.<sup>101</sup> tested different porous sintered titanium substrates when spray coated with an Ir-based catalyst layer compared to the PTLs pressed against the CCM. The worse performance of the PTE-based MEA-configurations was explained by the reduced direct protonic interface between catalyst layer and membrane. Choe et al. introduced a PTE with the iridium catalyst electrodeposited on a titanium mesh PTL. Therefore, an intermediate contact between catalyst particles and PTL was reached which increased the mass activity.<sup>135</sup> The reason for an increased mass activity when using PTEs was shown by Kang et al.<sup>152</sup> for the cathode side via visualization of hydrogen bubble formation at the platinum based catalyst layer. For this, a structured thin titanium foil with circular, straight pores was pressed against a reference CCM and compared with the approach of sputter coating the titanium foil directly with the platinum catalyst. For both configurations, hydrogen bubbles were only visible at the edges of the pores of the thin titanium foil and not in the area in between. This indicates that large parts of the catalyst layers in the CCM-configuration are inactive, when not in direct contact with the PTL. Increasing the catalyst mass activity is therefore one motivation for the development of PTE-based configurations, but also the possibility to substitute costly titanium substrates at the anode side. A stable PEMWE operation was shown e.g. for carbon paper coated either directly with the iridium-based catalyst or first with a titanium-based adhesive intermediate layer.<sup>153–155</sup> Besides high performance and low costs one major criteria for the applicability in commercial PEMWE is the long term stability. It is known from literature, that the single materials used in a PEMWE cell are prone to different degradation mechanisms which influence the polarization behavior and affect the mechanical stability.<sup>140, 156, 157</sup> When changing interfacial properties, as well as the microstructure of the catalyst layers, the long term behavior would most probably change for every MEA-configuration tested in this work.

PTE-configurations could be advantageous compared to CCM-based systems, since coating the titanium PTL directly with the catalyst layer could establish a corrosion protection layer for the titanium substrate<sup>135</sup> and ensure a stable electrical interface between catalyst particles and the PTL. The long term stability of the PTE-based configurations was however not tested in the frame of this work but is a crucial quality factor when searching for the best MEA-configuration for commercial applications.

All works on PTE-based configurations are first steps towards high performing PTE-configurations, but the reasons for a changed polarization behavior compared to CCM-configurations, have so far never been more deeply studied and understood. This study therefore investigates for the first time, the influence on the polarization behavior of a PEMWE, when the electrode-membrane interface of a PEMWE MEA was changed gradually from a CCM towards a cathodic PTE (cPTE) and anodic PTE (aPTE) configuration. In literature, there are modifications of the membrane-electrode interface in a PEMWE CCM setup such as roughening the membrane<sup>158</sup> or introducing an additional Nafion layer<sup>159</sup> on top of the PEM before depositing the catalyst layers. Consequently, in this work we also investigate a thin Nafion impregnation of the aPTE, with the expectation of an improved protonic interface.

A simple idea for a structural model was used to explain the influence of changed catalyst layer structures and interfaces on the polarization behavior. The model is based on three general cases connecting the size scales of catalyst particles with the pore space of different supports: (i) If the pore sizes of a substrate are smaller or in the range of the catalyst particle size, the catalyst layer will be homogeneous. (ii) If the pores are larger than the catalyst particles, the porous support is most likely infiltrated by the catalyst ink during deposition. This would result in a continuous, but rougher catalyst layer. (iii) If the pores are larger than the catalyst particles and additionally larger than the thickness of the catalyst layer, discontinuities of the catalyst layer can occur. In this work, we elucidate which of these cases are relevant, when changing from pure CCM to full PTE-based PEMWE MEA-configurations.

## 4.3 Experimental

### Membrane Electrode Assembly

Different MEA-configurations were tested in this work with a focus on systematically changing the membrane-electrode interfaces. To minimize the influence of catalyst and membrane materials as well as of different fabrication methods, materials purchased from the same manufacturer were used for all experiments. CCMs and half-sided CCMs with only the anode or cathode catalyst layer deposited on a Nafion N117 membrane were purchased from FuelCellsEtc. The samples had a catalyst loading of  $1.5 \text{ mg cm}^{-2}$   $\text{IrO}_2$  for the anode side and  $0.5 \text{ mg cm}^{-2}$  Pt/C (60 %) on the cathode side. A carbon cloth material (FuelCellsEtc, type GDL-CT) was chosen as cathode PTL (cPTL) and a sintered titanium fiber substrate (Bekaert, 1 mm thick, 57 % porosity, 20  $\mu\text{m}$  fiber diameter) was used as anodic PTL (aPTL). Free-standing cathode porous transport electrodes (cPTE) with a loading of  $0.5 \text{ mg cm}^{-2}$  Pt/C (60 %) were commercially available based on the GDL-CT (FuelCellsEtc, type SL-GDE). The carbon substrates and commercial cPTEs were punched out and the titanium PTLs laser cut into  $5 \text{ cm}^2$  squares to meet the same active areas as of the full and half-sided CCMs. Free-standing anodic porous transport electrodes (aPTEs) were not commercially available, and were therefore manufactured in-house. For this purpose, an  $\text{IrO}_2$ -based catalyst layer was spray coated on top of the Bekaert titanium fiber substrates as described below. To eliminate influences on the polarization behavior due to different fabrication parameters, a

second reference CCM\* was prepared for studying the anode side of the different MEA-configurations. The CCM\* was a commercial half-sided cathode CCM (FuelCellsEtc, 0.5 mg cm<sup>-2</sup> Pt/C (60 %) on Nafion N117) spray coated with the same anode catalyst ink as used for preparing the aPTEs.

The IrO<sub>2</sub> ink for spray coating the anodic catalyst layers consisted of 1 wt% solids and 99 wt% solvents (DI-water and 2-Propanol in equal parts). The solids consisted of 98 wt% IrO<sub>2</sub> Premion (Alfa Aesar) and 2 wt% Nafion D520 (FuelCellStore). The catalyst powder was weighed in a glass bottle and then wetted by the appropriate amount of DI-water. Afterwards 2-Propanol followed by Nafion was added. The ink for spray coating needs to be homogeneously mixed. To this end, the bottle was gently shaken after adding each new component. The final ink was continuously stirred and sonicated for 30 min (Hielscher, model UIS250L, 0.55 W, 90 % amplitude) in an ice bath. The ink was then placed on a magnetic stirrer overnight and the 30 min mixing procedure was repeated right before spray coating. A spray coater (Sono-Tek, model Exacta Coat) was used with an ultrasonic nozzle type AccuMist (48 kHz). The following parameters were used for spray coating: path speed of 170 mm/sec, shaping air of 0.6 kPa, hot plate temperature of 120 °C, 5 W ultrasonic power and flow rate of 0.45 ml/min. The spray pattern was meander shaped with a pitch of 0.75 mm. The nozzle height was set to 37 mm. To monitor the noble metal loading during spray coating, a 1 cm<sup>2</sup> rectangular metal piece was spray coated as well and weighed on a microscale (Sartorius, model ME 36S). To deposit the anode catalyst layers, the porous titanium substrates, as well as the half-sided cathode CCMs were fixed in PTFE frames. The exact amount of Nafion in the final self-made anodic catalyst layers, and based on that also the noble metal loading, was determined via thermo-gravimetric analysis (TGA) (Netsch, model STA 449F5) according to the burning characteristics of Nafion.<sup>160</sup> Powder for the TGA analysis was collected via scratching the catalyst layer off the PTFE frames. The collected sample was heated under air atmosphere at a rate of 5 K/min up to 1000 °C (hold for one hour). A Nafion content of ca. 9 wt% and a noble metal loading of 1.4 mg cm<sup>-2</sup> IrO<sub>2</sub> was determined. The difference between the as-mixed and final Nafion content could be a result of catalyst particle sedimentation along the tubing of the spray coater as well as in the syringe.

Since the cPTEs were commercially manufactured with a thin Nafion coating to improve the water management and adhesion towards the membrane, the same was tested for the aPTEs. Therefore, impregnated aPTEs (ai PTEs) were prepared by spray coating a thin Nafion layer (2.5 wt% D2020 in 2-Propanol) on the surface of the aPTEs. Spray parameters were: 90 mm/s path speed (meander shaped, 0.5 mm pitch), flow rate of 0.2 ml/min, 2.5 W ultrasonic power, 0.6 kPa shaping air, 37 mm nozzle height. The aPTEs were either placed on a hot plate at 65 °C or at 120 °C during spray coating. The average thickness of the final Nafion coating was calculated from Raman analysis to be approximately 1 ± 0.2 µm.

### Structural Characterization

Surfaces and cross-sections were analyzed in terms of porosity, thickness and homogeneity. To this end, images were taken using a focused ion beam (FIB) scanning electron microscope (SEM) (Zeiss, model Crossbeam 540 with GEMINI II). To analyze the distribution of Nafion at the surface of the ai PTEs as well as along the cross-sections, an EDX mapping was performed (Oxford Instruments, model X-Max 150 using Aztec software).

To determine the thickness of the additional Nafion layer on the aPTEs, a glass slide was coated with 36 layers of Nafion and then analyzed with a confocal Raman microscope (WITec, model alpha 300). The Raman microscope was equipped with a 532 nm laser, operated at 50 mW. The

microscope was coupled to a WITec UHTS VIS-NIR spectrometer with a 300 gr/mm optical grating and a thermoelectrically cooled CCD-camera for acquiring Raman spectra. A metallurgical objective (Zeiss, model LD EC Epiplan-Neofluar 50x/0.55) was used to operate the microscope. A confocal depth scan at a step size of 500 nm through the membrane was performed. After a background subtraction (WITec Project FIVE+), the summarized intensity of the  $\nu_s$  (C-F) mode (700 to 760  $\text{cm}^{-1}$ ) was used for a segmentation of the membrane within the line scan using Otsu's method in Matlab (MathWorks). The thickness was calculated from the segmented data and corrected for spherical aberration, induced by the refractive index mismatch between Nafion ( $n_{\text{Nafion}} = 1.38^{161}$ ) and air ( $n_{\text{air}} = 1$ ), by multiplying the obtained value with  $n_{\text{Nafion}}/n_{\text{air}}^{162}$ . A single point measurement of 36 layers of Nafion on the glass slide revealed a thickness of around  $7.6 \pm 0.9 \mu\text{m}$ .

### Electrochemical Characterization

The different MEA-configurations were tested at atmospheric pressure in a self-designed test cell setup. The outermost parts of the test cell were aluminum plates tightened with eight screws at 8.5 Nm to hold the inner cell parts. Two heating elements, set to 80 °C, were inserted into the Al plates. The inner cell parts were electrically connected to a potentiostat (Scribner, model 857) via two copper plates at the anode and cathode side respectively. The copper plates were electrically insulated on the side facing the aluminum plates via a self-adhesive PTFE foil. On the other side, titanium flow fields were in direct contact with the copper plates. The flow fields both at the anode and cathode side were made of titanium plates with a 5  $\text{cm}^2$  milled parallel finger structure to evenly distribute water towards the PTLs. The PTLs, were made of fiber sintered porous titanium at the anode and carbon cloth at the cathode. The PTLs had the same geometric area as the finger structure of the flow field. PTFE frames were used to align the PTLs and also acted as hard-stops to control the assembly pressure of the cell. The PTFE frame at the anode side was as thick as the titanium PTL (1 mm) to avoid a "step" between PTFE frame and hard titanium substrate towards the MEA. At the cathode side the PTFE frame was thinner (150  $\mu\text{m}$ ) than the carbon PTL (410  $\mu\text{m}$ ) to set a sufficient compression. The MEA was then sandwiched between the PTLs. Two metal pins were used to align the different materials and were removed before testing the cell. The internal cell resistance without membrane was calculated to ca. 0.091  $\Omega \text{ cm}^2$  from a set current and the corresponding cell voltage (repeated three times). To be able to reduce this high resistance, it is planned in future work to apply a conductive gold coating on top of the titanium flow fields to further reduce parasitic contact resistances.

Anode and cathode were supplied separately with DI-water via a peristaltic pump (Ismatec, model IP 65) at a flow rate of 40 ml/min. The tubing close to the inlets of the test cell was immersed into a water-filled thermostat set to 88 °C (Lauda, model Ecoline 003) to prevent temperature gradients in the cell. Once a stable cell temperature of 80 °C was observed (monitored continuously with a temperature sensor), the test cell was conditioned in potentiostatic mode from 1.4 V - 2.2 V in 200 mV steps. Each voltage step was held for 30 s and the complete range was scanned for 15 times. Afterwards polarization curves were recorded as follows: 0 A - 0.04 A in 10 mA steps, 0.05 A - 1 A in 50 mA steps, 1.25 A - 3 A in 250 mA steps, 3.5 A - 5 A in 500 mA steps and above 6 A in 1 A steps for the CCM-configurations and in 500 mA steps to record more data points of the lesser-known PTE-configurations. Every step was held for 120 s.

The high frequency resistance (HFR) was measured via the software "FlowCell" (Scribner) at a frequency of 1 kHz. The measured HFR was then applied to the experimental polarization curves for an analysis of the HFR-free cell voltage. The polarization data was analyzed in terms of contributions to the kinetic, ohmic and mass transport overpotential.<sup>141</sup> Three samples per MEA-

configuration were prepared and tested. The average values and standard deviation therefore gives an impression of the reproducibility of the respective MEA-configurations. To substantiate the gained knowledge regarding separate contributions of the anode and cathode side on the polarization behavior in changed MEA-configurations, the use of a reference electrode (e.g.<sup>153</sup>) was suggested. In future works such an extension would be beneficial.

## 4.4 Results and Discussion

### 4.4.1 Design of Experiments and Research Hypothesis

The aim of this study was to understand in depth what changes occur in an MEA upon changing from a CCM-type configuration towards a PTE-type configuration, with the electrodes deposited directly onto the PTLs. The leading questions in this study were: Is there a benefit when using PTE-type configurations? What are advantages and disadvantages of the different configurations? Are there potentials for a future change in the manufacturing process, which at the moment concentrates on CCM-based approaches? All this was discussed based on systematic and reproduced measurements, in which a gradual transition from a CCM-type configuration to a full PTE-type configuration (Fig. 23) was studied. To avoid unwanted cross dependencies of different fabrication techniques and catalyst materials, a second reference CCM\* was prepared (Fig. 23 C) for a direct comparison with the MEA-configurations using an aPTE. The anode side of the CCM\*-configuration consisted of the same anode catalyst layer and was prepared with the same manufacturing method (spray coating) and with the same parameters as used for preparing the anodes in the PTE-configurations. At the cathode side, the material composition and fabrication technique was constant for all MEA-configurations, since all materials could be purchased from the same supplier.

**MEA configurations tested in this work**

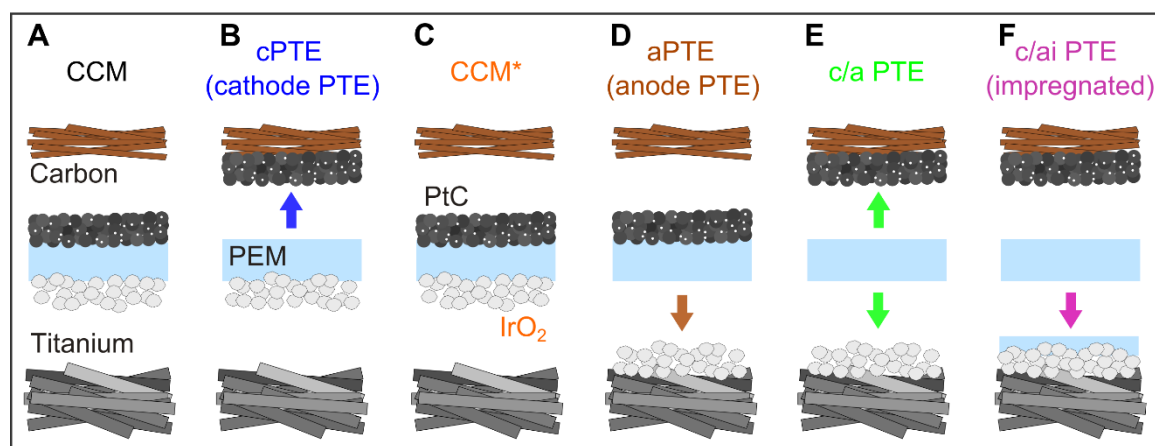


**Fig. 23** A Commercial catalyst coated membrane (CCM) with both electrodes deposited on the membrane. B Commercial catalyst coated cathode porous transport electrode (cPTE). C CCM with in-house manufactured anode catalyst layer deposited on a commercial half-sided cathode CCM denoted CCM\*. D Catalyst coated anode porous transport electrode (aPTE) produced with the same in-house manufactured anode as used for CCM\*. E Combined aPTE- and cPTE-configuration with a bare membrane in between, denoted as c/a PTE F cPTE and Nafion impregnated aPTE named as c/ai PTE.

We investigated all six different MEA-configurations in the following in terms of polarization curves and a breakdown analysis of kinetic contributions, ohmic resistance and mass transport. Complementarily, we analyzed the structure of the samples using methods based on electron microscopic methods.



Based on these considerations we used a simple structural model (Fig. 24) to clarify our expectations for the influence of the different MEA-configurations tested in this work (Fig. 23). When the catalyst layers are directly deposited onto flat membranes as in the CCM-configurations (Fig. 23 A,C), protonic transport is most likely improved, due to the geometrically shortest possible protonic pathway between all anode and cathode catalyst particles for a given PEM thickness. At the same time, the electrically conductive interface facing towards the PTLs could be suboptimal, since the PTLs are only mechanically pressed against the CCM. Therefore, at the anode side, only a few titanium fibers establish a direct electrical contact between catalyst layer and PTL (Fig. 24 A). Regarding mass transport, the distribution of water and gases within the catalyst layer could be less than optimal, since all transport must be performed through a compact catalyst layer. Mass transport through the pristine, uncoated PTLs pressed against the CCM however, is supposed to be optimal.

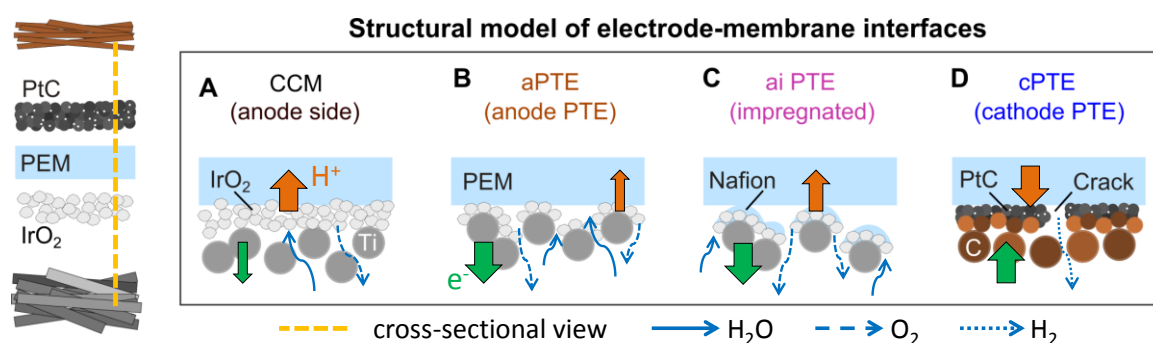


**Fig. 24** Model of the membrane-electrode interfaces and transport processes in different MEA-configurations. Thinner arrows imply a relative decrease of a certain transport process. A Anode side of a CCM pressed against titanium fibers B Anode-PEM interface facing towards a free-standing aPTE C Interface between PEM and impregnated ai PTE D Cathode-PEM interface when a cPTE is used.

When applying the anode catalyst layer directly on the titanium PTL as in the aPTE-configuration (Fig. 23 D), the deposition of large parts of the catalyst layer up to multiple hundreds of micrometers into the pores of the titanium PTL (Fig. 24 B) is expected. Grigoriev et al. discussed, that in this case fewer parts of the catalyst layer are in direct contact with the solid membrane.<sup>101</sup> Therefore, first the direct protonic interface between catalyst layer and the PEM is reduced, which would result in an increased ohmic resistance. Moreover, when some catalyst particles are disconnected from the protonic network within the catalyst layers, a lower catalyst utilization and therefore comparably worse kinetics are most likely to result. Depositing the catalyst particles directly on the titanium fibers however, improves the electrical interface compared to the CCM-configuration. The rough, porous electrode surface could improve mass transport, but the risk of blocked pores due to the comparably deeper infiltration of the aPTL during deposition of the catalyst material exists. This infiltration would then increase mass transport problems. For the cPTEs (Fig. 23 B), a much more planar carbon-based support compared to the titanium substrates is used. Therefore, one would assume less poorly connected catalyst areas (Fig. 24 D). Cracks in the micro porous layer (MPL) could however lead to similar effects as in the aPTE case. Consequently, worse kinetics, better mass transport and counteracting protonic vs. electrical resistance could appear. For the c/ai PTE (Fig. 23 F) we expected a behavior based on the aPTE and cPTE base cases, but an improvement of the ionic transport and consequently an improved HFR (Fig. 24 C).

#### 4.4.2 Influence of Cathode PTE (cPTE) on the Polarization Behavior

The influence of the position of the cathode catalyst layer on the polarization behavior was analyzed by comparing the performance of commercial CCMs with a commercial cPTE-configuration (Fig. 25 A). Both configurations were purchased from the same supplier, using the same loading of catalysts as well as the same manufacturing method (compare methods section). One polarization curve each of three different samples per configuration were analyzed. The size of the single standard deviation ( $\sim 68\%$  confidence interval), characterized the reproducibility of the considered MEA-configuration (Fig. 25 B). At the transition between 5 A and the last segment of the polarization curve starting at 6 A, unfortunately an inaccurate recording of the cell voltage at  $1.2 \text{ A cm}^{-2}$  (6 A) occurred for some samples of the CCM- and cPTE-configurations. This data points could not be used to calculate the average and standard deviation and are not shown in Fig. 25.

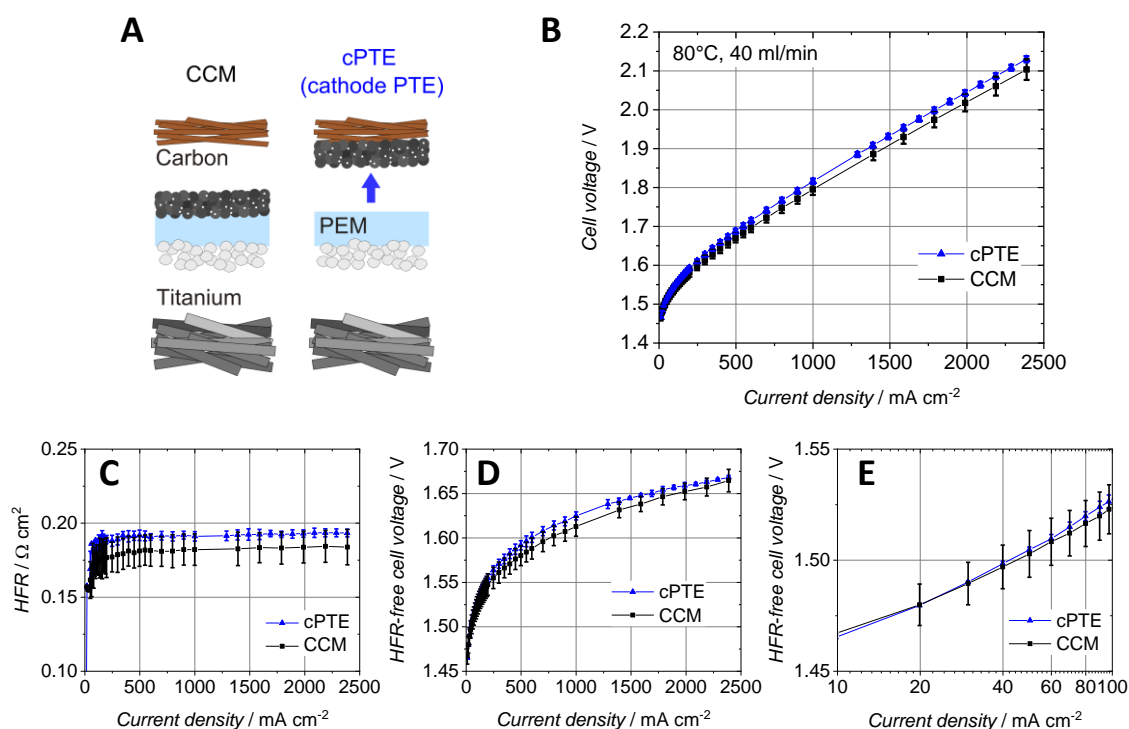


**Fig. 25** A Schematic of the tested MEA-configurations CCM vs. cPTE B Polarization curves C High frequency resistances D HFR-free cell voltage E HFR-free cell voltage at low current densities.

**Experimental results:** Full CCMs performed slightly better than cPTEs (Fig. 25 B), due to lower ohmic losses (Fig. 25 C) and barely better due to a better HFR-free cell voltage (Fig. 25 D). The kinetic region at low current densities was very similar for both configurations (Fig. 25 E). Interestingly, the standard deviation of the cPTE polarization curves was significantly smaller than of the full CCM. Particularly at higher current densities, the full CCM showed a less reproducible operation than the cPTEs (Fig. 25 B).

**Structural analysis:** SEM images and a FIB-SEM cross-section analysis confirmed, that the carbon-based cPTLs (Fig. 26 A) provided a comparably flat surface for depositing the cathode catalyst layer on top (Fig. 26 C), due to the MPL (Fig. 26 B). The cross-section showed the smooth interface between MPL and cathode catalyst layer (Fig. 26 D) of the cPTE. Consequently, there was no strong variation of the membrane-electrode interface between CCM- and cPTE-configuration. Some cracks were found throughout the MPL (Fig. 26 B). These cracks are less significant for the cPTE.

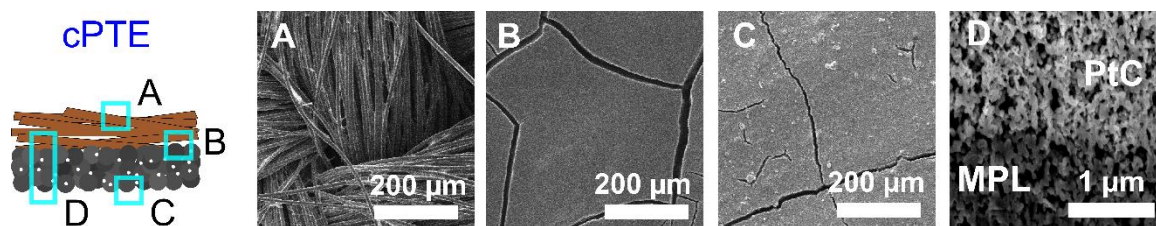


**Fig. 26** A Backside of the carbon cloth porous transport layer B Microporous layer (MPL) deposited on the carbon cloth material facing the electrode C Pt/C catalyst layer deposited on the microporous layer forming the final cPTE D Cross-section of the cPTE showing the MPL and Pt/C catalyst layer.

**Discussion of the results:** Due to the relatively smooth surfaces of both the carbon PTL as well as the cPTE, the loss of catalyst material in the cracks of the carbon materials was negligible. Therefore, no larger disconnected ‘catalyst islands’ and consequently no significant differences in the kinetic region were observed. In accordance with the above-discussed qualitative structural model (Fig. 24), we found slightly higher mass transport losses for the cPTEs. This might be since smaller cracks in the cPTE surface allowed for less water and gas distribution, compared to a cPTL with bigger cracks in the MPL being pressed onto the CCM. Coating the PTLs with catalyst material therefore reduces the pore size at the interface towards the catalyst layers, which was then most probably a hindrance for mass transportation through the electrodes. The slightly higher Tafel slope of the cPTE-configuration (Fig. 25 E) is as well an indication, that mass transport losses are more pronounced, when the PTL is coated with the catalyst material. Trinke et al. recently analyzed the correlation between cathode electrode structure and mass transport overpotential.<sup>112</sup> They found an increase of ionomer content within the cathode catalyst layer to cause higher mass transport resistances. The removal of hydrogen from the catalyst layer was impeded with increased ionomer contents, which is supposed to be due to a decreased pore space and longer transport paths within the ionomer. Consequently, this leads to high dissolved hydrogen concentrations at the interface between membrane and electrode. This supersaturation of dissolved hydrogen was then indicated as a reason for a higher gas crossover through the PEM and higher mass transport losses due to higher cathode half-cell potentials. For the cPTE-configuration tested in this work nevertheless, at higher current densities, the difference of the HFR-free voltage (kinetic and mass transport overpotential) between cPTE and CCM-configurations became smaller. One explanation could be a beneficial mass transport of the cPTEs at higher current densities, but also other contributions e.g. of the effective proton resistance within the catalyst layers have to be considered. The HFR as the combination of ionic and electrical resistances was either equally good or slightly worse for the cPTE compared to the CCM. This was not fully derivable from the HFR data due to the significantly higher variation of the CCM-configuration than compared to the cPTE-configuration. Reasons for the lower reproducibility of the CCMs were difficult to assess, as this also depends on the process parameters chosen for the production. One possible explanation would be the intermediate electrical interface between catalyst layer and PTLs in the PTE-configurations due to the direct deposition of the catalyst layers on the titanium and carbon substrates. In the CCM-configuration, bending of the membrane during assembly or operation of the membrane could lead to a changed number of direct contact points between CCM and PTLs which would then lead to e.g. different HFRs within the same MEA-configuration.

#### 4.4.3 Influence of Anode PTE (aPTE) and Symmetric PTE (c/a PTE) on the Polarization Behavior

In this section a spray coated aPTE with the anodic catalyst layer deposited directly on the porous titanium substrate was compared to a reference CCM\* with the same anodic catalyst layer deposited on a half-sided cathodic CCM (Fig. 27 A). In the combined c/a PTE-configuration, a membrane was sandwiched between the cPTE and aPTE. All experiments were performed at least three times with a single standard deviation (~68 % confidence interval) representing the reproducibility of the investigated MEA-configuration.

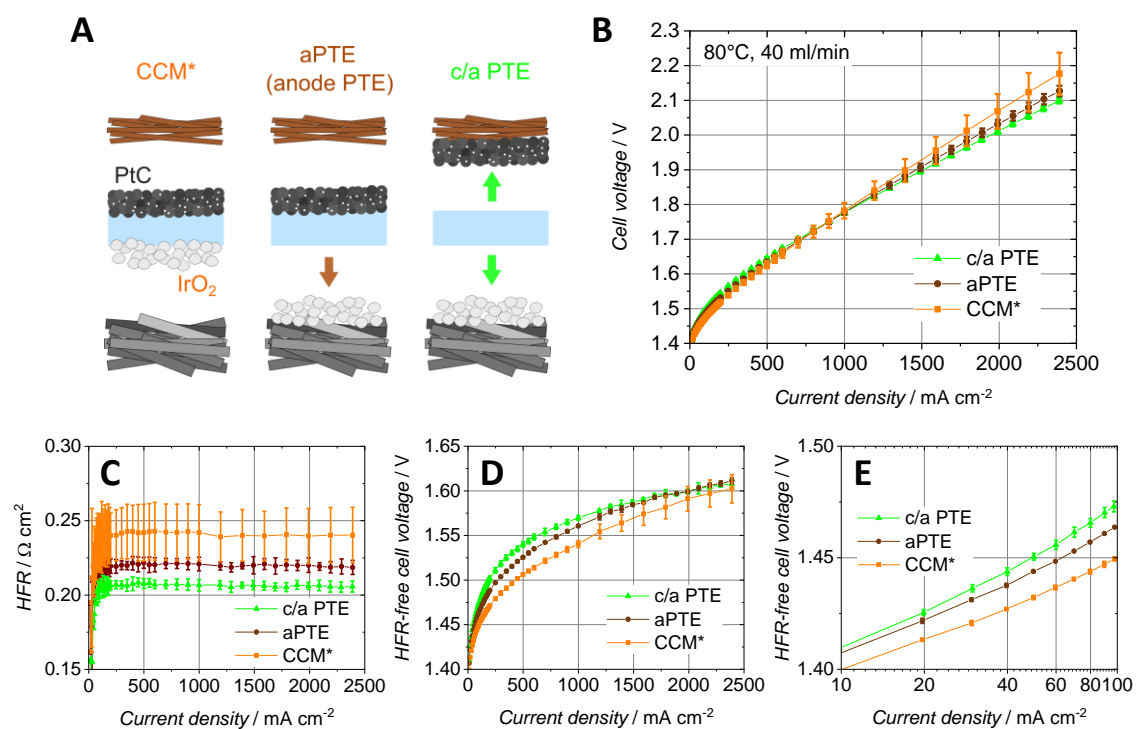


**Fig. 27** A Comparison of CCM\* vs. aPTE and c/a PTE-configuration B Polarization curves C High frequency resistances D HFR-free cell voltage E HFR-free cell voltage at low current densities.

**Experimental results:** As can be derived from Fig. 27 B, full CCM\*s performed slightly better at lower current densities (below ~750 mA cm<sup>-2</sup>) while both aPTE and c/a PTE performed better and were more reproducible at higher current densities (above ~750 mA cm<sup>-2</sup>). An analysis of the different contributions to the polarization curve revealed the reasons for this behavior: The kinetic losses can be derived from a semi-logarithmic plot of the HFR-free cell voltage (Fig. 27 E) at low current densities. The CCM\*-configuration showed the lowest kinetic overpotential, whereas the aPTE and c/a PTE-configurations were shifted to a higher value. With increasing current density, contributions of the mass transport overpotential became more and more pronounced as it was visible in the HFR-free cell voltage over the whole current density range (Fig. 27 D). The CCM\*-configuration showed the best HFR-free cell voltage, but with increasing current density the difference between the three configurations became less significant and variations between the different CCM\*-configurations became more pronounced. The reason for these trends should be further analyzed especially when aiming for PEMWE cells operating at higher current densities and when planning to apply pressure to the system. Suermann et al.<sup>163</sup> e.g. showed, that with increasing operating pressure, the mass transport overpotential is reduced. Therefore, the difference between the three CCM\* samples could have a minor impact on the reproducibility at higher operating pressures compared to atmospheric conditions in this work. The main reason for the worse overall performance of the CCM\*-configuration at higher current densities was a higher

average HFR (Fig. 27 C), which was significantly less reproducible than the HFR of the aPTE- and c/a PTE-configurations.

**Structural analysis:** As expected, SEM images showed a rough surface of the titanium-based PTLs (Fig. 28 A). In contrast to carbon-based PTLs no titanium PTL with MPL is commercially available. Consequently, the interface between membrane and anode was significantly changed when depositing the anode catalyst layer on top of the porous titanium substrate compared to a flat membrane. In the aPTE-configuration (Fig. 28 B), parts of the anode catalyst layer were deposited deep into the pores of the aPTL. Therefore, parts of the catalyst material are placed in great distance from the membrane. At the large scale, the catalyst layer of the aPTE showed an inhomogeneous distribution of the catalyst particles on top of the titanium fibers (Fig. 28 C). However, as can be derived from the cross-section (Fig. 28 D), the deposited layer itself is homogeneous.

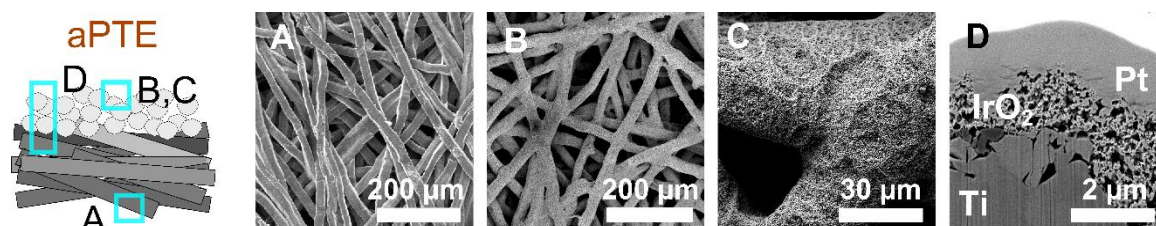


**Fig. 28** FIB-SEM analysis of the catalyst coated anodic porous transport electrode (aPTE) A Surface of the titanium fibers. In contrast to the porous carbon materials, no microporous layer was commercially available B,C IrO<sub>2</sub> coated Ti-fibers D FIB-SEM cross-section of the aPTE showing the titanium fibers, catalyst layer and Pt protection layer (deposited during the FIB-SEM imaging process).

**Discussion of the results:** According to the idea of a structural electrode model discussed above (Fig. 24), we had the case of a highly inhomogeneous electrode structure for the aPTEs. The resulting disconnected ‘catalyst islands’ were expected to result in worse kinetics, which was clearly the case (Fig. 27 E). When advancing from an aPTE to a c/a PTE, we observed only a slight increase of kinetic overpotential, which was expected according to the results when varying the cathode side in the previous section. The CCM\*-configuration showed the lowest HFR-free cell voltage (Fig. 27 D), but is approaching the PTE-based configurations at higher current densities. As discussed in the methods section, a beneficial mass transport behavior of PTE-configurations at high current densities compared to CCMs could be one explanation, but also e.g. the effective proton resistance has to be considered, as analyzed by Babic et al. for anodes in CCM-configurations.<sup>164</sup> When considering the HFR behavior however, the situation became more complicated: on the one hand, the ionic conductivity was expected to be worse in the aPTE and c/a PTE-configurations compared to the CCM\*, on the other hand, improvements in electrical conductivity were expected, due to a better electrical interface contact. In Fig. 27 C we observed that the CCM\* exhibited a worse average HFR (0.24  $\Omega \text{ cm}^2$ ) than the aPTE and c/a PTE-configurations. This HFR value was unexpected when compared to the value of the CCM from Fig. 25 C of which was 0.18  $\Omega \text{ cm}^2$ . We assume that our CCM\* manufacturing process could be further optimized with respect to ionic contact. Here also a hot-pressing step might be advantageous, but would have altered the catalyst layer structure compared to the aPTEs. This was to be avoided, as we concentrated on only structural layer effects in this study. Apart from that, we observed what we expected from the discussion of our model: the interfacial contact area between the catalyst layer and the membrane when using the aPTE-configuration was smaller compared to the cPTE-configuration with a flat carbon substrate. Therefore, the HFR of the aPTE-configuration was around 0.22  $\Omega \text{ cm}^2$  (Fig. 27 C) compared to the cPTE-configuration with a HFR of around 0.19  $\Omega \text{ cm}^2$  (Fig. 25 C). This explained, why, for the c/a PTE-configuration, as a combination of the



aPTE- and cPTE-configurations, we observed a decreased HFR of  $0.21 \Omega \text{ cm}^2$  compared to the aPTE (Fig. 27 C). Also in this study, we observed, that the reproducibility was highest for the c/a PTE-configuration, a bit lower for the aPTE-configuration and the CCM\* approach was found to have the worst reproducibility. The same effect was seen in the previous section when comparing the CCM with the cPTE polarization behavior. In summary, we saw a tendency in both studies that there was an improvement of the reproducibility when changing from a CCM-configuration to a PTE-configuration.

#### 4.4.4 Influence of Nafion Impregnated Anode PTE (ai PTE) on the Polarization Behavior

In this section, we investigated the influence of an additional Nafion D2020 layer deposited directly on the aPTE. The basic idea was that this kind of an approach could improve the ionic interface resistance between electrode and membrane. At higher temperatures of the aPTEs, the additional Nafion layer was expected to dry immediately at the aPTEs surface whereas at lower temperatures a certain degree of infiltration into the pores of the aPTE was expected. Therefore, two different types of ai PTEs were fabricated at a temperature of  $65^\circ\text{C}$  as well as  $120^\circ\text{C}$ . The c/ai PTE-configurations were then compared to the c/a PTE-configuration presented in the previous section (Fig. 29 A). Three samples per configuration were prepared and tested (Fig. 29 B).

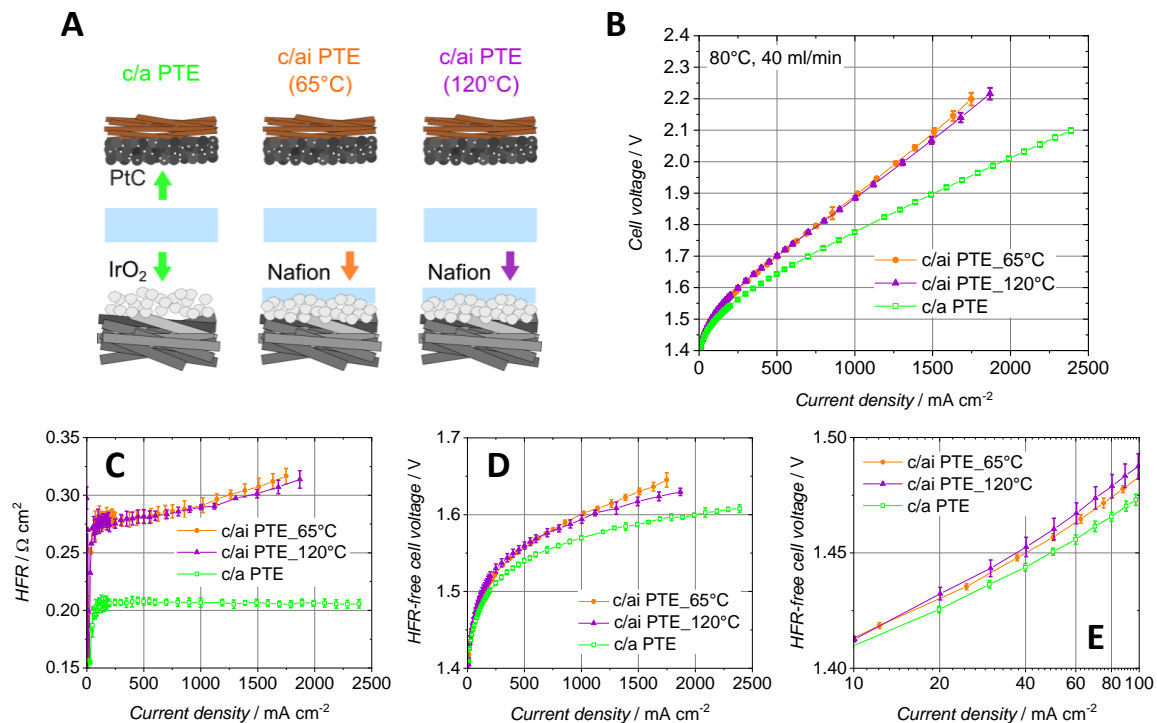


**Fig. 29** A Configurations c/a PTE vs. c/ai PTE (fabricated at  $65^\circ\text{C}$  and  $120^\circ\text{C}$ ) B Polarization curves C High frequency resistances D HFR-free cell voltage E HFR-free cell voltage at low current densities.

**Experimental results:** Impregnating the aPTE with Nafion strongly reduced the overall cell performance (Fig. 29 B). One reason was an increased HFR of the c/ai PTE-configurations with a strong dependency on the current density (Fig. 29 C). In both c/ai PTE-configurations mass transport losses were obvious when analyzing the HFR-free cell voltage (Fig. 29 D). The c/ai PTE prepared at  $65^\circ\text{C}$  showed a slightly stronger increase of mass transport overpotential with current density than the c/ai PTE prepared at higher temperature. The HFR-free cell voltage at low current densities (Fig. 29 E) showed similar kinetics for the c/ai PTE-configurations, which were both slightly worse than the c/a PTE-configuration. The reproducibility of the c/ai PTE prepared at  $120^\circ\text{C}$  was slightly worse in the kinetic region than for the other configurations.

**Structural analysis:** The surface of the ai PTE impregnated at 120 °C (Fig. 30 A) was analyzed with an EDX tool to map the fluorine content at the surface which showed large, inhomogeneous fields of Nafion covering the catalyst layer (Fig. 30 B). The cross-section revealed a continuous Nafion coating (Fig. 30 C). Therefore, voids between the Nafion coating and the catalyst layer were observed. A fluorine mapping of the cross-section showed the continuous character of the impregnation at 120 °C (Fig. 30 D) on the local scale. However, the samples showed a strong variation of the global thickness of the Nafion coating, first due to the rough surface of the aPTE itself and second most probably due to an inhomogeneous drying of the Nafion layer.

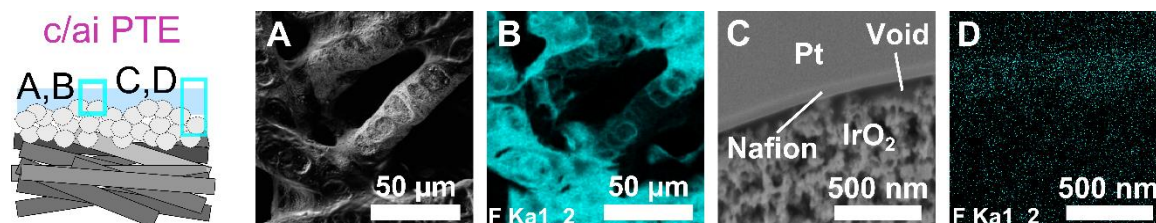


**Fig. 30** A Surface of the ai PTE coated at 120 °C B EDX mapping of F of the impregnated surface. C FIB-SEM cross-section of the ai 120 °C PTE with protective Pt layer showing voids between the Nafion coating and the catalyst layer. D EDX of the cross-section showing the Nafion coating on top of the aPTE (C and D do not show the same position).

**Discussion of the results:** For the c/ai PTE, we expected a behavior based on the c/a PTE-configuration, but with an improvement of the ionic transport and consequently a reduced HFR. However, the experimental results were not in line with this hypothesis: We not only found a higher initial HFR for the c/ai PTEs, but also discovered a worse mass transport. More interestingly, the additional Nafion impregnation caused an increase in HFR as a function of current density, indicating worse ionic transport and interfacial contact resistances. We used the following model to explain changes of the polarization behavior when a c/ai PTE-configuration impregnated at different temperatures (high T vs. low T) is used (Fig. 31):

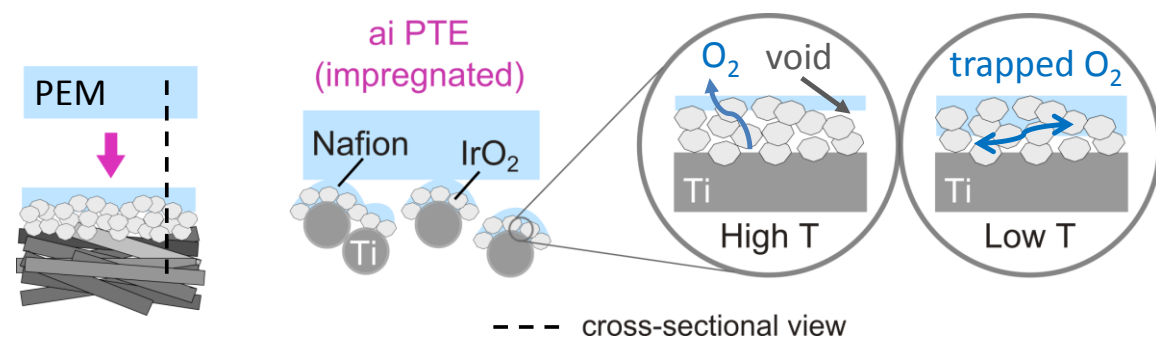


**Fig. 31** Model of oxygen transport pathways in the Nafion impregnated anodic porous transport electrodes (ai PTE). High T The impregnation at high temperatures prevents an infiltration of the catalyst layers pores, but leads to voids with no direct protonic interface. Low T Impregnating at lower temperatures could lead to a deeper infiltration of surface near pores of the catalyst layer and therefore the trapping of oxygen.

At high temperatures, solvents are expected to dry immediately at the surface of the aPTE (Fig. 31, high T). The fast drying of solvents prevents the deep infiltration of the pores of the catalyst layer with Nafion. Therefore, a continuous Nafion layer as seen in the cross-section of the c/ai PTE coated at 120 °C (Fig. 30 C) is most probably the case. Voids between the Nafion layer and the catalyst layer increase the protonic interfacial contact resistance and therefore the HFR. When coated at low temperatures (Fig. 31, low T), the additional Nafion layer is expected to infiltrate the pores of the aPTE to a further extend. This would lead to an intermediate contact of the surface of the aPTE with the Nafion layer and less voids on the one hand. On the other hand, the pores of the catalyst layer might be blocked, so that a higher mass transport overpotential at

higher current densities could be the case. We assume, that the Nafion coating on top of the catalyst layer in combination with the solid titanium fiber below acts as diffusion barrier for evolving gas bubbles and possibly also for water. When evolving oxygen is trapped in the PTE structure, active sites might be blocked, which would increase mass transport losses.<sup>76</sup> When the trapped gas additionally dries out parts of the Nafion phase within the catalyst layer, the proton conductivity is reduced and thus the HFR is increasing with increasing current densities.

## 4.5 Conclusions

In this work, we presented a detailed study on the effect on cell polarization when changing from a CCM-configuration in systematic steps to PTE configurations. PTE-based MEA-configurations showed a similar performance as CCM-based MEA-configurations and are thus suitable for PEMWE applications. Generally, PTE-type configurations showed a tendency towards worse kinetics than the CCM-configurations. The tendency of a stabilizing HFR-free cell voltage at high current densities could be an indicator for a beneficial mass transport behavior of PTE-based configurations. The HFR evaluation was not fully conclusive due to a significantly worse reproducibility of the HFR values of the CCM-configurations compared to the PTE-configurations. A Nafion coating did not improve the performance of the aPTEs. Instead, a Nafion coating led to a higher HFR, which further increased with current density. The Nafion coating additionally increased the mass transport overpotential. Interestingly, we found in general a strong increase in reproducibility when depositing the catalyst layers directly on the titanium and carbon substrates as in the PTE-based MEA-configurations.

We suggested a simple structural model for three different cases for porous support - catalyst layer interactions to explain the observed changes in polarization for CCM, aPTE and cPTE like structures. One key idea on the path towards understanding the polarization behavior of the analyzed MEA-configurations was the idea of disconnected 'catalyst islands' within porous supports. Based on that idea we were able to explain the differences in the contributions to the overpotential in all considered cases. By developing an idea of the structural interaction between catalyst layer, porous substrates and membrane, we intend to stimulate future improvements of the interfacial design of PEMWE MEAs.

In our study, we found that the interfaces between membrane and catalyst layer, as well as the porous transport layer have an influence on the polarization behavior of a PEMWE MEA. This highly interesting playground opens up the path towards novel MEA structures and MEA-PTL structure interactions beneficial for the PEMWE conversion efficiency. Optimizing porous transport electrodes for alternative PEMWE MEA-configurations is therefore highly promising since not only the performance can be improved. On top, also the fabrication costs could be reduced, when using a direct spray technique instead of a DECAL transfer process.

The interpretation and analysis of influences on the polarization behavior in this study were valid for a specific set of operation conditions, as well as a specific combination of material and fabrication techniques. When changing one of those parameters, the polarization behavior of the single MEA-configurations will most probably change and could therefore lead to a different picture as captured in this work. We therefore suggest to perform the presented analysis, which was a structural model idea in combination with a systematic structural and electrochemical investigation, for every new MEA-configuration at the given operation conditions. The influence of changed interfaces on the long term stability adds additional quality requirements on the way to choose the best possible MEA-configuration.



## 4.6 Critical discussion

The influence of gradually changing electrode-membrane interfaces from the CCM-configuration towards the PTE-configurations on the polarization behavior of six different MEA-configurations was analyzed in correlation with the analysis of the surface morphology and microstructure. The goal was to understand the importance of direct interfaces between the PEM and CLs (CCM-configuration) and between the PTLs and the CLs (PTE-configurations). Anode and cathode were studied separately from each other. The conclusions from this study need to be carefully drawn as other materials, fabrication techniques, test parameters or MEA-configurations most probably lead to other results.

**Reference CCM\***- Ideally all materials used for the different MEA-configurations could be purchased from the same supplier to prevent influences from own manufacturing techniques on the performance. However, no anodic PTEs are commercially available and had to be fabricated in-house. Therefore, to be able to compare the performance of the aPTEs and full PTE-configurations with the standard CCM-approach, a second reference CCM\* was prepared in-house with the same anodic catalyst ink deposited onto the PEM. For direct comparison with the anodic PTE, the CCM\* was not optimized via hot-pressing or an optimized catalyst layer composition. The overall performance of the PTE-configurations was better than the one of the CCM\*, but due to the missing optimization of the CCM\*, it cannot be necessarily concluded, that in any case the PTE-approach is superior to the CCM-configuration. Only with the fabrication technique und catalyst layer composition used in this work, the CCM was outperformed.

**Operation parameters** - The conclusion, that PTE-configurations can outperform standard CCMs or that one MEA-configuration works better than the other is not only dependent on materials and fabrication techniques used, but also on the operation parameters of the PEMWE cell. A pressurized application, higher temperatures or lower flow rates of the DI-water influence the polarization behavior leading most probably to a changed overall performance as discussed above.

**Fabrication parameters – influence on HFR and reproducibility** - Regarding the polarization data, some effects were not yet fully understood. The lower HFR of the c/a PTE-configurations is not in line with the structural changes of the interfaces when going from CCM (both catalyst layers on the membrane) via aPTE (anodic catalyst layer on the Ti-PTL) towards the full c/a PTE-configuration (freestanding membrane). Other, differently prepared commercial materials could influence the polarization behavior in other ways than observed in this work. The lower reproducibility of the CCMs compared to other MEAs was as well remarkable and could so far not be related to a structural effect or the influence of assembling or operating the PEMWE test cell.

**Longterm stability of PTE-configurations** - When developing novel MEAs for industrial PEMWE applications, the longterm stability is a major concern. The performance of the PTE-configurations tested in this chapter was not evaluated during a longterm experiment, which is however necessary to study degradation mechanisms in PEMWE MEAs.

As there are some unknown parameters when developing and characterizing PTE-configurations, the results presented in this study should be seen as basic step to motivate the better understanding, development and optimization of alternative MEA designs based on PTEs as compared to the standard CCM-configuration. By optimizing PTE-configurations, improvements in all regions of the polarization curve as well as reduced costs in manufacturing can probably be reached, as evaluate in the following chapter when optimizing the anodic PTE for the OER.



## 5 Optimization of anodic porous transport electrodes for proton exchange membrane water electrolyzers \*

### 5.1 Abstract

In this study we investigate the potential of porous transport electrode (PTE) based membrane electrode assemblies (MEAs) for proton exchange membrane water electrolysis. The focus is on the overpotential determining anodic PTE for the oxygen evolution reaction. The influences of catalyst loading, ionomer content and porous titanium substrate on the polarization behavior are analyzed. The comparison of a porous fiber-sintered with a powder-sintered substrate shows no significant differences in the kinetic and mass transport region. Ohmic losses however, are lower for fiber PTEs above a catalyst loading of  $1.0 \text{ mg}_{\text{IrO}_2} \text{ cm}^{-2}$ . Variations of the Nafion content in the catalyst layer reveal changes of mass transport and ohmic losses and have an influence on the reproducibility. Varying the noble metal loading and therefore the thickness of the applied catalyst layer influences the kinetic region and ohmic resistance of the MEAs. The best compromise between reproducibility and performance is found for a loading of  $1.4 \text{ mg}_{\text{IrO}_2} \text{ cm}^{-2}$  and 9 wt% Nafion. The stable operation of the aforementioned PTE is shown in a 200 h durability test at  $2 \text{ A cm}^{-2}$ .

---

\*The sections in this chapter (besides the critical discussion in section 6.5) have been published identically as an original research paper at the *Journal of Materials Chemistry A* (impact factor of 10.733 in 2018<sup>149</sup>)

Bühler, M., Hegge, F., Holzapfel, P., Bierling, M., Suermann, M., Vierrath, S. and Thiele, S., Optimization of anodic porous transport electrodes for proton exchange membrane water electrolyzers, *J. Mater. Chem. A*, **165**, F305 (2019).

The individual contributions were as follows:

- M. Bühler: idea, literature research, outline of the work, fabrication and electrochemical characterization of the anodic PTEs, writing the manuscript, design and building of the test cell and test bench
- F. Hegge: design and building of the test cell and test bench, FIB-SEM imaging
- P. Holzapfel: contribution to MEA fabrication and characterization
- M. Bierling: FIB-SEM imaging
- M. Suermann: discussion on the evaluation of the results and literature research
- S. Vierrath and S. Thiele: supervision of the scientific work

## 5.2 Introduction

One major focus of current research for proton exchange membrane water electrolysis (PEMWE) is the reduction of noble metal loadings while maintaining or even prolong durability. Due to the fast reaction kinetics of the hydrogen evolution reaction (HER), the platinum loading at the cathode can be reduced to several  $\mu\text{g cm}^{-2}$  without significantly affecting the performance.<sup>96</sup> This also applies for the sluggish oxygen evolution reaction (OER) when using advanced anode catalysts based on  $\text{IrO}_x$  nanoparticles or nanowires with low loadings in the range of  $0.08 - 0.1 \text{ mg}_{\text{IrO}_2} \text{ cm}^{-2}$ .<sup>165, 166</sup> The development of novel catalysts for the rate limiting OER is therefore a central measure to prevent limitations for a large scale implementation of PEMWEs in GW per year scale, as iridium is only mined as secondary metal and ten times scarcer than platinum.<sup>72</sup> One approach to further reduce the noble metal loading that has not yet been fully investigated is the development of novel designs for the membrane electrode assembly (MEA) addressing the electrode-membrane interface as previously investigated for PEM fuel cells (PEMFCs).<sup>167</sup>

PEMWE MEA-configurations are currently restricted to the CCM-configuration only (Fig. 32 A). Here a CCM is sandwiched between porous transport layers (PTLs) made of titanium, to meet the durability conditions at the anode<sup>97</sup>, and carbon PTLs at the cathode side. Sandwiching a membrane in-between the cathodic PTE (cPTE) and anodic PTE (aPTE), as shown in Fig. 32 B, will be named as PTE-configuration in the following. The PTE-configuration could be a promising alternative to the standard CCM-configuration, but is not yet commercially available.

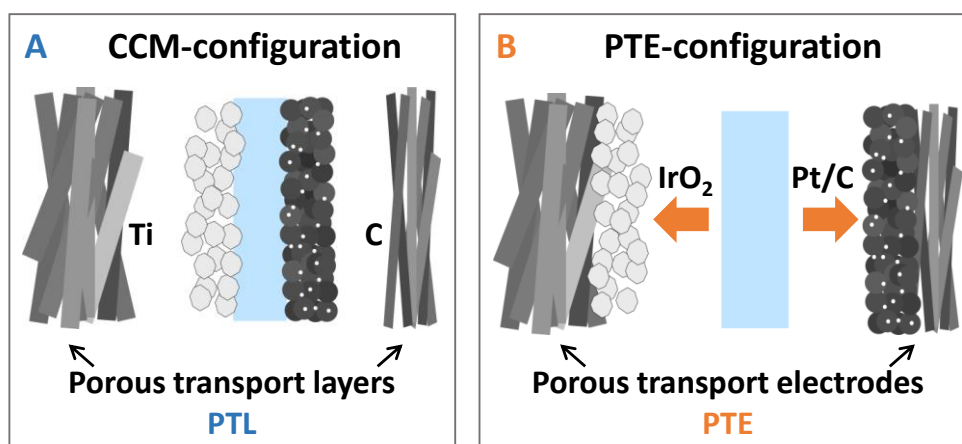


**Fig. 32** A CCM-configuration: a standard catalyst coated membrane (CCM) pressed against porous transport layers (PTLs) made of titanium and carbon. B PTE-configuration: the membrane sandwiched between a cathodic and anodic porous transport electrode (PTE).

The challenging electrode side for implementing PTE-configurations is not the cathode, where usually the same cPTEs as in PEMFCs are used. The cPTEs are available as porous carbon cloth or paper substrates with or without an additional microporous layer (MPL), hydrophobic treatment and with various Pt/C loadings.<sup>168</sup> Anodic PTEs however, consisting of porous titanium substrates coated with an iridium-based catalyst for the OER are not commercially available. One reason might be the costly and challenging fabrication of customized sintered titanium substrates for depositing the iridium-based catalyst layer on top. Already small variations of sintering process parameters like pressure and temperature can lead to cracks or bending of the substrates. The rapid formation of an oxide layer at the surface of the titanium structures increases the electric interfacial contact resistances and impurities in the gas atmosphere during sintering can cause mechanical instability.<sup>99</sup> Currently available porous titanium substrates were initially developed e.g. for industrial filter applications and are not yet optimized for PEMWE. Since also titanium-

based MPLs to smoothen the titanium substrates<sup>102</sup> are still on a research level, the subsequent deposition of smooth catalyst layers on top of the coarse titanium substrate is not trivial as well.

Despite the challenging fabrication of aPTEs for PEMWE, there are some studies on novel anode electrode designs available in literature. Grigoriev et al. compared the performance of different powder-sintered PTLs with different porosities and therefore changed transport properties.<sup>101</sup> Their self-made PTLs were tested either in a CCM-configuration using a Nafion 115 membrane or in a PTE-configuration. The noble metal loading of the spray coated anode was  $2 \text{ mg}_{\text{Irblack}} \text{ cm}^{-2}$ . The PTE-configurations performed slightly worse, which was explained by a reduced direct protonic contact area between catalyst layer and membrane compared to the CCM setup. Sapountzi et al. introduced a carbon paper substrate sputter-coated with titanium and subsequently  $0.55 \text{ mg}_{\text{IrO}_2} \text{ cm}^{-2}$ . The electrode was then coated with Nafion prior to hot-pressing the compound onto a Nafion 117 membrane.<sup>155</sup> At an optimum Nafion loading of  $1.5 \text{ mg}_{\text{Nafion}} \text{ cm}^{-2}$  a current density of  $0.9 \text{ A cm}^{-2}$  was measured at 1.75 V (tested at 60 °C). The cathode electrode was coated with  $1.5 \text{ mg}_{\text{Nafion}} \text{ cm}^{-2}$  as well, to improve the mechanical stability during and after hot pressing. Lee et al. also used a carbon paper substrate, but applied a thin  $\text{IrO}_2$  layer directly via electrodeposition without a titanium based intermediate layer.<sup>154</sup> The highest performance was found for a loading of  $0.1 \text{ mg}_{\text{IrO}_2} \text{ cm}^{-2}$ , with a current density of  $1.92 \text{ A cm}^{-2}$  at 1.8 V using a Nafion 212 membrane (tested at 90 °C). Compared to previous works, the mass activity was significantly improved when directly depositing the iridium based catalyst on the electronically conductive carrier substrate. Besides an improved performance and reduced material costs, the use of carbon substrates is still a critical issue, since only a small crack in the deposited layers would start a rapid corrosion process at the anode side in PEMWEs as mentioned above.<sup>97</sup> Choe et al. went one step further and electrodeposited an iridium based catalyst layer directly on a porous titanium substrate instead of using a carbon paper.<sup>135</sup> The  $\text{IrO}_2$  layer not only acted as catalyst but also as corrosion-protective layer for the titanium substrate. The electrodes were tested in the PTE-configuration with a Nafion 212 membrane at 120 °C. Catalyst loadings as low as  $0.4 \text{ mg}_{\text{IrO}_2} \text{ cm}^{-2}$  showed a sufficient cell performance with a current density of  $0.97 \text{ A cm}^{-2}$  at 1.6 V. The stability of the electrodeposited catalyst layer was higher than for a spray coated catalyst layer, but it can be argued, that the coating had to be perfect to prevent corrosion of the porous substrate. However, with a continuous and defect-free Ir-coating, the durability of the MEAs was found to be increased due to the reduced Ti-PTL surface area exposed to the oxidative environment.

The question if and how the deposition of the anodic catalyst layer directly on top of the titanium PTL influences the long-term behavior of PTE-based MEAs extends the already intensively discussed topic regarding corrosion protective layers for PTLs. Rakousky et al. e.g. found that 78 % of the degradation rate during a long-term experiment originated in the degradation of the Ti-PTL.<sup>139</sup> A protective sputter deposited platinum layer on top of the PTL reduced the degradation remarkably. Due to concerns regarding the formation of an oxide layer on the Pt-coating, Liu et al. presented a thin sputtered iridium layer on top of the titanium PTL to improve electrical resistance and long-term durability.<sup>169</sup> Since coating the titanium PTL with a noble metal layer of Au, Pt or Ir increases the cost of PEMWEs, Bystron et al. presented an etching technique to remove the oxide layer of the titanium PTLs (reduced electrical resistance) while at the same time introducing Ti hydride on the titanium surface (corrosion protective layer, reduced oxide layer formation).<sup>170</sup> This cheap and effective alternative to expensive protective noble metal coatings improved the cell performance compared to untreated PTLs as well in terms of electrical resistance and durability. However, the degradation mechanisms and associated need to coat Ti-PTLs are not yet fully understood. Suermann et al. demonstrated the operation of pristine PTLs in

CCM configurations for several hundred hours at elevated cell voltages without significant degradation.<sup>140</sup>

In a recent publication we showed that PTE based approaches can perform as good or even better as CCM based approaches.<sup>1</sup> To stimulate the further development of aPTEs for PEMWEs, there is the need to show the potential of improving the performance and fabrications costs when using the PTE-configuration instead of the standard CCM-configuration. Therefore, in this study, we focus on the optimization of spray coated aPTEs made of porous titanium substrates coated with an IrO<sub>2</sub> and Nafion-based catalyst layer. To the best of our best knowledge, no attempts to further optimize catalyst layers for aPTEs based on different commercial porous titanium substrates exist so far. We consequently evaluated the optimum noble metal loading and ionomer content in the catalyst layers of the aPTEs as well as the influence of different titanium substrates. We furthermore showed the stable operation of the most reproducible aPTE developed in this work for 200 h at a constant current of 2 A cm<sup>-2</sup>.

### 5.3 Experimental

#### MEA

The reference CCM-configuration in this work consisted of a commercial half-sided cathode CCM (FuelCellsEtc) with 0.5 mg<sub>Pt/C</sub> cm<sup>-2</sup> (60 % platinum on vulcan) on a Nafion 117 membrane, which was spray coated with 1.4 mg<sub>IrO<sub>2</sub></sub> cm<sup>-2</sup> (Alfa Aesar) and 9 wt% Nafion D520 (FuelCellStore) on the anode side. The CCM was sandwiched between a porous carbon cloth substrate (FuelCellsEtc, type GDL-CT) at the cathode and a titanium fiber PTL (Bekaert, 1 mm thick, 56 % porosity) at the anode side. The geometric active area of all MEAs used in this work was 5 cm<sup>2</sup>.

For the PTE-configurations, commercial carbon cloth based cPTEs (FuelCellsEtc, type SL-GDE) with a catalyst loading of 0.5 mg<sub>Pt/C</sub> cm<sup>-2</sup> (60 % platinum on vulcan) were purchased. The aPTEs were fabricated via spray coating an IrO<sub>2</sub>-based anode catalyst layer with varying noble metal and Nafion loadings on different porous titanium substrates. One PTL was the same as used in the CCM-configuration (Bekaert, 1 mm thick, 57% porosity), the second was a titanium powder-sintered PTL (Mott, 1 mm thick, 40 % porosity). Prior to deposition of the catalyst layer, burrs (residues from laser cutting) at the edges of the 5 cm<sup>2</sup> sized titanium PTLs were removed with a scalpel. The PTLs were then immersed in an alkaline cleaning solvent (Borer Chemie, 5 vol% Deconex OP153 in DI-water) and sonicated for 10 min to remove organic contaminations. Afterwards, the PTLs were rinsed and sonicated again for 10 min in 2-Propanol followed by DI-water. The aPTE and cPTE were pressed against a Nafion 117 membrane to complete the PTE-configuration.

The IrO<sub>2</sub>-based catalyst inks for spray coating the aPTEs contained 1 wt% solids (metal and Nafion D520, FuelCellsEtc) in a mixture of 2-Propanol and DI-water (equal parts). After wetting the IrO<sub>2</sub> powder with water, 2-Propanol and Nafion were added. The bottle was stirred after adding a new component. The ink was then continuously ultra-sonicated in an ice bath for 30 min (Hielscher, model UIS250L, 0.55 W, 90 % amplitude) and stirred at the same time. After stirring the ink overnight, the sonication step was repeated, before filling the ink into the syringe of the spray coater (SonoTek, model Exacta Coat). An ultrasonic nozzle type AccuMist (48 kHz) set to 5 W at a height of 37 mm was used. The titanium substrates were laser cut into 5 cm<sup>2</sup> squares and placed in 1 mm thick PTFE frames on the hot plate of the spray coater. The hot plate was set to 120 °C, the shaping air to 0.6 kPa, the path speed to 170 mm sec<sup>-1</sup> and the flow rate to 0.45 ml min<sup>-1</sup>. The

ink was stirred within the syringe during spray coating with a magnetic stirrer. A meander shaped path with a pitch of 1.5 mm was set. The additional ink for re-loading the syringe was placed on a magnetic stirrer to keep the particles in the ink well dispersed within the solvents. The noble metal loading was determined via spray coating on a 1 cm<sup>2</sup> rectangular metal sheet, which was weighted on a microscale (Sartorius, model ME 36S). Since catalyst material was found to partly sediment in the syringe and long-tubing of the spray coater, the final Nafion content in the sprayed catalyst layers was determined via a thermo-gravimetric analysis (Netsch, model STA 449F5) according to the work of Feng et al.<sup>160</sup> The TGA-measurement was performed under controlled air conditions at a heating rate of 5 K min<sup>-1</sup>. The final temperature of 1000 °C was held for 1 h. The Nafion content was found to be approximately five times higher as expected from the ink preparation. We therefore suggest TGA measurements after manufacturing to be sure about the final composition of the sprayed catalyst layers.

### Electrochemical testing

A two electrode test cell was used to study the CCM and PTE-configurations. Eight M6 screws tightened at 8.5 Nm were used to fix the cell. The screws were inserted in two aluminum end plates holding the inner cell parts, as well as the heating elements, which were set to 80 °C. The potentiostat was connected to copper plates, which were electrically insulated from the end plates with a self-adhesive PTFE foil and on the other side in contact with the titanium flow fields. The flow fields were designed with a 5 cm<sup>2</sup> parallel finger structure to evenly distribute water towards the PTLs. The PTLs were placed within PTFE frames, which at the same time acted as hard-stops setting the compression of the PTLs. For the titanium PTL a 1 mm thick PTFE sheet was used since the compressibility of the 1 mm thick titanium material was expected to not change significantly when being assembled in the test cell. To ensure a sufficient contact of the PTEs with the membrane, a relatively high compression of 60 % was chosen for the carbon cloth based cPTE via using a 150 µm thick PTFE frame. The membrane was placed between the PTLs. A relatively high internal cell resistance of around 0.091 Ω cm<sup>2</sup> without the membrane was measured and will be addressed in future test cell design via coating the flow fields with a thin gold layer. Both electrodes were supplied separately with DI-water (Ismatec peristaltic pump, model IP 65) at a flow rate of 40 ml min<sup>-1</sup>. The tubing at the inlets of the test cell was placed in a water bath (Lauda, model Ecoline 003) to preheat the process water. The temperature, which was measured at three different points, was monitored: at the anodic water inlet and outlet, as well as directly in the titanium flow field. Measurements were performed at atmospheric pressure and were started when all temperature sensors showed a constant value of 80 °C.

The MEA was conditioned with a potentiostat (Scribner, model 857) from 1.4 V – 2.2 V in 200 mV steps (each hold for 30 s, 15 repetitions). The polarization curve was recorded in several segments with the highest resolution in the kinetic region at low current densities. Every set current density was held for 120 s before recording the corresponding cell voltage. In the first segment, the current density was increased from 0 A – 40 mA in 10 mA steps, then from 50 mA – 1 A in 50 mA steps, followed by the third segment from 1.25 A – 3 A in 250 mA steps. At higher current densities, the step size was increased to 500 mA in the range of 3.5 A – 6 A and finally to 1 A in the last segment starting at 7 A.

In the results section, the recorded cell voltage, the HFR (measured in parallel at 1 kHz) and the resulting HFR-free cell voltage are used for the electrochemical analysis of the aforementioned MEA-configurations. A combination of the structural data with electrochemical data goes far beyond the material screening in this work. Therefore, a more detailed structural analysis will be

performed in a separate paper, using FIB-SEM, similar to previous work done with CCMs<sup>147</sup>, as well as a more detailed electrochemical characterization. In order to further break the overpotential down into kinetic and mass transport, the HFR-free cell voltage is shown in the corresponding relevant current density range.

For the stability test, the standard measurement protocol as used for all the PTEs tested in this work was enhanced by a constant current hold of  $2 \text{ A cm}^{-2}$  for 200 h. As no ion exchanger was available, the DI-water was precautionary exchanged every second day. By this, the conductivity of the water did not exceed  $1.5 \text{ } \mu\text{S cm}^{-1}$ . To enable the regular manual exchange of the DI-water and recording of polarization curves, the 200 h constant current hold was applied as the sum of 45 h current holds followed by a polarization curve.

## Structural analysis

To study structural characteristics of the aPTEs, focused ion beam scanning electron microscopes (FIB-SEM) were used (Zeiss, model Crossbeam 540 with GEMINI II and model Neon 40 EsB). Images taken from the surface of the aPTEs allowed investigating the homogeneity of the deposited catalyst layers. With the possibility to image cross-sections, the interfacial contact area between titanium and catalyst layer, as well as the porosity and pore size distribution within the catalyst layer could be investigated.

## 5.4 Results and Discussion

### 5.4.1 Influence of the titanium porous transport layer on cell polarization

Porous titanium layers can be made of powder-sintered or fiber-sintered materials and are characterized via e.g. the size of the pristine powder particles or fibers as well as the final porosity, pore size and layer thickness. The structure of the PTLs has a crucial impact on the manufacturing of aPTEs and furthermore influences the performance of the MEA.<sup>6, 101</sup> In case the pores are much larger than the size of the catalyst particles, parts of the catalyst layer could be sprayed deep into the pores in great distance from the membrane and could be therefore inactive for the OER. The pore size and therefore the surface roughness were also expected to have a similar impact as in CCM-configurations on the interfacial contact area between PTL and catalyst layer as well as on the mass transport behavior.<sup>111, 163</sup>

**Microstructure.** The surface and cross-sections of powder- and fiber-sintered titanium substrates spray coated with  $1.0 \text{ mgIrO}_2 \text{ cm}^{-2}$  and 5 wt% Nafion are shown in Fig. 33. The surface of the fiber PTE was very inhomogeneous due to large pores in the  $100 \text{ } \mu\text{m}$  range of the pristine titanium PTL (Fig. 33 A), whereas the aPTE based on the denser powder-sintered PTL showed a continuous catalyst layer (Fig. 33 B). The local thickness of the catalyst layer on the titanium fibers was almost constant (Fig. 33 C) but only for the powder-sintered substrate the gaps between different titanium parts could be closed by the catalyst material (Fig. 33 D). No significant differences of the porosity of the catalyst layer as well as the interface towards the PTLs could be seen when using fiber-sintered or powder-sintered substrates (Fig. 33 E,F). For the subsequent analysis of the performance of the different aPTEs, a schematic representation of the electrode structure with respect to the preferred transport pathways is shown in Fig. 33 G,H. We assumed, that the larger pores of the aPTE based on a fiber-sintered substrate are an advantage for the distribution of gases and water through the aPTE but at the same time a disadvantage due to loss of active sites in the pores and therefore an increased kinetic overpotential was assumed. The smoother surface



of the powder-sintered substrates was considered to improve protonic and electrical interfaces, but to increase the mass transport resistances.

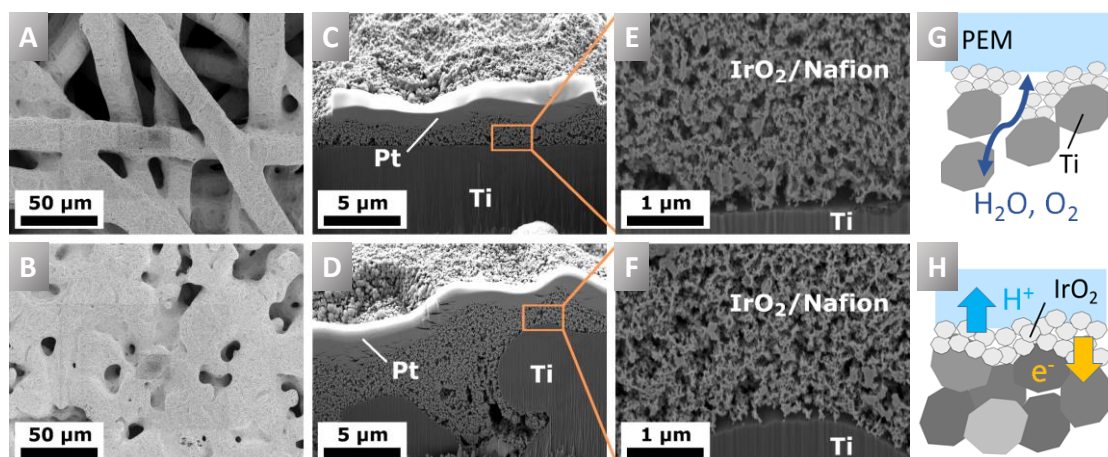


**Fig. 33** Structural investigation of aPTEs consisting of a porous titanium PTL spray coated with  $1.0 \text{ mg}_{\text{IrO}_2} \text{ cm}^{-2}$  and 5 wt% Nafion. A,B Surface of the aPTEs, when using a titanium fiber- or powder-sintered substrate. C,D Cross-sections of the aPTEs showing the titanium PTL,  $\text{IrO}_2$  catalyst layer and protective Pt-layer deposited during the FIB-SEM analysis. E,F Cross-sections of the aPTEs showing the porosity of the  $\text{IrO}_2$  catalyst layers as well as its interfaces towards the different titanium substrates. G,H Assumption of improved interfacial resistances and mass transport properties along the cross-section of the aPTEs when using a fiber or powder-sintered PTE.

**Electrochemical performance.** Fig. 34 shows the electrochemical measurement data of aPTEs using a powder- or fiber-sintered substrate spray coated with different noble metal loadings of 0.5, 1.0 and  $1.4 \text{ mg}_{\text{IrO}_2} \text{ cm}^{-2}$ , while keeping a constant Nafion content of 5 wt%.

Surprisingly, the aPTEs based on the denser powder-sintered PTLs did not outperform the fiber-sintered substrates, as it was expected from the structural analysis. On the contrary, the fiber PTE-configuration exhibited a better cell polarization behavior for loadings above  $1.0 \text{ mg}_{\text{IrO}_2} \text{ cm}^{-2}$  (Fig. 34 A). The HFR-free cell voltage (Fig. 34 B) showed no significant differences of mass transport losses between the different aPTEs. There were however, differences in the HFR between the different loadings as well as the different titanium substrates (Fig. 34 C). The HFRs of the aPTEs with a loading of  $1.0 \text{ mg}_{\text{IrO}_2} \text{ cm}^{-2}$  and  $1.4 \text{ mg}_{\text{IrO}_2} \text{ cm}^{-2}$  were lower when using a fiber PTL. This was not expected, since in theory the smoother surface of the powder-sintered substrates should have increased the electrical contact area between catalyst layer and PTL. The opposite effect was the case, with even a stronger difference in HFR between fiber and powder-sintered materials at higher noble metal loadings.

The higher HFR for the powder-sintered aPTEs could be explained by an effect visible on the cross-sections of that layer (Fig. 34 D). The smaller pores of the powder-sintered PTL were partly filled with catalyst material leading to a locally increased thickness of the catalyst layer and therefore longer pathways for electrons. However, for noble metal loadings as low as  $0.5 \text{ mg}_{\text{IrO}_2} \text{ cm}^{-2}$  the HFR was lower when using the smoother powder-sintered PTL. A smoother PTL could therefore be beneficial for the in-plane conductivity of low-loaded catalyst layers. A slight decrease in the HFR with increasing current density may be explained due to the increase in waste heat production and a deviation from the thermal equilibrium (see e.g.<sup>111, 141, 163</sup>). In general, the higher the noble metal loading of the aPTEs, the lower was the kinetic overpotential (Fig. 34 D). Contrary to our expectations, the deposition of catalyst material into the bigger pores of the titanium fibers did not significantly affect the kinetic overpotential. The direct electrical interface between catalyst layer and PTL, as it is the case for both the fiber and powder-sintered aPTEs, could therefore have

had a greater influence on the kinetic overpotential than a changed protonic interface between catalyst layer and membrane. The direct electrical interface between catalyst layer and electrically conductive substrate, was at least according to Mo et al. essential for a sufficient catalyst utilization in CCM-configurations.<sup>171</sup>

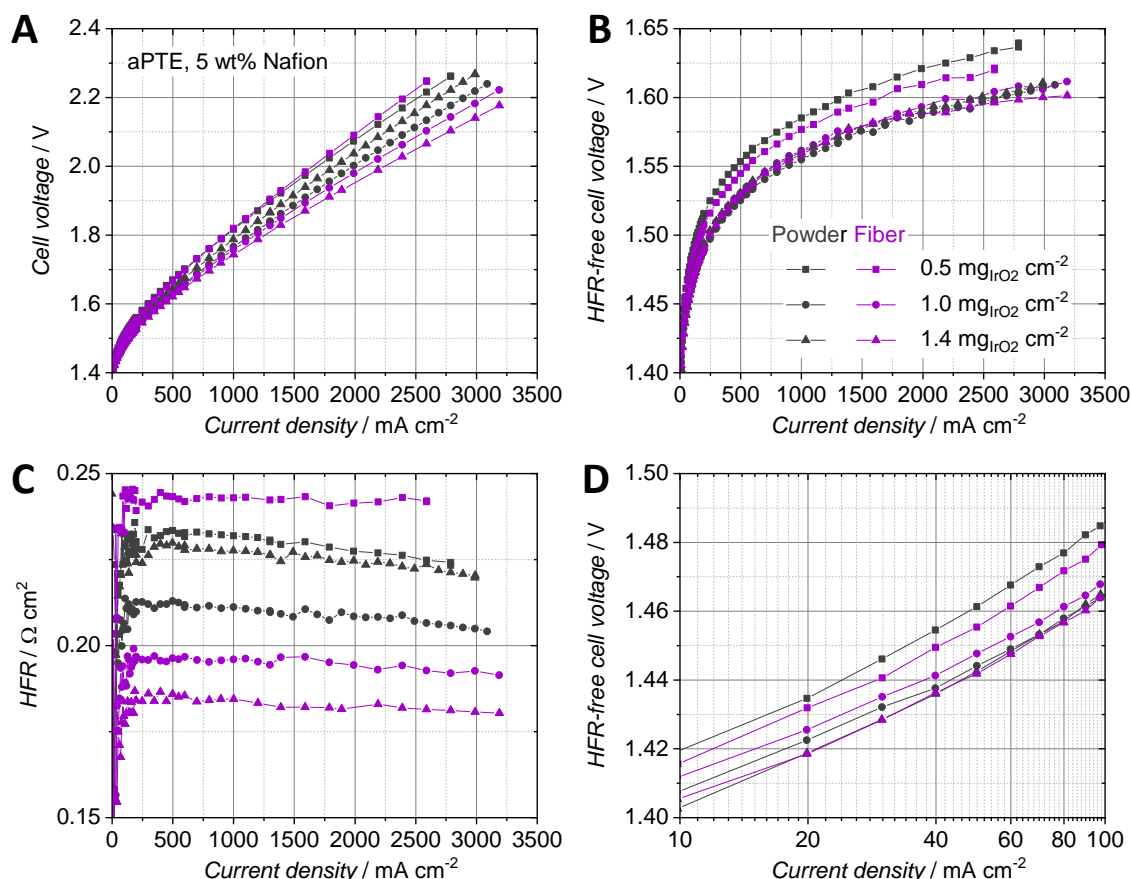


**Fig. 34** A Polarization curves of anodic porous transport electrodes (aPTEs) with different  $\text{IrO}_2$  loadings based on a powder- vs. fiber-sintered substrate. B HFR-free cell voltage. C HFR D Kinetic region of the HFR-free cell voltage.

Due to the in average better performance, as well as the superior material characteristics such as a higher degree of interconnected pores<sup>172</sup>, pores, fiber-sintered PTLs were used as substrates for the aPTEs further investigated in this work.

#### 5.4.2 Influence of the Nafion content in the catalyst layer

The Nafion content in the catalyst layer is a key parameter to reduce all three main contributions to the overpotential, i.e. ohmic, kinetic and mass transport. The amount of ionomer in the catalyst layer has an influence on its structure itself as well as on the electrical interface towards the PTL and on the protonic interface towards the membrane.<sup>173, 174</sup> An optimized three-phase boundary between catalyst particles, water supply and ionomer is essential to achieve the highest activity of the catalyst material possible. The ratio between ionomer and catalyst particles also influences the ohmic region, due to influences on the electrical resistance within the catalyst layer as well as the electrical resistance towards the PTL. A reduced porosity of the catalyst layer depending on the Nafion content as well as increased protonic resistances within the catalyst layer could furthermore pronounce mass transport losses. For anodes in the CCM-configuration, several optimum Nafion contents were found depending on the catalyst material and fabrication technique. Xu et al. e.g. reported an optimum Nafion content of 25 wt% for a CCM with 1.5 mg

$\text{cm}^{-2}$   $\text{Ru}_{0.7}\text{Ir}_{0.3}\text{O}_2$  spray coated on a PTFE sheet and hot-pressed onto a Nafion 117 membrane.<sup>174</sup> A similar value of 30 wt% Nafion was found for a CCM with  $1.5 \text{ mg}_{\text{Irblack}} \text{ cm}^{-2}$  brushed onto a Nafion 1135 membrane.<sup>173</sup> Bernt et al. reported a lower optimum Nafion content of 11.6 wt% when using  $2 \text{ mg}_{\text{Ir}} \text{ cm}^{-2}$  of a supported  $\text{IrO}_2/\text{TiO}_2$  catalyst.<sup>175</sup> Since a porous titanium substrate was used for depositing the catalyst layer on top and not a flat membrane, we expected the optimum Nafion content of anodes in the PTE- configuration to vary from the values reported for the CCM- configurations.

**Microstructure.** The surface and cross-sections of two aPTEs based on titanium fibers with a loading of  $1.4 \text{ mg}_{\text{IrO}_2} \text{ cm}^{-2}$  and different Nafion contents of 21 wt% and 12 wt% were analyzed (Fig. 35). The sample with 21 wt% Nafion showed parts of the catalyst layer peeling off the titanium fibers due to large agglomerations of Nafion (Fig. 35 A). The cross-section indicated, that pores in the catalyst layer could be partly blocked by Nafion. The catalyst particles were disconnected from the titanium fiber at some spots due to electrically insulating layers of Nafion (Fig. 35 B) or voids between catalyst layer and PTL. The surface (Fig. 35 C) of the aPTE with 12 wt% Nafion showed a rough catalyst layer but no obvious discontinuities as seen for the aPTE with a higher Nafion content. The cross-section of the aPTE with 12 wt% Nafion in the catalyst layer (Fig. 35 D) showed a higher porosity and was therefore expected to perform better than the aPTE with 21 wt% Nafion.

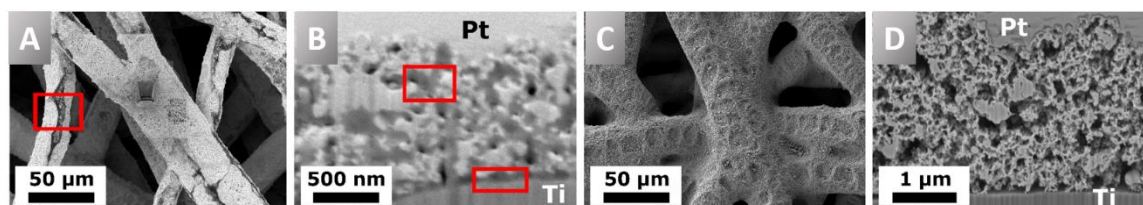


**Fig. 35** A,B Surface and cross-section of the aPTE with 21 wt% Nafion in the catalyst layer. Red squares indicate peeled off parts of the catalyst layer, blocked pores and electrically insulated interface between PTL and catalyst layer. C,D Surface and cross-section of the aPTE with 12 wt% Nafion in the catalyst layer. The catalyst layer did not peel off, the porosity and interface towards the PTL was not affected significantly by the ionomer in the catalyst layer.

**Electrochemical performance.** Fig. 36 shows the results of three types of aPTEs based on titanium fibers with different Nafion contents in the catalyst layers (5 wt%, 9 wt% and 12 wt%) and a constant loading of  $1.4 \text{ mg}_{\text{IrO}_2} \text{ cm}^{-2}$ . Since the aPTEs with 12 wt% (Fig. 35 C,D) already showed a comparably bad polarization behavior, the inhomogeneous aPTE with 21 wt% Nafion content (Fig. 35 A,B) was not electrochemically investigated. Below a Nafion content of 5 wt% the catalyst ink started to be unstable, which led to inhomogeneous spray patterns during fabrication of the aPTE. Therefore, aPTEs with lower Nafion contents than 5 wt% were not electrochemically investigated in this study. Every PTE-configuration was fabricated three times to calculate an average value and standard deviation for the cell voltage.

The lower the Nafion content, the better was the overall performance of the aPTEs (Fig. 36 A). The HFR-free cell voltage (Fig. 36 B) was increased with increasing Nafion contents, most probably due to the filling of pores with Nafion and therefore increased mass transport losses. The significant increase of the HFR (Fig. 36 C) at 12 wt% Nafion could be explained with a worse electrical interface between catalyst layer and titanium PTL (compare to Fig. 35 B). Since increasing the Nafion content also increased the thickness of the catalyst layer, pathways became longer which additionally could have led to a higher ohmic but also mass transport overpotential. The polarization data for the aPTEs was in good agreement with findings for anode catalyst layers in the CCM-configuration. Bernt et al. also saw a significant increase of the HFR when the Nafion loading was above a certain threshold, which was around 20 wt% for the supported  $\text{IrO}_2$  catalyst

in their CCM-configuration.<sup>175</sup> The reproducibility was worst for the fiber aPTE with 5 wt% Nafion already in the kinetic region (Fig. 36 D) and got more pronounced with increasing current density. A higher Nafion content did slightly increase the kinetic overpotential most likely caused by the occurrence of mass transport losses already at relatively small current densities. To further study the impact of different noble metal loadings on the polarization behavior, fiber aPTEs with a Nafion content of 9 wt% and varying IrO<sub>2</sub> loadings were fabricated as compromise between performance and reproducibility.

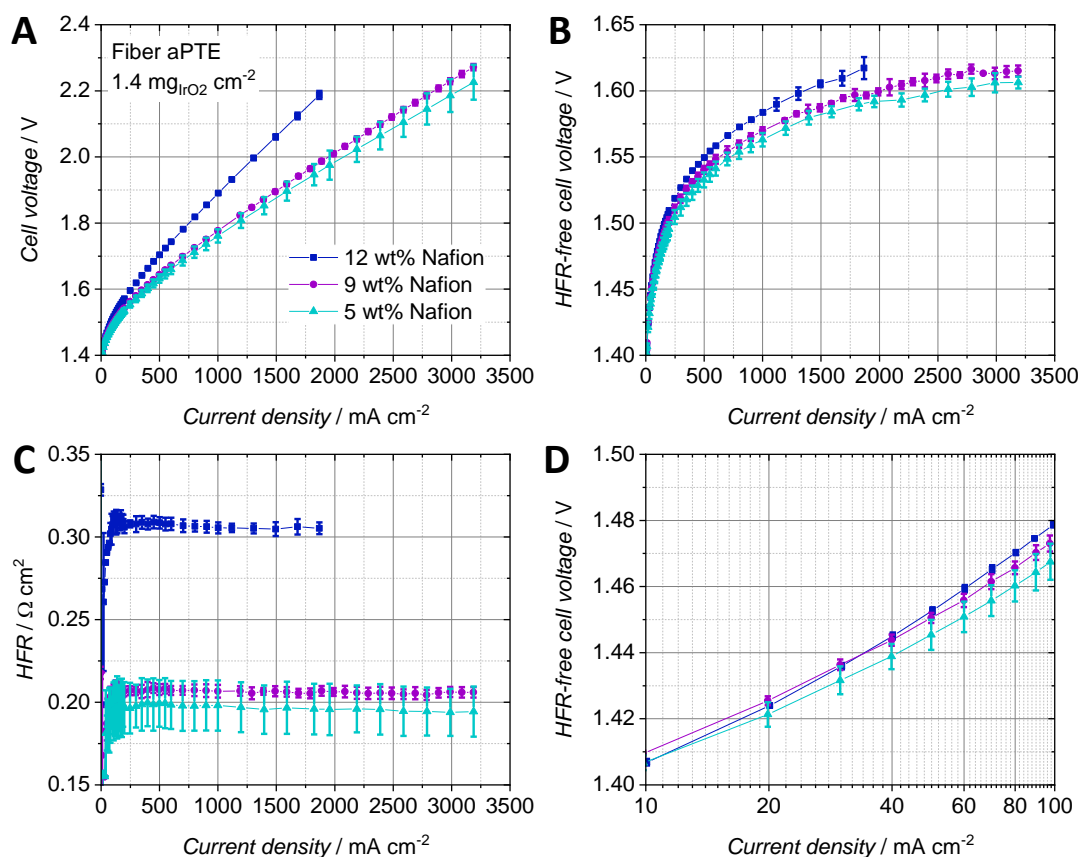


**Fig. 36** A Polarization data of aPTE Fiber electrodes with different Nafion contents in the catalyst layers but the same noble metal loading of 1.4 mg<sub>IrO<sub>2</sub></sub> cm<sup>-2</sup>. B HFR-free cell voltage. C HFR D Kinetic region of the HFR-free cell voltage.

### 5.4.3 Influence of the IrOx loading

To increase the activity of the anodic catalyst layer, the catalyst loading and therefore the number of active sites need to be increased. But when increasing the noble metal loading, also both the thickness of the catalyst layer as well as the amount of the material that is deposited into the pores of the PTL is typically increased.<sup>1</sup> Therefore, mass transport properties change as a function of catalyst layer thickness. For anodes in the CCM-configuration, several studies on the influence of the noble metal loading and ionomer content exist. Rozain et al. e.g. found an optimal catalyst loading at the anode when using 0.5 mg<sub>IrO<sub>2</sub></sub> cm<sup>-2</sup> with 10 wt% Nafion.<sup>128</sup> For loadings below 0.5 mg<sub>IrO<sub>2</sub></sub> cm<sup>-2</sup>, the use of a conductive support was suggested, to electrically contact and activate every catalyst particle due to the reduced in-plane conductivity, which was also identified by Bernt et al. as structural challenge for low loaded electrodes.<sup>96</sup> When using aPTEs, the electrical contact area between catalyst particles and the PTL is good compared to CCM type configurations but still the in-plane conductivity of the catalyst layer is highly dependent on the roughness of the PTL as discussed when comparing the powder- with the fiber-sintered substrates. Su et al. studied low loading anodes with respect to the Nafion content and concluded, that for loadings as low as

0.38 mg<sub>IrO<sub>2</sub></sub> cm<sup>-2</sup> a Nafion content of 5 wt% is still sufficient.<sup>176</sup> The influence of the iridium loading on the polarization behavior of aPTEs was investigated in the following and compared to studies on the anode catalyst layer in CCM-configurations.

**Electrochemical performance.** Fiber aPTEs with 9 wt% Nafion in the catalyst layer but with varying noble metal loadings of 0.5, 1.0, 1.4 and 1.9 mg<sub>IrO<sub>2</sub></sub> cm<sup>-2</sup> were fabricated. To compare the performance of the fiber aPTE with a CCM-configuration, a half-sided cathodic CCM, with 0.5 mg<sub>Pt/C</sub> cm<sup>-2</sup> (60 % platinum on vulcan) on a Nafion 117 membrane, was spray coated on the anode side with 1.4 mg<sub>IrO<sub>2</sub></sub> cm<sup>-2</sup> and 9 wt% Nafion. Three samples per configuration were prepared to calculate an average value for the cell voltage and the standard deviation (Fig. 37).

For the tested fiber aPTEs with 9 wt% Nafion, an optimum loading of 1.4 mg<sub>IrO<sub>2</sub></sub> cm<sup>-2</sup> was found (Fig. 37 A). The best aPTE showed a better average overall performance than the reference CCM with the same anode catalyst layer composition. The HFR-free cell voltage as a combination of kinetic and mass transport losses (Fig. 37 B) interestingly showed no significant difference between aPTEs with 1.4 and 1.9 mg<sub>IrO<sub>2</sub></sub> cm<sup>-2</sup> loading. The CCM-configuration performed best in HFR-free cell voltage. It should be noted, however, that the relative better polarization behavior of the CCM-configuration diminished with increasing current densities.

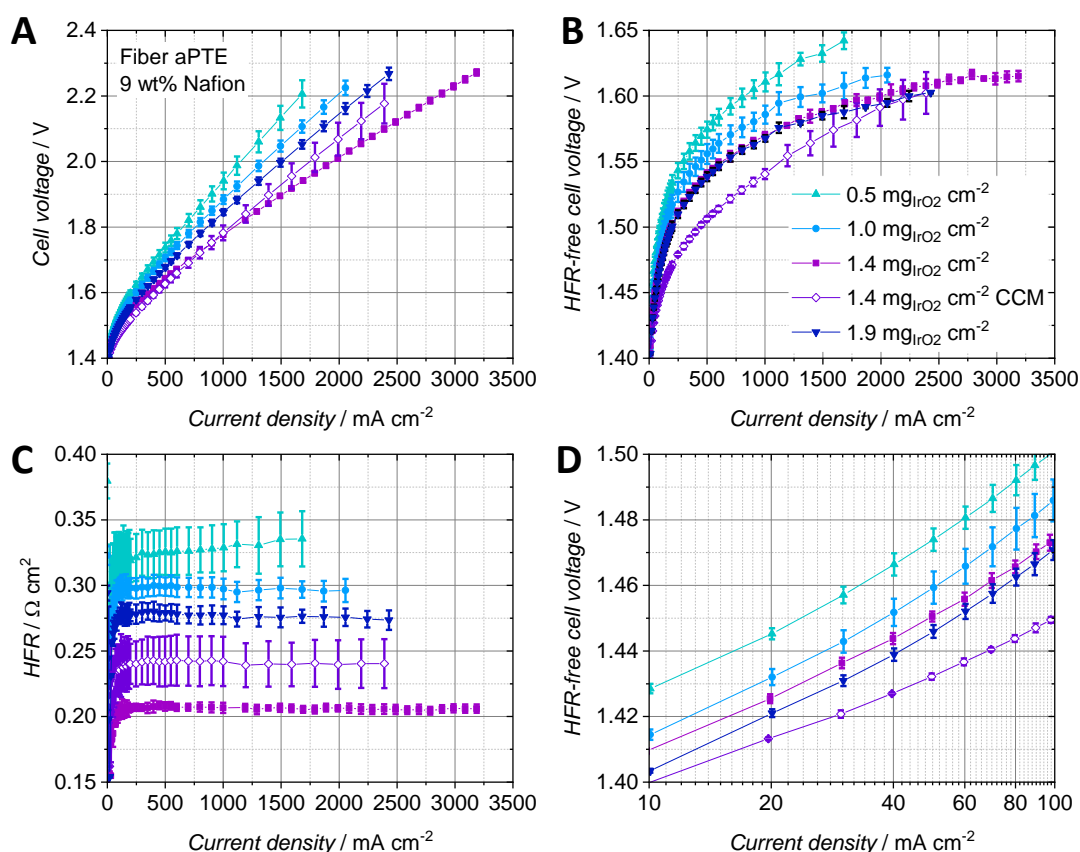


**Fig. 37** A Polarization data of the fiber aPTE with constant Nafion content of 9 wt% and varying noble metal contents. B HFR-free cell voltage. C HFR D Kinetic region of the HFR-free cell voltage.

The superior overall performance of the aPTE with 1.4 mg<sub>IrO<sub>2</sub></sub> cm<sup>-2</sup> compared to the other MEA-configurations was most likely due to the lowest HFR (Fig. 37 C) which also showed the best reproducibility. With reduced catalyst layer loadings, the reproducibility of the HFR of the aPTEs became worse. The CCMs showed an in average higher HFR than the PTE with the same catalyst



loading. It has to be stated, however, that the anode catalyst layer deposited on the reference CCM was optimized for the PTEs in terms of Nafion content. Thus, an optimized CCM-configuration with the same noble metal loading but an optimized amount of Nafion could lead to an improved HFR and therefore better performance of the CCM-configuration. Nevertheless, in this work the same anode catalyst layer composition was chosen for the sake of comparability and simplicity. The kinetic region of the HFR-free cell voltage (Fig. 37 D) showed the CCM with the best performance, most probably due to the largest direct protonic contact area of the catalyst layer with the PEM. The higher the noble metal loading of the aPTEs, the smaller was the kinetic overpotential. The kinetic region was however affected already at about  $20 \text{ mA cm}^{-2}$  by mass transport losses. Since at such low current densities bubble and diffusion overpotentials should not dominate<sup>104</sup>, a changed proton conductivity within the catalyst layer could have been the reason for this behavior. As already described by Babic et al. for CCMs<sup>164</sup>, the thickness of the catalyst layers increased with increasing noble metal loadings and therefore protonic pathways increased. This then most probably led to increased protonic resistances within the catalyst layer.

A comparison between the HFR-free cell voltage at low current densities (Fig. 37 D) with the HFR-free cell voltage at low current densities per milligrams  $\text{IrO}_2$  (Fig. 38 A), helped to further study the impact of the noble metal loading on the cell performance. At an HFR-free cell voltage of 1.47 V all PTE-configurations were compared with each other in terms of current density and mass specific activity dependent on the noble metal loading (Fig. 38 B). The reference CCMs showed both the best catalyst utilization due to the lowest HFR-free cell voltage per noble metal loading (Fig. 38 A) and the lowest overpotential in the kinetic region (Fig. 37 D). Increasing the noble metal loading of the aPTEs reduced the kinetic overpotential (Fig. 37 D), but at the same time the effective catalyst utilization was reduced (Fig. 38 A). This opposing trend of kinetic losses vs. mass activity is shown in a combined graph (Fig. 38 B). The cell current and mass activity at a set HFR-free cell voltage of 1.47 V were plotted in dependency of the  $\text{IrO}_2$  loading. The higher the noble metal loading, the specific current density, but at the same time, the mass specific activity was reduced. Babic et al. reported a similar opposing trend of activation losses vs. effective catalyst utilization for anode catalyst layers with different loadings for the CCM-configuration<sup>164</sup>.

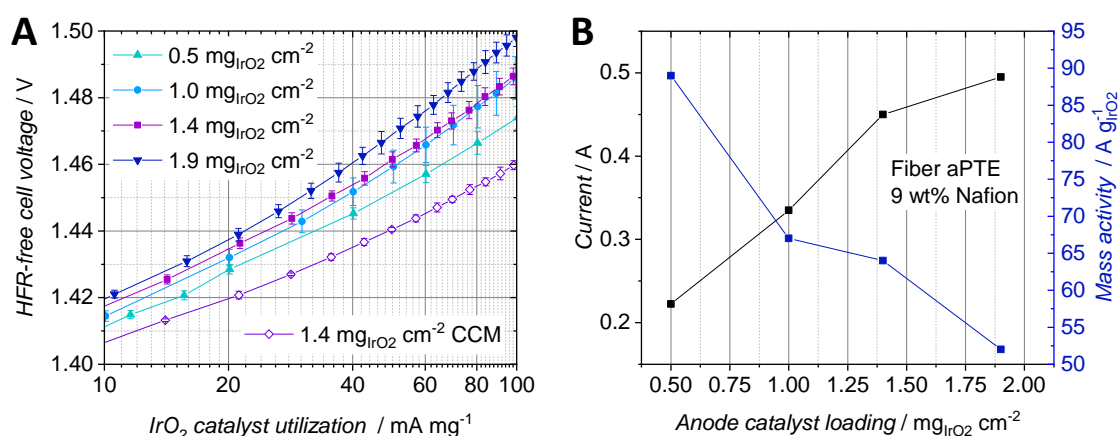


**Fig. 38** A HFR-free cell voltage of the fiber aPTE with constant Nafion content of 9 wt% and varying noble metal content dependent on the current per mg noble metal loading. B Average values of the current and mass activity dependent on the  $\text{IrO}_2$  loading per active area at a given HFR-free cell voltage of 1.47 V.

### Stability test

The fiber-sintered PTE with a loading of  $1.4 \text{ mg cm}^{-2}$  and 9 wt% Nafion showed the highest reproducibility and reasonable performance in comparison with the CCM-configuration with the same anodic catalyst layer sprayed on the membrane, and was therefore chosen for the durability test. Fig. 39 shows the cell voltage over time while applying a constant current of  $2 \text{ A cm}^{-2}$ . Polarization curves were recorded for the pristine PTE and after every segment (Fig. 40).

The cell voltage improved significantly during the first hold of 45 h, as well did the HFR-free cell voltage and the HFR of the PTE-configuration (Fig. 39). This behavior can be related to the break-in of the cell due to the activation of the catalyst and e.g. washed-out impurities of the Nafion membrane. In the second constant current hold of 45 h, the overall cell voltage and HFR stabilized and so did the HFR-free cell voltage. Subsequently, increased degradation of approx.  $200 \text{ } \mu\text{V h}^{-1}$  was observed in segment 3 and  $260 \text{ } \mu\text{V h}^{-1}$  in segment 4, which can be assigned almost exclusively to the HFR-free cell voltage and in particular to the anodic catalyst. However, these are of apparent nature and reversible as soon as lower potentials are present and the metal oxide catalyst is reduced with permeated hydrogen.<sup>140, 156</sup>

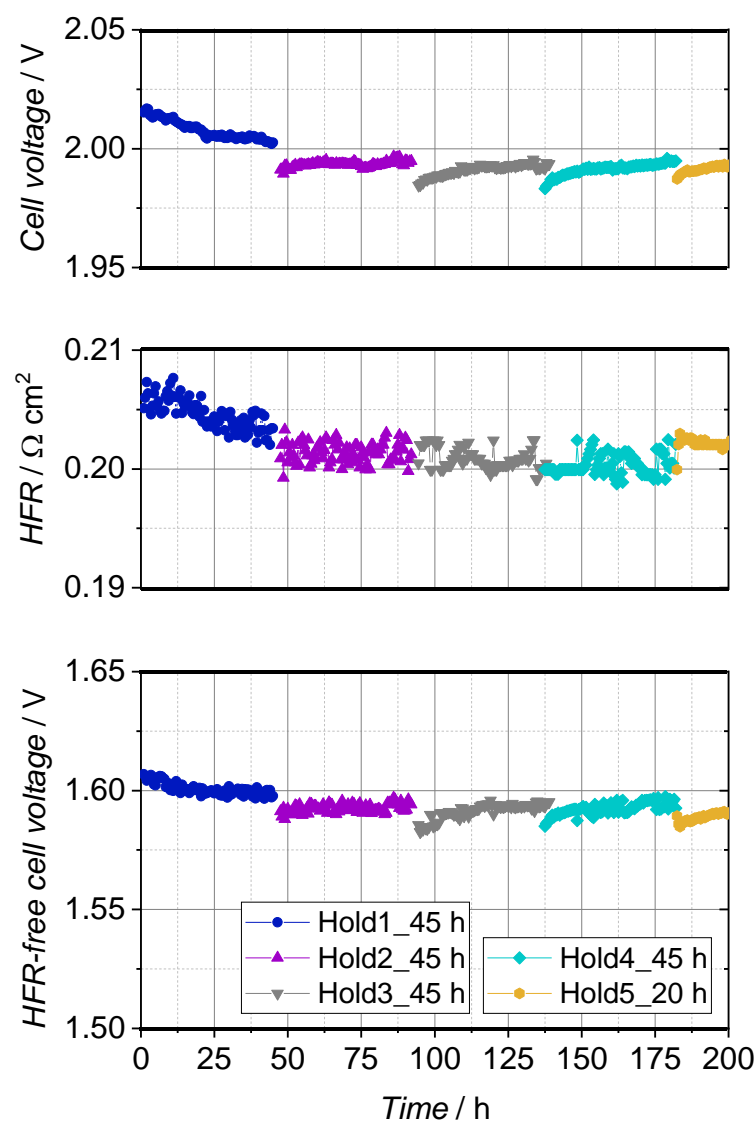


**Fig. 39** Cell voltage, HFR and HFR-free cell voltage during the 200 h stability test. A constant current of  $2 \text{ A cm}^{-2}$  was set and polarization curves were recorded after every segment.

The polarization curves recorded for the pristine PTE-configuration as well as after every segment of the constant current hold, showed a significant improvement of cell performance after the first constant current hold of 45 h (Fig. 40 A). The cell voltage was then stable for the subsequent 155 h of the durability test. The HFR-free cell voltage (Fig. 40 B) as combination of the kinetic and mass transport overpotential as well significantly improved by 20 mV at  $2 \text{ A cm}^{-2}$  after the first 45 h constant current hold and did not show remarkable changes during the remaining time of the test. The HFR (Fig. 40 C) improved by ca.  $8 \text{ m}\Omega \text{ cm}^2$  at  $2 \text{ A cm}^{-2}$  after the first constant current hold and stabilized around a value of  $200 \text{ m}\Omega \text{ cm}^2$ . The reduction of the kinetic overpotential by ca. 10 mV at low current densities was probably due to the activation of the catalyst during the first constant current hold (Fig. 40 D). The kinetic overpotential slightly increased for the polarization curves recorded in the subsequent hours.

The PTE-configuration tested in this work showed a similar stability compared to literature regarding the characterization of commercial CCM-configurations<sup>139, 140</sup>.

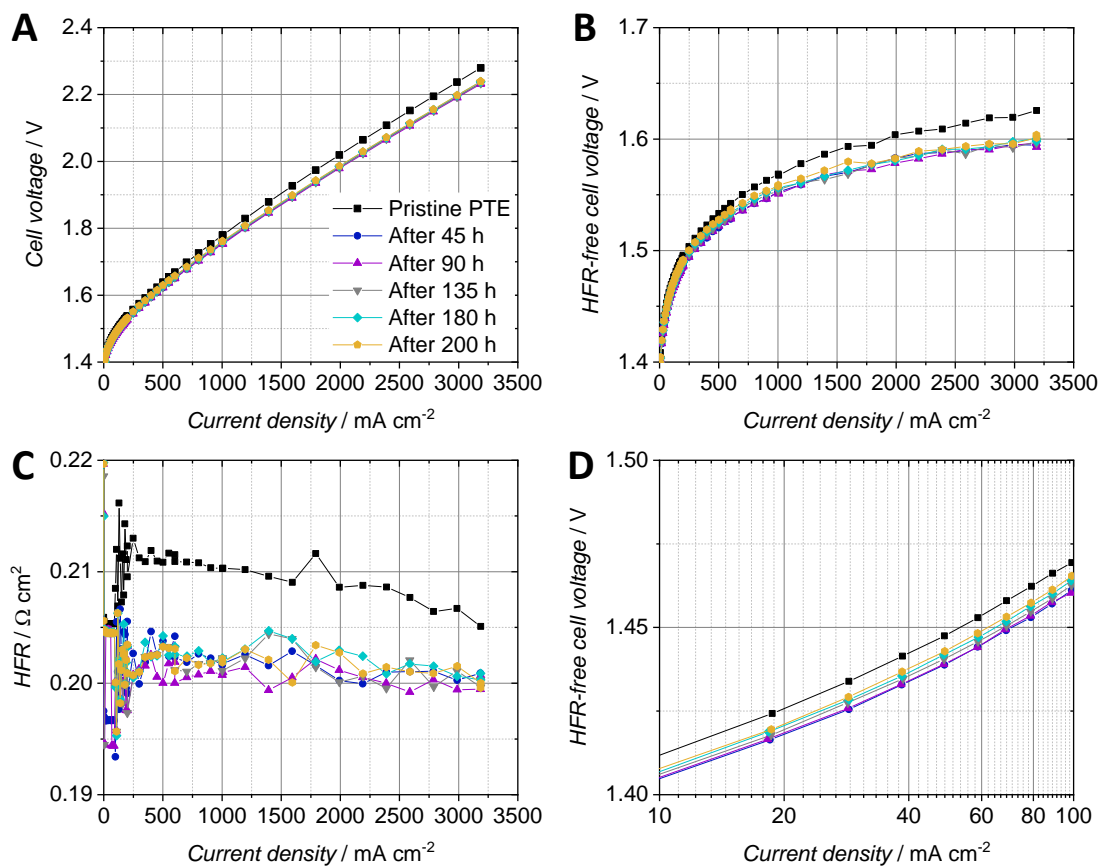


**Fig. 40** Polarization data of the pristine PTE-configuration as well as after every segment of the constant current hold. A Cell voltage B HFR-free cell voltage. C HFR D Kinetic region of the HFR-free cell voltage.



## 5.5 Conclusions

In this work, anodic porous transport electrodes (aPTEs) were fabricated via spray coating of IrO<sub>2</sub> and Nafion-based catalyst layers on top of two different titanium porous transport layers (PTLs). The aPTEs were then pressed against a Nafion 117 membrane and a cathodic porous transport electrode (cPTE) made of a carbon cloth material coated with 0.5 mg<sub>Pt/C</sub> cm<sup>-2</sup> (60 % platinum on vulcan). The fiber-sintered PTL outperformed the powder-sintered aPTE for loadings above 1.0 mg<sub>IrO<sub>2</sub></sub> cm<sup>-2</sup> despite a coarser surface. Reducing the amount of ionomer in the catalyst layers with a loading of 1.4 mg<sub>IrO<sub>2</sub></sub> cm<sup>-2</sup> to only 5 wt% showed a reduced ohmic and mass transport overpotential. Reducing the Nafion content in the catalyst ink however led to inhomogeneous spray patterns and therefore a worse reproducibility. Optimizing the deposition technique is therefore suggested to further reduce the Nafion content for the development of high performing fiber-sintered aPTEs. When keeping the Nafion content at 9 wt% in the catalyst layer, the optimum noble metal loading was 1.4 mg<sub>IrO<sub>2</sub></sub> cm<sup>-2</sup>. With this amount of Nafion in the catalyst layer, a very good reproducibility was reached, especially when compared to CCMs with the same anode catalyst layer composition. The optimum Nafion content and noble metal loading for aPTEs are most likely different for every new material combination, due to the complex interplay of porous substrate, catalyst loading, Nafion content as well as operating conditions. Optimizing every aPTE step by step as shown in this work is therefore too time consuming and advanced structural models are more than needed to help to reduce and define the wide range of fabrication parameters.

In the applied test cell setup, the aPTEs fabricated in this work outperformed a reference CCM with equivalent catalyst loading in terms of HFR, reproducibility and the tendency of an improved mass transport at high current densities. The development and further optimization of aPTEs for PEMWEs is therefore highly interesting and promising since not only the performance could be further improved but also fabrication efforts reduced. Due to the simplified direct spraying of the anode catalyst layer on top of the titanium substrates, no hot pressing or transfer substrate are needed to manufacture a PTE-type MEA.

The stable operation of the most reproducible fiber-sintered aPTE was shown in a 200 h durability test when applying 2 A cm<sup>-2</sup> constant current. The overall cell voltage improved significantly after the first 45 h mainly due to an improved kinetic and ohmic region. The cell performance stabilized then for the remaining time of the durability test. The directly spray deposited anodic catalyst layer therefore showed a mechanically stable interface between catalyst layer and anodic PTL ensuring a high catalyst utilization, electrical connectivity as well as sufficient mass transport.

## 5.6 Critical Discussion

This study was a first step to provide an engineering approach to characterize and optimize anodic PTEs fabricated with standard materials and deposition techniques. There was however only a limited amount of materials and fabrication parameters tested as discussed herein.

**PTLs** - As only two different Ti-PTLs were tested in this work (fiber- and powder-sintered) the potential of other commercial porous titanium substrates was not investigated and could lead to a different picture of how anodic spray coated PTEs should be optimized. Especially denser Ti-PTLs or PTLs with a gradient pore-size could have a great potential when approaching low loadings, as the denser powder-sintered PTL surface seemed to improve the interfacial contact area between thin CL and PTL. The thickness of the Ti-PTL could be reduced as well, to decrease ohmic losses originated from PEMWE cell components.

**Catalyst/ionomer interaction** - Every catalyst powder behaves differently in an ink of solvents and ionomer as the particle size and morphology are different. The optimization of the Nafion content in this work is therefore a good first indication for the used IrO<sub>2</sub> Premion catalyst (AlfaAesar) but when using other catalysts, the optimum Nafion content might be around another value. Results show, that the electrochemical performance improves with lower ionomer contents, but the reproducibility gets worse. An improved ink stability in combination with an improved spray coater setup or even other deposition technique is therefore an essential parameter to improve, to be able to fabricate reproducible anodic PTEs with lower Nafion contents. In addition, the choice of ionomer material changes the performance of the PTEs: Nafion was used, as it is a standard material in PEMWE. As the PEM is as well made of Nafion, the interface between ionomer in the catalyst layer as well as the PEM is expected to be optimized. There are however concerns on using Nafion due to the fluorine content and sustainable alternatives should be investigated. The optimum ionomer content could then as well differ from the results of this work.

**Reference CCM** - The reference CCM used in this work was not optimized via hot pressing or the adjustment of the Nafion content in the anodic catalyst layer, as a direct comparison to the anodic PTEs was desired. The overall performance of an optimized CCM with the anodic catalyst layer used in this work could therefore exhibit a much better performance. The interpretation of the data in this work was therefore limited to the direct comparison but not to an overall valid statement regarding the performance of an optimized CCM-configuration vs. an optimized PTE-configuration.

**Noble metal loading vs. ionomer content** - For the loading study, an ionomer content of 9 wt% was used as anodic PTEs with a loading of 1.4 mg cm<sup>-2</sup> showed the best reproducibility with this Nafion content in the Nafion study. However, when reducing the noble metal loading, ideally also the Nafion content should be reduced, as less catalyst particles need less ionomer to establish enough three-phase boundaries. The anodic PTEs with a higher or a lower loading could therefore perform probably better as shown in this work, with an individually adjusted Nafion content in the catalyst layers.

In summary, there is great room to further optimize and study anodic PTEs for PEMWE and ideally, the same studies should be performed for the cathode side as well, as so far commercial carbon and Pt/C based cathodic PTEs developed for PEMFC are used in PEMWE applications.

## 6 IrO<sub>2</sub> coated TiO<sub>2</sub> core-shell microparticles advance performance of low loading proton exchange membrane water electrolyzers \*

The work presented in this chapter was submitted in 2019 as full research paper with the author of this thesis being the joint first author together with Dr. Chuyen Pham. The author of this thesis contributed with MEA fabrication and characterization to the work and Dr. Chuyen Pham with the synthesis and characterization of the catalyst. The contributions to the sections discussed in this work are:

- Section 6.1 (introduction) contains minor contributions of the author of this thesis and was left as submitted
- Section 6.2 (synthesis and characterization of the IrO<sub>2</sub>@TiO<sub>2</sub> catalyst) was written by the author of this thesis based on the scientific data and images provided by Dr. Chuyen Pham. A more detailed description and analysis can be found in the submitted manuscript.
- Sections 6.3 and 6.4 (MEA preparation and characterization) were left as submitted and contain the major contribution of the author of this thesis to the work discussed in this chapter. FIB-SEM images and data of the ink-stability test were provided by co-authors of the submitted manuscript.
- Section 6.5 (summary and conclusion) was left as submitted and contains minor contributions of the author of this thesis
- Section 6.6 (supporting information) shows parts of the originally submitted supporting information as needed in the context of this thesis. Contributions are indicated.

In section 6.7 preliminary results of developing gradient sized CLs to further enhance the performance of anodic PTEs when e.g. applying the presented IrO<sub>2</sub>@TiO<sub>2</sub> catalyst are presented.

---

\*submitted manuscript (2019)

*Pham, C.\*\*, Bühler, M.\*\*, Knöppel, J., Bierling, M., Seeberger, D., Escalera-López, D., Mayrhofer, K. J. J., Cherevko, S., and Thiele, S., IrO<sub>2</sub> coated TiO<sub>2</sub> core-shell microparticles advance performance of low loading proton exchange membrane water electrolyzers*

\*\*joint first authorship

## 6.1 Introduction

Wind and solar energy technologies are increasingly important for a sustainable energy supply. However, both technologies suffer from intermittent natural supply, which makes energy storage e. g. in the form of a chemical fuel, such as hydrogen a necessity. Among water electrolysis technologies, proton exchange membrane water electrolyzers (PEMWEs) are expected to play an important role due to their ability for fast load change, high power and energy efficiency, and high gas purity.<sup>177</sup> Due to the sluggish kinetics of the oxygen evolution reaction (OER) and the corrosive operation conditions at the anode, so far only IrO<sub>2</sub> is known to be a suitable catalyst that meets the criteria of activity and stability for PEM OER catalysts.<sup>178</sup> However, the scarcity and high cost of this precious metal are challenges for sustainable development of PEMWEs. A development of alternative non-noble OER catalysts has only achieved limited successes so far.<sup>179–181</sup> Extensive research has been therefore devoted to improve the effectiveness of Ir based OER catalysts. The research activities so far can be categorized into two categories: enhanced intrinsic activity of the catalysts by material design on the one hand and by advanced electrode morphologies and cell configurations on the other hand. The intrinsic activity of OER catalysts has been dramatically improved over the last few years. One of the most active OER catalysts are mixed oxides of IrO<sub>2</sub> and RuO<sub>2</sub> with different Ir:Ru ratios (Ir<sub>x</sub>Ru<sub>1-x</sub>O<sub>2</sub>).<sup>182, 183</sup> As a result, high performing PEMWEs have been achieved even with low OER catalyst loadings (e.g. 0.2–0.5 mg cm<sup>-2</sup>).<sup>184–186</sup> By this way, the loading of precious Ir metal can be reduced. However, the stability of Ir<sub>x</sub>Ru<sub>1-x</sub>O<sub>2</sub> is still a concern due to the dissolution of the Ru component under typical operation conditions.<sup>187</sup>

At catalyst layer scale, using catalyst supports could largely enhance catalyst utilization<sup>188</sup> and improve the interfacial and structural stability of catalyst layers at low loadings.<sup>79</sup> However, again the highly corrosive conditions of the PEMWE anode restrict the support selection. Several candidates have been tested as supports for OER catalysts, including NbO<sub>2</sub>,<sup>189</sup> antimony doped tin oxide (ATO),<sup>190</sup> fluorine doped tin oxide (FTO),<sup>191</sup> TaC,<sup>134</sup> doped TiO<sub>2</sub>,<sup>192</sup> TiN,<sup>193</sup> Ti metal,<sup>188</sup> and TiO<sub>2</sub>.<sup>87</sup> Of those, TiO<sub>2</sub><sup>87</sup> and FTO<sup>191</sup> are promising due to their stability. Millet et al. reported the application of micrometer sized Ti metal particles as support for IrO<sub>2</sub> catalysts by physically mixing the two components.<sup>188</sup> This strategy improved the dispersion of IrO<sub>2</sub> within the anodes, leading to an unprecedented high catalyst utilization, and allowed achieving 1 A cm<sup>-2</sup> at 1.73 V with low catalyst loadings of 0.12 mg<sub>Ir</sub> cm<sup>-2</sup> on the anode. This demonstrated the necessity of catalyst support for reducing Iridium loading. Still, Ti metal micro particles might be oxidized gradually in electrolysis working conditions, increasing the internal electrical resistance of the anode. In spite of low conductivity of TiO<sub>2</sub>, catalysts using TiO<sub>2</sub> support exhibit good performance.<sup>87, 189</sup> TiO<sub>2</sub> is thus a promising OER catalyst support for large scale application, given its high stability, low cost, abundance, and a mature production industry. The electrical interaction between oxide support and IrO<sub>2</sub> could improve the stability of supported catalysts<sup>194</sup> and even, according to some reports, enhance intrinsic activity of IrO<sub>2</sub>.<sup>195</sup> Mazur et al.<sup>129</sup> studied the use of IrO<sub>2</sub>/TiO<sub>2</sub> supported catalyst, synthesized by a modified Adam fusion method, and found an enhanced performance compared to unsupported IrO<sub>2</sub> catalyst. Bernt et al. extensively optimized catalyst layers of IrO<sub>2</sub>/TiO<sub>2</sub> supported catalyst (Umicore), targeting a maximal catalyst utilization to reduce the Ir loading.<sup>189</sup> The study found that with this catalyst, the optimal Ir loading is in the range of 1–2 mg cm<sup>-2</sup> to obtain optimal overall performances. At loadings lower than 0.5 mg<sub>Ir</sub> cm<sup>-2</sup>, the catalyst layers were too thin and structurally not a homogeneous layer anymore. Generally, due to the low conductivity of the TiO<sub>2</sub> support, large amounts of IrO<sub>2</sub> catalyst are needed to form an electrically percolating structure.<sup>87, 129</sup> The authors suggested that a core-shell design of IrO<sub>2</sub>/TiO<sub>2</sub> could increase the IrO<sub>2</sub> utilization, maximizing the IrO<sub>2</sub> dispersion the catalyst layer.

Elsewhere, core-shell catalysts with non-noble metal cores of such as Ni or Sr, and IrO<sub>2</sub> rich shells have been developed, allowing high precious metal utilizations.<sup>196–198</sup> Unfortunately, in these approaches only a portion of the Ir core was replaced with Ni or Sr, moreover Ni and Sr are likely dissolved in acidic solution during operation.<sup>199</sup> So far, core-shell structured catalysts with a core of stable nonprecious metals and a nanoscale-thin shell of high crystalline IrO<sub>2</sub> have not been realized due to catalyst - metal oxide support interaction leading to the disturbance of crystal structure of the IrO<sub>2</sub> shells.<sup>200</sup> In this context, we introduce an approach that combines an advanced structural IrO<sub>2</sub> catalyst with a porous transport electrode (PTE) configuration to form a catalyst layer with optimal IrO<sub>2</sub> catalyst dispersion. The catalyst consists of IrO<sub>2</sub> coated TiO<sub>2</sub> core-shell microparticles (IrO<sub>2</sub>@TiO<sub>2</sub>) with 50 wt% of IrO<sub>2</sub> synthesized by a facile method. To form a catalyst layer, IrO<sub>2</sub>@TiO<sub>2</sub> microparticles were directly deposited on a titanium porous transport layer (PTL). This allowed an optimal electrical contact of IrO<sub>2</sub>@TiO<sub>2</sub> microparticles with the large pore sized titanium PTL current collector. As a result, PEMWEs with an anodic catalyst loading of 0.4 mg<sub>Ir</sub> cm<sup>-2</sup>, using the IrO<sub>2</sub>@TiO<sub>2</sub> catalyst, achieved 1 A cm<sup>-2</sup> at 1.67 V, outperforming both unsupported and supported commercial catalysts from Alfa Aesar and Umicore, respectively. Despite relatively low Ir loading, this performance is amongst the best reported in literature.<sup>79, 188</sup>

## 6.2 Synthesis and characterization of the IrO<sub>2</sub>@TiO<sub>2</sub> catalyst

The advantage of the synthesis method of the core-shell catalyst presented in this work is the 100 % yield of the precursors TiO<sub>2</sub> (Sigma Aldrich, rutile, < 5 µm) and H<sub>2</sub>IrCl<sub>6</sub>·4H<sub>2</sub>O (VWR, 99 % metal basis). To reach this maximum yield, the surface charge of the TiO<sub>2</sub> support particles was first modified from negative to positive by reducing the pH-value with acetic acid (Fig. 41 a-b). The negatively charged [IrCl<sub>6</sub>]<sup>2-</sup> anions of the precursor were then able to attach to the surface of the modified TiO<sub>2</sub>-particles (Fig. 41 c). The Zeta-potential (measured by using Malvern Panalytical) shown in Fig. 41 is a measure for the surface charge dependent on the pH-value of the reaction solution. The reaction solution was stirred at 100 °C to dry out the solvents (Fig. 41 d). Via pyrolysis, the attached H<sub>2</sub>IrCl<sub>6</sub> shell was transformed into IrO<sub>2</sub> in a tubular furnace heated up to 500 °C in the presence of air (Fig. 41 e). The final IrO<sub>2</sub>@TiO<sub>2</sub> powder was homogeneously grinded and comprised of 50 wt% TiO<sub>2</sub> and 50 wt% IrO<sub>2</sub>.

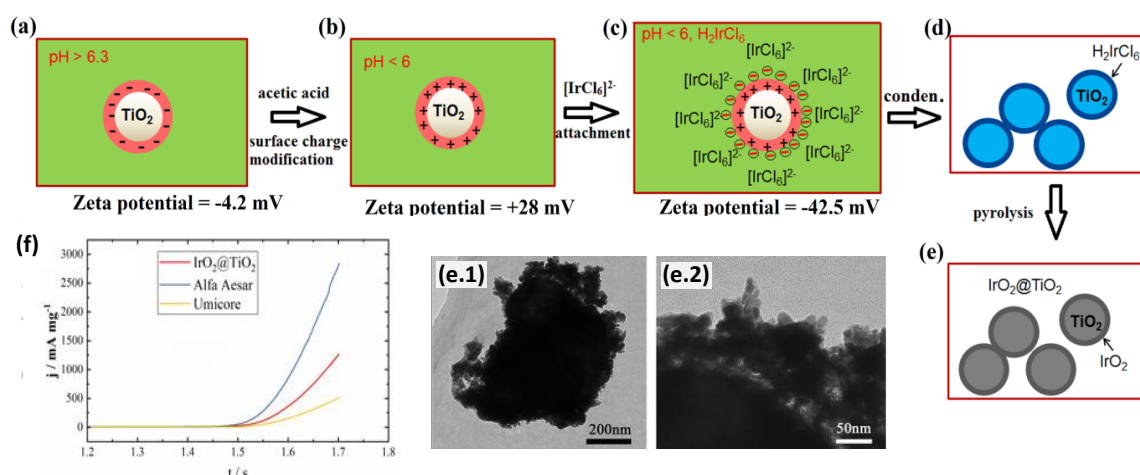


**Fig. 41** Schematic illustration of the synthesis process of the IrO<sub>2</sub>@TiO<sub>2</sub> catalyst. The Zeta potential of TiO<sub>2</sub> particles in the reaction solution shows the change from negative to positive surface charges when reducing the pH-value of the solution (a,b). By this, the negatively charged [IrCl<sub>6</sub>]<sup>2-</sup> anions attach to the surface of the TiO<sub>2</sub>-particles (c) and the solvents can be evaporated (d). A pyrolysis step transforms the H<sub>2</sub>IrCl<sub>6</sub> shell into IrO<sub>2</sub> (e). TEM images (e.1 and e.2) show the complete coverage of the TiO<sub>2</sub>-core with a porous IrO<sub>2</sub>-shell. The activity of the core-shell catalyst is higher than of the commercial IrO<sub>2</sub>/TiO<sub>2</sub> catalyst from Umicore (f).

TEM images (Talos L120C (FEI)) show the  $\text{TiO}_2$ -cores fully covered by a porous  $\text{IrO}_2$ -shell (Fig. 41 e.1 and e.2). The core-shell particles show a high distribution of the  $\text{IrO}_2$ -catalyst and an improved ink stability for spray coating when compared to mixed  $\text{IrO}_2+\text{TiO}_2$  catalyst powder. The activity of the synthesized powder was compared to a commercial unsupported  $\text{IrO}_2$ -catalyst (AlfaAesar, type Premion) and a commercial supported  $\text{IrO}_2/\text{TiO}_2$  catalyst (Umicore, type Elyst 75 % Ir). Measurements were performed in a three electrode scanning flow cell (SFC) setup.<sup>199</sup> The activity of the unsupported  $\text{IrO}_2$  catalyst (AlfaAesar) was the highest with  $279 \text{ mA mg}_{\text{Ir}}^{-1}$  at 1.55 V (vs. RHE) in a 0.1 M  $\text{HClO}_4$  solution. The commercial supported catalyst (Umicore) showed the lowest activity with  $47 \text{ mA mg}_{\text{Ir}}^{-1}$  at the same potential. The in-house synthesized core-shell catalyst ( $\text{IrO}_2@\text{TiO}_2$ ) revealed an activity in between the two commercial catalysts of  $112 \text{ mA mg}_{\text{Ir}}^{-1}$  at 1.55 V.

## 6.3 MEA preparation and characterization

### 6.3.1 Catalyst inks: preparation and stability test

The goal of this work was to evaluate the potential of the novel in-house synthesized  $\text{IrO}_2@\text{TiO}_2$  catalyst for PEMWE. To be able to compare the influence of microstructure and membrane electrode assembly (MEA) performance with other benchmark catalyst powders, the fabrication (catalyst ink mixing and spray parameters) and catalyst layer composition (Nafion content, noble metal loading) of the PTE catalyst layers were kept as close as possible. An individual optimization of all the process parameters for every different catalyst material for ultrasonic spray coating was beyond the scope of this work. The  $\text{IrO}_2$  catalyst layer was studied extensively in our previous work and was optimized regarding reproducibility and performance.<sup>2</sup>

Three different catalyst powders were used to form the porous transport electrode: the in the current work synthesized  $\text{IrO}_2@\text{TiO}_2$  particles as well as two commercially available catalyst materials for the oxygen evolution reaction. These were 75 wt% Ir supported on  $\text{TiO}_2$  ( $\text{IrO}_2/\text{TiO}_2$ , Umicore) and unsupported  $\text{IrO}_2$  (Premion, Alfa Aesar). The solvents for the  $\text{IrO}_2/\text{TiO}_2$  and  $\text{IrO}_2$  ink were DI-water and IPA (1:1). For the  $\text{IrO}_2@\text{TiO}_2$  ink, DI-water and methanol were used in a 1:3 ratio, since using IPA instead of methanol resulted in a less homogeneous catalyst ink mixture. All catalyst inks contained 1 wt% solids, which consisted of 99 wt% catalyst material and 1 wt% Nafion (D520, FuelCellStore). The catalyst powder was weighted in a glass bottle prior to adding the solvents and finally Nafion. After adding a new component, the ink was stirred for a short time. After all components were added, the ink was continuously stirred overnight after an additional 30 min mixing step using an ultrasonic tip (Hielscher UIS250L, 90 % amplitude, continuous mode, 0.55 W). The bottle was placed in an ice bath during ultrasonication and stirred continuously. After being stirred overnight, the ultrasonication step was repeated prior to spray coating.

Besides comparing the  $\text{IrO}_2@\text{TiO}_2$  catalyst with the  $\text{IrO}_2$  and  $\text{IrO}_2/\text{TiO}_2$  catalyst, a fourth catalyst ink with just mixing the same  $\text{IrO}_2$  and  $\text{TiO}_2$  particles ( $\text{IrO}_2+\text{TiO}_2$ ) which were used to synthesize the  $\text{IrO}_2@\text{TiO}_2$  particles was prepared for spray coating. A stable dispersion of catalyst particles in a matrix of solvents and Nafion was required to prevent particle precipitation in the long tubing of the spray coater, when the ink was pumped from syringe reservoir towards the ultrasonic nozzle. Since the  $\text{IrO}_2+\text{TiO}_2$  ink showed insufficient ink stability due to particle precipitation already during ink preparation, no PTE and subsequently MEA could be fabricated with that catalyst. To quantify the unstable character of the  $\text{IrO}_2+\text{TiO}_2$  based ink, a turbiscan stability index (TSI) measurement was performed. The prepared  $\text{IrO}_2@\text{TiO}_2$  and  $\text{IrO}_2+\text{TiO}_2$  inks were transferred to glass vials (length = 45 mm) and placed in the measurement chambers of a Turbiscan Tower (Formulation,

France). The temperature in the chambers was set to 25 °C. After an equilibration time of 5 min, the transmission and backscattering signals of the luminescent diode ( $\lambda_{\text{Air}} = 880 \text{ nm}$ ) were collected at an angle of 180° and 45°, respectively. The signals were collected over the full length of the sample, acquiring transmission and backscattering data every 40  $\mu\text{m}$ . Scans were taken over a course of 24 h. After the first measurement, the samples were scanned every 20 minutes during the first 2 h, every hour the following 10 hours and every 2 hours during the last 12 hours. The transmission and backscattering data was recorded by the device software, in the range from the bottom of the vial to the meniscus of the ink.

### 6.3.2 Fabrication of porous transport electrodes

To prepare the porous transport electrodes, the catalyst inks containing  $\text{IrO}_2/\text{TiO}_2$ ,  $\text{IrO}_2@\text{TiO}_2$  and unsupported commercial  $\text{IrO}_2$  were spray coated on top of 4  $\text{cm}^2$  fiber sintered titanium substrates (Bekaert, 1 mm thick, 57 % porosity) using an Exacta Coat (Sono-Tek) ultrasonic spray coater. The titanium substrates were placed on a hot plate set to 120 °C. An ultrasonic nozzle of the type AccuMist™ (48 kHz) was used. A meander shaped pattern (pitch of 1.5 mm) was sprayed at a speed of 170  $\text{mm s}^{-1}$ , a flow rate of 0.45  $\text{ml min}^{-1}$  and the ultrasonic powder of the nozzle set to 5 W. The height of the nozzle was 37 mm and the shaping air was set to 0.6 kPa. The noble metal loading was controlled several times during spray coating via weighing a 1  $\text{cm}^2$  reference metal sheet on a microscale (Sartorius ME 36S) which was spray-coated in parallel to the titanium substrates. The syringe of the spray coater was not fully filled with the ink to prevent particle sedimentation during spray coating. The way of refilling the syringe more often whilst stirring the bigger part of the ink on a separate magnetic stirrer, led to more homogeneous spray patterns due to a stable smaller portion of the ink in the syringe of the spray coater. An additional magnetic stirrer in the syringe helped to keep the ink homogeneous.

Since still some precipitation of catalyst material was observed in the syringe of the spray-coater, the final Nafion vs. noble metal ratio in the catalyst layers was measured by a thermogravimetric analysis (TGA, Netsch STA 449F5) of the sprayed catalyst layer was performed and revealed an actual Nafion content of around 5 wt%. For TGA, the Nafion part in the sprayed catalyst layer was burned according to Feng et al.<sup>148</sup> under air atmosphere to analyze the loss of weight. The heating rate was 5  $\text{K min}^{-1}$  up to a temperature of 1000 °C, which was held for one hour. Due to the discrepancy between ‘as mixed’ and final catalyst layer, we suggest TGA analysis as a tool for controlling the results of the spray-coating procedure.

### 6.3.3 Structural characterization of porous transport electrodes

The surface and cross-sections of the different porous transport electrodes were studied with a focused ion beam (FIB) SEM (Zeiss Crossbeam 540 with GEMINI II). By this method the homogeneity and porosity of the deposited catalyst layers were studied to explain influences on the polarization behavior. The interfacial area between titanium fibers and catalyst layer was analyzed to explain possible influences on the electrical resistance.

### 6.3.4 MEA testing

For PEMWE cell tests, the fabricated porous transport electrodes were pressed against a Nafion N212 membrane (FuelCellStore) and a carbon cloth based gas diffusion electrode (0.5  $\text{mg cm}^{-2}$  (60 %) Pt/C (SL-GDE, FuelCellsEtc). The test-cell was designed in-house and consisted basically of the MEA sandwiched between two titanium flow fields, two copper plates for the electrical connection towards the potentiostat and two aluminium end plates to fix the inner cell parts. The test cell was tightened with 8 screws at 8.5 Nm. Two heating elements inserted in the end plates were set to 80 °C. The titanium flow fields were designed with a parallel finger structure. The

porous transport electrodes at the anode side were placed in a 1 mm thick PTFE frame, the cathode electrode was placed in a 150  $\mu\text{m}$  thick PTFE frame. The PTFE frames were used to set the compression level of the porous supports of the electrodes. The titanium material was not significantly compressed, but the thickness of the carbon cloth based cathode was reduced by almost 40 %. The test cell was connected to a peristaltic pump (Ismatec IP 65) which supported both the anode and cathode separately with DI-water at a flow rate of 40  $\text{ml min}^{-1}$ . The tubing at the inlets of the test cell were immersed in a water bath (Lauda Ecoline 003, 88  $^{\circ}\text{C}$ ) to pre-heat the inflowing water and therefore prevent temperature gradients within the cell. Two in-line temperature sensors in the tubing at the in- and outlet of the anode side, as well as one temperature probe inserted in the flow field were assembled. After a stable temperature of 80  $^{\circ}\text{C}$  was observed at all temperature sensors, the conditioning of the MEA was started with a potentiostat type 857 from Scribner: the voltage was varied for 15 times from 1.4 V – 2.2 V in 200 mV steps (30 s per step). Afterwards, a polarization curve was recorded via controlling the current density. Every step was held for 120 s and started in a range of 0 A – 40 mA in 10 mA steps. When proceeding to higher current densities, the step size was increased to 50 mA in the range of 50 mA-1 A and to a step size of 250 mA between 1.25 A and 3 A. From 3.5 A-6 A the step size was 500 mA. Above 7 A, the step size was increased to 1 A. The frequency to measure the high frequency resistance (HFR) was 1 kHz.

The polarization curves were analyzed according to the contributions of the kinetic overpotential at low current densities, ohmic losses at moderate current densities towards mass transport losses when high current densities were applied.<sup>141</sup> To study differences in the reproducibility of different types of porous transport electrodes, the average cell voltage and standard deviation was calculated for the three samples tested per configuration.

## 6.4 Results: MEA preparation and characterization

### 6.4.1 Catalyst inks: preparation and stability test

As the stability of the catalyst ink is a crucial parameter for the application of spray coating and other MEA manufacturing techniques, we examined the stability of our ink formula for  $\text{IrO}_2@\text{TiO}_2$  compared to an ink with mixed  $\text{TiO}_2+\text{IrO}_2$  powders. Both inks contained 1 wt% solids mixed with methanol and water (3:1 vol. ratio). The solid content was the sum of 1 wt% Nafion and 99 wt% metal powder. The stability was studied by measuring the effect of ink destabilization on backscattering signal intensity. In general, a drop of backscattering intensity indicates instability of the tested ink. The results in Fig. 42 a show that the backscattering intensity of  $\text{IrO}_2@\text{TiO}_2$  ink dropped by only < 2 % during 2.5 h aging, which is ten-fold less than that of the ink with the same ink formula but using mixed  $\text{IrO}_2+\text{TiO}_2$  particles (> 10 %). As such, the results demonstrated that the  $\text{IrO}_2@\text{TiO}_2$  ink was stable, while ( $\text{IrO}_2+\text{TiO}_2$ ) ink was unstable. This result was also corroborated in digital images (Fig. 42 b), in which the white colour of  $\text{TiO}_2$  was observed at the bottom of the test vial of the ( $\text{IrO}_2+\text{TiO}_2$ ) ink, while it was absent for the  $\text{IrO}_2@\text{TiO}_2$  ink.

The stability of  $\text{IrO}_2@\text{TiO}_2$  ink can be explained by surface covering of  $\text{IrO}_2$  over  $\text{TiO}_2$  particle, which changes the surface properties of the received  $\text{IrO}_2@\text{TiO}_2$  core-shell particles. At the same conditions, the bare  $\text{TiO}_2$  particles were demonstrated to be unstable in suspension. Therefore, it was not practically feasible to use the catalyst ink with physically-mixed  $\text{IrO}_2$  and  $\text{TiO}_2$  to fabricate spray coated anodes. To our knowledge, the stability of the  $\text{TiO}_2+\text{IrO}_2$  mix based inks was not investigated before but is an important factor for future catalyst development: an unstable ink with its corresponding catalyst will not make it into the device.



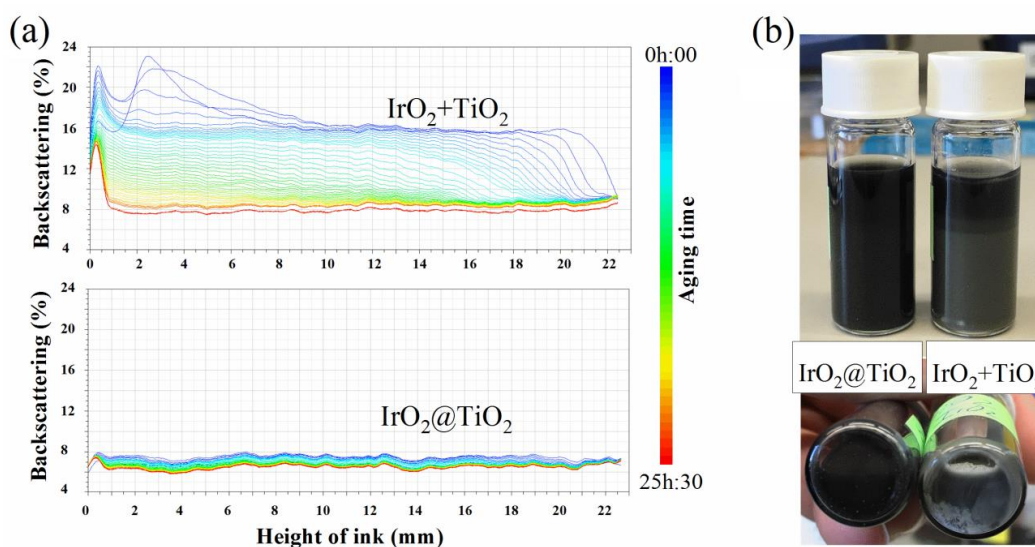


**Fig. 42** Ink stability study for  $\text{IrO}_2@ \text{TiO}_2$  in comparison with an ink made by physically mixed  $\text{IrO}_2 + \text{TiO}_2$  in the same conditions. (a) Evolution of backscattering spectra of the  $\text{IrO}_2@ \text{TiO}_2$  ink and the reference  $\text{IrO}_2 + \text{TiO}_2$  ink upon aging time. (b) Digital images of two compared inks, which were taken prior to stability test.  $\text{IrO}_2@ \text{TiO}_2$  ink remained homogenous, while the  $\text{IrO}_2 + \text{TiO}_2$  ink segregated into two layers due to the precipitation of  $\text{TiO}_2$  particles onto bottom of the vial.

Due to the insufficient stability for spray coating with the device used in this work, no MEAs were fabricated using the mixed  $\text{IrO}_2 + \text{TiO}_2$  catalyst ink. In former works from Rozain et al.<sup>188</sup> it was claimed that pure Ti particles were mechanically mixed with an  $\text{IrO}_2$  catalyst powder. As the Ti powder however is exposed to air, there will be at least a small oxide layer forming on the Ti particles and the oxide layer will dominate the surface chemistry and physics of the particles when mixed into the solution of a catalyst ink. In our investigation the catalyst ink with the mixed  $\text{IrO}_2 + \text{TiO}_2$  catalyst ink like shown in Fig. 42 undergoes sedimentation. Consequently, when aiming towards preparing large area electrodes with sizes of up to  $1 \text{ m}^2$ , homogeneous deposition of the electrode and thus reproducibility cannot be ensured with  $\text{IrO}_2 + \text{TiO}_2$  type catalyst systems. Therefore, the following structural characterization and MEA testing was performed on PTEs prepared with the  $\text{IrO}_2@ \text{TiO}_2$  catalyst, the unsupported  $\text{IrO}_2$  and the supported  $\text{IrO}_2/\text{TiO}_2$  catalyst.

#### 6.4.2 Structural characterization of porous transport electrodes

A structural analysis of the cross-section of the different types of porous transport electrodes is shown in Fig. 43. The catalyst layers contained  $1.2 \text{ mg}_{\text{Ir}} \text{ cm}^{-2}$  for the  $\text{IrO}_2@ \text{TiO}_2$  and unsupported  $\text{IrO}_2$  catalysts, and  $1.4 \text{ mg}_{\text{Ir}} \text{ cm}^{-2}$  for  $\text{IrO}_2/\text{TiO}_2$  (Umicore) and 5 wt% Nafion. By the decision to take the same Nafion content and spray parameters for all different catalyst layers, the performance of the different MEAs, with respect to e.g. changes of the microstructure, was directly comparable.

The reference PTE made of commercial unsupported  $\text{IrO}_2$  catalyst (Premion, Alfa Aesar) showed a good porosity and a homogeneous catalyst layer (Fig. 43 a). When using the micrometer scale  $\text{IrO}_2@ \text{TiO}_2$  catalyst particles, the structure of the catalyst layer was clearly altered (Fig. 43 b). The relatively large  $\text{TiO}_2$  cores in the range of 500 nm led to a different distribution of  $\text{IrO}_2$  catalyst material within the catalyst layer compared to the unsupported  $\text{IrO}_2$  catalyst. An EDX analysis of the  $\text{IrO}_2@ \text{TiO}_2$  catalyst layer (Fig. 46 and Fig. 47) showed the consistency of the catalyst composition with the material characterization (Fig. 48). The supported  $\text{IrO}_2/\text{TiO}_2$  catalyst (Umicore) (Fig. 43 c) showed particle sizes in the size range of the unsupported  $\text{IrO}_2$  catalyst which

was approximately 100 nm. Therefore, the  $\text{TiO}_2$  particles were much smaller compared to the  $\text{TiO}_2$  cores used to prepare the  $\text{IrO}_2@\text{TiO}_2$  catalyst.

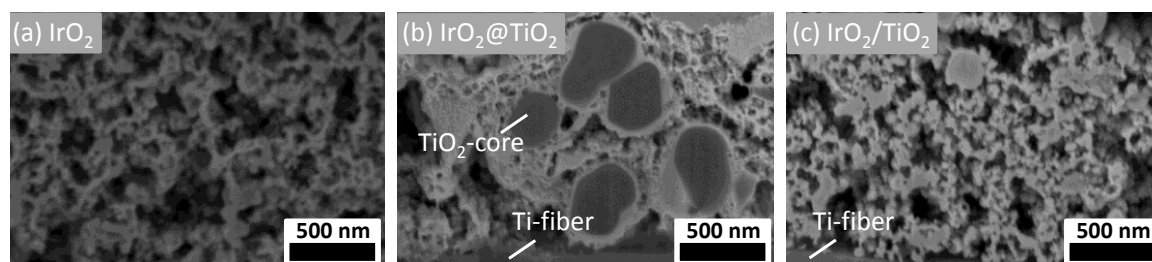


**Fig. 43** FIB/SEM cross-sections of the anodic catalyst layers deposited on titanium based porous transport layers (PTLs) containing 5 wt% Nafion and three different  $\text{IrO}_2$  based catalysts. (a) Unsupported  $\text{IrO}_2$  Premion powder from Alfa Aesar; (b)  $\text{IrO}_2@\text{TiO}_2$  catalyst. (c)  $\text{IrO}_2/\text{TiO}_2$  supported catalyst from Umicore. The Pt-pad was deposited for assisting FIB/SEM analysis.

According to the fabrication procedure, more layers of the supported catalysts have to be sprayed to reach the same overall loading as when the unsupported  $\text{IrO}_2$  powder is used. Therefore, the average thickness of the catalyst layers increased with an increasing wt% of  $\text{TiO}_2$  in the supported catalyst powder. The volume of the catalyst layer is additionally increasing with an increasing particle size of the  $\text{TiO}_2$  support. The  $\text{IrO}_2@\text{TiO}_2$  catalyst layer has the in comparison biggest particle size and highest wt% of the  $\text{TiO}_2$  support and is therefore thicker, than the  $\text{IrO}_2$  and  $\text{IrO}_2/\text{TiO}_2$  based catalyst layer. The increased thickness of the  $\text{IrO}_2@\text{TiO}_2$  catalyst layer was supposed to have an influence on mass transport properties. Also, the  $\text{TiO}_2$  was supposed to improve the mechanical stability of the catalyst layer. Conventional catalyst layers with loading  $< 0.5 \text{ mg cm}^{-2}$  are often too thin, leading to mechanical instability when assembling in the PEMWE cell and an inefficient electrical contact with current collector as pointed out by Bernt et al.<sup>79</sup> The average thickness of the catalyst layers fabricated in this work was however not trivial to analyze due to the rough surface of the PTEs (Fig. 49). A difference of several  $\mu\text{m}$  in local catalyst layer thickness made a direct comparison between the three different PTEs via the method of cross-sectional FIB-SEM analysis inaccurate and time consuming.

### 6.4.3 MEA testing

The MEAs used for electrochemical testing were made of a Nafion 212 membrane sandwiched between a PTE anode and Pt/C based cathode. To assess the reproducibility, three samples were prepared and tested for every type of PTE. Each curve shown in Fig. 44 is plotted using the average data of the three samples for each PTE type cell with the standard deviation included.

When analyzing the polarization curves (Fig. 44 a), all PTEs showed a very good reproducibility, as the standard deviation of all polarization curves was in the range of 0.2 %. The  $\text{IrO}_2@\text{TiO}_2$  catalyst showed a superior performance compared to the unsupported  $\text{IrO}_2$  and supported  $\text{IrO}_2/\text{TiO}_2$  catalyst, which even had a  $0.2 \text{ mg}_{\text{Ir}} \text{ cm}^{-2}$  higher Ir-loading. The HFR-free cell voltage (Fig. 44 b) was similar for the  $\text{IrO}_2$  and  $\text{IrO}_2@\text{TiO}_2$ -based PTEs of ca. 1.6 V at  $2 \text{ A cm}^{-2}$ , but a ca. 40 mV higher overpotential for the supported  $\text{IrO}_2/\text{TiO}_2$  catalyst was measured at the same current density. Due to no significant differences in the slopes of the HFR-free curves, differences in mass transport were rather small despite different catalyst layer thicknesses when using supported catalysts compared to unsupported  $\text{IrO}_2$  powder. The presence of  $\text{TiO}_2$  particles had in general a positive impact on reducing the HFR (Fig. 44 c), which was almost  $37 \text{ m}\Omega \text{ cm}^2$  higher at  $2 \text{ A cm}^{-2}$  for the unsupported  $\text{IrO}_2$  catalyst. A possible reason for the decreased HFR when  $\text{TiO}_2$  was added to the catalyst layer might be an increased percolation of  $\text{IrO}_2$  particles compared to the unsupported case.

Also, the wider the IrO<sub>2</sub> network, the more direct contact points within the titanium PTL can be established and the more electrical pathways via the IrO<sub>2</sub> network are present. Rozain et al. analyzed the influences of adding conductive micro-sized Ti-particles to an IrO<sub>2</sub>-based catalyst layer in a CCM.<sup>188</sup> Due to the high electrical conductivity of the Ti-support, not only a structural effect regarding the dispersion of IrO<sub>2</sub> particles was beneficial for the performance, but also the additional Ti-network within the catalyst layer distributing the electrical current from the PTL deep into the catalyst layer. An improved electrical resistance due to the material of the support itself is most probably not the case for the PTEs in this work, since less conductive TiO<sub>2</sub> particles were used and not Ti metal-powder.

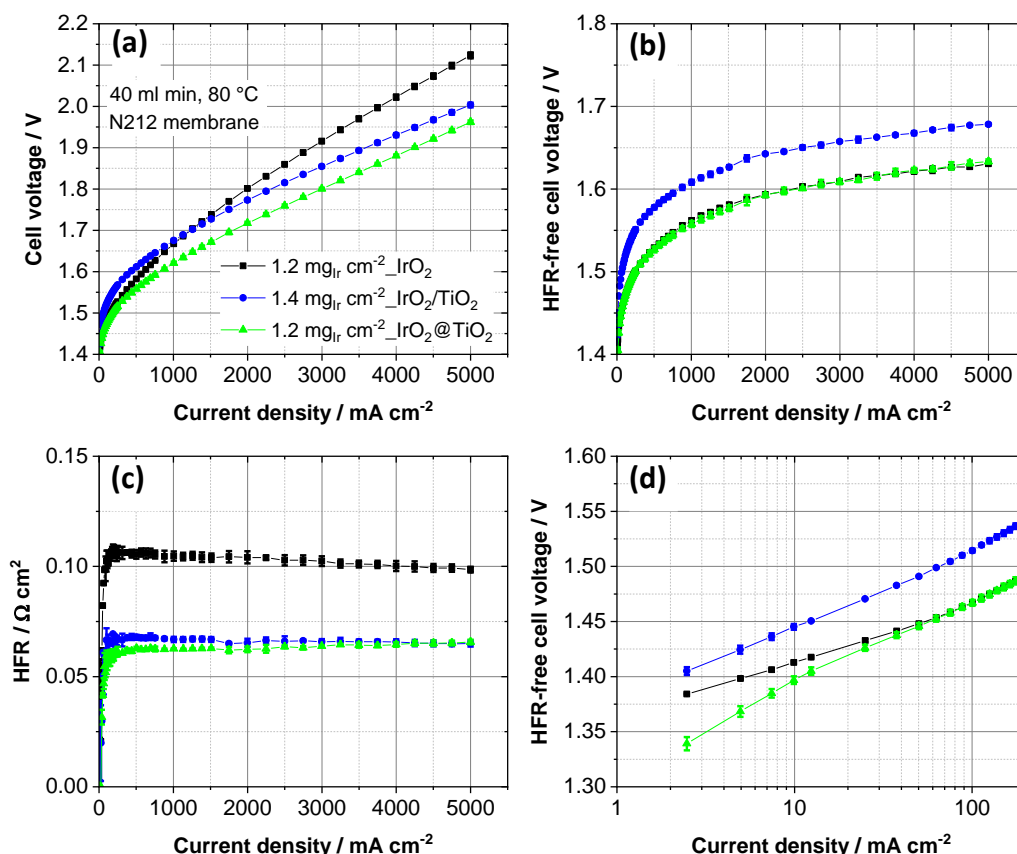


**Fig. 44** Full-cell characterizations of the IrO<sub>2</sub>@TiO<sub>2</sub> catalyst in comparison with commercial reference catalysts. (a) Polarization curves of PEMWE cells using IrO<sub>2</sub>@TiO<sub>2</sub> catalysts, unsupported IrO<sub>2</sub> (Alfa Aesar), and IrO<sub>2</sub>/TiO<sub>2</sub> (Umicore). Catalyst loadings are 1.2 mg<sub>Ir</sub> cm<sup>-2</sup> for IrO<sub>2</sub>@TiO<sub>2</sub> and unsupported IrO<sub>2</sub> (Alfa Aesar) catalysts, and 1.4 mg<sub>Ir</sub> cm<sup>-2</sup> for IrO<sub>2</sub>/TiO<sub>2</sub>; Nafion 212 membranes with thicknesses of 50.8 μm were used for all cells. (b) HFR-free cell voltage. (c) HFRs of the different PTE. (d) Kinetic region of the HFR-free cell voltages.

A magnification of the kinetic region of the HFR-free cell voltage (Fig. 44 d) revealed the reason for the worse HFR-free cell voltage of the IrO<sub>2</sub>/TiO<sub>2</sub> catalyst despite a similar mass transport overpotential. The IrO<sub>2</sub>/TiO<sub>2</sub> catalyst showed a significantly worse activity on the cell level compared to the other catalyst systems. The activity of the IrO<sub>2</sub>@TiO<sub>2</sub> catalyst was even slightly better than that of the unsupported, pure IrO<sub>2</sub>. This is a surprising result, since half-cell measurements (Fig. 50 a) showed the unsupported IrO<sub>2</sub> catalyst being most active for the OER. The use of bigger TiO<sub>2</sub> particles in the case of the IrO<sub>2</sub>@TiO<sub>2</sub> (Fig. 43 b) compared to the smaller particles in the IrO<sub>2</sub>/TiO<sub>2</sub> catalyst (Fig. 43 c) seemed to increase the accessible catalyst surface area and therefore the iridium catalyst utilization.

The combination of both a low HFR and high activity was the reason for the superior performance of the  $\text{IrO}_2@\text{TiO}_2$  based PTE configuration compared to the pure  $\text{IrO}_2$  and  $\text{IrO}_2/\text{TiO}_2$  based MEAs. These results demonstrate that the intrinsic catalyst activity showed in half-cell measurement is not always consistent with its performance at full-cell level due to the catalyst morphology incompatible with device configurations. In this case we suggest the evaluation of novel catalyst materials for a first screening in half-cell tests but then in a full-cell tester to state the final usability for PEMWE application.

Due to the need of reducing the overall noble metal content used in PEMWE applications, the goal of electrode fabrication in this section was to test the applicability of the novel  $\text{IrO}_2@\text{TiO}_2$  catalyst for low loadings. The aims were first, to fabricate a homogeneous catalyst layer and second to determine the reproducibility and sufficient performance of the MEAs when tested in a full-cell. Due to the worse overall performance of the unsupported  $\text{IrO}_2$  catalyst already at higher loadings, only the two supported catalyst materials were further investigated. The Ir loading was  $0.4 \text{ mg}_{\text{Ir}} \text{ cm}^{-2}$  for the  $\text{IrO}_2@\text{TiO}_2$  and  $0.5 \text{ mg}_{\text{Ir}} \text{ cm}^{-2}$  for  $\text{IrO}_2/\text{TiO}_2$  (Umicore). The Nafion content in the catalyst layers was again constant at 5 wt%. The configurations with lower loadings were tested two times (Fig. 45).

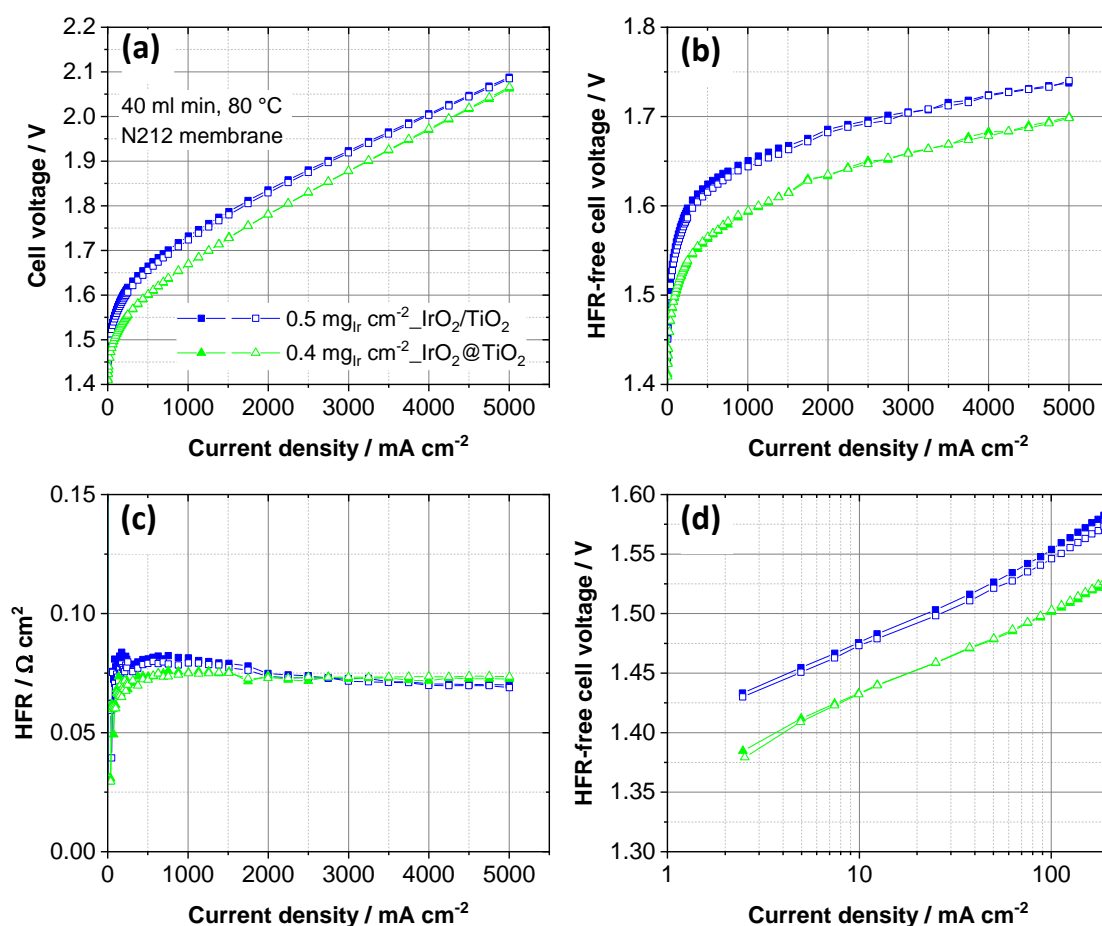


**Fig. 45** PEMWE performance at reduced catalyst loadings. (a) Polarization curves of PEMWE using  $\text{IrO}_2@\text{TiO}_2$  catalysts in comparison to the  $\text{IrO}_2/\text{TiO}_2$ . Catalyst loadings were  $0.4 \text{ mg}_{\text{Ir}} \text{ cm}^{-2}$  for  $\text{IrO}_2@\text{TiO}_2$  and  $0.5 \text{ mg}_{\text{Ir}} \text{ cm}^{-2}$  for  $\text{IrO}_2/\text{TiO}_2$ . A Nafion 212 membrane with a thickness of  $50.8 \mu\text{m}$  was used. (b) HFR-free cell voltage. (c) HFR of the different PTEs (d) Kinetic region of the HFR-free cell voltage.

The  $\text{IrO}_2@\text{TiO}_2$  catalyst did also perform significantly better than the  $\text{IrO}_2/\text{TiO}_2$  catalyst at low Ir-loadings (Fig. 45 a). When comparing the polarization behavior of the PTEs in this work, the higher

performance of the low loading  $0.4 \text{ mg}_{\text{Ir}} \text{ cm}^{-2} \text{ IrO}_2\text{@TiO}_2$  PTE was obvious. The same parameters for spray coating were used for all three catalysts. At a current density of  $1 \text{ A cm}^{-2}$ , a cell voltage of 1.67 V for the  $0.4 \text{ mg}_{\text{Ir}} \text{ cm}^{-2} \text{ IrO}_2\text{@TiO}_2$  PTE, and 1.72 V for  $0.5 \text{ mg}_{\text{Ir}} \text{ cm}^{-2} \text{ IrO}_2/\text{TiO}_2$  PTE, were measured, respectively. The unsupported  $\text{IrO}_2$  and  $\text{IrO}_2/\text{TiO}_2$  based PTEs required a loading of  $1.2 \text{ mg}_{\text{Ir}} \text{ cm}^{-2}$  and  $1.4 \text{ mg}_{\text{Ir}} \text{ cm}^{-2}$ , respectively, for achieving similar performances as the low loading  $\text{IrO}_2\text{@TiO}_2$  PTE (Fig. 51). The HFR-free cell voltage (Fig. 45 b) showed no significant differences in the slopes of the curves indicating as for the higher loadings (Fig. 44 b), a similar mass transport behavior. The  $\text{IrO}_2\text{@TiO}_2$ -based PTE showed an almost stable HFR of ca.  $75 \text{ m}\Omega \text{ cm}^2$  (Fig. 45 c). The HFR of the  $\text{IrO}_2/\text{TiO}_2$ -based PTE however decreased when approaching to higher current densities. Starting with an initially higher HFR than for the  $\text{IrO}_2\text{@TiO}_2$ -based PTE, the  $\text{IrO}_2/\text{TiO}_2$  samples showed lower HFRs above  $3 \text{ A cm}^{-2}$ . This trend of the decreasing HFR with current density was already present at higher loadings (Fig. 44 c) and might be the reason for the smaller difference in cell voltage when approaching higher current densities. Comparing the HFR of the low loading PTEs with the higher loadings, the HFRs are in the same range. Therefore, the positive influence of improving the in-plane conductivity within the catalyst layer via adding  $\text{TiO}_2$  support was more pronounced at lower loadings. A zoom in the HFR-free cell voltage (Fig. 45 d) shows again the superior OER kinetics on the  $\text{IrO}_2\text{@TiO}_2$  as already analyzed for the PTEs with higher Ir loadings (Fig. 44 d). The reproducibility of the  $\text{IrO}_2/\text{TiO}_2$ -based PTEs was slightly worse compared to PTEs prepared with the  $\text{IrO}_2\text{@TiO}_2$  catalyst and could be related to an increased homogeneity due to an increased thickness as already discussed in the structural analysis section.

Overall,  $\text{IrO}_2\text{@TiO}_2$  catalyst demonstrated notably superior performance compared to unsupported  $\text{IrO}_2$  and supported  $\text{IrO}_2/\text{TiO}_2$  commercial catalysts at full-cell level in our experimental systems. To compare the performance of  $\text{IrO}_2\text{@TiO}_2$  PTE with state of the art PEM, we used an Ir-specific power density metric, which focuses on catalyst utilization, excluding the influence of other testing factors.<sup>79</sup> The Ir-specific power density is calculated via dividing the noble metal loading by the cell power at a fixed cell voltage of 1.79 V, which corresponds to a target cell voltage efficiency of 70 % (based on lower heating value of hydrogen). For the PTEs with  $0.4 \text{ mg}_{\text{Ir}} \text{ cm}^{-2} \text{ IrO}_2\text{@TiO}_2$  catalyst, the cell voltage of 1.79 V corresponded to a current density of ca.  $2.1 \text{ A cm}^{-2}$  and therefore a Ir-specific power density of ca.  $0.106 \text{ g}_{\text{Ir}} \text{ kW}^{-1}$ . This value was close to the minimum Ir-specific power density of ca.  $0.08 \text{ g}_{\text{Ir}} \text{ kW}^{-1}$  of the CCM MEA with the lowest loading ( $0.2 \text{ mg}_{\text{Ir}} \text{ cm}^{-2}$ ) prepared by Bernt et al.<sup>79</sup> Rozain et al.<sup>188</sup> achieved the value of ca.  $0.05 \text{ g}_{\text{Ir}} \text{ kW}^{-1}$  for CCM MEA using  $0.12 \text{ mg cm}^{-2} \text{ IrO}_2$ -loading of  $\text{IrO}_2/\text{Ti}$  supported catalyst. However, the use of Ti metal particle support bears the stability and cost concern as mentioned previously. It should be noted, that in this work the same spray and ink parameters optimized for the unsupported  $\text{IrO}_2$  were the same for all three catalysts to have a comparable morphology. Neither the  $\text{IrO}_2/\text{TiO}_2$  catalyst, nor the  $\text{IrO}_2\text{@TiO}_2$  catalyst therefore were optimized in terms of the catalyst layers. Although, the Ir-specific power density of  $\text{IrO}_2\text{@TiO}_2$  PTE cell is still slightly inferior to the  $\text{IrO}_2/\text{TiO}_2$  CCM cell, the  $\text{IrO}_2\text{@TiO}_2$  PTE configuration has an advantage of a straightforward manufacturing process resulting in mechanically stable and homogeneous catalyst layers, and reproducible PTEs at low catalyst loadings. In PTEs, all catalyst particles being connected with each other and with the titanium PTL could lead to an interface connection stability, mitigating the passivation problem of PTL current collectors.<sup>135</sup>

## 6.5 Summary and Conclusion

A high catalyst dispersed electrode has been accomplished, allowing a high PEMWE performance at low Ir loading. This is achieved by the combination of a unique microstructural catalyst, IrO<sub>2</sub> coated TiO<sub>2</sub> core-shell microparticles, with new electrode configuration, catalyst coated porous transport layer (PTE). The core-shell catalyst (IrO<sub>2</sub>@TiO<sub>2</sub>) has been synthesized by a facile and scalable method. The method works on the basis of electrostatic interaction of [IrCl<sub>6</sub>]<sup>2-</sup> precursors to positively-charged surface of TiO<sub>2</sub> microparticles to form H<sub>2</sub>IrCl<sub>6</sub>-coated TiO<sub>2</sub> particles intermediate product, followed by pyrolysis to form IrO<sub>2</sub>@TiO<sub>2</sub>. TEM and SEM investigations revealed the core-shell like structures of IrO<sub>2</sub>@TiO<sub>2</sub> microparticles with high coverage of IrO<sub>2</sub> on the surface of TiO<sub>2</sub> particles. High resolution TEM revealed high crystallinity of rutile IrO<sub>2</sub> shell. Electrochemical testing by scanning flow cell (SFC) revealed that IrO<sub>2</sub>@TiO<sub>2</sub> exhibits a two-fold higher mass activity than commercial IrO<sub>2</sub>/TiO<sub>2</sub> (Umicore) towards oxygen evolution reaction (OER) in acidic solution.

When implemented in PTE-configurations for PEMWEs, IrO<sub>2</sub>@TiO<sub>2</sub> anode catalyst layers demonstrated a notably superior performance compared to two commercial benchmark catalysts: unsupported IrO<sub>2</sub> (Alfar Aesar) and IrO<sub>2</sub>/TiO<sub>2</sub> (Umicore). The different catalysts layers were prepared with the same fabrication technique and compared at the same electrochemical testing parameters. IrO<sub>2</sub>@TiO<sub>2</sub> PTEs with a loading as low as 0.4 mg<sub>Ir</sub> cm<sup>-2</sup> yielded current densities of 1 A cm<sup>-2</sup> at 1.67 V, still outperforming the benchmark IrO<sub>2</sub>/TiO<sub>2</sub> PTE with a 3-fold higher loading (1.4 mg<sub>Ir</sub> cm<sup>-2</sup>). This high performance was mainly attributed to the combination of the best kinetics and low HFR. Conversely, the unsupported IrO<sub>2</sub> catalyst PTE showed good kinetics but a higher HFR, and the IrO<sub>2</sub>/TiO<sub>2</sub> PTE showed a low HFR but worst kinetics. The better catalyst utilization in the IrO<sub>2</sub>@TiO<sub>2</sub> configuration was related to its catalyst morphology, as the high dispersion of IrO<sub>2</sub> within porous structured catalyst layers was confirmed by FIB/SEM investigation. The addition of TiO<sub>2</sub> particles reduced the ohmic resistance, which was related to an increased in-plane conductivity and electrical contact area between catalyst layer and titanium porous transport layer. It was found that the intrinsic catalyst activity showing in half-cell measurements is not always consistent with its performance in full-cell level due to the catalyst morphology incompatible with device configurations.

Overall, in comparison to state-of-the-art PEMWE, the IrO<sub>2</sub>@TiO<sub>2</sub> PTE exhibited amongst the best performances reported in the literature. The potential of our novel IrO<sub>2</sub>@TiO<sub>2</sub> catalyst for industrial PEMWE applications was motivated in this work, given the facile synthesis route and high MEA performance at low Ir loadings. Further optimization of the IrO<sub>2</sub>@TiO<sub>2</sub> catalyst layer in terms of Nafion content and fabrication parameters could result in even further reduced Ir loading while maintaining high cell performance. For a better comparison to state-of-the-art PEMWE performance, catalyst coated membranes will be investigated. Still, the stability of IrO<sub>2</sub>@TiO<sub>2</sub> in OER condition was not optimal, and still inferior to that of commercial IrO<sub>2</sub>/TiO<sub>2</sub> (Umicore). We suggest that the stability could be improved by the optimization of thermal treatment process in the future.<sup>199, 201</sup>



## 6.6 Supporting information

Figure numbers of the original manuscript and supporting information are referenced in this chapter. The author of this thesis contributed to Fig. 51.

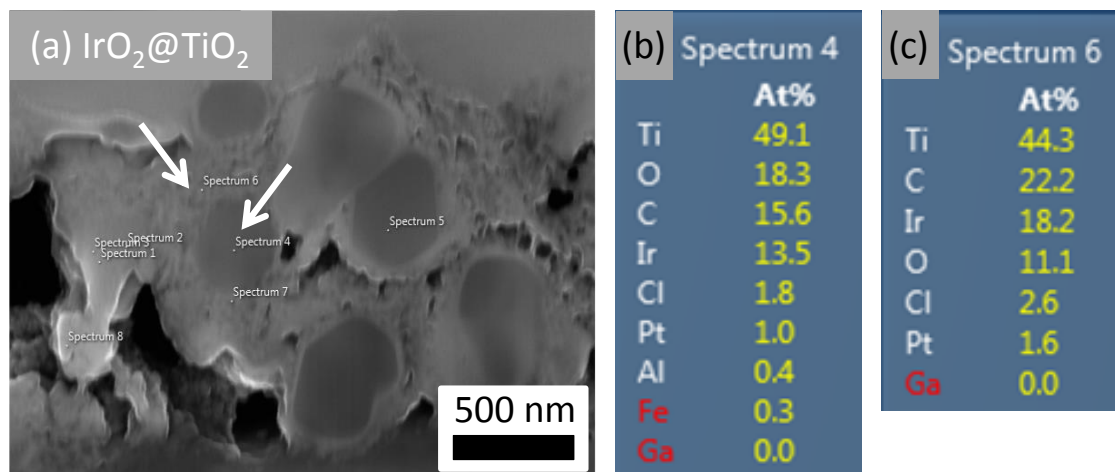


**Fig. 46** EDX mapping of the  $\text{IrO}_2@\text{TiO}_2$  catalyst layer. (a) Different positions along the cross-section of the  $\text{IrO}_2@\text{TiO}_2$  catalyst layer, where an EDX analysis performed (b) Selected EDX-data from position 4 (on the  $\text{TiO}_2$  core) and 6 (on the  $\text{IrO}_2$  shell) showing the the Ir and Ti content in good agreement with the material characterization. (original: Fig. S5)



**Fig. 47** (a) Cross-section of the  $\text{IrO}_2@\text{TiO}_2$  catalyst layer, on which an EDX-scan was performed (b) EDX mapping showing the  $\text{TiO}_2$  cores (c) EDX mapping showing the  $\text{IrO}_2$  shell. (original: Fig. S6)

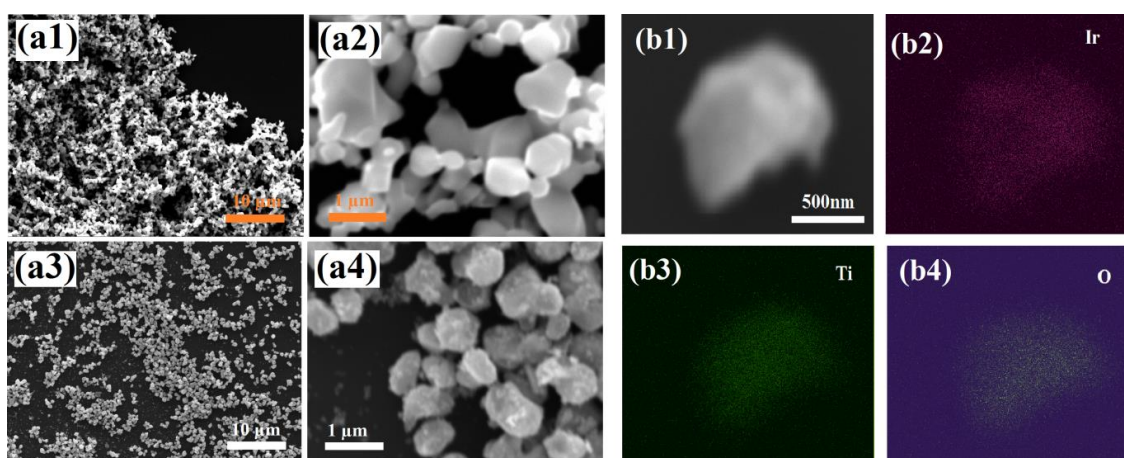


**Fig. 48** SEM images of blank  $\text{TiO}_2$  particles (a1) and (a2), and of  $\text{IrO}_2@\text{TiO}_2$  (a3) and (a4). EDX elemental mapping images for Ir (b2), Ti (b3), and O (b4), respectively for a single particle of  $\text{IrO}_2@\text{TiO}_2$  in (b1) SEM image, showing homogenously covering of Ir over the  $\text{TiO}_2$  particle. (original: Fig. 3)

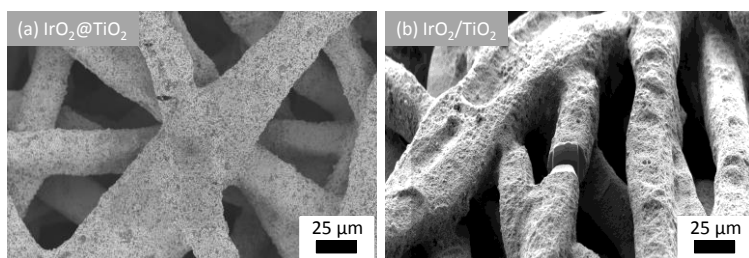


**Fig. 49** Surfaces of the porous transport electrodes (PTEs). **(a)**  $\text{IrO}_2@\text{TiO}_2$  catalyst based PTE. **(b)**  $\text{IrO}_2/\text{TiO}_2$  catalyst based PTE. (original: Fig. S7)

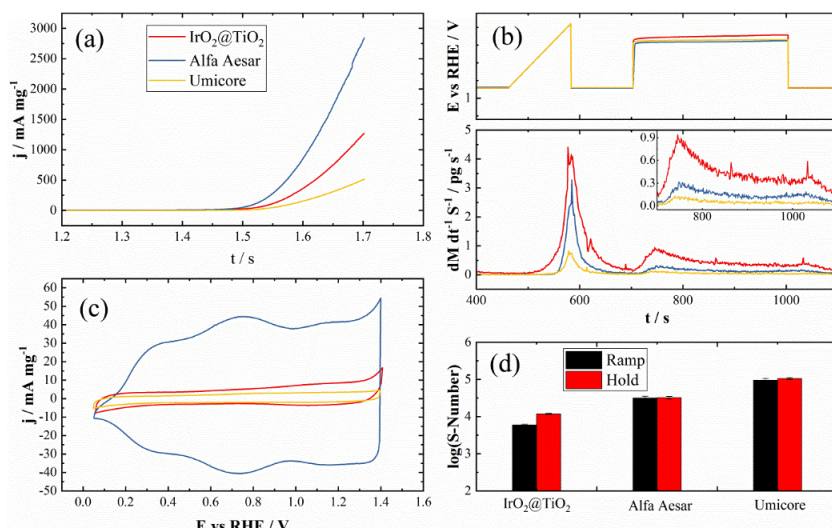


**Fig. 50** Electrochemical performances of  $\text{IrO}_2@\text{TiO}_2$  in comparison with  $\text{IrO}_2$  reference catalysts from Alfa Aesar and Umicore. **(a)** Linear sweep voltammograms (LSVs); **(b)** Stability investigation based on detected iridium dissolution during OER: potential profiles (upper image) and detected Ir concentration in the electrolyte during ramping potential to 1.65 V vs. RHE and constant current at 100  $\text{mA mg}^{-1}$  for  $\text{IrO}_2@\text{TiO}_2$  and  $\text{IrO}_x$  (Alfa Aesar) and 20  $\text{mA mg}^{-1}$  for  $\text{IrO}_2/\text{TiO}_2$  (Umicore). **(c)** CVs recorded before AST for all catalysts. **(d)** S-numbers of the studied catalyst. Catalyst loadings: 10  $\mu\text{g cm}^{-2}$  for  $\text{IrO}_2@\text{TiO}_2$  and  $\text{IrO}_x$  (Alfa Aesar) and 50  $\mu\text{g cm}^{-2}$  for  $\text{IrO}_2/\text{TiO}_2$  (Umicore), LSVs without iR drop correction. (original: Fig. 4)

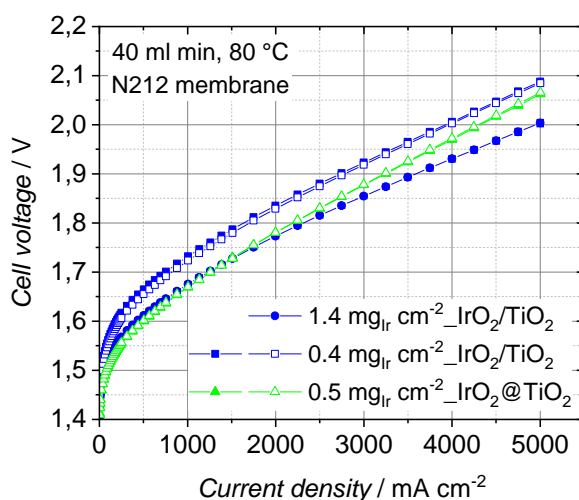


**Fig. 51** Polarization data comparing the supported  $\text{IrO}_2@\text{TiO}_2$  and  $\text{IrO}_2/\text{TiO}_2$  based MEAs, with a loading of 0.5  $\text{mg}_{\text{Ir}} \text{cm}^{-2}$  for the  $\text{IrO}_2@\text{TiO}_2$  samples and 0.4  $\text{mg}_{\text{Ir}} \text{cm}^{-2}$  as well as 1.4  $\text{mg}_{\text{Ir}} \text{cm}^{-2}$  for the  $\text{IrO}_2/\text{TiO}_2$  based MEAs. The low loaded  $\text{IrO}_2@\text{TiO}_2$  MEA performed better than the  $\text{IrO}_2/\text{TiO}_2$  samples with almost the same loading and up to a current density of ca. 1.5  $\text{A cm}^{-2}$  even better as the  $\text{IrO}_2/\text{TiO}_2$  sample with an almost three times higher Ir-loading. (original: Fig. S8)



## 6.7 Outlook: gradient sized catalyst layers based on $\text{IrO}_2@\text{TiO}_2$ to reduce the noble metal loading

As the core-shell structure of the supported  $\text{IrO}_2$ -catalyst increases the average particle size of the material deposited in the CL, the interface towards the coarse PTL is improved. To smoothen the CL surface towards the PEM, a particle size gradient from PTL towards the PEM could be one solution to optimize both interfaces, as well as the catalyst utilization due to an optimized distribution throughout the catalyst layer. Gradient catalyst layers were fabricated via spray coating a core-shell layer and unsupported  $\text{IrO}_2$  (Alfa Aesar, type Premion) on top of a fiber-sintered PTL (Fig. 52).

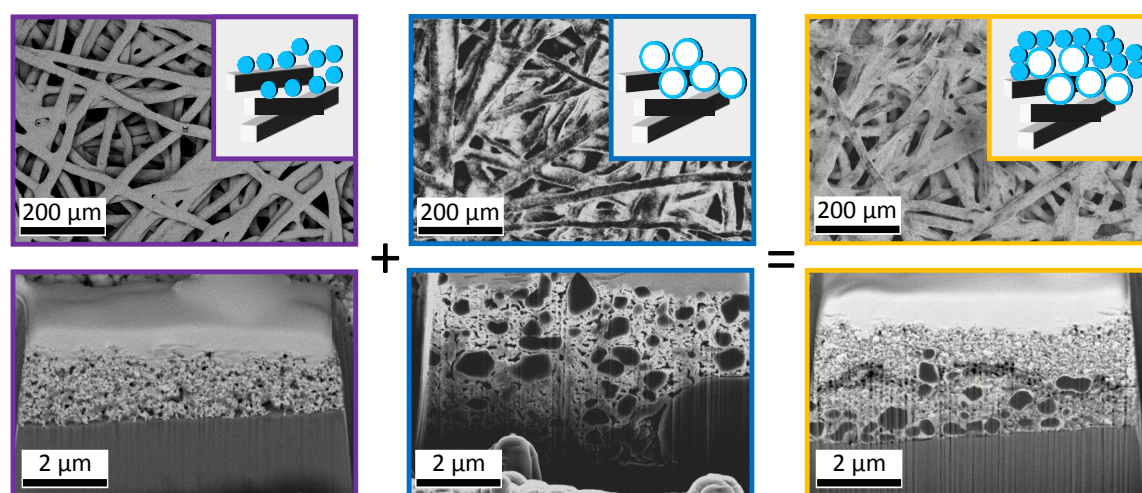


**Fig. 52** Gradient sized catalyst layer with core-shells coated with unsupported  $\text{IrO}_2$ .

The overall loading for PEMWE testing was  $1.5 \text{ mg cm}^{-2}$  with 75 wt%  $\text{IrO}_2$  in the core-shell layer. Fig. 53 A shows the cell voltage and HFR-free cell voltage of a gradient PTE compared to the core-shell catalyst. Ohmic resistances were quite high in this study, as a Nafion N117 membrane and flow fields without gold coating were used. The performance of the gradient PTE was only slightly better than the core-shell PTE due to a better HFR (Fig. 53 B). However, according to FIB-SEM evaluations (Fig. 52), a stronger effect of the gradient PTE on the polarization behavior was expected. Further optimization studies regarding the ratio between supported and unsupported catalyst and the Nafion content in the different layers are therefore planned.

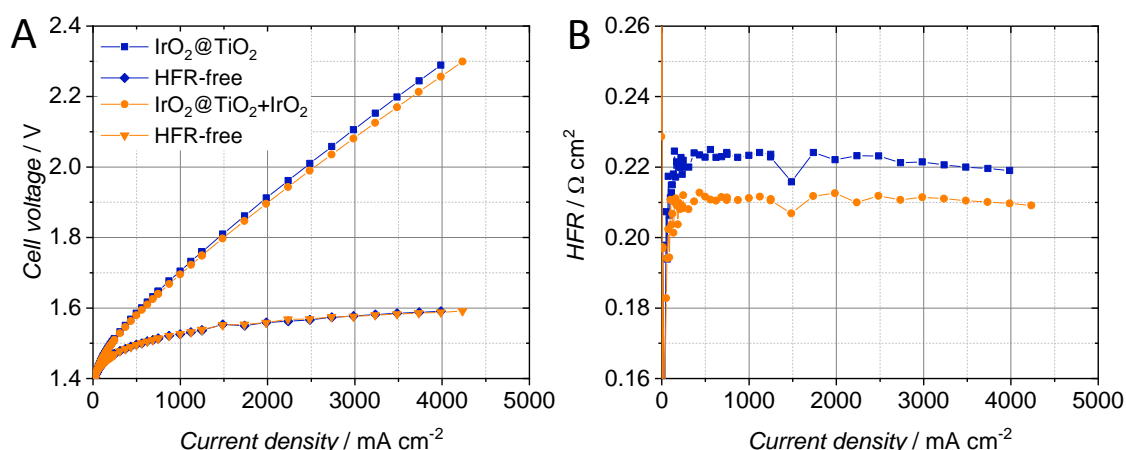


**Fig. 53** Polarization data of the core-shell and the gradient PTE. A Cell voltage and HFR-free cell voltage. B HFR.

The second gradient catalyst layer that was evaluated was the combination of unsupported IrO<sub>2</sub>-catalyst coated with IrO<sub>2</sub>-nanoparticles (NPs) synthesized by PhD student Jan Bucher (University of Bern). A standard ethylene-synthesis route was used as described elsewhere.<sup>202, 203</sup> The NPs had a size of 4-5 nm and were mixed with 5 wt% Nafion in the final catalyst layer. The NP-PTE showed a smooth surface with a few cracks and almost no porosity (Fig. 54). The IrO<sub>2</sub>-based PTE showed an increased porosity but rougher surface. When coating the IrO<sub>2</sub>-based PTE with NPs, the surface could be smoothened. The gradient sample was fabricated with a ratio of 75:25 wt% IrO<sub>2</sub> in the IrO<sub>2</sub> layer vs. the NP layer.

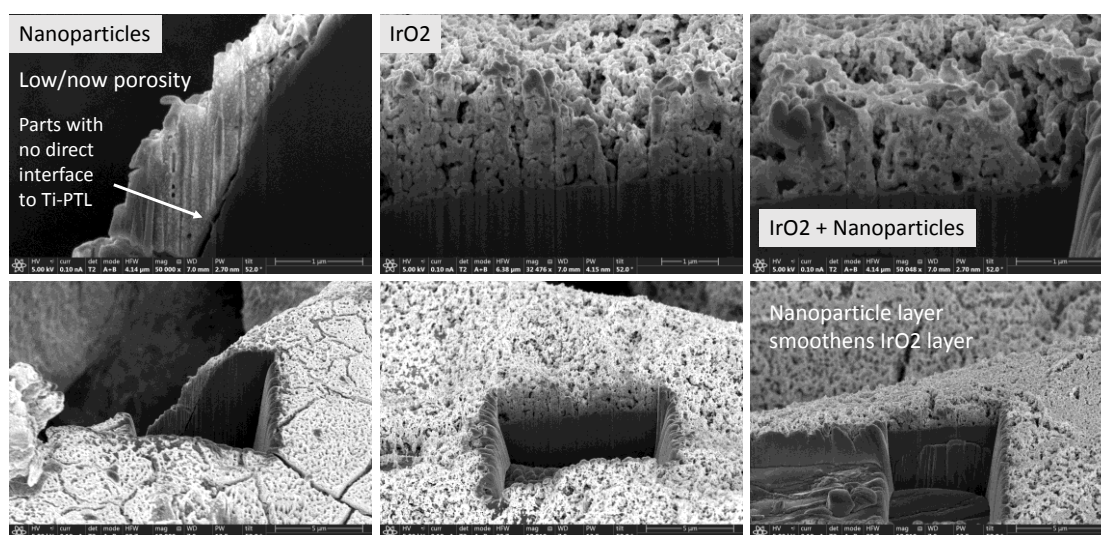


**Fig. 54** FIB-SEM cross-sections: The NP catalyst layer shows almost no porosity, cracks and a discontinuous electrical interface towards Ti-PTL. The IrO<sub>2</sub> layer is porous and has a good electrical interface towards the Ti-PTL. The combination of both layers still has a good electrical interface towards the PTL and sufficient porosity. The surface was smoothened by the NPs.

The impact of the microstructure and morphology is directly visible in the polarization data with the different PTEs pressed against a N212 Nafion membrane and a carbon cloth based cathodic PTE (Fig. 55 A). The NP-PTE shows high mass transport losses (Fig. 55 B) due to the very low porosity as well as the highest ohmic resistance (Fig. 55 C). The Nafion content might be too high in combination with the NPs leading to only a few direct electrical contact points towards the PTL. The kinetic region (Fig. 55 D) is however improved by the use of nanoparticles, due to the increased specific surface area. The combination of larger IrO<sub>2</sub> particles with the nanoparticle-layer shows a slightly worse kinetic region as the average particle size of the catalyst was increased, but the mass transport region improved significantly due to the larger pores within the gradient catalyst layer compared to the pure nanoparticle based layer. The HFR was improved as well, as the gradient catalyst layer combines both: a good interface towards the PTL as well as towards the PEM via a smooth nanoparticle surface. The decreasing HFR with increasing current density is not yet fully understood. The effect was more pronounced for the NP-PTE and could be again related to the reduced release of waste heat of the dense catalyst layer (see e.g.<sup>111, 141, 163</sup>). Nevertheless, the better ohmic region (Fig. 55 C) compared with stable mass transport (Fig. 55 B) and better kinetic region (Fig. 55 C) led to a superior performance of the gradient PTE compared to the pure IrO<sub>2</sub>-based PTE. The dense NP structure therefore needs a porous support (gradient structure) to show a sufficient mass transport and to benefit from both: a good interface towards the PTL as well as towards the PEM in combination with lower kinetic overpotential.

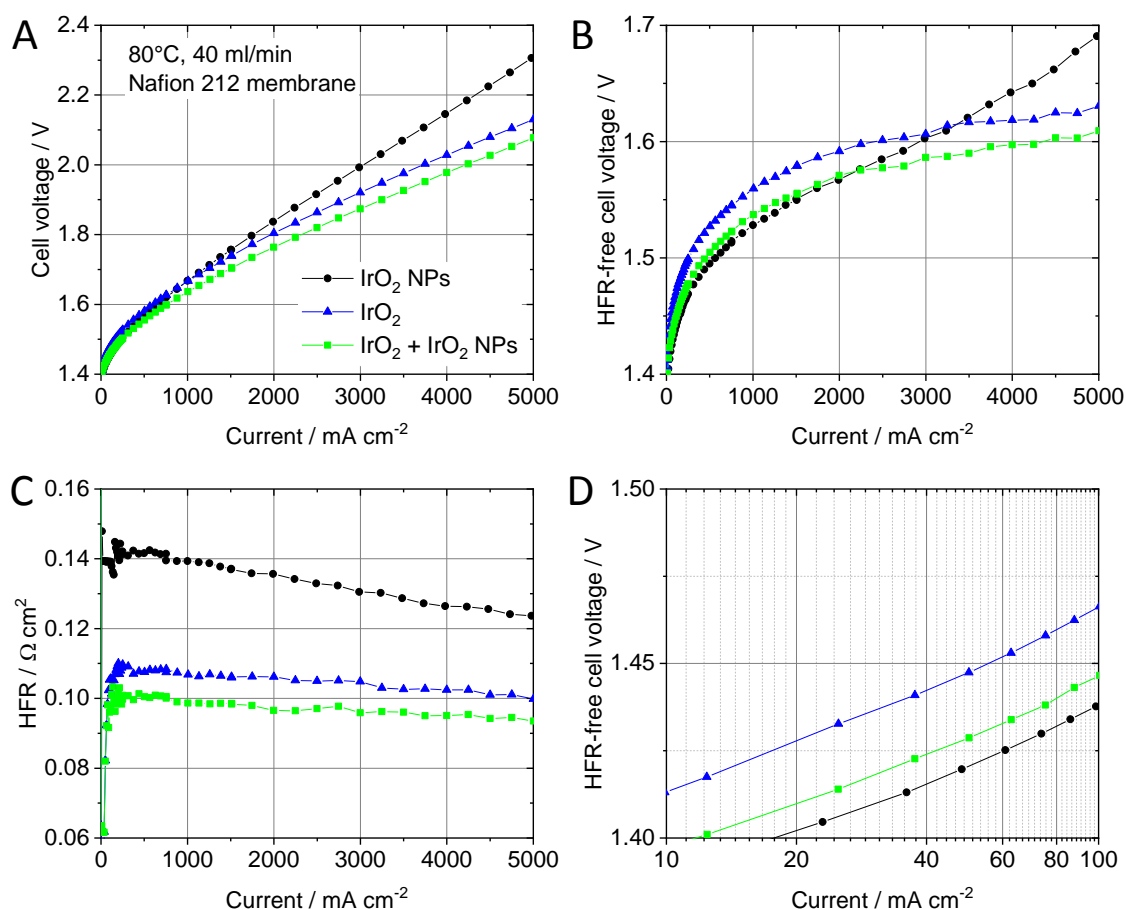


**Fig. 55** Polarization data of Ti-fiber PTEs with a total  $\text{IrO}_2$  loading of  $1.5 \text{ mg cm}^{-2}$ . A Cell voltage B HFR-free cell voltage. C HFR D Kinetic region of the HFR-free cell voltage.

The advantage of fabricating gradient catalyst layers for a better catalyst particle distribution was shown with positive effects on the HFR and kinetic region. However, to understand the effects on the polarization behavior in combination with a structural analysis, more measurements and variations are needed. The Nafion content is e.g. a crucial parameter when developing novel catalyst layers. Smaller catalyst particles as the nanosized  $\text{IrO}_2$  theoretically need far less Nafion to establish protonic pathways between the particles and to be connected with the PEM. The ratio of  $\text{IrO}_2$  in the different layers as well needs to be optimized as the average porosity of the gradient catalyst layers is influenced by the porosity of the single contributing layers.



## 7 Development of titanium based MPLs for anodic Ti-PTLs

The deposition of the OER catalyst layer with thicknesses in the 5  $\mu\text{m}$  range directly on top of commercial Ti-PTLs with pores in the 100  $\mu\text{m}$  range, leads to the deep infiltration of the PTL with active material and inhomogeneous, rough electrode surfaces. To show the effect of infiltration, when no MPL is available, IrO<sub>2</sub>-based catalyst layers were printed (Fig. 56 A,B) and spray coated (Fig. 56 C,D) on top of powder- and fiber-sintered PTLs, respectively. The larger printed ink droplets compared to the fine sprayed layer, dried mostly on top of the substrates, when an appropriate temperature higher than the evaporation point of the solvents was set. The formation of a catalyst layer was therefore in principle possible, but cross-sections prepared via breaking the samples in liquid N<sub>2</sub> showed the deep infiltration of the PTLs. Via spray coating, thinner CLs were deposited, but the fine atomized mist was sprayed deep into the pores of the porous PTLs. As catalyst particles were found in several hundred  $\mu\text{m}$  distance to the membrane, the catalyst utilization was significantly reduced and the protonic interface towards the membrane can therefore only be established at direct contact points with the PTE.

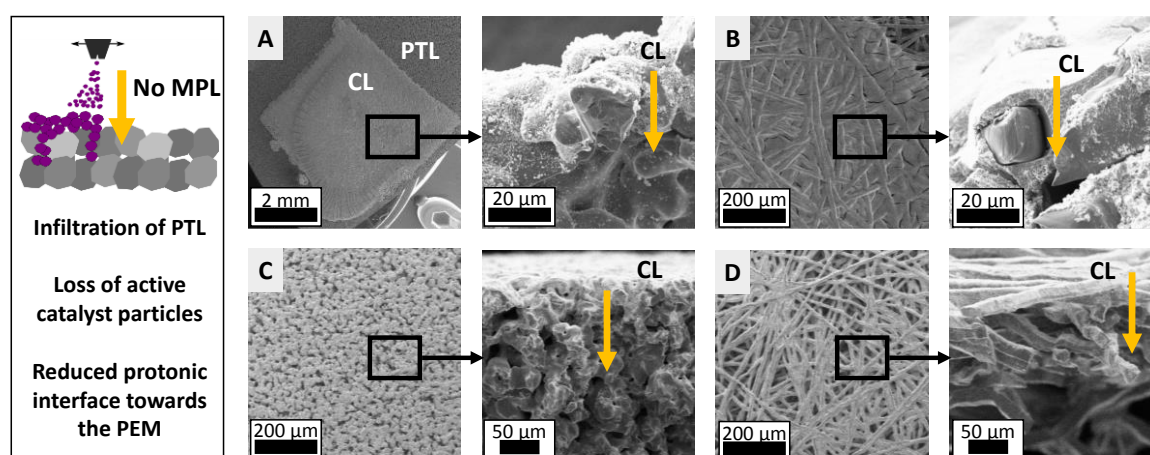


**Fig. 56** Schematic of titanium powder- and fiber-sintered PTLs without MPL directly printed (A,B) and spray coated (C,D) with the CL. Cross-sections reveal the deep infiltration of the porous titanium substrates with catalyst particles..

The availability of a titanium based intermediate layer between PTL and CL could establish a smooth surface to deposit the catalyst particles on top. Lettenmeier et al. presented a vacuum plasma sprayed MPL as free-standing porous layer with suitable porosity and surface roughness for an application in PEMWE.<sup>102</sup> Vacuum plasma spraying is however a costly manufacturing method that is due to the size of the device and the need of trained staff usually not available in a standard laboratory or company. Therefore, more facilitated and cost efficient methods to manufacture a Ti-based MPL were evaluated in this work. Ti-inks containing Ti-powder, binder and solvents were directly deposited with simple methods like spray coating, painting and printing on porous Ti-PTLs that are commercially available for the anode side in PEMWEs. Sintering was used to fabricate binder-free, interconnected titanium layers. The influence of different deposition techniques, temperatures, binder contents and sinter parameters on the mechanical stability, homogeneity and electrical conductivity of the Ti-layers was evaluated.

A short outlook motivates the development of Ti-MPLs not only to improve the direct electrical and protonic interface of the CL towards the PTL and PEM, but as well as to allow for the direct deposition of the membrane material on smooth anodic electrode surfaces. This approach was introduced as direct membrane deposition (DMD) in the fuel cell community and is now slowly



transferred to PEMWE.<sup>204</sup> Due to the lack of a MPL at the anode side in PEMWE, so far no continuous CL and subsequently no closed membrane layer could be formed on the anodic PTE.

## 7.2 First studies on developing a binder based Ti-MPL

Depending on the deposition technique of a powder based layer, a binder is needed to stabilize the metal particles in the liquid ink (e.g. for printing). A binder also increases the mechanical stability of the final MPL on top of the porous substrate. The binder should be thermally conductive and chemically stable in acidic conditions at the anode in PEMWEs. As water needs to be supplied from the anodic PTL through the MPL towards the active sites of the CL, the polymeric binder needs to be water-insoluble but not hydrophobic. Nafion was studied as binder for the MPL, as a sufficient binding with the Nafion phase in the CL was expected.

**Influence of the substrate temperature:** The deposited MPL-ink ideally dries immediately at the surface of the PTL to prevent infiltration and to form a porous layer. Fig. 57 shows a Ti-ink printed on Ti-PTLs when varying the substrate temperature. The ink consisted of Ti-particles <20  $\mu\text{m}$  (Alfa Aesar) and 15 wt% Nafion ionomer which together accounted for 10 wt% solid parts in the ink. The solids were mixed with DI-water and the ink was then stirred for 3 h prior to sonicating for 15 min. The printing parameters (Biofluidix, model BioSpot) were: 1 mm s<sup>-1</sup> path speed, 50  $\mu\text{l}$  droplet volume, 0.3 mm pitch. At room temperature, the ink was soaked in by the porous PTL as the solvents did not dry at the surface. When setting the hot plate temperature to 120 °C (above the evaporation point of H<sub>2</sub>O), the deposited MPL stayed more on top of the PTL as it dried at the hot surface (Fig. 57 A). However, when the temperature was set to 145 °C, the Ti-ink dried too fast to form a continuous layer (Fig. 57 B). To avoid a rough and inhomogeneous MPL, the hot plate temperature was set to 120 °C for the subsequent tests.

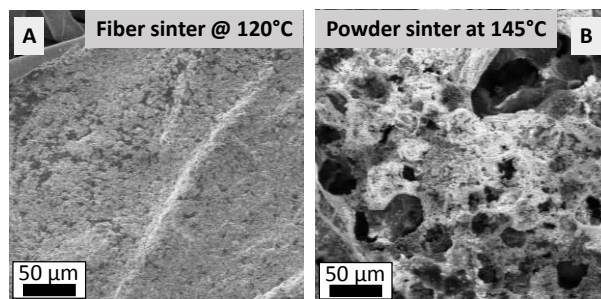


**Fig. 57** Effect of the hot-plate temperature on the drying behavior of the deposited MPL. At 120 °C a continuous MPL could be formed, whereas the Ti-ink did dry too fast at 145 °C.

**Influence of the Nafion binder content:** The binder content should be as low as possible to increase the electrical conductivity of the MPL, but as high as needed to stabilize the metal particles in the ink as well as to deposit a homogeneous MPL. Fig. 58 shows the result of pipetting (Fig. 58 A, B, D) and printing (Fig. 58 C) the above described Ti-particle ink (Ti < 20  $\mu\text{m}$ , Alfa Aesar) with different wt% of Nafion ionomer binder on different Ti-PTLs. The inks contained 10 wt% solids and H<sub>2</sub>O as solvent. Printing parameters were the same as stated for above with the hot plate set to 120 °C. When using an ink with 25 wt% Nafion, the deposited MPL was stable and reduced the pore size of the Ti-PTL (Fig. 58 A.1). The porosity was however too low to allow the distribution of gases and water and no titanium particles did protrude from the surface of the MPL (Fig. 58 A.2). A direct access to the Ti-particles in the MPL however, is needed to electrically connect the catalyst particles. With a reduced Nafion content of 15 wt% (Fig. 58 B.1), more Ti-particles were directly visible and thus available without being electrically insulated by the binder (Fig. 58 B.2). To fabricate a porous MPL, the Nafion content was further reduced. Fig. 58 C.1 shows a printed

pattern on a Ti-powder sintered MPL with 10 wt% Nafion. The MPL led to a reduced pore size of the Ti-PTL (Fig. 58 C.2) while showing a high porosity and directly accessible Ti-particles (Fig. 58 C.3). Further reducing the Nafion content to 5 wt%, formed a brittle, inhomogeneous MPL (Fig. 58 D). A Nafion content of 10 wt% was therefore chosen for the subsequent tests.

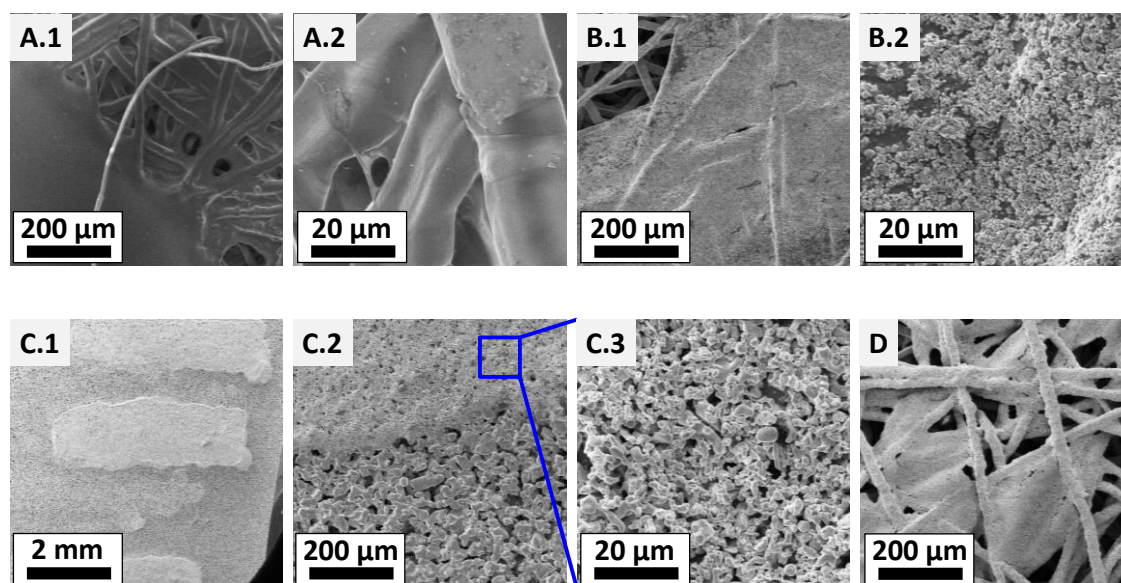


**Fig. 58** Pipetted (A,B,D) and printed (C) Ti-MPL with various Nafion contents as binder influencing the mechanical stability, electrical conductivity and porosity of the MPL. A 25 wt% Nafion B 15 wt% Nafion C 10 wt% Nafion. D 5 wt%.

**Towards up-scalable deposition techniques:** As Ti-particles sediment in the tubing of the printer, alternative deposition techniques that require a lower stability of the Ti-inks, were evaluated. A doctor-bladed Ti-ink with 20 wt% solids (Ti-particles as used above and 10 wt% Nafion) deposited on a fiber-sintered PTL is shown in (Fig. 59). The PTL was placed on a hot plate set to 120 °C and therefore the formation of a continuous MPL that dried at the surface of the PTL was reached. The setup for doctor blading was not optimized for large areas but was suitable to show the feasibility of the deposition technique. The MPL showed directly accessible Ti-particles and a sufficient porosity.

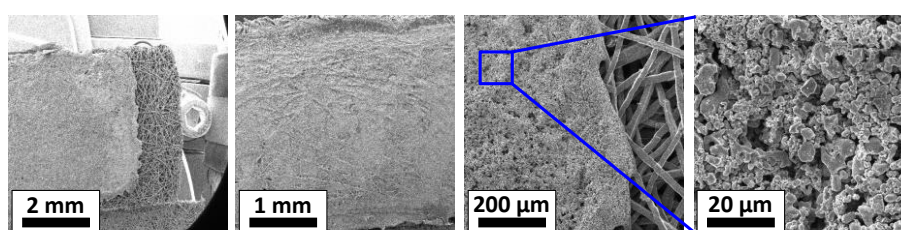


**Fig. 59** Doctor bladed Ti-MPL with 10 wt% Nafion. Large areas can be coated in a short time but the setup need to be adjusted to prevent an inhomogeneous distribution of the layer thickness esp. at the edges.

A drawback of doctor blading was the amount of ink mechanically pressed into the pores of the PTL. As the doctor blade is moved over the substrate in a certain distance to the surface, to set the layer thickness, the ink is weather moved forward in forward direction or it is pressed into the pores. Doctor blading might therefore be a useful tool to coat dense surfaces, but for coating porous PTLs it might be not the best choice. Painting the Ti-ink on top of the PTLs was therefore evaluated as fast and gentle deposition technique. As the force applied on the ink is rather small, the amount of Ti-particles that are pressed into the PTL can be reduced compared to doctor blading. A stable ink is as well not required and the surface of the PTL can be homogeneously covered. An ink containing 10 wt% Nafion, H<sub>2</sub>O as binder and the same Ti-particles (Ti < 20 μm,

Alfa Aesar) as used for the previous tests was applied. The amount of deposited ink volume per run was reduced compared to doctor blading or printing and therefore the amount of liquid ink on the surface of the PTL was reduced. The temperature of the hot plate could therefore be reduced to 100 °C as water was evaporated immediately out of the thin painted layers. Room temperature was not sufficient to stabilize the MPL on top of the PTL and the layer did not dry homogeneously (Fig. 60, left side). 100 °C were however sufficient, as showed in SEM-images of the surface of the pristine PTL compared to the PTL coated with the MPL (Fig. 60, right side).

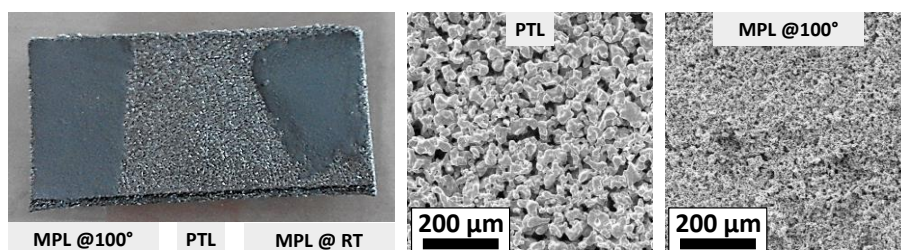


**Fig. 60** *Ti-MPL fabricated via painting a powder sintered Ti-PTL. Different substrate temperatures led to different infiltration depths and thickness distributions after drying. A temperature of 100 °C resulted in a smooth MPL structure.*

**Towards a full anodic PTE based on the PTL+MPL compound:** For an electrochemical test in the self-designed test cell, a 4 cm<sup>2</sup> fiber-sintered Ti-PTL was painted with the above described Ti-MPL and subsequently spray-coated with an IrO<sub>2</sub>-based catalyst layer (Fig. 61 A). The spray parameters were: ultrasonication power of 2.5 W, 90 °C hot plate temperature, 0.6 kPa shaping air, 0.1 ml min<sup>-1</sup> flow rate and 90 mm s<sup>-1</sup> path speed. The IrO<sub>2</sub>-based ink consisted of 2 wt% solids (13 wt% Nafion ionomer) and a solvent ratio of 1:5 (H<sub>2</sub>O:IPA). Despite a smooth MPL and catalyst layer (Fig. 61 A), the recording of a full polarization curve was not possible, due to the high ohmic resistance. An analysis of the cross-section of the system revealed the electrically in-plane insulation of the Ti-particles by the Nafion binder as main problem (Fig. 61 B,C).

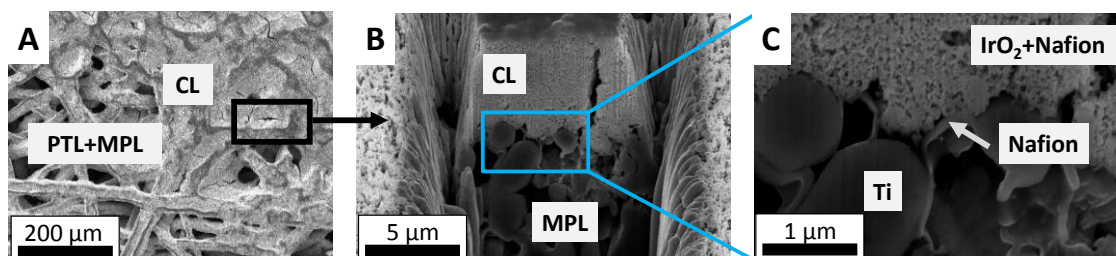


**Fig. 61** *A Painted MPL with spray coated IrO<sub>2</sub>-based catalyst layer on top. B,C The Nafion binder in the MPL surrounds the Ti-particles leading to a high electrical resistance.*

Reducing the binder content could increase the electrical conductivity, but at the same time the mechanical stability of the MPL is reduced. The use of an electrically conductive binder is therefore highly suggested and should be taken into account in future development steps. To be independent from the binder content and properties at all, the approach of sintering Ti-particles is presented in the next section.

### 7.3 First studies on developing sintered Ti-powder MPLs

Ti-layers with and without binder were sintered for a proof of principle in this work. Two different types of titanium powders were tested, with the first one being the Ti-powder used in the previous section (Ti-particles < 20 µm) and the second one being a titanium hydride powder (TiH<sub>2</sub>) with particles in the 1-3 µm range (Alfa Aesar). The smaller TiH<sub>2</sub> particles were expected to vary the porosity and smoothness of the MPL and the hydride was interesting in combination with a



reducing atmosphere in the sinter furnace to increase the purity of the final MPL.<sup>136, 137</sup> As the sinter parameters like temperature and duration of holding times as well as heating and cooling rates define the quality of the sintered MPLs, an intense parameter study is necessary to fabricate sintered MPLs in a reproducible quality. Fig. 62 A shows the applied sinter curve with reduced heating rates compared to a previous test in which a strong bending of the substrates and cracks in the MPL were observed. The samples used in this test are shown in Fig. 62 B and consisted titanium fiber- and powder sintered PTLs coated with  $\text{TiH}_2$ - and Ti- powders mixed with  $\text{H}_2\text{O}$  or polyethylene glycol (PEG 400, Sigma Aldrich) as binder. The basic ink composition and deposition parameters were the same as in the previous section.

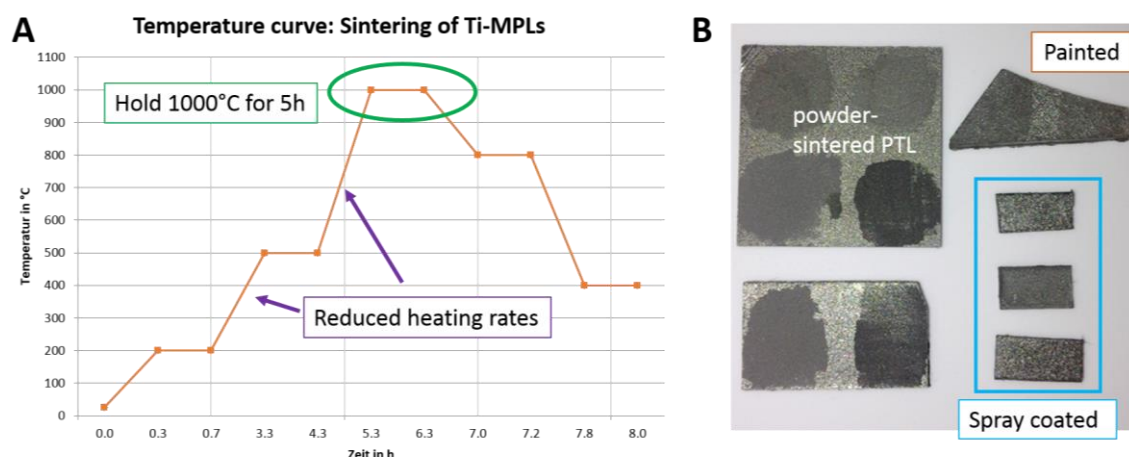


**Fig. 62** A Sinter curve with the maximum temperature of 1000 °C held for 5 h B PTLs coated with Ti- and  $\text{TiH}_2$ -based MPLs prior to sintering in the high temperature furnace.

The spray coated samples were used to be able to directly see the MPL-PTL interface after sintering, as the titanium PTL is not directly visible after painting an MPL on top. Fig. 63 shows the result of sintering a  $\text{TiH}_2$ - and Ti-based MPL on top of a fiber-sintered PTL. In both cases, the titanium particles were sintered to the Ti-PTL indicating the right choice of sinter parameters. Spray coating is however not suitable to fabricate a continuous MPL as the porous substrate was infiltrated by the MPL preventing the formation of a continuous layer.

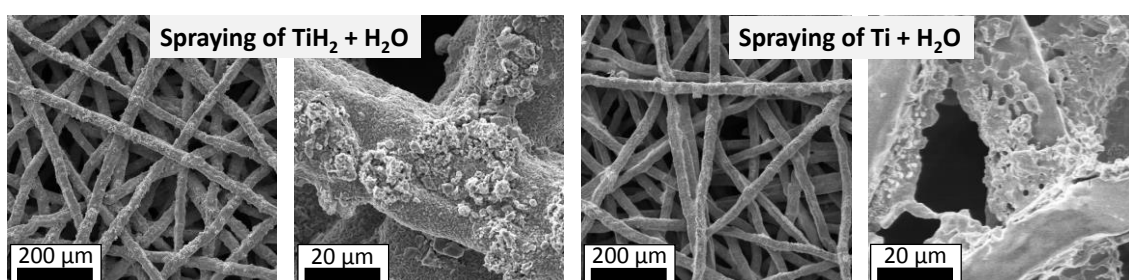


**Fig. 63** Results of sintering a spray coated  $\text{TiH}_2$ -based MPL (left side) and Ti-based MPL (right side) on a fiber-sintered PTL. An intermediate interface of the Ti-MPL with the Ti-PTL was reached.

Painting the Ti-based inks on top of the titanium substrates led to a more homogeneous coverage of the PTLs and thus to a more continuous MPL as shown in Fig. 64. All samples showed Ti-particles of the MPL connected with the PTL. Sintering with the parameters used in this work is therefore in principle applicable to fabricate MPLs directly on top of the Ti-PTLs. The homogeneous coverage of the PTL was however not yet reached, which might be the result of shrinking of the Ti-layer during the sinter process. The use of Ti-powder vs. smaller  $\text{TiH}_2$ -particles showed the possibility to trigger the surface roughness of the MPL. The addition of PEG as binder varied the infiltration of

the PTL and porosity and needs to be further optimized.<sup>205</sup> The degree of roughness, porosity and infiltration of the PTL will determine the functionality of the MPL, which needs to be evaluated in PEMWE full-cell tests.

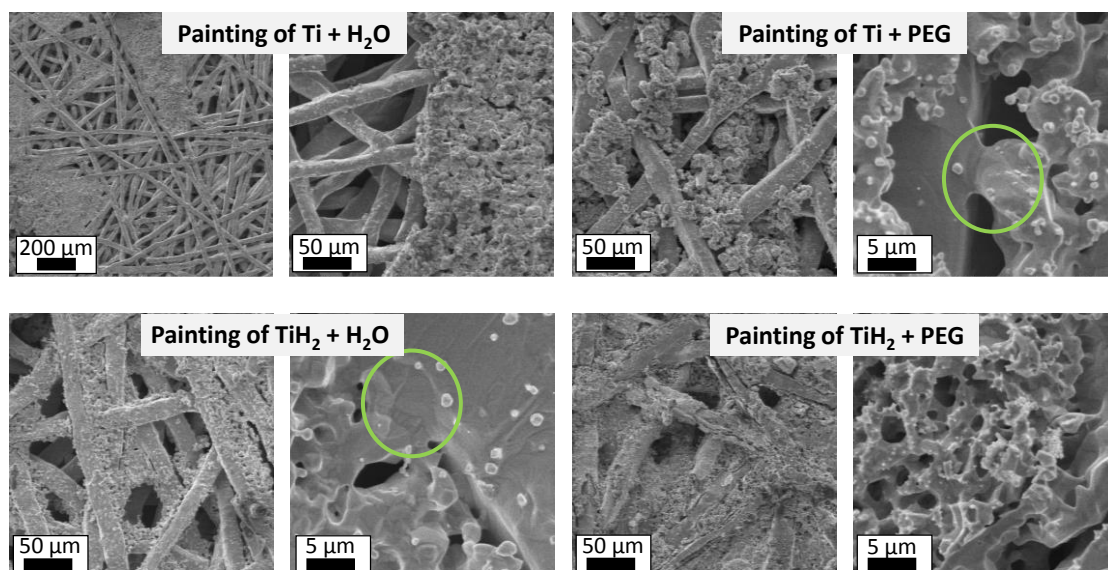


**Fig. 64** Sintering of Ti-based MPLs deposited via painting on Ti-fiber PTLs. The MPLs with larger Ti-particles ( $< 20 \mu\text{m}$ ) showed a rougher surface than the MPLs fabricated with smaller  $\text{TiH}_2$  particles ( $1\text{--}3 \mu\text{m}$ ).

The results of sintering Ti-based MPLs on top of powder-sintered PTLs are shown in Fig. 65. The larger Ti-particles led to partly inhomogeneous layer thicknesses on the PTL as marked with a red circle in Fig. 65 A. The thickness of the deposited MPLs needs to be optimized, as a too thick painted  $\text{TiH}_2$ -MPL showed cracks and a brittle structure after sintering (red circles in Fig. 65 B). For thinner  $\text{TiH}_2$ -MPLs, a stable and smooth MPL could be fabricated, which however slightly infiltrated the PTL. (Fig. 65 C).

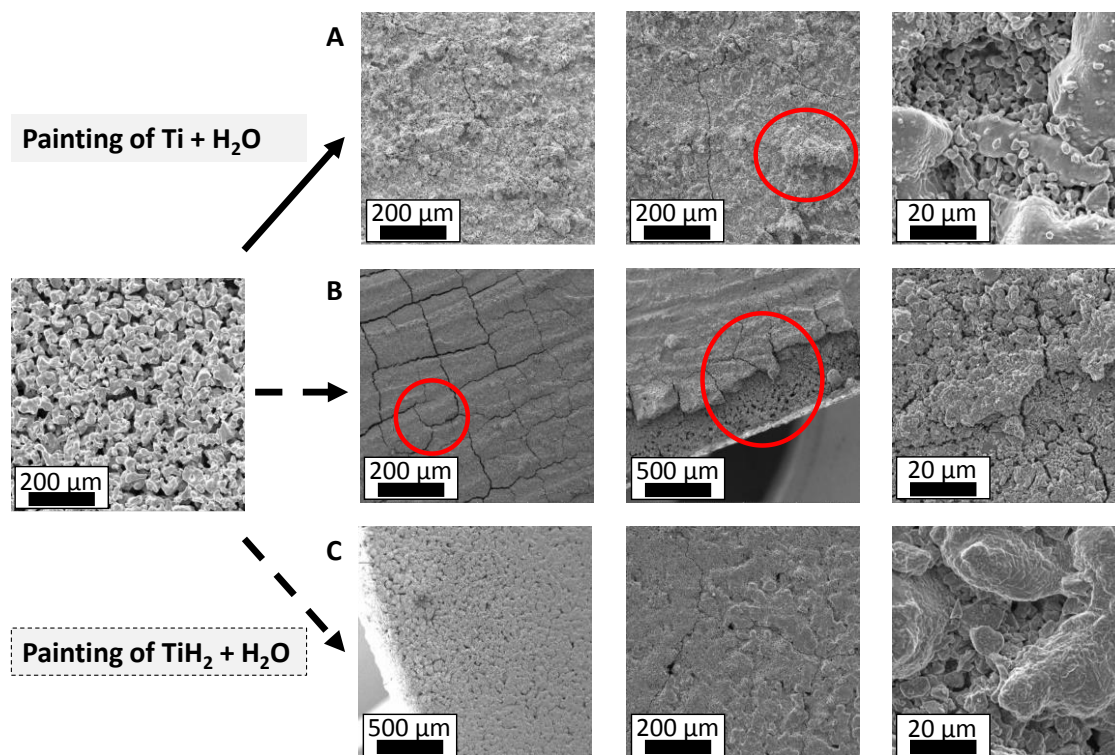


**Fig. 65** Sintered Ti-MPLs based on Ti- and  $\text{TiH}_2$ -powder painted on top of a powder-sintered titanium PTL.

To summarize the results of the preliminary tests shown in this section, doctor-blading or painting at appropriate temperatures showed the potential of being an up-scalable technique for the deposition of MPLs on porous Ti-PTLs. Cross-sections of PTL+MPL compounds should be imaged, to study the influence of fabrication parameters as the temperature, deposition rate and layer thickness. For final MPLs containing a binder, electrically conductive binders should be evaluated to reduce the ohmic resistances of the MPL. For sintering, the composition of the deposited MPLs as well as the sinter parameters need to be adjusted to prevent bending of the substrates, brittle MPLs or the formation of oxide layers during sintering.

## 7.4 Outlook: via MPLs towards advanced DMD-configurations for PEMWE

The development of MPLs for anodic PTLs is not only motivated by an increased contact area towards the CL, but moreover as requirement when transferring the approach of MEAs fabricated by direct membrane deposition (DMD) from PEMFC to PEMWE.<sup>204</sup> As no commercial anodic PTL with smooth MPL was available so far, Stähler et al. used carbon based PTEs at the anode and cathode side to be coated with the membrane material.<sup>206</sup> However, due to degradation concerns, titanium is required at the anode.<sup>97</sup> Holzapfel et al. therefore used aPTEs developed in the frame of this work to fabricate an asymmetric DMD-MEA.<sup>5</sup> The PEM was hereby spray coated directly on a commercial cathodic PTE+MPL and pressed against the in-house fabricated anodic PTE (Fig. 66, asymmetric DMD). The DMD-configuration showed to potential to particularly reduce ohmic losses compared to CCM- and PTE-based MEAs. Reasons for the improved ohmic region could on the one hand be the improved interface between the PEM and CL, but on the other hand also the changed membrane structure when using spray coating instead of e.g. casting. With the availability of a Ti-based MPL, the surface of the anodic PTE could be smoothened and thus a transition from the asymmetric DMD approach towards a symmetric configuration (Fig. 66, symmetric DMD) as in PEMFC could be possible.<sup>81</sup> The MPL could as well be used to increase the interface between anodic PTL and CL when modifying the asymmetric DMD approach towards a bottom-up design by additionally depositing the anodic catalyst layer and MPL on top of the cathode-PEM compound (Fig. 66, bottom-up MEA).

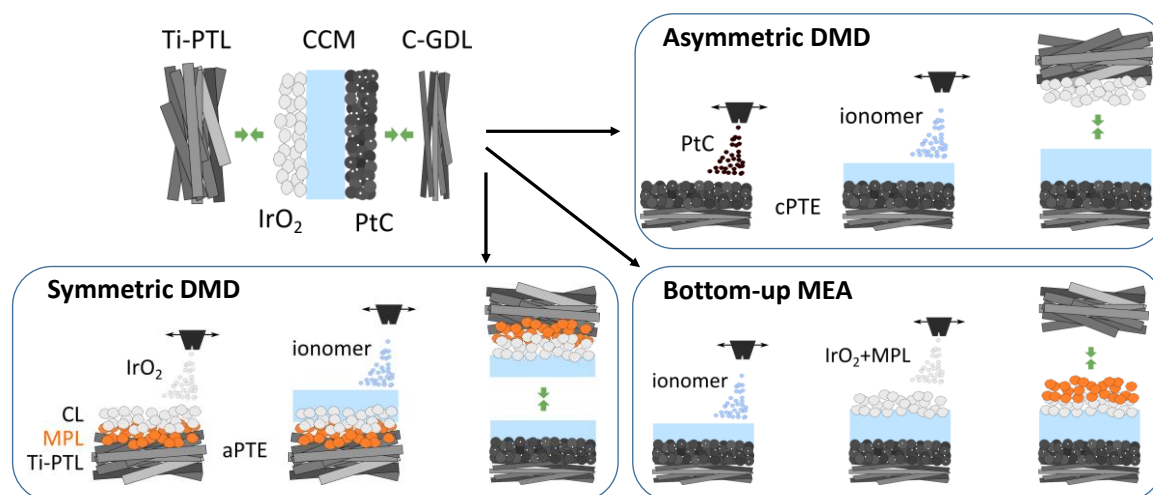


**Fig. 66** Future MEA-configurations for PEMWEs based on the PTEs developed in this work and the deposition of the PEM via DMD on the electrodes. The asymmetric DMD approach<sup>5</sup> can be modified via using an MPL at the anode side towards a symmetric DMD approach or a full bottom-up manufactured MEA with increase interfacial area between the Ti-PTL and CL.



## 8 Noble metal free Mo<sub>3</sub>S<sub>13</sub>-NCNT catalyst based cathodic PTEs\*

This chapter presents the electrochemical and structural characterization of a Mo<sub>3</sub>S<sub>13</sub>-NCNT based catalyst in a PTE-configuration as promising non-noble alternative to platinum for the HER in PEMWEs. The work presented in this chapter was submitted as full research paper with the author of this thesis as joint 1<sup>st</sup> author. The contributions of the author of this thesis to this chapter are:

- Section 8.1 (introduction) was written by the author of this thesis to give an overview on the development of Mo<sub>3</sub>S<sub>13</sub>-NCNT catalyst for the HER in PEMWE
- Section 8.2 (synthesis and characterization of Mo<sub>3</sub>S<sub>13</sub>-NCNT catalyst) was written by the author of this thesis. Data regarding the characterization of the catalyst material was provided by co-authors of the submitted manuscript.
- Sections 8.3 and 8.4 (MEA preparation and characterization) were left as submitted and contain the major contribution of the author of this thesis to the work discussed in this chapter.

In section 8.5, a critical discussion on the performance and applicability of the Mo<sub>3</sub>S<sub>13</sub>-NCNT catalyst was added by the author of this thesis. Data regarding the catalyst activity was provided by co-authors of the submitted manuscript.

---

\*submitted manuscript (2019)

*Holzapfel, P. \*\*, Bühler, M. \*\*, Escalera-López, D., Bierling, M., Speck, F., Vierrath, S., Breitwieser, M., Cherevko, S., Pham, C. and Thiele, S., Fabrication of a robust PEM water electrolyzer based on non-noble metal cathode catalyst: [Mo<sub>3</sub>S<sub>13</sub>]<sup>2-</sup> anchored to N-doped carbon nanotubes*

*\*\*joint first authorship*

## 8.1 Introduction

Alternatives for the costly and precious platinum-based catalysts for the HER in PEMWEs are desperately needed when installing large-scale PEMWE plants to produce green hydrogen.<sup>72, 207</sup> This work focused on the HER in PEMWE cathodes to substitute platinum while maintaining a high performance and durability. From biomimetic studies, molybdenum sulfides ( $\text{MoS}_x$ ) were suggested as promising non-noble electrocatalysts for the HER in acidic environments<sup>208</sup> and a few examples exist in literature using  $\text{MoS}_x$ -based catalyst for the cathode side in full-cell PEMWE operation.<sup>209–211</sup> The high activity for the HER of  $\text{MoS}_2$  NPs was attributed to sulfur atoms at the edges of the molecules and therefore motivates the synthesis of nanosized  $\text{MoS}_x$ -based catalysts with an increased number of active sites (S-atoms at the edges).<sup>212, 213</sup> Kibsgaard et al. therefore synthesized thiomolybdate  $[\text{Mo}_3\text{S}_{13}]^{2-}$  nanoclusters, with nearly all S-atoms having an appropriate atomic structure at edges of the clusters.<sup>214</sup> The number of active sites was drastically increased and the scalable synthesis in combination with a straightforward fabrication of functional layers via drop casting on various supports further motivated the use of the  $[\text{Mo}_3\text{S}_{13}]^{2-}$  clusters to fabricate HER electrodes.

To increase the distribution of the nanosized catalytically active sites as well as the electron conductivity, graphene is a highly interesting support material due to its high electrical conductivity as well as chemical and mechanical stability.<sup>215</sup> Reduced graphene oxide (rGO) as product of chemically modified graphene is a promising supporting material for active sites due to its high electrical conductivity and hydrophilic parts.<sup>216</sup> To decorate rGO with catalyst NPs, a two-step synthesis method was proposed by Pham et al. via decorating sulfur doped reduced graphene oxide (S-rGO) with NPs.<sup>217</sup> In a first step the functionalization of graphene oxide with thiol (-S-H) groups replaced O-atoms by S-atoms and simultaneously partly reduced the graphene oxide to rGO due to the formation of the by-product  $\text{H}_2\text{S}$ . By this, restacking of graphene sheets prior to decoration with NPs was prevented. In the second step, a homogeneous self-assembly of nanoparticles on the S-rGO surface was reached as the thiol groups strongly bind e.g. to transition metal nanoparticles.

Pham et al. successfully showed the applicability of  $[\text{Mo}_3\text{S}_{13}]^{2-}$  cluster decorated S-rGO as noble-metal free catalyst for the HER in PEMWEs as tested in acidic media in a three-electrode setup.<sup>123</sup> The supported  $\text{Mo}_3\text{S}_{13}$ -SrGO catalyst showed a Tafel slope of  $40 \text{ mV dec}^{-1}$  and a current density of  $10 \text{ mA cm}^{-2}$  at an overpotential of 174 mV compared to the unsupported  $[\text{Mo}_3\text{S}_{13}]^{2-}$  clusters with a Tafel slope of  $53 \text{ mV dec}^{-1}$  and overpotential of 244 mV at the same current density. The S-rGO support favoured the availability of active sites as high loadings due to the porous structure and high electrical conductivity. The sufficient stability of the supported  $\text{Mo}_3\text{S}_{13}$ -SrGO catalyst was explained by the strong bond between the S-atoms of the support with the Mo-atoms of the  $[\text{Mo}_3\text{S}_{13}]^{2-}$  clusters. Another advantage of the S-rGO support was the formation of additional active sites due to the S-Mo bond between support and active clusters.

In this work, a commercially available nitrogen doped carbon nanotubes (NCNTs) support for the  $[\text{Mo}_3\text{S}_{13}]^{2-}$  clusters was used. The NCNT support was expected to facilitate the synthesis of a supported  $\text{Mo}_3\text{S}_{13}$  catalyst as well as to increase the porosity, chemical and mechanical stability, and electrical conductivity of the catalyst layer.<sup>218</sup> The supported  $\text{Mo}_3\text{S}_{13}$ -NCNT catalyst was spray coated on carbon PTLs for form cPTEs. The cPTEs were tested in full-cell PEMWE application to study the influence of the catalyst loading, high current densities and constant current operation. The influence of the break-in procedure to activate the catalyst and membrane is discussed in the final section of this chapter.



## 8.2 Synthesis and characterization of Mo<sub>3</sub>S<sub>13</sub>-NCNT catalyst

[Mo<sub>3</sub>S<sub>13</sub>]<sup>2-</sup> clusters<sup>123</sup> were added to commercial NCNTs (ACS materials LLC, USA, > 98 % with 5 wt% N) in dimethyl formamide (DMF) and ultrasonicated for 10 min. The homogeneous mixture was continuously stirred for 24 h during heat-treatment at 140 °C. Distillation under vacuum at 90 °C was used to evaporate the DMF solvent and the dry Mo<sub>3</sub>S<sub>13</sub>-NCNT catalyst was grinded to a homogeneous powder. Fig. 67 shows a TEM image of the decorated Mo<sub>3</sub>S<sub>13</sub>-NCNTs with the flake like clusters homogeneously covering the NCNTs leading to an increased surface roughness.

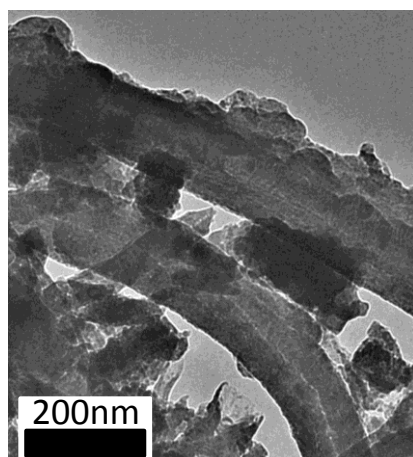


**Fig. 67** TEM image of the NCNTs coated with [Mo<sub>3</sub>S<sub>13</sub>]<sup>2-</sup> clusters.

XPS spectra of the supported and unsupported clusters showed a similar atomic composition indicating the successful coverage of the NCNTs with the [Mo<sub>3</sub>S<sub>13</sub>]<sup>2-</sup> clusters. To evaluate the chemical composition of the clusters after synthesis of Mo<sub>3</sub>S<sub>13</sub>-NCNTs compared to the unsupported clusters, XPS was used to calculate the atomic percentage and ratio of the different functional S-atoms in the compound (terminate, bridge and apical S).<sup>214</sup> XPS revealed, that the ratio of 2.5 of bridge and apical S vs. terminate S was the same in both materials and therefore the catalytic activity for the HER was not reduced when depositing the [Mo<sub>3</sub>S<sub>13</sub>]<sup>2-</sup> clusters on the NCNT support.

The activity of the Mo<sub>3</sub>S<sub>13</sub>-NCNT catalyst was analyzed in a three-electrode-setup (0.5 M H<sub>2</sub>SO<sub>4</sub>, N<sub>2</sub>-saturated) and compared to the unsupported the [Mo<sub>3</sub>S<sub>13</sub>]<sup>2-</sup> clusters and a Pt-disc reference. The Tafel slope of the supported Mo<sub>3</sub>S<sub>13</sub>-NCNT catalyst was ca. 40 mV dec<sup>-1</sup> and therefore lower than the Tafel slope of the unsupported [Mo<sub>3</sub>S<sub>13</sub>]<sup>2-</sup> clusters that was ca. 58 mV dec<sup>-1</sup> and in the same range of the Tafel slope of the Pt-disc reference that was ca. 38 mV dec<sup>-1</sup>. The Mo<sub>3</sub>S<sub>13</sub>-NCNT catalyst showed an activity at 10 mA cm<sup>-2</sup> at an overpotential of 188 mV compared to an overpotential of 233 mV of the unsupported clusters. Whereas the Tafel slope and therefore the reaction mechanism of the HER at the active sites of the supported Mo<sub>3</sub>S<sub>13</sub>-NCNT catalyst was comparable to the Pt-reference, the almost 150 mV higher onset potential is a major drawback of the non-noble Mo<sub>3</sub>S<sub>13</sub>-NCNT catalyst. The higher onset potential and overpotential will determine the overall cell performance in the full-cell characterization regarding the maximum current density that can be applied to the system before reaching a safety limit of the cell voltage due to high overpotentials. It is therefore a crucial engineering task to develop a porous, highly conductive catalyst layer with perfect interfaces towards the PTL and PEM to not further limit the performance of the Mo<sub>3</sub>S<sub>13</sub>-NCNT based catalyst in a MEA configuration by introducing mass transport resistances or high ohmic resistances.

### 8.3 MEA preparation and characterization

For the full-cell tests, two different MEA-configurations were used. For the loading variation, a half-sided anodic CCM ( $1.5 \text{ mg}_{\text{IrO}_2} \text{ cm}^{-2}$  on N115 membrane) purchased from FuelCellsEtc was contacted via a fiber-sintered PTL at the anode side (Bekaert, 1 mm thick,  $20 \mu\text{m}$  fiber diameter). The cathode side consisted of the synthesized  $\text{Mo}_3\text{S}_{13}$ -NCNT catalyst spray coated on a carbon cloth PTL with MPL (FuelCellsEtc, type GDL-CT). The loading of the  $\text{Mo}_3\text{S}_{13}$ -NCNT catalyst was varied while keeping the Nafion content in the catalyst layer constant. For the stability tests, a full PTE-configuration was used with a freestanding N212 membrane sandwiched between two free standing PTEs. The PTEs for the anode side consisted of the same Ti-fiber PTL as used for the loading study but spray coated with  $1.4 \text{ mg}_{\text{IrO}_2} \text{ cm}^{-2}$ -based catalyst layer as described in a previous work.<sup>1</sup> The PTE for the cathode side was a spray coated  $\text{Mo}_3\text{S}_{13}$ -NCNT-based catalyst layer with a loading of  $3 \text{ mg cm}^{-2}$  deposited on the same carbon cloth based PTL+MPL as used in the loading study. A commercial Pt/C based cathodic PTE as well based on the same carbon cloth PTL+MPL was used as reference (FuelCellsEtc,  $0.5 \text{ mg}_{\text{Pt}} \text{ cm}^{-2}$ ). The active areas were  $5 \text{ cm}^2$ .

The catalyst layers were spray coated with the device Exacta Coat from Sono-Tek with an ultrasonic nozzle type AccuMist (48 kHz). The catalyst inks consisted of 98 wt% solvents (1:3 DI-water vs. 2-Propanol). The solids consisted of 75 wt%  $\text{Mo}_3\text{S}_{13}$ -NCNTs mixed with 10 wt% carbon black (Vulcan XC-72R, FuelcellsEtc) to increase the electrical conductivity and porosity of the catalyst layer, as well as 20 wt% Nafion ionomer (Nafion® D520, FuelCellStore). First, the catalyst and carbon black powder were inserted in a glass bottle followed by the DI-water. 2-Propanol and Nafion® were added afterwards and the glass bottle was agitated after adding every new component. After sonication for 30 min (Hielscher, model UIS250L, 0.55 W, 90 % amplitude) in an ice bath under continuous stirring, the ink was further stirred for 48 h. Right before spray coating, the ink was sonicated and vortexed again before filling a portion of the ink in the syringes of the spray coater. The other part of the ink was stirred to not risk the sedimentation of particles. For spray coating, a meander shaped pattern with a pitch of 1.5 mm and path offset of every second path of 0.75 mm was set and a path speed of  $170 \text{ mm sec}^{-1}$ . The temperature of the hot plate was set to  $110^\circ\text{C}$ . A flow rate of  $0.45 \text{ ml min}^{-1}$  combined with an ultrasonic power of 5 W ensured a homogeneous spray mist. The shaping air was set to 0.6 kPa and the height of the nozzle was set to 37 mm. To determine the catalyst loading, the catalyst layer was as well spray coated on a  $1 \text{ cm}^2$  rectangular metal piece, which was weighted on a microscale (Sartorius, model ME 36S).

The test cell, test bench and parameters of the break-in as well as the recording of the polarization curves was described in chapter 3. The impact of the break-in procedure on the catalyst performance and stability will be discussed in the last section of this chapter.

### 8.4 Full-cell characterization

The performance of the  $\text{Mo}_3\text{S}_{13}$ -NCNT catalyst for the HER in PEMWE was tested in full-cell MEA-configurations with first studying the impact of varying the loading of the catalyst on the polarization behavior followed by a 100 h stability test at a constant current of  $1 \text{ A cm}^{-2}$ .

#### 8.4.1 Variation of the $\text{Mo}_3\text{S}_{13}$ -NCNT-loading

For the loading variation, cathodes with  $[\text{Mo}_3\text{S}_{13}]$  catalyst loading of 1.5, 3, 4.5 and  $5.8 \text{ mg cm}^{-2}$  were fabricated tested in a full-cell setup. Fig. 68 shows the cell voltage, HFR and HFR-free cell voltage as well as a zoom in the kinetic region of the HFR-free cell voltage plotted on a semi-logarithmic scale to study the kinetic region.



The overall cell performance (Fig. 68 A) was improved when increasing the loading, but did not significantly vary for  $[\text{Mo}_3\text{S}_{13}]$  catalyst loadings between 3.0 and 5.8  $\text{mg cm}^{-2}$  at the maximum current density of 2  $\text{A cm}^{-2}$ . There were however differences in the kinetic, ohmic and mass transport region of the polarization curve due to varying the catalyst loading. The HFR-free data (Fig. 68 B) combines kinetic and mass transport losses and showed no increased slope when approaching higher loadings. The porous and highly conductive NCNT support therefore led to a high availability of active sites while maintaining a sufficient mass transport even at a  $[\text{Mo}_3\text{S}_{13}]$  catalyst loading of 5.8  $\text{mg cm}^{-2}$ , which showed only a slightly higher HFR-free cell voltage compared to the lower loading of 4.5  $\text{mg cm}^{-2}$ .

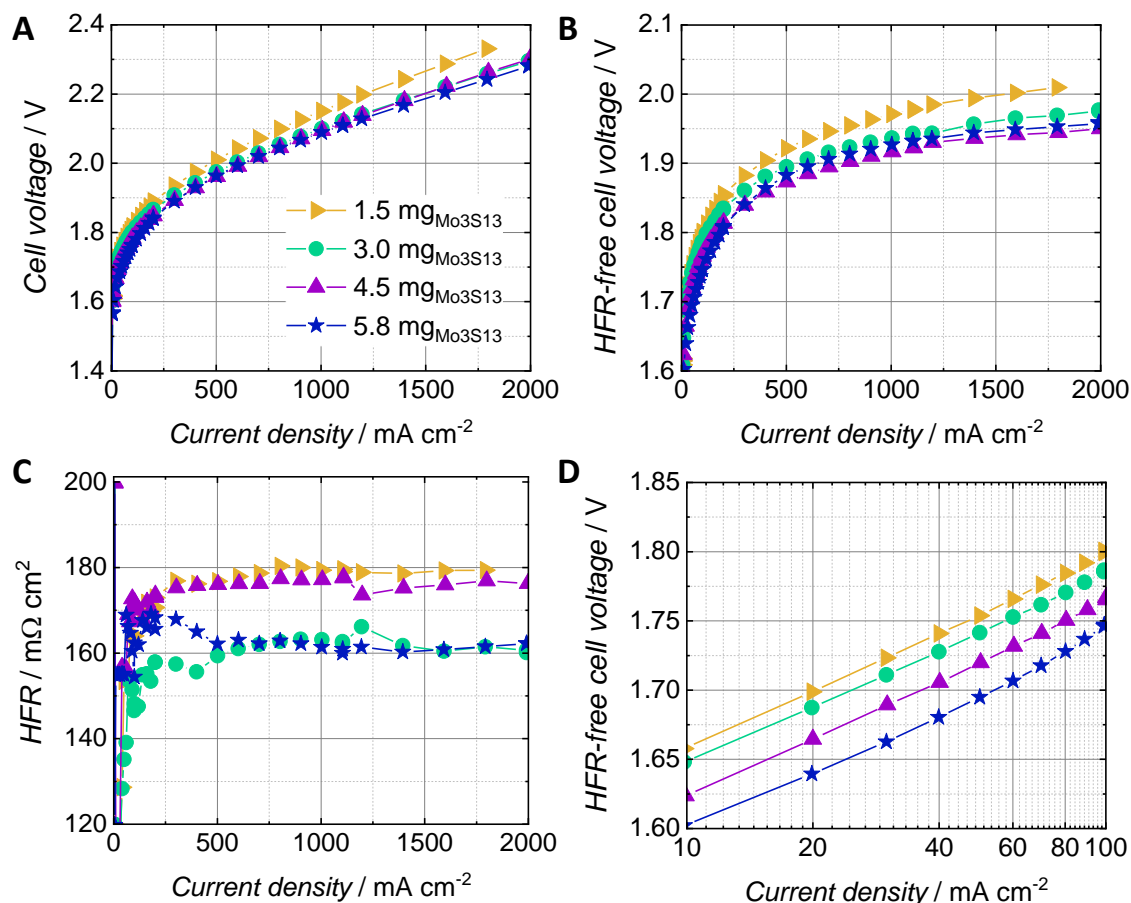


**Fig. 68** A Cell voltage of the cPTes with varying  $\text{Mo}_3\text{S}_{13}$ -loadings of 1.5, 3, 4.5 and 5.8  $\text{mg cm}^{-2}$  B HFR-free cell voltage C HFR D Zoom in the kinetic region of the HFR-free cell voltage.

No trend of the HFRs of the different samples (Fig. 68 C) related to the increase of the catalyst loading was seen but the tendency of a decreasing HFR with increasing current density for a loading of 5.8  $\text{mg cm}^{-2}$ . This could be related to the production of waste heat at high currents in the thick catalyst layer by around 20  $\text{m}\Omega \text{ cm}^2$ , which in turn could reduce protonic resistances in the ionomer.<sup>111, 141, 163</sup> The kinetic region (Fig. 68 D) showed an improved activity when increasing the catalyst loading. To compare the performance of the  $\text{Mo}_3\text{S}_{13}$ -NCNT catalyst in this work with a publication by Ng et al.<sup>209</sup> a  $[\text{Mo}_3\text{S}_{13}]$  catalyst loading of 3.0  $\text{mg cm}^{-2}$  was used for the stability test in section 8.4.2.

#### 8.4.2 Performance of Mo<sub>3</sub>S<sub>13</sub>-NCNT under high cell current density

To show the capability of the non-noble Mo<sub>3</sub>S<sub>13</sub>-NCNT catalyst for high current density application, the MEA-configuration was changed from half-sided CCM-configuration as used for the loading study to a full PTE-configuration. In the full PTE-configuration, a free standing membrane is pressed against two PTEs as the anode and cathode side respectively. The full-PTE configuration with an in-house fabricated IrO<sub>2</sub>-based anodic PTE showed superior performance compared to the half-sided CCM-configuration in earlier studies<sup>1</sup> and was therefore chosen to be able to increase the current density during full-cell tests in this work. To further increase the current density, a thinner N212 membrane instead of the N115 membrane in the loading study was applied. At high current densities, a high amount of protons is generated at the anode side, which need to be electrochemically reduced at the cathode side to form hydrogen. The catalyst layer at the cathode side therefore needs to exhibit enough active sites for a high reaction rate. The high amount of hydrogen evolving at the cathode is then critical for the degradation rate of the catalyst layer. Gas bubbles could lead to mechanical stress between the cPTL and CL as well as at the active sites itself and in case of an insufficient porosity of the CL, mass transport problems could occur. The performance under high current densities and the stability during a constant current hold of the Mo<sub>3</sub>S<sub>13</sub>-NCNT-based cathode with a loading of 3 mg cm<sup>-2</sup> was compared to a Pt/C-reference cathode with a standard loading of 0.5 mg cm<sup>-2</sup>.

The stability of the cPTE with a [Mo<sub>3</sub>S<sub>13</sub>] catalyst loading of 3 mg cm<sup>-2</sup> was tested for 100 h at a constant current of 1 A cm<sup>-2</sup>. Fig. 69 shows the cell voltage, HFR and HFR-free cell voltage recorded during the stability test. The cell voltage (Fig. 69 A) of the MEA with Mo<sub>3</sub>S<sub>13</sub>-NCNT cathode did slightly increase (degrade) with a rate of 83  $\mu$ V h<sup>-1</sup> due to the increase in HFR-free cell voltage (Fig. 69 B). The HFR (Fig. 69 C) of the Mo<sub>3</sub>S<sub>13</sub>-NCNT cathode stabilized at a value of around 105 m $\Omega$  cm<sup>2</sup> after ca. 30 h constant current hold. The HFR of the Pt/C-reference was in the range of 88 m $\Omega$  cm<sup>2</sup> and showed no significant change during the stability test, which was as well true for the HFR-free cell voltage and thus the overall cell voltage.

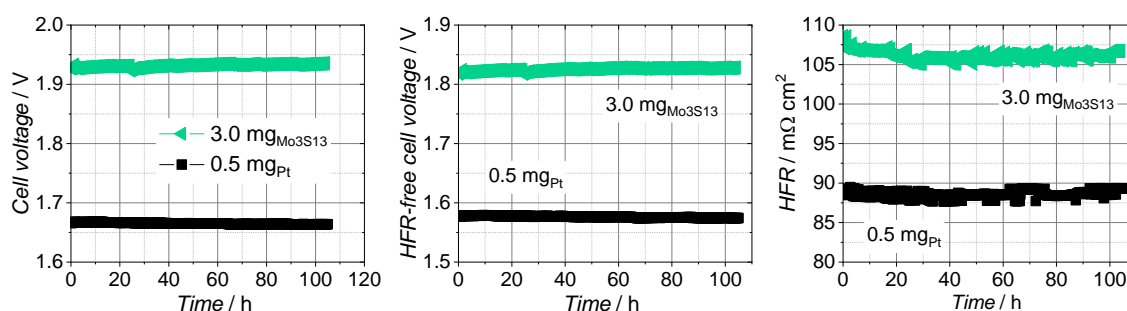


**Fig. 69** A Cell voltage B HFR C HFR-free cell voltage during 100 h at 1 A cm<sup>-2</sup> constant current hold.

To study the changes in polarization behavior of the pristine vs. the MEA after the 100 h stability test, polarization curves were recorded prior to the test and after 100 h (Fig. 70). The Mo<sub>3</sub>S<sub>13</sub>-NCNT catalyst based cathode delivered a high current density of 4 A cm<sup>-2</sup> at a cell voltage of 2.36 V (Fig. 70 A). To our knowledge, this is an unprecedented high current density reported for a noble metal free HER catalyst of PEMWE. The HFR-free cell voltage (Fig. 70 B) showed slightly higher mass transport losses compared to the Pt/C reference which could be the result of the thicker Mo<sub>3</sub>S<sub>13</sub>-NCNT catalyst layer with a 6 times higher catalyst loading than the reference. The HFR-free cell voltage of the Pt/C-reference slightly improved (decreased) due to the 100 h constant current hold, whereas the HFR-free cell voltage of the Mo<sub>3</sub>S<sub>13</sub>-NCNT catalyst based cathode slightly increased. The HFR (Fig. 70 C) of the Pt/C-reference slightly improved after the 100 h stability test

and showed no significant change with increasing current density. The HFR of the  $\text{Mo}_3\text{S}_{13}$ -NCNT based cathode however changed with increasing current density. The pristine non-noble metal MEA showed a reducing HFR with increasing current density, whereas the 100 h altered MEA showed a HFR which was strongly increasing with increasing current density. Both HFRs approached a value of around  $112 \text{ m}\Omega \text{ cm}^2$  at the final current density of  $4 \text{ A cm}^{-2}$  compared to the HFR of the reference MEA of  $92 \text{ m}\Omega \text{ cm}^2$ . The change of the HFR with current density is not yet fully understood but the opposing trend of the pristine vs. the MEA after 100 h constant current hold is an interesting finding and should be investigated in more detail. Fig. 70 D shows the kinetic region of the HFR-free cell voltage revealing the most prominent drawback of the non-noble  $\text{Mo}_3\text{S}_{13}$ -NCNT catalyst which is the lower activity for the HER and worse kinetics when in the electrode configuration. The HFR-free cell voltage of the pristine  $\text{Mo}_3\text{S}_{13}$ -NCNT catalyst at a current density of  $10 \text{ mA cm}^{-2}$  is almost  $113 \text{ mV}$  higher compared to the Pt/C-reference.

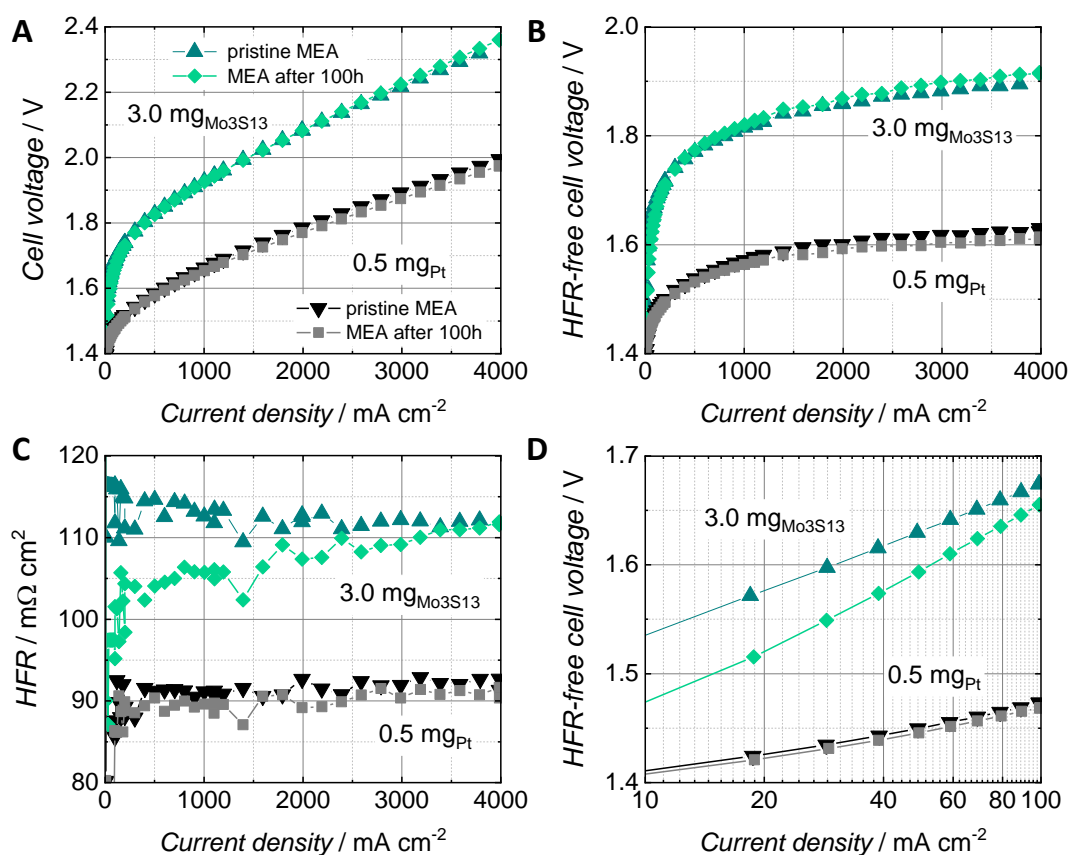


**Fig. 70** Polarization curves recorded of the pristine MEAs and after the 100 h constant current hold at  $1 \text{ A cm}^{-2}$ . A Cell voltage B HFR-free cell voltage C HFR D Zoom in the kinetic region of the HFR-free cell voltage.

The constant current hold could however improve the HFR-free cell voltage of the  $\text{Mo}_3\text{S}_{13}$ -NCNT-based cathode at  $10 \text{ mA cm}^{-2}$  by around  $63 \text{ mV}$  that could be related to more active sites being available. As the slope of the curve in the kinetic region is increasing stronger for the  $\text{Mo}_3\text{S}_{13}$ -NCNT-based cathode being tested for 100 h, mass transport losses with increasing current density indicate the insufficient transport of protons in the catalyst layer and towards the PEM. One explanation for these effects could be the exposure of more active sites after 100 h constant current hold, which are not as good connected to the ionic network as the pristine active sites. Therefore, a higher activity at low current densities would be the case but as more protons need to be transported with increasing current density, the ionic network is not sufficient. The availability of more active sites not well connected to the ionomer in the catalyst layer could be

an indication for catalyst support degradation. This idea would be supported by the increasing HFR with increasing current density as for high currents the electrical conductivity within the catalyst layer or at the interface towards the PTL seems to be insufficient.

The stability of the  $\text{Mo}_3\text{S}_{13}$ -NCNT cathode presented in this work was superior to the  $3 \text{ mg cm}^{-2}$   $\text{Mo}_3\text{S}_{13}$ -CB (carbon black) based cathode in CCM-configuration using a N115 membrane as presented by Ng et al.<sup>209</sup>. In that work, a constant voltage of 1.85 V was held for 24 h and the required cell voltage to reach  $0.5 \text{ A cm}^{-2}$  was increased by 150 mV after the 24 h stability test. The cell voltage at  $0.5 \text{ A cm}^{-2}$  when using the  $\text{Mo}_3\text{S}_{13}$ -NCNT-based cathodes in PTE-configuration in this work was even 2.4 mV lower after the 100 h constant current operation at  $1 \text{ A cm}^{-2}$ . The current density of the full-cell test in this work using the  $\text{Mo}_3\text{S}_{13}$ -NCNT-based cathode was to the best of our knowledge the highest reported so far, as Ng et al. showed a maximum current density of ca.  $1.1 \text{ A cm}^{-2}$  at 2 V and King et al.<sup>219</sup> demonstrated a maximum current density of around  $1.8 \text{ A cm}^{-2}$  at 2.3 V when using  $1 \text{ mg cm}^{-2}$  of a non-noble cobalt phosphide (CoP) catalyst for the HER in a full PTE-configuration with a N117 Nafion membrane. King et al. however reported a remarkable stability of the CoP-based cathode when applying a constant current of  $1.86 \text{ A cm}^{-2}$  for more than 1700 h even when carbon based PTLs at the anode and cathode were used. In our work, a current density as high as  $4 \text{ A cm}^{-2}$  at a cell voltage of 2.36 V could be demonstrated even after 100 h of constant current operation at  $1 \text{ A cm}^{-2}$ .

## 8.5 Critical discussion

The suitability of the synthesized  $\text{Mo}_3\text{S}_{13}$ -NCNT catalyst as non-noble substitute for Pt/C-based catalysts for full-cell PEMWE application was successfully evaluated in this work. The catalyst was capable of driving current densities as high as  $4 \text{ A cm}^{-2}$  at a cell voltage below 2.4 V when mounted in a full PTE-configuration with a  $50 \mu\text{m}$  thin N212 membrane. Increasing the  $\text{Mo}_3\text{S}_{13}$ -NCNT catalyst loading to almost  $6 \text{ mg cm}^{-2}$  did not significantly increase mass transport losses and showed an improved kinetic region indicating the positive impact of the porous and highly conductive NCNT support. In three-electrode-setup measurements, the  $\text{Mo}_3\text{S}_{13}$ -NCNT catalyst showed a similar Tafel slope compared to the Pt-disc reference indicating a similar reaction mechanism for the HER of the non-noble catalyst synthesized in this work. The activity of the supported non-noble catalyst was lower compared to the Pt-reference and the onset potential was ca. 150 mV higher. These material specific voltage losses are most probably one major drawback for an industrial application of the  $\text{Mo}_3\text{S}_{13}$ -NCNT-based non-noble metal catalyst but might on the other hand be suitable for the production of hydrogen by electrolysis when using excess electrical energy produced by renewables with negligible energy costs.

To increase the activity, the loading can be increased. However, this comes along with fabrication limitations as high loadings lead to deposition times of several hours already per  $200 \text{ cm}^{-2}$  active area when using spray coating. Thick layers also bear the risk of getting brittle during drying. The crack-free assembly of brittle electrodes in the test cells cannot be ensured and parts of the catalyst layer could even peel off the cathodic PTL+MPL substrate. Therefore, other methods to improve the performance should be applied as e.g. reducing ohmic and mass transport losses. Ohmic losses can be reduced via improving interfacial contact areas between the CL and the PTL+MPL as well as between the CL and the PEM and via increasing the electrical conductivity of the bulk material. Mass transport losses can be avoided by using thin and porous layers indicating that e.g. a study dedicated to the MPL at the cathode side could be a promising development step (for PEMWE in general). Depositing the membrane directly on the CL could as well improve the interfacial contact area between PEM and CL as shown in DMD approaches for the PEMFC.<sup>220</sup>

Regarding the activation of the MEA, the influence of the break-in procedure should be studied in more detail. Fig. 71 shows the break-in data of the full PTE-configuration using a thinner N212 membrane sandwiched between an in-house fabricated anodic PTE and a cathodic PTE with a  $\text{Mo}_3\text{S}_{13}$ -NCNT catalyst loading of  $3 \text{ mg cm}^{-2}$  (samples of the 100 h stability test). The break-in procedure consists of three subsequent voltage-cycling steps, each repeated for 10 times, while recording the current density of the MEA (Fig. 71). The current density is shown on the x-axis for better comparison with the depiction of the polarization curves. The “large” curves correspond to the 1<sup>st</sup> and 3<sup>rd</sup> cycling between 1.4 and 2.2 V and the “smaller” curves to the 2<sup>nd</sup> cycling between 2.2 and 2.3 V. The change in current density between start and end point of each cycling step but even more between the start and end point of the complete break in procedure (1<sup>st</sup> and 3<sup>rd</sup> cycling) can be attributed to the activation of the catalyst layer as well as of the membrane. Fig. 71 shows the Pt-reference nearly unaffected by the voltage cycling, as the current density did not increase significantly during the break-in. The voltage cycling above 2 V could not be performed as the current would have exceeded  $4 \text{ A cm}^{-2}$ , which corresponds to the limiting current of the potentiostat of 20 A as the active area was  $5 \text{ cm}^2$ . The break-in procedure had however a significant impact on the cell performance when using  $\text{Mo}_3\text{S}_{13}$ -NCNT cathodes. The current density was increased by ca.  $600 \text{ mA cm}^{-2}$  at 2.2 V due to the break-in procedure (difference between first current density measured at 2.2 V of the 1<sup>st</sup> cycling step and the final current density measured at 2.2 V of the 3<sup>rd</sup> cycling step).

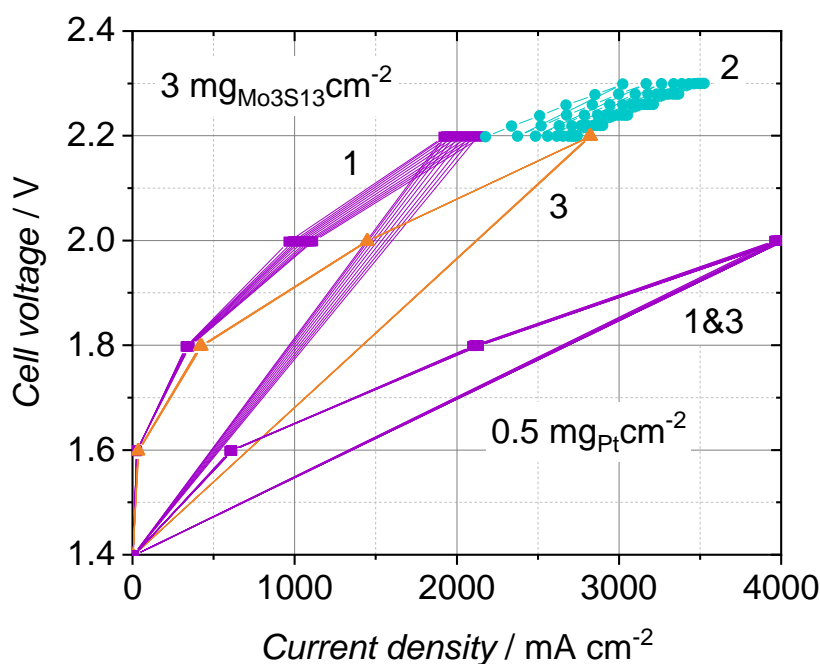


**Fig. 71** Break-in data of the  $\text{Mo}_3\text{S}_{13}$ -NCNT-based cPTE with a loading of  $3 \text{ mg cm}^{-2}$  vs. the Pt/C-reference with a loading of  $0.5 \text{ mg}_{\text{Pt}} \text{ cm}^{-2}$ . The cPTEs were tested in a full PTE-configuration using a N212 membrane (see 100 h stability test). The numbers indicate the break-in steps with the 1<sup>st</sup> and 3<sup>rd</sup> being the voltage cycling between 1.4 and 2.2 V and the 2<sup>nd</sup> one the voltage cycling between 2.2 and 2.3 V.

Conditioning of the MEA containing the  $\text{Mo}_3\text{S}_{13}$ -NCNT at high voltages showed a positive effect on the cell performance, as the maximum current density could be significantly increased. An increased current density leads to an increased formation of hydrogen bubbles at the cathode and could therefore as well be a risk for the mechanical stability of the catalyst layer. Further studies including characterization of the  $\text{Mo}_3\text{S}_{13}$ -NCNT catalyst degradation under accelerated stress test conditions in a three-electrode scanning flow cell connected downstream to a mass spectrometer, are therefore ongoing.



## 9 Summary

The most important findings and conclusions of this work on developing novel electrodes for PEMWE are highlighted in this chapter. The content of chapters marked with a star\* has been published or submitted as full scientific research papers.

**Fabrication of porous transport electrodes via spray coating** - Spray coating was used as fast and up-scalable deposition technique for the fabrication of PTEs, but a sophisticated material preparation and parameter control was necessary for reproducible results. Especially particle sedimentation in metal based inks during ink mixing or spray coating increased the final Nafion loading in the sprayed CLs by almost five times, as evaluated with TGA-measurements.

**From Catalyst Coated Membranes to Porous Transport Electrode Based Configurations in PEM Water Electrolyzers\*** - In chapter 4, MEA-configurations were gradually changed from the standard CCM-type approach to full PTE-type configurations. The influence of the changed membrane-electrode interface on the polarization behaviour was correlated to structural data of the electrodes. The cathodic membrane-electrode interface had a rather small impact but the rate determining anode side showed reduced ohmic losses and the tendency of a stabilizing mass transport overpotential at high current densities when using anodic PTEs. The reduced protonic interface of PTEs towards the membrane however led to a non-optimal kinetic region. The potential of PTE-configurations to perform similar to CCM-type approaches, but with the advantage of a facilitated manufacturing was indicated.

**Optimization of anodic porous transport electrodes for proton exchange membrane water electrolyzers\*** - In chapter 5, anodic PTEs based on commercial porous powder- and fiber-sintered Ti-PTLs were optimized. Coarser fiber-sintered PTLs showed an unexpected better cell performance at loadings above  $1 \text{ mg}_{\text{IrO}_2} \text{ cm}^{-2}$ . A variation of the Nafion loading revealed showed an in average improved performance at lower ionomer contents but also a worse reproducibility. The stability of the most reproducible PTE with 9 wt% Nafion at a loading of  $1.4 \text{ mg}_{\text{IrO}_2} \text{ cm}^{-2}$  was demonstrated for 200 h at a constant current hold of  $1 \text{ A cm}^{-2}$ . The presented material study is, to the best of the authors knowledge, the first approach reported to optimize spray coated anodic PTEs and could be transferred as well to the cathode side.

**IrO<sub>2</sub> coated TiO<sub>2</sub> core-shell microparticles advance performance of low loading proton exchange membrane water electrolyzers\*** - In chapter 6, the fabrication of high performing aPTEs at low noble metal loadings was presented by combining the gained knowledge of optimizing anodic PTEs with a supported IrO<sub>2</sub>@TiO<sub>2</sub> core-shell catalyst synthesized by Dr. C. Pham. The improved kinetic and ohmic region of the core-shell structure when deposited on a titanium fiber-sintered substrate led to a by 160 mV improved performance of 1.95 V at  $5 \text{ A cm}^{-2}$  when using a N212 Nafion membrane in the PTE-configuration at a loading of  $1.2 \text{ mg}_{\text{Ir}} \text{ cm}^{-2}$ . Gradient sized catalyst layers for the anode side showed the potential of further improving the cell performance.

**Development of titanium based MPLs for anodic Ti-PTLs** – In chapter 7 preliminary studies to fabricate Ti-powder based MPLs directly on commercial Ti-PTL substrates were evaluated to form a smooth, microporous transition layer on top of coarse PTLs towards the CL. To increase the electrical conductivity of the MPLs containing a binder, the use of an electrically conductive polymer binder was suggested. Sintering of Ti-MPLs showed promising results, a sophisticated process control is however required for upscaling. MPLs were motivated as key functional layer in advanced DMD-configurations to be able to deposit both, the catalyst and membrane, respectively on the PTL+MPL compound.

**Noble metal free Mo<sub>3</sub>S<sub>13</sub>-NCNT -based cathodic PTEs\*** - Chapter 8 presented the work on a noble-metal free Mo<sub>3</sub>S<sub>13</sub>-NCNT-based cathodic CL deposited on a carbon cloth PTL. A 100 h constant current hold at 1 A cm<sup>-2</sup> was performed as stability test of a Mo<sub>3</sub>S<sub>13</sub>-NCNT -based cathode with a loading of 3 mg cm<sup>-2</sup>. The Mo<sub>3</sub>S<sub>13</sub>-NCNT-PTE was capable of high current densities of 4 A cm<sup>-2</sup> at a cell voltage of 2.36 V and showed only small degradation of 83  $\mu\text{V h}^{-1}$ . This performance is to the best of the authors knowledge, the highest reported for a PEMWE MEA with non-noble HER catalyst. The voltage driven break-in of the Mo<sub>3</sub>S<sub>13</sub>-NCNT-cathodes had a positive impact on the MEA-performance, and is therefore planned to be further investigated in combination with degradation studies of the catalyst.



## 10 Outlook

The development of anodic and cathodic PTEs in this work showed the potential of PTE-based MEAs to increase the performance and to reduce manufacturing costs compared to state-of-the-art CCM-based approaches. The results and identified challenges regarding the development of PTEs for PEMWE can now serve as base studies for further development steps as described below.

**Advanced electrochemical and structural characterization to support an extensive screening of materials and fabrication parameters** – A deeper understanding of the interfacial properties and composition of the different functional layers of the MEA is expected to reveal further parameters to optimize the performance and fabrication of novel MEA-configurations for PEMWEs. Especially when approaching low noble metal loadings, e.g. the amount of ionomer needs to be adjusted and the influence of interfacial surface properties of the porous substrates in contact with the thin CLs increases. To guide the extensive parameter and material screening and to be able to better distinguish between contributions of kinetic, mass transport and ohmic losses on the polarization behaviour, impedance spectroscopy and a variation of operation parameters as e.g. the temperature are planned. The availability of a reference electrode at the interface between the PEM and CL could as well deliver a more detailed picture of the performance of the MEAs. Results of the advanced electrochemical analysis could then be correlated to a more detailed structural analysis of the porous electrodes gained from tomographic analysis using FIB-SEM data. An advanced material study on suitable PTLs, MPLs and the catalyst layer composition is expected to not only contribute to anode PTE development but as well to optimizations at the cathode side.

**Evaluation of gradient size effects in porous electrodes** - The development of a cost efficient and stable Ti-based MPL for the anode side is one major goal for the future optimization of Ti-PTLs for PEMWE. By the MPL, a pore size gradient from the coarse titanium based PTL towards thin catalyst layers can be established leading to first an increased electrical interface between CL and PTL. A MPL in the PTE setup would on top increase the protonic interface between PTE and PEM due to the smooth surface of the electrode. In addition, the infiltration of the PTL by catalyst particles could be prevented by an MPL and therefore the catalyst utilization increased. A homogeneous, smooth anodic PTL+MPL compound with the CL deposited on top could then allow for a symmetric DMD-design with the membrane deposited directly on the free standing anodic and cathodic PTEs. The MPL is therefore a key functional layer to allow for a more flexible and advanced MEA-design for PEMWEs. The MPL is also interesting in combination with the idea of a gradient particle sized CL as presented in the context of supported core-shell particles. The evaluation of an advanced electrode structure by first reducing the surface near pores of the PTL via the MPL, followed by the deposition of bigger catalyst particles closer to the MPL and smaller catalyst particles closer to the dense surface of the membrane is therefore planned.

**Characterization of the longterm stability of PTE-configurations** – The test bench used in this work was not designed for longterm tests, which are however a crucial characterization criteria when developing novel electrodes and MEAs for industrial applications. In this work, continuous operation at a maximum of 200 h was performed, while profound degradation studies deliver tests in the range of 400-1000 h continuous operation even at literature level.<sup>139, 140, 221</sup> For this, a modified test bench and test cell are needed to prevent degradation and to allow for a safe operation of the PEMWE equipment over several hundred hours. Minimum requirements are e.g. longterm corrosion stable coatings for the Ti-flow fields, an ion-exchanger to purify the DI-water during operation as well as the possibility to take and analyse samples of the gaseous and liquid phase to monitor degradation of the MEA materials and gas crossover.



## List of publications

### Publications in peer reviewed journals

2019

- **M. Bühler**, P. Holzapfel, D. McLaughlin and S. Thiele, *From catalyst coated membranes to porous transport electrode based configurations in PEM water electrolyzers*, *J. Electrochem. Soc.*, **166**(14), F1070-F1078 (2019).
- **M. Bühler**, P. Holzapfel, F. Hegge, M. Bierling, S. Vierrath and S. Thiele, *Optimization of porous transport electrodes for PEM water electrolysis*, *J. Mater. Chem. A*, **165**, F305 (2019)
- C. Pham\*, **M. Bühler\***, J. Knöppel, M. Bierling, D. Seeberger, D. Escalera-López, K. J. J. Mayrhofer, S. Cherevko and S. Thiele, *IrO<sub>2</sub> coated TiO<sub>2</sub> core-shell microparticles advance performance of low loading proton exchange membrane water electrolyzers*, 2019 [submitted manuscript]  
\*joint first authors
- P. Holzapfel, **M. Bühler**, C. Pham, F. Hegge, T. Böhm, D. McLaughlin, M. Breitwieser and S. Thiele, *Directly coated membrane electrode assemblies for proton exchange membrane water electrolysis*, 2019 [submitted manuscript]
- P. Holzapfel\*, **M. Bühler\***, D. Escalera-López, M. Bierling, F. Speck, S. Vierrath, M. Breitwieser, S. Cherevko, C. Pham and S. Thiele, *Fabrication of a robust PEM water electrolyzer based on non-noble metal cathode catalyst: [Mo<sub>3</sub>S<sub>13</sub>]<sup>2-</sup> anchored to N-doped carbon nanotubes*, 2019 [submitted manuscript]  
\*joint first authors

### Conference contributions

2019

- P. Holzapfel\*, **M. Bühler\***, C. Pham and S. Thiele, *Molybdenum sulphide based cathodes for PEM water electrolysis – catalyst synthesis and loading variation*, EFCD Conference 15<sup>th</sup>-18<sup>th</sup> September 2019, La Grande Motte, France (Talk)  
\*joint first authors
- **M. Bühler**, P. Holzapfel, M. Bierling and S. Thiele, *Porous transport electrodes for PEM water electrolysis: improved performance via studying materials interfaces*, ICE Conference 9<sup>th</sup>-13<sup>th</sup> June 2019, Loen, Norway (Talk)

2018

- **M. Bühler**, F. Hegge, P. Holzapfel and S. Thiele: *Towards direct membrane deposition (DMD) for PEM water electrolyzers – development of innovative electrodes deposited directly on porous transport substrates*, f-cell 18<sup>th</sup>-19<sup>th</sup> September 2018, Stuttgart, Germany (Poster)

- **M. Bühler**, F. Hegge, P. Holzapfel and S. Thiele: Porous Transport Electrodes – The Influence of Depositing Electrodes on Porous Transport Layers on the Polarization Behaviour of PEM Water Electrolyzers, ISE Meeting 2<sup>nd</sup>-7<sup>th</sup> September 2018, Bologna, Italy (Poster)

2017

- S. Vierrath, M. Breitwieser, **M. Bühler**, C. Klose, R. Zengerle and S. Thiele: Additive Fertigung für Brennstoffzellen und Elektrolyse, MST Kongress 22<sup>th</sup>-25<sup>th</sup> October 2017, Munich, Germany, (Conference article)
- **M. Bühler**, C. Klose, F. Hegge, T. Lickert and S. Thiele: *A Novel Fabrication Technique for Electrodes of PEM Water Electrolyzers*, ECS Transactions 80.8, 1069-1075 (2017) & 232nd ECS MEETING 1<sup>st</sup>-5<sup>th</sup> October 2017, Washington DC, USA (Talk and conference article)
- C. Klose, **M. Bühler**, S. Vierrath, N. Baumann, T. Lickert, A. Fallisch and S. Thiele: *Direct membrane deposition – a novel fabrication method for PEMWEs*, ICE Conference 12<sup>th</sup>-15<sup>th</sup> June 2017, Copenhagen, Denmark (Poster)

## Acknowledgements

I would like to thank all members of the group Electrochemical Energy Systems (EES) for the extraordinary working atmosphere. The enthusiasm not only for the own research questions but for the entire portfolio of EES technologies, materials and applications is a unique chance to connect smart people with smart ideas to crosslink their knowledge. Thanks for supporting me especially at long laboratory days with some nice words and a smile. I would particularly like to express my thanks to:

Matthias Breitwieser and Severin Vierrath, for their support, fruitful discussions as well as constructive criticism. Thanks for showing us every day that everyone is a valuable member of the group and that we can only successfully grow and learn when we all work together.

Carolyn Klose and Lena Bleck, for their support especially in the final phase of preparing this thesis. Thanks for helping me, whenever I had a question.

Friedemann Hegge, for the great time when designing the test cell and test bench. I think we were both very proud when what we finally assembled even turned out to work quite nicely. Thank you also for motivating me several times and the reliable supply with suits.

Peter Holzapfel and Dunia Abed-el-Hafez for being the best master students I have ever had. You motivated me several times and I learned many new things from you.

Chuyen Pham, for teaching me how to carefully read and write scientific articles, and being more than once a scientific mentor. Thanks as well for motivating me and for the many good discussions we had.

Michel Suermann, for his great help when discussing paper work and his critical input regarding the work of this thesis.

The many technical and administrative staff members of the IMTEK who support us every day. Especially Gerhard Birkle, Melanie Baumann, Ulrike Grundmann, Antigoni Zouridaki, Zsolt Kis and Michael Reichel. The straightforward, smart and fast solutions for IT-problems, lab equipment or administrative questions saved a lot of time and nerves.

I would further like to thank my former group leader and scientific supervisor Prof. Dr. Simon Thiele for the opportunity to work as PhD-student in his group. Thanks for giving me the freedom to follow any research question that came up along the way and for guiding me through the various challenges and topics during the whole time. I thank Prof. Dr. Stefan Glunz for evaluating and examining this thesis. I would finally like to acknowledge the acceptance of Prof. Dr. Thomas Hanemann and Prof. Dr. Oliver Paul as assessor and chair of the PhD-committee and their time and interest in the research topic of this thesis.

Finally, I would like to thank my family and Matthias for the endless support and believe in me during the last years. You were always able to keep me grounded to not forget the truly important things in life.



## References

1. M. Bühler, P. Holzapfel, D. McLaughlin and S. Thiele, *J. Electrochem. Soc.*, **166**(14), F1070-F1078 (2019).
2. M. Bühler, F. Hegge, P. Holzapfel, M. Bierling, M. Suermann, S. Vierrath and S. Thiele, *J. Mater. Chem. A*, **165**, F305 (2019).
3. Pham, C.\*, Bühler, M.\*, Knöppel, J., Bierling, M., Seeberger, D., Escalera-López, D., Mayrhofer, K. J. J., Cherevko, S., and Thiele, S, *IrO<sub>2</sub> coated TiO<sub>2</sub> core-shell microparticles advance performance of low loading proton exchange membrane water electrolyzers* (2019, submitted manuscript).
4. Holzapfel, P. \*, Bühler, M. \*, Escalera-López, D., Bierling, M., Speck, F., Vierrath, S., Breitwieser, M., Cherevko, S., Pham, C. and Thiele, S., *Fabrication of a robust PEM water electrolyzer based on non-noble metal cathode catalyst: [Mo<sub>3</sub>S<sub>13</sub>]<sup>2-</sup> anchored to N-doped carbon nanotubes* (2019, submitted manuscript).
5. Holzapfel, P., Bühler, M., Pham, C.V., Hegge, F., Böhm, T., McLaughlin, D., Breitwieser, M. and Thiele, S., *Directly coated membrane electrode assemblies for proton exchange membrane water electrolysis* (2019, submitted manuscript).
6. M. Bühler, C. Klose, F. Hegge, T. Lickert and S. Thiele, *ECS Trans.*, **80**(8), 1069–1075 (2017).
7. J. T. Houghton, G. J. Jenkins and J. J. Ephraums, *Climate change*, Published for the Intergovernmental Panel on Climate Change[by]Cambridge University Press (1990).
8. P. M. Vitousek, *Ecology*, **75**(7), 1861–1876 (1994).
9. F. B. Wood, *Bull. Amer. Meteor. Soc.*, **71**(1), 42–52 (1990).
10. B. R. Mackenzie and D. Schiedeck, *Global Change Biol*, **13**(7), 1335–1347 (2007).
11. L. Hughes, *Trends in Ecology & Evolution*, **15**(2), 56–61 (2000).
12. D. R. Stille, *The greenhouse effect*, COMPASS POINT Books (2007).
13. S. H. Schneider, *Science*, **243**(4892), 771–781 (1989).
14. S. L. Horstmeyer, *The weather almanac: A reference guide to weather, climate, and related issues in the united states and its key cities*, Hoboken, N.J., Wiley (2013).
15. J. K. Casper, *Greenhouse gases: Worldwide impacts*, New York, Facts on File (2010).
16. J. L. Ramseur, *Greenhouse gases: Management, reduction, and impact*, New York, Novinka Books (2008).
17. M. A. K. Khalil, *Annu. Rev. Energy. Environ.*, **24**(1), 645–661 (1999).
18. United Nations Framework Convention on Climate Change (UNFCCC), National greenhouse gas inventory data for the period 1990–2017. Report by the secretariat (2019).
19. D.M. Etheridge, L.P. Steele, R.L. Langenfelds, R.J. Francey, J.-M. Barnola and V.I. Morgan, *Historical CO<sub>2</sub> records from the Law Dome DE08, DE08-2, and DSS ice cores. In Trends: A Compendium of Data on Global Change*, Carbon Dioxide Information Analysis Center, Oak Ridge National Laboratory, U.S. Department of Energy, Oak Ridge, Tenn., U.S.A. (1998).
20. J. J. McCarthy, *Climate change 2001: Impacts, adaptation and vulnerability ; contribution of Working Group II to the third assessment report of the Intergovernmental Panel on Climate Change*, Cambridge, Cambridge Univ. Press (2001).
21. Stocker T. F., D. Qin, G.-K. Plattner, M. M. B. Tignor, S. K. Allen, J. Boschung, A. Nauels, Y. Xia, V. Bex and P. M. Midgley, *Climate change 2013: the physical science basis: Contribution of Working Group I to the Fifth Assessment Report of the Intergovernmental Panel on Climate Change*, Cambridge, Cambridge University Press (2013).
22. World Meteorological Organization (WMO)(ISSN 2078-0796).
23. <https://de.co2.earth/daily-co2>, (2019-11-06).

24. NOAA National Centers for Environmental Information, *State of the Climate: Global Climate Report for 2018* (2018).
25. S. Oberthür and H. E. Ott, *Das Kyoto-Protokoll: Internationale Klimapolitik für das 21. Jahrhundert*, Wiesbaden, VS Verlag für Sozialwissenschaften; Imprint (2000).
26. J. B. Durkee, *Management of industrial cleaning technology and processes*, Oxford, Elsevier (2006).
27. D. \*Kaniaru, *The Montreal Protocol: celebrating 20 years of environmental progress--ozone layer and climate protection*, England, CameronMay (2008).
28. A. Wysocka-Czubaszek, R. Czubaszek, S. Roj-Rojewski and P. Banaszuk, *J. Ecol. Eng.*, **19**(3), 206–217 (2018).
29. C. Rosenzweig and D. Hillel, *Soil Science*, **165**(1), 47–56 (2000).
30. C. S. Snyder, T. W. Bruulsema, T. L. Jensen and P. E. Fixen, *Agriculture, Ecosystems & Environment*, **133**(3-4), 247–266 (2009).
31. R. A. Houghton, E. A. Davidson and G. M. Woodwell, *Global Biogeochem. Cycles*, **12**(1), 25–34 (1998).
32. L. D. D. Harvey, *Global Warming*, Florence, Routledge (1999).
33. N. Gruber, M. Gloor, S. E. Mikaloff Fletcher, S. C. Doney, S. Dutkiewicz, M. J. Follows, M. Gerber, A. R. Jacobson, F. Joos, K. Lindsay, D. Menemenlis, A. Mouchet, S. A. Müller, J. L. Sarmiento and T. Takahashi, *Global Biogeochem. Cycles*, **23**(1), n/a-n/a (2009).
34. T. M. L. Wigley, *Climatic Change*, **5**(4), 315–320 (1983).
35. M. Stuiver, *Science (New York, N.Y.)*, **202**(4372), 1109 (1978).
36. D. M. Etheridge, L. P. Steele, R. L. Langenfelds, R. J. Francey, J.-M. Barnola and V. I. Morgan, *J. Geophys. Res.*, **101**(D2), 4115–4128 (1996).
37. T. R. Anderson, E. Hawkins and P. D. Jones, *Endeavour*, **40**(3), 178–187 (2016).
38. A. A. Lacis, G. A. Schmidt, D. Rind and R. A. Ruedy, *Science (New York, N.Y.)*, **330**(6002), 356–359 (2010).
39. P. L. Munday, M. I. McCormick and G. E. Nilsson, *The Journal of experimental biology*, **215**(Pt 22), 3865–3873 (2012).
40. O. Hoegh-Guldberg, *J. Geophys. Res.*, **110**(C9), 85 (2005).
41. J. Veron, O. Hoegh-Guldberg, T. M. Lenton, J. M. Lough, D. O. Obura, P. Pearce-Kelly, C. Sheppard, M. Spalding, M. G. Stafford-Smith and A. D. Rogers, *Marine Pollution Bulletin*, **58**(10), 1428–1436 (2009).
42. M. McCulloch, J. Falter, J. Trotter and P. Montagna, *Nature Clim Change*, **2**(8), 623–627 (2012).
43. K. Frieler, M. Meinshausen, A. Golly, M. Mengel, K. Lebek, S. D. Donner and O. Hoegh-Guldberg, *Nature Clim Change*, **3**(2), 165–170 (2013).
44. J. Hansen, M. Sato, P. Hearty, R. Ruedy, M. Kelley, V. Masson-Delmotte, G. Russell, G. Tselioudis, J. Cao, E. Rignot, I. Velicogna, B. Tormey, B. Donovan, E. Kandiano, K. von Schuckmann, P. Kharecha, A. N. Legrande, M. Bauer and K.-W. Lo, *Atmos. Chem. Phys.*, **16**(6), 3761–3812 (2016).
45. M. Brzoska and C. Fröhlich, *Migration and Development*, **5**(2), 190–210 (2015).
46. K. Hastrup and K. Fog Olwig, *Climate Change and Human Mobility*, Cambridge, Cambridge University Press (2012).
47. R. Cléménçon, *The Journal of Environment & Development*, **25**(1), 3–24 (2016).
48. *Energy 2020: A strategy for competitive, sustainable, and secure energy*, Luxembourg, Publications Office (2011).



49. A. Das, L. Emele, F. Meinke-Hubeny, I. Moorkens, C. Nissen and M. Tomescu, *Renewable energy in Europe 2018: Recent growth and knock-on effects*, Luxembourg, Publications Office of the European Union (2018).
50. *Energy roadmap 2050*, Luxembourg, Publications Office of the European Union (2012).
51. M. Beaudin, H. Zareipour, A. Schellenberglobe and W. Rosehart, *Energy for Sustainable Development*, **14**(4), 302–314 (2010).
52. M. Black and G. Strbac, *IEEE Trans. On Energy Conversion*, **22**(1), 197–205 (2007).
53. A. Castillo and D. F. Gayme, *Energy Conversion and Management*, **87**, 885–894 (2014).
54. N.-K. C. Nair and N. Garimella, *Energy and Buildings*, **42**(11), 2124–2130 (2010).
55. A. Ursua, L. M. Gandia and P. Sanchis, *Proc. IEEE*, **100**(2), 410–426 (2012).
56. A. Buttler and H. Spliethoff, *Renewable Sustainable Energy Rev.*, **82**, 2440–2454 (2018).
57. A. Godula-Jopek, Editor, *Hydrogen Production: By Electrolysis*, Weinheim, WILEY-VCH (2015).
58. B. Pivovar, N. Rustagi and S. Satyapal, *Electrochem. Soc. Interface*, **27**(1), 47–52 (2018).
59. M. Ball and M. Wietschel, *The Hydrogen Economy: Opportunities and Challenges*, Cambridge University Press (2009).
60. F. Barbir, *Energy*, **34**(3), 308–312 (2009).
61. B. L. Salvi and K. A. Subramanian, *Renewable and Sustainable Energy Reviews*, **51**, 1132–1155 (2015).
62. P. D. Stolten and D. B. Emonts, *Hydrogen Science and Engineering: Materials, Processes, Systems and Technology*, Weinheim, Germany, Wiley-VCH Verlag GmbH & Co. KGaA (2016).
63. G. Gahleitner, *International Journal of Hydrogen Energy*, **38**(5), 2039–2061 (2013).
64. M. Götz, J. Lefebvre, F. Mörs, A. McDaniel Koch, F. Graf, S. Bajohr, R. Reimert and T. Kolb, *Renewable Energy*, **85**, 1371–1390 (2016).
65. IEA, *Technology Roadmap Hydrogen and Fuel Cells*, 2015 (2015).
66. M. Kopp, D. Coleman, C. Stiller, K. Scheffer, J. Aichinger and B. Scheppat, *International Journal of Hydrogen Energy*, **42**(19), 13311–13320 (2017).
67. D. G. Bessarabov and P. Millet, *PEM water electrolysis*, Amsterdam, Academic press (2018).
68. J. van Straelen, F. Geuzebroek, N. Goodchild, G. Protopapas and L. Mahony, *International Journal of Greenhouse Gas Control*, **4**(2), 316–320 (2010).
69. M. Schalenbach, G. Tjarks, M. Carmo, W. Lueke, M. Mueller and D. Stolten, *J. Electrochem. Soc.*, **163**(11), F3197-F3208 (2016).
70. K. Zeng and D. Zhang, *Progress in Energy and Combustion Science*, **36**(3), 307–326 (2010).
71. M. Sankir and N. D. Sankir, *Hydrogen Production Technologies*, John Wiley & Sons (US) (2017).
72. U. Babic, M. Suermann, F. N. Büchi, L. Gubler and T. J. Schmidt, *J. Electrochem. Soc.*, **164**(4), F387-F399 (2017).
73. M. David, C. Ocampo-Martínez and R. Sánchez-Peña, *Journal of Energy Storage*, **23**, 392–403 (2019).
74. S. Shiva Kumar and V. Himabindu, *Materials Science for Energy Technologies*, **2**(3), 442–454 (2019).
75. F. Tietz, D. Sebold, A. Brisse and J. Schefold, *Journal of Power Sources*, **223**, 129–135 (2013).
76. D. G. Bessarabov, H. H. Wang, H. Li and N. Zhao, Editors, *PEM electrolysis for hydrogen production: Principles and applications*, Boca Raton, CRC Press (2016).
77. K. Frölich, *Der Decal-Prozess zur Herstellung katalysatorbeschichteter Membranen für PEM-Brennstoffzellen*, KIT Scientific Publishing (2015).

78. H. J. Cho, H. Jang, S. Lim, E. Cho, T.-H. Lim, I.-H. Oh, H.-J. Kim and J. H. Jang, *Int. J. Hydrogen Energy*, **36**(19), 12465–12473 (2011).
79. M. Bernt, A. Siebel and H. A. Gasteiger, *J. Electrochem. Soc.*, **165**(5), F305-F314 (2018).
80. P. Millet, A. Ranjbari, F. de Guglielmo, S. A. Grigoriev and F. Auprêtre, *HySafe 1*, **37**(22), 17478–17487 (2012).
81. M. Klingele, S. Vierrath, M. Breitwieser, C. Klose and S. Thiele, *ECS Transactions*, **80**(8), 571–576 (2017).
82. F. Barbir, *Solar Energy*, **78**(5), 661–669 (2005).
83. P. Millet, N. Mbemba, S. A. Grigoriev, V. N. Fateev, A. Aukauloo and C. Etiévant, *3rd International Workshop in Hydrogen Energy*, **36**(6), 4134–4142 (2011).
84. H. A. Gasteiger, *Polymer electrolyte fuel cells 14: (PEFC14)*, Pennington, New Jersey, Electrochemical Society (2014).
85. J. O. Majasan, J. I. Cho, I. Dedigama, D. Tsaoulidis, P. Shearing and D. J. Brett, *International Journal of Hydrogen Energy*, **43**(33), 15659–15672 (2018).
86. C. Immerz, M. Paidar, G. Papakonstantinou, B. Bensmann, T. Bystron, T. Vidakovic-Koch, K. Bouzek, K. Sundmacher and R. Hanke-Rauschenbach, *J Appl Electrochem*, **48**(6), 701–711 (2018).
87. M. Bernt and H. A. Gasteiger, *J. Electrochem. Soc.*, **163**(11), F3179-F3189 (2016).
88. K. Sasaki, H.-W. Li, A. Hayashi, J. Yamabe, T. Ogura and S. M. Lyth, *Hydrogen Energy Engineering: A Japanese Perspective*, Tokyo, Springer Japan (2016).
89. D. Stolten, R. C. Samsun and N. Garland, *Fuel cells: Data, facts and figures*, Weinheim, Germany, WILEY-VCH (2016).
90. D. Minic, Editor, *Hydrogen Energy - Challenges and Perspectives*, InTech (2012).
91. K. A. Mauritz and R. B. Moore, *Chem. Rev.*, **104**(10), 4535–4586 (2004).
92. D. E. Curtin, R. D. Lousenberg, T. J. Henry, P. C. Tangeman and M. E. Tisack, *J. Power Sources*, **131**(1-2), 41–48 (2004).
93. X. Ling, M. Bonn, K. F. Domke and S. H. Parekh, *Proceedings of the National Academy of Sciences of the United States of America*, **116**(18), 8715–8720 (2019).
94. G. A. Ludueña, T. D. Kühne and D. Sebastiani, *Chem. Mater.*, **23**(6), 1424–1429 (2011).
95. B. G. Pollet and J. T. Goh, *Electrochimica Acta*, **128**, 292–303 (2014).
96. M. Bernt, A. Siebel and H. A. Gasteiger, *J. Electrochem. Soc.*, **165**(5), F305-F314 (2018).
97. M. Carmo, D. L. Fritz, J. Mergel and D. Stolten, *Int J Hydrogen Energy*, **38**(12), 4901–4934 (2013).
98. J. Zhang, *PEM fuel cell electrocatalysts and catalyst layers: fundamentals and applications*, Springer Science & Business Media (2008).
99. M. Qian and F. H. Froes, *Titanium powder metallurgy: Science, technology and applications*, Waltham, MA, Butterworth-Heinemann is an imprint of Elsevier (2015).
100. J. O. Majasan, F. Iacoviello, P. R. Shearing and Brett, Dan J. L., *Energy Procedia*, **151**, 111–119 (2018).
101. S. A. Grigoriev, P. Millet, S. A. Volobuev and V. N. Fateev, *Int. J. Hydrogen Energy*, **34**(11), 4968–4973 (2009).
102. P. Lettenmeier, S. Kolb, F. Burggraf, A. S. Gago and K. A. Friedrich, *J. Power Sources*, **311**, 153–158 (2016).
103. T. Schuler, R. de Bruycker, T. J. Schmidt and F. N. Büchi, *Journal of The Electrochemical Society*, **166**(4), F270-F281 (2019).
104. D. G. Bessarabov, H. Wang, H. Li and N. Zhao, *PEM electrolysis for hydrogen production: Principles and applications*, Boca Raton, Florida, CRC Press (2016).

105. C. E. Mortimer, U. Müller and J. Beck, *Chemie: Das Basiswissen der Chemie : 410 Abbildungen, 545 Formelbilder*, Stuttgart, New York, Georg Thieme Verlag (2015).
106. I. Dedigama, K. Ayers, P. R. Shearing and D. J. L. Brett, *International Journal of Electrochemical Science*, **9**, 2662–2681 (2014).
107. J. J. Spivey and K. M. Dooley, *Catalysis: A review of recent literature*, Cambridge, The Royal Society of Chemistry (2011).
108. J. O. Bockris, *The Journal of Chemical Physics*, **24**(4), 817–827 (1956).
109. J. Ahn and R. Holze, *J. Appl. Electrochem.*, **22**(12), 1167–1174 (1992).
110. J. Durst, A. Siebel, C. Simon, F. Hasché, J. Herranz and H. A. Gasteiger, *Energy Environ. Sci.*, **7**(7), 2255–2260 (2014).
111. T. Schuler, T. J. Schmidt and F. N. Büchi, *Journal of The Electrochemical Society*, **166**(10), F555-F565 (2019).
112. P. Trinke, G. P. Keeley, M. Carmo, B. Bensmann and R. Hanke-Rauschenbach, *J. Electrochem. Soc.*, **166**(8), F465-F471 (2019).
113. Schroeder, V. and Holtappels, K., *International Conference on Hydrogen Safety*, **2005**.
114. A. Nouri-Khorasani, E. Tabu Ojong, T. Smolinka and D. P. Wilkinson, *International Journal of Hydrogen Energy*, **42**(48), 28665–28680 (2017).
115. X. Li, X. Hao, A. Abudula and G. Guan, *J. Mater. Chem. A*, **4**(31), 11973–12000 (2016).
116. Y.-T. Kim, K. Ohshima, K. Higashimine, T. Uruga, M. Takata, H. Suematsu and T. Mitani, *Angewandte Chemie (International ed. in English)*, **45**(3), 407–411 (2006).
117. R. Sha, S. Solomon Jones and S. Badhulika, *Surface and Coatings Technology*, **360**, 400–408 (2019).
118. K. Yamagiwa and J. Kuwano, *Materials Chemistry and Physics*, **204**, 323–327 (2018).
119. P. Paciok, M. Schalenbach, M. Carmo and D. Stolten, *Journal of Power Sources*, **365**, 53–60 (2017).
120. Y. Zhang, M. L. Toebe, A. van der Eerden, W. E. O'Grady, K. P. de Jong and D. C. Koningsberger, *J. Phys. Chem. B*, **108**(48), 18509–18519 (2004).
121. J. Wang, G. Yin, Y. Shao, S. Zhang, Z. Wang and Y. Gao, *Journal of Power Sources*, **171**(2), 331–339 (2007).
122. F.-D. Kong, S. Zhang, G.-P. Yin, J. Liu and Z.-Q. Xu, *International Journal of Hydrogen Energy*, **38**(22), 9217–9222 (2013).
123. C. V. Pham, A. Zana, M. Arenz and S. Thiele, *ChemElectroChem*, **38**, 4901 (2018).
124. Y. Zeng, X. Guo, Z. Shao, H. Yu, W. Song, Z. Wang, H. Zhang and B. Yi, *Journal of Power Sources*, **342**, 947–955 (2017).
125. T. Audichon, T. W. Napporn, C. Canaff, C. Morais, C. Comminges and K. B. Kokoh, *J. Phys. Chem. C*, **120**(5), 2562–2573 (2016).
126. V. A. Saveleva, L. Wang, W. Luo, S. Zafeiratos, C. Ulhaq-Bouillet, A. S. Gago, K. A. Friedrich and E. R. Savinova, *The Journal of Physical Chemistry Letters*, **7**(16), 3240–3245 (2016).
127. M. Faustini, M. Giraud, D. Jones, J. Rozière, M. Dupont, T. R. Porter, S. Nowak, M. Bahri, O. Ersen, C. Sanchez, C. Boissière, C. Tard and J. Peron, *Adv. Energy Mater.*, **9**(4), 1802136 (2019).
128. C. Rozain, E. Mayousse, N. Guillet and P. Millet, *Applied Catalysis B: Environmental*, **182**, 153–160 (2016).
129. P. Mazúr, J. Polonský, M. Paidar and K. Bouzek, *International Journal of Hydrogen Energy*, **37**(17), 12081–12088 (2012).
130. E. Oakton, D. Lebedev, M. Povia, D. F. Abbott, E. Fabbri, A. Fedorov, M. Nachtegaal, C. Copéret and T. J. Schmidt, *ACS Catal.*, **7**(4), 2346–2352 (2017).

131. L. Wang, P. Lettenmeier, U. Golla-Schindler, P. Gazdzicki, N. A. Canas, T. Morawietz, R. Hiesgen, S. S. Hosseiny, A. S. Gago and K. A. Friedrich, *Physical chemistry chemical physics : PCCP*, **18**(6), 4487–4495 (2016).
132. H. Yoo, K. Oh, Y. R. Lee, K. H. Row, G. Lee and J. Choi, *International Journal of Hydrogen Energy*, **42**(10), 6657–6664 (2017).
133. Z. Kang, J. Mo, G. Yang, S. T. Retterer, D. A. Cullen, T. J. Toops, J. B. Green Jr, M. M. Mench and F.-Y. Zhang, *Energy Environ. Sci.* (2016).
134. J. Polonský, P. Mazúr, M. Paidar, E. Christensen and K. Bouzek, *Int J Hydrogen Energ*, **39**(7), 3072–3078 (2014).
135. S. Choe, B.-S. Lee, M. K. Cho, H.-J. Kim, D. Henkensmeier, S. J. Yoo, J. Y. Kim, S. Y. Lee, H. S. Park and J. H. Jang, *Applied Catalysis B: Environmental*, **226**, 289–294 (2018).
136. Bidaux.
137. Z. S. Rak and J. Walter, *Journal of Materials Processing Technology*, **175**(1-3), 358–363 (2006).
138. L.-j. CHEN, T. LI, Y.-m. LI, H. HE and Y.-h. HU, *Transactions of Nonferrous Metals Society of China*, **19**(5), 1174–1179 (2009).
139. C. Rakousky, U. Reimer, K. Wippermann, M. Carmo, W. Lueke and D. Stolten, *J. Power Sources*, **326**, 120–128 (2016).
140. M. Suermann, B. Bensmann and R. Hanke-Rauschenbach, *J. Electrochem. Soc.*, **166**(10), F645-F652 (2019).
141. M. Suermann, T. J. Schmidt and F. N. Büchi, *Electrochim. Acta*, **211**, 989–997 (2016).
142. N. Eliaz and E. Gileadi, *Physical electrochemistry: Fundamentals, techniques and applications*, Weinheim, Germany, Wiley-VCH Velag (2019).
143. N. Dubouis and A. Grimaud, *Chem. Sci.*, **10**(40), 9165–9181 (2019).
144. Y. Leng, *Materials characterization: Introduction to microscopic and spectroscopic methods*, Singapore, J. Wiley & Sons (2009).
145. S. K. Sharma, D. Singh Verma, S. Kumar, S. Bahadar Khan and L. Ullah Khan, *Handbook of materials characterization*, Cham, Springer International Publishing AG, part of Springer Nature (2018).
146. S. Zhang, L. Li and A. Kumar, *Materials characterization techniques*, Boca Raton, CRC Press (2009).
147. F. Hegge, R. Moroni, P. Trinke, B. Bensmann, R. Hanke-Rauschenbach, S. Thiele and S. Vierrath, *Journal of Power Sources*, **393**, 62–66 (2018).
148. M. Feng, R. Qu, Z. Wei, L. Wang, P. Sun and Z. Wang, *Sci. Rep.*, **5**, 9859 (2015).
149. <https://clarivate.com/webofsciencegroup/blog/announcing-the-2019-journal-citation-reports> (2019-11-21).
150. L. Zielke, A. Fallisch, N. Paust, R. Zengerle and S. Thiele, *RSC Adv.*, **4**(102), 58888–58894 (2014).
151. N. Zamel and X. Li, *Prog. Energy Combust. Sci.*, **39**(1), 111–146 (2013).
152. Z. Kang, G. Yang, J. Mo, Y. Li, S. Yu, D. A. Cullen, S. T. Retterer, T. J. Toops, G. Bender, B. S. Pivovar, J. B. Green and F.-Y. Zhang, *Nano Energy*, **47**, 434–441 (2018).
153. E. Slavcheva, I. Radev, S. Bliznakov, G. Topalov, P. Andreev and E. Budevski, *Electrochimica Acta*, **52**(12), 3889–3894 (2007).
154. B.-S. Lee, S. H. Ahn, H.-Y. Park, I. Choi, S. J. Yoo, H.-J. Kim, D. Henkensmeier, J. Y. Kim, S. Park, S. W. Nam, K.-Y. Lee and J. H. Jang, *Applied Catalysis B: Environmental*, **179**, 285–291 (2015).
155. F. M. Sapountzi, S. C. Divane, E. I. Papaioannou, S. Souentie and C. G. Vayenas, *Journal of Electroanalytical Chemistry*, **662**(1), 116–122 (2011).

156. A. Weiß, A. Siebel, M. Bernt, T.-H. Shen, V. Tileli and H. A. Gasteiger, *J. Electrochem. Soc.*, **166**(8), F487-F497 (2019).
157. Q. Feng, X. Yuan, G. Liu, B. Wei, Z. Zhang, H. Li and H. Wang, *Journal of Power Sources*, **366**, 33–55 (2017).
158. Y. Zhang, C. Wang, N. Wan, Z. Liu and Z. Mao, *Electrochem. Commun.*, **9**(4), 667–670 (2007).
159. S. Song, H. Zhang, B. Liu, P. Zhao, Y. Zhang and B. Yi, *Electrochem. Solid-State Lett.*, **10**(8), B122 (2007).
160. M. Feng, R. Qu, Z. Wei, L. Wang, P. Sun and Z. Wang, *Sci. Rep.*, **5**, 9859 (2015).
161. J. S. Santos, I. M. Raimundo, C. M. Cordeiro, C. R. Biazoli, C. A. Gouveia and P. A. Jorge, *Sens. Actuators B Chem.*, **196**, 99–105 (2014).
162. S. H. Wiersma, P. Török, T. D. Visser and P. Varga, *J. Opt. Soc. Am. A*, **14**(7), 1482 (1997).
163. M. Suermann, K. Takanohashi, A. Lamibrac, T. J. Schmidt and F. N. Büchi, *J. Electrochem. Soc.*, **164**(9), F973-F980 (2017).
164. U. Babic, E. Nilsson, A. Pătru, T. J. Schmidt and L. Gubler, *J. Electrochem. Soc.*, **166**(4), F214-F220 (2019).
165. H. Yu, N. Danilovic, Y. Wang, W. Willis, A. Poozhikunnath, L. Bonville, C. Capuano, K. Ayers and R. Maric, *Applied Catalysis B: Environmental*, **239**, 133–146 (2018).
166. S. M. Alia, S. Shulda, C. Ngo, S. Pylypenko and B. S. Pivovar, *ACS Catal.*, **8**(3), 2111–2120 (2018).
167. M. Breitwieser, M. Klingele, S. Vierrath, R. Zengerle and S. Thiele, *Adv. Energy Mater.*, **38**, 1701257 (2017).
168. L. Cindrella, A. M. Kannan, J. F. Lin, K. Saminathan, Y. Ho, C. W. Lin and J. Wertz, *Journal of Power Sources*, **194**(1), 146–160 (2009).
169. C. Liu, M. Carmo, G. Bender, A. Everwand, T. Lickert, J. L. Young, T. Smolinka, D. Stolten and W. Lehnert, *Electrochemistry Communications*, **97**, 96–99 (2018).
170. T. Bystron, M. Vesely, M. Paidar, G. Papakonstantinou, K. Sundmacher, B. Bensmann, R. Hanke-Rauschenbach and K. Bouzek, *J Appl Electrochem*, **48**(6), 713–723 (2018).
171. J. Mo, Z. Kang, S. T. Retterer, D. A. Cullen, T. J. Toops, J. B. Green, JR, M. M. Mench and F.-Y. Zhang, *Science Advances*, **2**(11), e1600690 (2016).
172. P. Liu and G.-F. Chen, *Porous materials: Processing and applications*, Amsterdam, Boston, Paris, Elsevier; Butterworth-Heinemann (2014).
173. L. Ma, S. SUI and Y. ZHAI, *International Journal of Hydrogen Energy*, **34**(2), 678–684 (2009).
174. W. Xu and K. Scott, *International Journal of Hydrogen Energy*, **35**(21), 12029–12037 (2010).
175. M. Bernt and H. A. Gasteiger, *J. Electrochem. Soc.*, **163**(11), F3179-F3189 (2016).
176. H. Su, V. Linkov and B. J. Bladergroen, *International Journal of Hydrogen Energy*, **38**(23), 9601–9608 (2013).
177. M. Carmo, D. L. Fritz, J. Mergel and D. Stolten, *International Journal of Hydrogen Energy*, **38**(12), 4901–4934 (2013).
178. C. Spöri, J. T. H. Kwan, A. Bonakdarpour, D. P. Wilkinson and P. Strasser, *Angewandte Chemie (International ed. in English)*, **56**(22), 5994–6021 (2017).
179. J. Soriano-López, S. Goberna-Ferrón, L. Vígara, J. J. Carbó, J. M. Poblet and J. R. Galán-Mascarós, *Inorganic Chemistry*, **52**(9), 4753–4755 (2013).
180. J. S. Mondschein, K. Kumar, C. F. Holder, K. Seth, H. Kim and R. E. Schaak, *Inorganic Chemistry*, **57**(10), 6010–6015 (2018).
181. M. Blasco-Ahicart, J. Soriano-López, J. J. Carbó, J. M. Poblet and J. R. Galan-Mascaros, *Nature Chemistry*, **10**(1), 24–30 (2018).

182. L. Wang, V. A. Saveleva, S. Zafeiratos, E. R. Savinova, P. Lettenmeier, P. Gazdzicki, A. S. Gago and K. A. Friedrich, *Nano Energy*, **34**, 385–391 (2017).
183. S. Siracusano, N. van Dijk, E. Payne-Johnson, V. Baglio and A. S. Aricò, *Applied Catalysis B: Environmental*, **164**, 488–495 (2015).
184. H. Su, V. Linkov and B. J. Bladergroen, *International Journal of Hydrogen Energy*, **38**(23), 9601–9608 (2013).
185. S. Siracusano, V. Baglio, S. A. Grigoriev, L. Merlo, V. N. Fateev and A. S. Aricò, *Journal of Power Sources*, **366**, 105–114 (2017).
186. S. Siracusano, N. Hodnik, P. Jovanovic, F. Ruiz-Zepeda, M. Šala, V. Baglio and A. S. Aricò, *Nano Energy*, **40**, 618–632 (2017).
187. O. Kasian, S. Geiger, P. Stock, G. Polymeros, B. Breitbach, A. Savan, A. Ludwig, S. Cherevko and Mayrhofer, Karl J. J., *Journal of The Electrochemical Society*, **163**(11), F3099-F3104 (2016).
188. C. Rozain, E. Mayousse, N. Guillet and P. Millet, *Applied Catalysis B: Environmental*, **182**, 123–131 (2016).
189. F. Karimi and B. A. Peppley, *Electrochimica Acta*, **246**, 654–670 (2017).
190. G. Liu, J. Xu, Y. Wang and X. Wang, *J. Mater. Chem. A*, **3**(41), 20791–20800 (2015).
191. S. Geiger, O. Kasian, A. M. Mingers, Mayrhofer, Karl J. J. and S. Cherevko, *Scientific reports*, **7**(1), 4595 (2017).
192. C. Hao, H. Lv, Q. Zhao, B. Li, C. Zhang, C. Mi, Y. Song and J. Ma, *International Journal of Hydrogen Energy*, **42**(15), 9384–9395 (2017).
193. G. Li, K. Li, L. Yang, J. Chang, R. Ma, Z. Wu, J. Ge, C. Liu and W. Xing, *ACS Appl. Mater. Interfaces* (2018).
194. H.-S. Oh, H. N. Nong, T. Reier, A. Bergmann, M. Gliech, J. Ferreira de Araújo, E. Willinger, R. Schlögl, D. Teschner and P. Strasser, *Journal of the American Chemical Society*, **138**(38), 12552–12563 (2016).
195. E. Oakton, D. Lebedev, M. Povia, D. F. Abbott, E. Fabbri, A. Fedorov, M. Nachtegaal, C. Copéret and T. J. Schmidt, *ACS Catal.*, **7**(4), 2346–2352 (2017).
196. B. M. Tackett, W. Sheng, S. Kattel, S. Yao, B. Yan, K. A. Kuttiyiel, Q. Wu and J. G. Chen, *ACS Catal.*, **8**(3), 2615–2621 (2018).
197. L. C. Seitz, C. F. Dickens, K. Nishio, Y. Hikita, J. Montoya, A. Doyle, C. Kirk, A. Vojvodic, H. Y. Hwang, J. K. Nørskov and T. F. Jaramillo, *Science*, **353**(6303), 1011–1014 (2016).
198. H. N. Nong, L. Gan, E. Willinger, D. Teschner and P. Strasser, *Chem. Sci.*, **5**(8), 2955–2963 (2014).
199. S. Geiger, O. Kasian, M. Ledendecker, E. Pizzutilo, A. M. Mingers, W. T. Fu, O. Diaz-Morales, Z. Li, T. Oellers, L. Fruchter, A. Ludwig, Mayrhofer, Karl J. J., M. T. M. Koper and S. Cherevko, *Nat Catal*, **1**(7), 508–515 (2018).
200. M. Ledendecker, S. Geiger, K. Hengge, J. Lim, S. Cherevko, A. M. Mingers, D. Göhl, G. V. Fortunato, D. Jalalpoor, F. Schüth, C. Scheu and Mayrhofer, Karl J. J., *Nano Res.*, **163**, F3099 (2019).
201. S. Geiger, O. Kasian, B. R. Shrestha, A. M. Mingers, Mayrhofer, Karl J. J. and S. Cherevko, *Journal of The Electrochemical Society*, **163**(11), F3132-F3138 (2016).
202. Y. Wang, J. Ren, K. Deng, L. Gui and Y. Tang, *Chem. Mater.*, **12**(6), 1622–1627 (2000).
203. S. Neumann, S. Grotheer, J. Tielke, I. Schrader, J. Quinson, A. Zana, M. Oezaslan, M. Arenz and S. Kunz, *J. Mater. Chem. A*, **5**(13), 6140–6145 (2017).
204. M. Breitwieser, M. Klingele, C. Klose, S. Vierrath, R. Zengerle and S. Thiele, *EMEA-Conference*, Bad Zwischenahn (2017).

205. M. H. Zare, N. Hajilary and M. Rezakazemi, *Materials Science for Energy Technologies*, **2**(1), 89–95 (2019).
206. M. Stähler, A. Stähler, F. Scheepers, M. Carmo and D. Stolten, *International Journal of Hydrogen Energy*, **44**(14), 7053–7058 (2019).
207. L. Bertuccioli, A. Chan, F. Hart, F. Lehner, B. Madden and E. Staden, **2014**.
208. B. Hinnemann, P. G. Moses, J. Bonde, K. P. Jørgensen, J. H. Nielsen, S. Horch, I. Chorkendorff and J. K. Nørskov, *J. Am. Ceram. Soc.*, **127**(15), 5308–5309 (2005).
209. J. W. D. Ng, T. R. Hellstern, J. Kibsgaard, A. C. Hinckley, J. D. Benck and T. F. Jaramillo, *ChemSusChem*, **8**(20), 3512–3519 (2015).
210. T. Corrales-Sánchez, J. Ampurdanés and A. Urakawa, *International Journal of Hydrogen Energy*, **39**(35), 20837–20843 (2014).
211. J. H. Kim, H. Kim, J. Kim, H. J. Lee, J. H. Jang and S. H. Ahn, *Journal of Power Sources*, **392**, 69–78 (2018).
212. T. F. Jaramillo, K. P. Jørgensen, J. Bonde, J. H. Nielsen, S. Horch and I. Chorkendorff, *Science*, **317**(5834), 100–102 (2007).
213. D. Gopalakrishnan, D. Damien and M. M. Shaijumon, *ACS Nano*, **8**(5), 5297–5303 (2014).
214. J. Kibsgaard, T. F. Jaramillo and F. Besenbacher, *Nat. Chem.*, **6**(3), 248–253 (2014).
215. A. K. Geim and K. S. Novoselov, *Nat. Mater.*, **6**(3), 183–191 (2007).
216. S. Pei and H.-M. Cheng, *Carbon*, **50**(9), 3210–3228 (2012).
217. C. V. Pham, M. Eck and M. Krueger, *Chem. Eng. J.*, **231**, 146–154 (2013).
218. A. Capezza, R. L. Andersson, V. Ström, Q. Wu, B. Sacchi, S. Farris, M. S. Hedenqvist and R. T. Olsson, *ACS Omega*, **4**(2), 3458–3468 (2019).
219. L. A. King, M. A. Hubert, C. Capuano, J. Manco, N. Danilovic, E. Valle, T. R. Hellstern, K. Ayers and T. F. Jaramillo, *Nature Nanotechnology* (2019).
220. S. Vierrath, M. Breitwieser, M. Klingele, B. Britton, S. Holdcroft, R. Zengerle and S. Thiele, *J. Power Sources*, **326**, 170–175 (2016).
221. K. E. Ayers, C. Capuano and E. B. Anderson. in *220th ECS Meeting*, p. 15, ECS (2012).





## Erklärung

„Ich erkläre hiermit, dass ich die vorliegende Arbeit ohne unzulässige Hilfe Dritter und ohne Benutzung anderer als der angegebenen Hilfsmittel angefertigt habe. Die aus anderen Quellen direkt oder indirekt übernommenen Daten und Konzepte sind unter Angabe der Quelle gekennzeichnet. Insbesondere habe ich hierfür nicht die entgeltliche Hilfe von Vermittlungs- oder Beratungsdiensten (Promotionsberaterinnen oder Promotionsberater oder anderer Personen) in Anspruch genommen.

Niemand hat von mir unmittelbar oder mittelbar geldwerte Leistungen für Arbeiten erhalten, die im Zusammenhang mit dem Inhalt der vorgelegten Dissertation stehen. Die Arbeit wurde bisher weder im In- noch im Ausland in gleicher oder ähnlicher Form einer anderen Prüfungsbehörde vorgelegt.“

Freiburg, den





